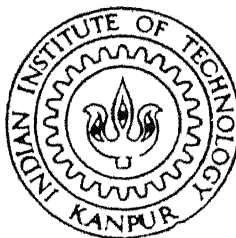


Effect of Grain Size and Microstructural Correlations in the Plastic Behaviour of 316L Austenitic Stainless Steel

by

KAMLESH KUMAR SINGH

TH
MME/1998/P
Sic4e



DEPARTMENT OF MATERIALS AND METALLURGICAL ENGINEERING
INDIAN INSTITUTE OF TECHNOLOGY KANPUR

APRIL, 1998

Effect of Grain Size and Microstructural Correlations in the Plastic Behaviour of 316L Austenitic Stainless Steel

A Thesis Submitted

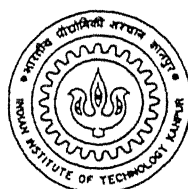
in Partial Fulfilment of the Requirements

for the Degree of

Doctor of Philosophy

by

Kamlesh Kumar Singh

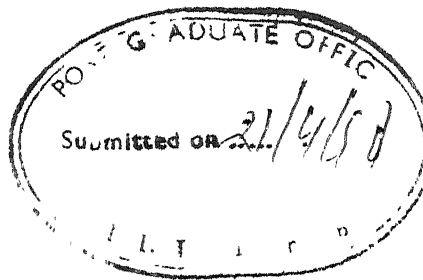


to the

DEPARTMENT OF MATERIALS AND METALLURGICAL ENGINEERING

INDIAN INSTITUTE OF TECHNOLOGY KANPUR

April, 1998



C E R T I F I C A T E

It is certified that the work contained in this thesis entitled "Effect of Grain Size and Microstructural Correlations in the Plastic Behaviour of 316L Austenitic Stainless Steel", by Kamlesh Kumar Singh, has been carried out under our supervision and that this work has not been submitted elsewhere for any degree.

Dr. S. Sangal
Associate Professor
Department of Materials and
Metallurgical Engg.
Indian Institute of Technology
Kanpur

Dr. G. S. Murty,
Professor (Retd.)
Department of Materials and
Metallurgical Engg.
Indian Institute of Technology
Kanpur

March, 1998

[4 AUG 1999] MME
CENTRAL LIBRARY
I. I. T., KANPUR

Vol. No. A 128771

TH
MME/1998/1
S1611



A128771

Dedicated to -

Srila Prabhupada

(for enlightenment through his teachings)

My Parents

Shree Rameshwar Singh

and

Smt. Panwati Devi

(for their love and blessing)

My wife and lovely son

Mrs. Bharti

and

Kishan

(for their love and caring)

Acknowledgements

It is a great pleasure in expressing my sense of profound gratitude and indebtedness to my thesis supervisors **Dr. S. Sangal** and **Prof. G. S. Murty** for their able guidance, valuable suggestions and constant encouragements which brought forth the culmination of the study.

I acknowledge Dr. S. L. Mannan (IGCAR, Kalpakkam) for kindly providing the stainless steel plate at crucial time. I am extremely thankful to prof. A. Ghosh for allowing me to sit and use his laboratory facility. I also feel grateful for his encouragements and appreciation throughout my thesis work. Help received from the Institute, especially from the Materials and Metallurgical engineering department, is highly acknowledged.

Among the laboratory staff members, my sincere thanks are due to Mr. B. K. Jain, Mr. A. Sharma, Mr. H. C. Srivastva, Dr. M. N. Mongole, Mr. P. K. Pal, Mr. R. P. Singh, Mr. C. Barthwal, Mr. K. P. Mukhargee, Mr. A. Biswas, Mr. K. S. Vamra and Mr. G. S. Sharma for their various help in carrying out the experiment. Help received from Mr. Sadgopan in taking the print out of the thesis is highly acknowledged. I also acknowledge my wife Bharti and sister in-law Ratna for their help in typing of some part of my thesis.

Author would also like to thank his friends Mr. Sudipto Ghosh, Mr. Devendra Singh, Mr. Satyam Suwas, Dr. S. K. Choudhary, Dr. T. K. Roy, Dr. G. G. Roy, Dr. M. Sujata, Dr. B. S. Daniel and Dr. B. Bhattacharya for their support, help and encouragements.

I am extremely thankful to the members of the Bhaktivedanta club especially to Dr. S. Mishra, Mr. S. Ghosh, Mr. P. K. Giri, Mr. Manoranjan Sinha, Mr. P. K. Singh, Dr. S. Bhattacharya, Dr. S. Mandal, Mr. Paritosh, Hare Krishna (both U. G. and P. G.), Varun, Bhaskar, Basudev, Ramgopal, Vijay and all others, who given a wonderful association and truly friendly atmosphere during my stay period in C-203, Hall V and SBRA-C1, IIT Kanpur. I feel greatly indebtedness to others whose names are not mentioned above for their valuable and important contribution directly or indirectly in this study.

Finally, I most gratefully acknowledge my parents for their continuous support in each step of my life, without which its impossible for me to reach at this stage. I am also grateful to my wife, Bharti, for her proper care with love throughout the busy period of this study. I also acknowledge the indirect and most important contribution of my little son, Kishan, for providing refreshment of mind by his innocent talk and smile.

At last, I thanks omnipotent lord Krishna and his associates for their unlimited mercy to keep my mind and health in healthy state during this study. Without their mercy it was certainly impossible for this insignificant soul to produce this work.

I. I. T. Kanpur

Kamlesh Kumar Singh

Contents

List of Figures	xv
List of Tables	xxvii
List of Symbols	xxxi
List of Abbreviation	xxxv
Synopsis	xxxvii
1 Introduction and Objectives	1
2 Plastic deformation of crystalline materials	5
2.1 Plastic deformation of single crystals	5
2.1.1 Slip systems	5
2.1.2 Stress-strain curves of metal crystals	6
2.1.3 Mechanisms of strain hardening	8

2.2	Plastic Deformation of Polycrystals	12
2.2.1	Computation of stress-strain curves	13
2.2.2	Experimental stress-strain curves	15
2.2.3	Effect of temperature on flow stress	18
2.3	Grain size effect in plastic deformation	20
2.3.1	Hall-Petch relation	21
2.3.2	Grain size strengthening models	24
2.3.3	Effect of other microstructural parameters on flow stress	29
2.3.4	Effect of temperature	35
2.3.5	Deviation from Hall-Petch relationship	36
2.3.6	Hall-Petch behaviour in high temperature deformation	38
2.4	Summary	39
3	Experimental procedure	41
3.1	Material	41
3.2	Sample preparation for tensile testing	41
3.2.1	Cold rolling and Machining	41
3.2.2	Heat treatment	42
3.3	Optical and Scanning Electron Microscopy	43

3.3.1	Specimen preparation and examination	43
3.3.2	Quantitative Metallography	44
3.4	Tensile testing	46
3.4.1	At room temperature	46
3.4.2	At elevated temperatures	46
3.5	Hardness measurements	47
4	Results	49
4.1	Characterisation of initial microstructures	50
4.2	Deformation at room temperature	62
4.2.1	Hall-Petch behaviour	62
4.2.2	Microstructural characterisation of deformed samples	68
4.2.3	Microhardness variation in deformed samples	77
4.3	Elevated temperature deformation behaviour	78
4.3.1	Hall-Petch behaviour	90
4.3.2	Microstructural characterisation of deformed samples	105
4.3.3	Microhardness variation in deformed samples	118
4.4	Estimation of true dihedral angle (TDA) distribution	127
4.4.1	Relation between TDA and PDA	127

4.4.2	Probability of intersection of a triple edge with plane of polish . . .	130
4.4.3	Distribution of plane dihedral angles when all the true dihedral angles are 120°	131
4.4.4	Distribution of plane dihedral angles obtained from a distribution of true dihedral angles	135
4.4.5	Transformation of plane dihedral angle distribution to true dihedral angle distribution	139
5	Discussion	143
5.1	Deformation at room temperature	144
5.1.1	Hall-Petch behaviour	144
5.1.2	Effect of strain on Hall-Petch parameters	155
5.2	Deformation at elevated temperature	167
5.2.1	Hall-Petch behaviour	167
5.2.2	Effect of strain on Hall-Petch parameters	173
5.2.3	Effect of temperature on Hall-Petch parameters	190
5.3	Effect of temperature on flow stress	196
5.3.1	A model based on dislocation dynamics to estimate the dislocation density at and in the vicinity of the grain boundaries	202
5.3.2	Comparison of the calculated variation of dislocation density with the observed variation in the flow stress	208

5.4	Strain hardening behaviour	220
5.4.1	Stress-Strain relation	221
5.4.2	Dependence of strain hardening rate on flow stress	223
5.4.3	Effect of grain size and temperature on various parameters of empirical equations	229
6	Conclusions and suggestions	241
	Bibliography	247
	Appendix A: Annealing data of 316L austenitic stainless steel	257
	Appendix B: Probability of orientation in space	261
	Appendix C: Optimization method to minimise a function	263
	Appendix D: Optimization Programs	265
	D.1 Program to generate the coefficients	265
	D.2 Optimization Program to calculate the unknown parameters of linear simultaneous equations by minimising the error	269
	Appendix E: Values of strain hardening parameters	273

List of Figures

2.1	Typical stress-strain curve of a pure FCC metal single crystal.	7
2.2	Experimental stress-strain curves at room temperature of polycrystalline specimens ($d = 0.2mm$) and theoretical stress-strain curves calculated on the basis of (a) Taylor model and (b) Taylor as well as the modified Sachs model [36].	16
2.3	Normalised σ_y against temperature plots for micro-grained 316L austenitic stainless steel [11].	19
2.4	Experimentally observed variation in yield and flow stress with temperature in 316L austenitic stainless steel. The range of temperature corresponding to the jerky flow is shown by the bar [113].	19
2.5	Yield stress-grain size relationship at room temperature [36].	22
2.6	Flow stress (σ_e) dependence on grain size at various strains for 30 at. %Zn brass at room temperature [62].	22
2.7	The dependence of Hall-Petch parameters (a) σ_0 and (b) K on strain [41].	23
2.8	TEM micrographs: (a) showing EGBDs at grain boundary and (b) after annealing in-situ, EGBDs have disappeared [85].	33

2.9	Temperature dependence of the Hall-Petch parameters [88].	36
3.1	Schematic representation of operations to obtain tensile Specimens (all dimensions are in mm)	43
4.1	Vickers hardness vs annealing time for various annealing temperatures in batch 1.	51
4.2	Vickers hardness vs annealing temperature for various annealing times in batch 1.	51
4.3	Mean grain size vs annealing time at various annealing temperatures in batch 1.	52
4.4	Mean grain size vs annealing temperature at various annealing times in batch 1.	52
4.5	Microstructures of annealed samples of batch 1 with grain sizes: (a) $4.5\mu m$ and (b) $26.5\mu m$	53
4.6	Microstructures of annealed samples of batch 2 with grain sizes: (a) $4.0\mu m$ and (b) $29.0\mu m$	53
4.7	Variation of (a) relative frequency and (b) cumulative frequency with normalised equivalent grain diameter ($\frac{d_{eq}}{\bar{d}_{eq}}$) for batch 1.	57
4.8	Variation of (a) relative frequency and (b) cumulative frequency with normalised equivalent grain diameter ($\frac{d_{eq}}{\bar{d}_{eq}}$) for batch 2.	58
4.9	Comparison of (a) relative frequency and (b) cumulative frequency with normalised equivalent grain diameter ($\frac{d_{eq}}{\bar{d}_{eq}}$).	59

4.10 Variation of metallographic parameters: (a) standard deviation of PDA distribution (β_{SD}), (b) relative frequency of $115^0 - 125^0$ class of PDA distribution (β_{120}), (c) grain shape factor (S_F) and (d) coefficient of variation of grain size (C_v) with mean grain size. 60

4.11 Distribution of PDAs in the annealed samples of (a) batch 1 ($d=3.9\mu m$), (b) batch 1 ($d=26.5\mu m$), (c) batch 2 ($d=4.0\mu m$) and (d) batch 2 ($d=29.0\mu m$). 61

4.12 True stress-true strain curves for various grain sizes (batch 1). 64

4.13 True stress-true strain curves for various grain sizes (batch 2). 64

4.14 Comparison of true stress-true strain curves of batch 1 and batch 2 for different grain sizes. 65

4.15 Hall-Petch plots at different strain levels (batch 1). 65

4.16 Hall-Petch plots at different strain levels (batch 2). 66

4.17 Tensile flow stress vs d^{-1} for fine grain regime of batch 1. 67

4.18 Comparison of H-P plots between batch 1 (solid lines) and batch 2 (broken lines) at different strain levels. 67

4.19 Variation of H-P parameters: (a) $\sigma_0(\epsilon)$ and (b) $K(\epsilon)$ with strain in the coarse grain regime of batch 1. 69

4.20 Variation of H-P parameters: (a) $\sigma_0(\epsilon)$ and (b) $K(\epsilon)$ with strain in the fine grain regime of batch 1. 70

4.21 Microstructures of the samples ($d = 29.0\mu m$) deformed at room temperature up to the strains of (a) 5 %, (c) 10 % and (d) 20 %. 73

4.22 Variation of metallographic parameters: (a) standard deviation of PDA distribution (β_{SD}), (b) relative frequency of $115^{\circ} - 125^{\circ}$ degree class of PDA distribution (β_{120}), (c) grain aspect ratio (AR), (d) grain shape factor (S_F) and (e) coefficient of variation of grain size (C_v) with strain.	75
4.23 PDA distribution in the fine grain size ($d = 4.0\mu m$) at strains: (a) 0 %, (b) 5 %, (c) 10 % and (d) 20 %.	76
4.24 PDA distribution in the coarse grain size ($d = 29.0\mu m$) at strains: (a) 0 %, (b) 5 %, (c) 10 % and (d) 20 %.	76
4.25 Microhardness variation at different strain levels across grains of sizes: (a) $18.3\mu m$ (batch 1), (b) $26.4\mu m$ (batch 1) and (c) $29\mu m$ (batch 2). . .	79
4.26 Variation of average microhardness with strain, deformed at room temperature.	80
4.27 True stress-true strain curves for various grain sizes of batch 1 at temperatures: (a) $200^{\circ}C$, (b) $400^{\circ}C$, (c) $600^{\circ}C$ and (d) $800^{\circ}C$	83
4.28 True stress-true strain curves for various grain sizes of batch 2 at temperatures: (a) $400^{\circ}C$ and (b) $800^{\circ}C$	84
4.29 Comparison of flow stress of batch 1 and batch 2 at temperatures: (a) $400^{\circ}C$ and (b) $800^{\circ}C$	85
4.30 True stress-true strain curves at different temperatures (batch 1) for grain sizes: (a) $4.5\mu m$ and (b) $26.4\mu m$	86
4.31 True stress-true strain curves at different temperatures (batch 2) for grain sizes: (a) $4.0\mu m$ and (b) $29.0\mu m$	87

4.32	Normalised flow stress (σ/E) vs temperature (batch 1) at strains: (a) 0.2 %, (b) 2 %, (c) 10 % and (d) 20 %.	89
4.33	Hall-Petch plots at different strain levels (batch 1) for temperatures: (a) 200 °C, (b) 400 °C, (c) 600 °C and (d) 800 °C.	98
4.34	Hall-Petch plots at different strain levels (batch 2) for temperatures: (a) 400 °C and (b) 800 °C.	99
4.35	Tensile flow stress vs d^{-1} for fine grain size of batch 1 at temperatures: (a) 200 °C, (b) 400 °C and (c) 600 °C.	101
4.36	Comparison of H-P plots of batch 1 and batch 2 at different strain levels for temperatures: (a) 400 °C and (b) 800 °C.	102
4.37	Variation of (a) $\sigma_0(\epsilon)$ and (b) $K(\epsilon)$, with strain at different temperatures in the coarse grain size region. The numbers in the brackets indicate the batch number.	103
4.38	Variation of (a) $\sigma_0(\epsilon)$ and (b) $K(\epsilon)$, with strain at different temperatures in the fine grain region of batch 1.	104
4.39	Variation of (a) $\sigma_0(\epsilon)$ and (b) $K(\epsilon)$, with temperature at various strain levels in the coarse grain regime of batch 1.	109
4.40	Variation of (a) $\sigma_0(\epsilon)$ and (b) $K(\epsilon)$, with temperature at various strain levels in the fine grain regime of batch 1.	110
4.41	Microstructures of the samples ($d = 29.0\mu m$) deformed at 400 °C up to the strains of (a) 5 %, (b) 10 % and (c) 20 %.	111
4.42	Microstructures of the samples ($d = 29.0\mu m$) deformed at 800 °C up to the strains of (a) 5 %, (b) 10 % and (c) 20 %.	113

- 4.43 Variation of metallographic parameters: (a) standard deviation of PDA distribution (β_{SD}), (b) relative frequency of $115^0 - 125^0$ class of PDA distribution (β_{120}), (c) grain aspect ratio (AR), (d) grain shape factor (S_F) and (e) coefficient of variation of grain size (C_v) as a function of strain at 400^0C for $d = 29.0\mu m$ 115
- 4.44 Variation of metallographic parameters: (a) standard deviation of PDA distribution (β_{SD}), (b) relative frequency of $115^0 - 125^0$ class of PDA distribution (β_{120}), (c) grain aspect ratio (AR), (d) grain shape factor (S_F) and (e) coefficient of variation of grain size (C_v) as a function of strain at 800^0C for $d = 29.0\mu m$ 116
- 4.45 PDA distribution at 400^0C in the fine grain size ($d = 4.0\mu m$) at % strains: (a) 0, (b) 5, (c) 10 and (d) 20. 117
- 4.46 PDA distribution at 400^0C in the coarse grain size ($d = 29.0\mu m$) at % strains: (a) 0, (b) 5, (c) 10 and (d) 20. 117
- 4.47 PDA distribution at 800^0C in the fine grain size ($d = 4.0\mu m$) at % strains: (a) 0, (b) 5, (c) 10 and (d) 20. 119
- 4.48 PDA distribution at 800^0C in the coarse grain size ($d = 29.0\mu m$) at % strains: (a) 0, (b) 5, (c) 10 and (d) 20. 119
- 4.49 Variation of metallographic parameters: (a) standard deviation of PDA distribution (β_{SD}), (b) relative frequency of $115^0 - 125^0$ class of PDA distribution (β_{120}), (c) grain aspect ratio (AR), (d) grain shape factor (S_F) and (e) coefficient of variation of grain size (C_v) as a function of temperature at 5 % strain for $d = 29.0 \mu m$ 120

4.50 Variation of metallographic parameters: (a) standard deviation of PDA distribution (β_{SD}), (b) relative frequency of $115^0 - 125^0$ class of PDA distribution (β_{120}), (c) grain aspect ratio (AR), (d) grain shape factor (S_f) and (e) coefficient of variation of grain size (C_v) as a function of temperature at 10 % strain for $d = 29.0 \mu m$ 121

4.51 Variation of metallographic parameters: (a) standard deviation of PDA distribution (β_{SD}), (b) relative frequency of $115^0 - 125^0$ class of PDA distribution (β_{120}), (c) grain aspect ratio (AR), (d) grain shape factor (S_f) and (e) coefficient of variation of grain size (C_v) as a function of temperature at 20 % strain for $d = 29.0 \mu m$ 122

4.52 Microhardness variation across grains, $d = 29 \mu m$ (batch 2) at different strain levels for temperatures: (a) 400^0C and (b) 800^0C 123

4.53 Variation of microhardness across grains ($d = 29 \mu m$) at different temperatures for strains: (a) 5 % , (b) 10 % and (c) 20 % 125

4.54 Variation of microhardness (a) with strain and (b) with temperature in the sample of $29.0\mu m$ grain size. 126

4.55 A random section through two grain boundary planes meeting at an angle of α . The normal to the plane of section makes an angle θ with the Z- axis and the projection of the normal on the XY- plane makes an angle ϕ with the X- axis. The line of intersection of grain boundaries on plane of polish makes an angle β 129

4.56 A triple edge in an unit cube and the sectioning plane is parallel to the XY- plane 131

4.57 Randomly oriented triple edges in an unit cube and sectioning plane is parallel to the XY-plane. 133

4.58	The distribution of PDAs for 120° TDA (ideal case).	134
4.59	The distribution of PDA for TDAs: (a) 110° and (b) 130° .	136
5.1	Distribution of TDAs, in annealed samples of batch 1 with grain sizes (a) $3.9\mu\text{m}$ and (b) $26.5\mu\text{m}$ and in annealed samples of batch 2 with grain sizes (c) $4.0\mu\text{m}$ and (d) $29.0\mu\text{m}$.	147
5.2	Variation of different parameters of TDA distribution: (a) standard deviation (b) relative frequency of 120° class (c) relative frequency of 110° class and (d) relative frequency of 130° class with grain size.	148
5.3	Reanalysis of Kashyap <i>et al.</i> [41] data: (a) $\sigma(\epsilon)$ vs $d^{-1/2}$ and (b) $\sigma(\epsilon)$ vs d^{-1} in the fine grain regime.	152
5.4	TEM micrographs of the samples of 316L austenitic stainless steel ($d = 86.7\mu\text{m}$) deformed at room temperature up to strains of (a) 2 % and (b) 34 % [41].	157
5.5	TDA distributions in samples of grain size, $d = 4.0\mu\text{m}$, in batch 2 at various % strains: (a) 0 (b) 5 (c) 10 and (d) 20.	160
5.6	TDA distributions in samples of grain size, $d = 29.0\mu\text{m}$, in batch 2 at various % strains: (a) 0 (b) 5 (c) 10 and (d) 20.	160
5.7	Variation of different parameters of TDA distribution: (a) standard deviation (b) relative frequency of 120° class (c) relative frequency of 110° class and (d) relative frequency of 130° class for different grain sizes with true strain.	161

5.8	TEM micrographs of the samples of 316L austenitic stainless steel ($d = 5.0\mu m$) deformed at room temperature up to strains of (a) 2 % and (b) 24 % [113].	165
5.9	TDA distributions in the samples of batch 2 with grain size, $d = 4.0\mu m$, deformed at $400^{\circ}C$ up to various % strains: (a) 0 (b) 5 (c) 10 and (d) 20. .	176
5.10	TDAs distribution in the samples of batch 2 with grain size, $d = 29.0\mu m$, deformed at $400^{\circ}C$ up to various % strains: (a) 0 (b) 5 (c) 10 and (d) 20. .	176
5.11	Variation of different parameters of TDA distribution: (a) standard deviation (b) relative frequency of 120° class (c) relative frequency of 110° class and (d) relative frequency of 130° class with strain for different grain sizes at $400^{\circ}C$	177
5.12	TEM micrographs of the samples of 316L austenitic stainless steel deformed up to 34 % strains at $400^{\circ}C$ with grain sizes: (a) $5.1\mu m$ and (b) $86.7\mu m$ [41].	181
5.13	TDA distributions in the samples of batch 2 with grain size, $d = 4.0\mu m$, deformed at $800^{\circ}C$ up to various % strains: (a) 0 (b) 5 (c) 10 and (d) 20. .	183
5.14	TDA distribution in the samples of batch 2 with grain size, $d = 29.0\mu m$, deformed at $800^{\circ}C$ up to various % strains: (a) 0 (b) 5 (c) 10 and (d) 20. .	183
5.15	Variation of different parameters of TDA distribution: (a) standard deviation (b) relative frequency of 120° class (c) relative frequency of 110° class and (d) relative frequency of 130° class with strain for different grain sizes at $800^{\circ}C$	184

5.16	TEM micrographs of the samples of 316L austenitic stainless steel deformed up to 34 % strains at 700 °C with grain sizes: (a) 5.1 μm and (b) 86.7 μm [41].	187
5.17	Variation of normalised Hall-Petch parameters: (a) σ_0/E (b) K/E with temperature in the coarse grain regime of batch 1.	195
5.18	Variation of normalised Hall-Petch parameters: (a) σ_0/E (b) K/E with temperature in the fine grain regime of batch 1.	197
5.19	Variation of relative contribution of grain boundary regime (C_b) and grain interior regime (C_i) with temperature at different strain levels in the sample with grain sizes: (a) 2.7 μm , (b) 4.5 μm , (c) 18.3 μm and (d) 64.0 μm	201
5.20	A schematic of (a) pile-up of dislocations and accumulated EGBDs at grain boundaries, and (b) Pile-ups and process of annihilation of EGBDs through vacancy flow at a grain boundary segment.	205
5.21	Variation of net dislocation density with temperature at % strains: (a) 0.2, (b) 2, (c) 10 and (d) 20.	211
5.22	Variation of net dislocation density with temperature in the sample of 2.7 μm grain size at 0.2% strain for ρ_0 values of (a) 0 and 10^6 , (b) 10^8 , (c) 10^9 and (d) 10^{10}	212
5.23	Variation of net dislocation density with temperature in the sample of 64.0 μm grain size at 0.2% strain for ρ_0 values of (a) 0 and 10^6 , (b) 10^8 , (c) 10^9 and (d) 10^{10}	213
5.24	Variation of net dislocation density with temperature in the sample of 2.7 μm grain size at % strains: (a) 0.2, (b) 2, (c) 10 and (d) 20.	214

5.25 Variation of net dislocation density with temperature in the sample of 64.0 μm grain size at % strains: (a) 0.2, (b) 2, (c) 10 and (d) 20. 215

5.26 Variation of net dislocation density with strain at different temperatures in the sample with grain sizes of (a) 2.7 μm and (b) 64.0 μm 216

5.27 Variation of the transition temperature with grain size for different values of ρ_0 at % strains: (a) 0.2 and (b) 2. 217

5.28 Variation of the transition temperature with strain for different values of ρ_0 in the sample of grain sizes of (a) 2.7 μm and (b) 64.0 μm 218

5.29 Plots of stress vs strain for different grain sizes at temperatures: (a) room temperature, (b) 400 $^{\circ}\text{C}$ and (c) 800 $^{\circ}\text{C}$ 225

5.30 Plots of $d\sigma/d\epsilon$ vs strain for different grain sizes at temperatures: (a) room temperature, (b) 400 $^{\circ}\text{C}$ and (c) 800 $^{\circ}\text{C}$ 226

5.31 Comparison of stress vs strain curves calculated by using different strain hardening equations: (a) at room temperature and 400 $^{\circ}\text{C}$, (b) at 800 $^{\circ}\text{C}$ for 2.7 μm grain size and (c) at 800 $^{\circ}\text{C}$ for 26.5 μm grain size. 228

5.32 Variation of $\sigma\theta$ with stress at room temperature for grain sizes: (a) 2.7 μm and (b) 26.5 μm 230

5.33 Variation of $\sigma\theta$ with stress at 400 $^{\circ}\text{C}$ for grain sizes: (a) 2.7 μm and (b) 26.5 μm 231

5.34 Variation of $\sigma\theta$ with stress at 800 $^{\circ}\text{C}$ for grain sizes: (a) 2.7 μm and (b) 26.5 μm 232

5.35 Variation of $\sigma\theta$ with stress at different temperatures for grain sizes: (a) 2.7 μm and (b) 26.5 μm 233

5.36	Variation of Voce parameter, σ_s with (a) grain size and (b) temperature. .	235
5.37	Variation of Voce parameter, σ_1 with (a) grain size and (b) temperature. .	236
5.38	Variation of Voce parameter, n_V with (a) grain size and (b) temperature. .	237
5.39	Variation of critical strain (ϵ_L) calculated using Ludwigson equation with (a) grain size and (b) temperature.	238
B.1	The fraction of the surface area of the unit sphere occupied by the orien- tation range ϕ to $\phi + d\phi$, and θ to $\theta + d\theta$, is $1(d\theta)(1)(\sin\theta d\phi)$	262

List of Tables

2.1	The main operative slip systems in three crystal structures	6
3.1	Chemical composition (Wt %) of commercially available 316L austenitic stainless Steel	42
4.1	Microstructural parameters of annealed samples.	55
4.2	Room temperature tensile properties of samples with various grain sizes. .	63
4.3	Values of $\sigma_0(\epsilon)$ and $K(\epsilon)$ at different strain levels.	71
4.4	Goodness of fit using correlation coefficient for different values of n in the relation, $\sigma(\epsilon) = \sigma_0(\epsilon) + Kd^{-n}$, at room temperature.	72
4.5	Microstructural parameters at various strain levels for the samples of different grain sizes (batch 2).	77
4.6	Average microhardness values for the samples of different grain sizes at several strain levels, deformed at room temperature.	78
4.7	Tensile properties of the samples with different grain sizes.	92
4.8	Values of $\sigma_0(\epsilon)$ and $K(\epsilon)$ at different temperatures.	94

4.9	Goodness of fit using correlation coefficient for different values of n in relation, $\sigma(\epsilon) = \sigma_0(\epsilon) + Kd^{-n}$ at various temperature.	97
4.10	Microstructural parameters at various temperatures and strain levels for different grain size samples of batch 2.	107
4.11	Average microhardness values at different temperature and strain for batch 2 (d=29 μm).	124
4.12	Relative frequencies of different class of PDA distribution and standard deviation of PDA distribution, obtained from different values of TDA. . . .	135
4.13	Computed values of the coefficients a_{ij}	141
4.14	Relative frequencies of measured PDA distribution and calculated TDA distribution by Gauss elimination and optimisation methods of 316L austenitic stainless steel sample annealed at 950°C and 35 Minutes.	142
5.1	Values of the parameters of equation 5.18 for 316L austenitic stainless steel	208
5.2	Estimated statistical error (SE) in using different empirical equations at different temperatures and grain sizes	224
A.1	Grain size and hardness data for different annealing treatments.	257
E.1	Values of the parameters of Hollomon equation (2.13) and Ludwigson equation (2.17) in different regions of strains at various temperatures and for grain sizes.	274
E.2	Values of the parameters of Ludwik equation (2.14) in different regions of strains at various temperatures and for grain sizes.	276

E.3 Values of the parameters of Ludwik equation (2.14) in different regions of strains at various temperatures and for grain sizes 277

E.4 Values of the parameters of Ludwik equation (2.14) at various temperatures and for grain sizes in the entire range of strains. 278

E.5 Values of the parameters of Voce equation (2.15) at various temperatures and for grain sizes in the entire range of strains. 279

List of Symbols

t_0	critical resolved shear stress, $[N/m^2]$
$\theta_1, \theta_2, \theta_3$	linear strain hardening rate in stages 1, 2 and 3 respectively $[N/m^2]$
τ	shear stress, $[N/m^2]$
γ	shear strain
G	shear modulus, $[N/m^2]$
ν	poission's ratio
b	burger vector, $[m]$
T	temperature, $[K]$
τ_G	athermal component of stress, $[N/m^2]$
U_0	activation energy, $[N/m]$
κ	Boltzaman's constant
ν_0	frequency factor
V	activation volume, $[m^3]$
N	number of dislocation sweeping on area, A
τ_s	thermal component of stress, $[N/m^2]$
τ_{P-N}	Pearls-Nabarro stress, $[N/m^2]$

τ_f	resistance from forest dislocations, $[N/m^2]$
τ_{im}	resistance from impurity atoms, $[N/m^2]$
τ_{dp}	resistance from dispersed particles, $[N/m^2]$
τ_{pd}	resistance from point defects, $[N/m^2]$
ρ	dislocation density, $[m^{-2}]$
σ	tensile stress, $[N/m^2]$
σ_G	tensile yield stress, $[N/m^2]$
γ	shear stress, $[N/m^2]$
\overline{m}	average orientation factor
ϵ	tensile strain
$d\epsilon$	increment in tensile strain
$d\gamma$	increment in shear strain
$k_1, k_2, k_h, k_l, \sigma_s, k_s$	strain hardening coefficients
n_1, n_h, n_l, n_v, n_s	strain hardening exponents
E	elastic modulus, $[N/m^2]$
T_m	absolute melting temperature, $[K]$
$\sigma_0(\epsilon)$	Hall-Petch intercept, $[N/m^2]$
$K(\epsilon)$	Hall-Petch slope, $[N/m^{3/2}]$
d	grain size, $[m]$
τ_c	critical shear stress, $[N/m^2]$
τ_s	effective shear stress, $[N/m^2]$
τ_i	friction stress, $[N/m^2]$
K_y	Hall-Petch slope at yield stress, $[N/m^{3/2}]$
ρ^s	statistically stored dislocation density, $[/m^2]$
ρ^g	geometrically necessary dislocation density, $[/m^2]$

l_s	geometrical slip distance, [m]
ρ^t	total density of dislocation, [m^{-2}]
M	number of class of TDA or PDA
N_A	number of grain boundary segment pairs making an angle between $(i - 1)\Delta\beta$ to $i\Delta\beta$ per unit area of the plane of polish
$N_{A_{ij}}$	individual contribution to i^{th} class of PDA from j^{th} class of TDA
P_2	probability of cutting a triple edge
a_{ij}	probability of obtaining PDA in class range $(i - 1)\Delta\beta$ to $i\Delta\beta$ from the j^{th} class of TDA
N_{V_j}	number of grain boundary segments having TDA between $(j - 1)\Delta\alpha$ to $j\Delta\alpha$ in per unit volume
N_v	total number of grain boundary pairs per unit volume
N_a	total number of triple point per unit area
x_j	relative frequency of the j^{th} class of TDA
y_i	relative frequency of the i^{th} class of PDA
Δ_i	measurement error in y_i
C_i	fractional contribution to flow stress from grain interior
C_b	fractional contribution to flow stress from grain boundary
D_0	lattice diffusion coefficient at absolute temperature
r_0	equal to burger vector (b), [m]
R_0	half of the length of the grain boundary segment i.e., $L/2$, [m]
$\dot{\epsilon}$	strain rate, [s^{-1}]
ρ_0	initial dislocation density per unit length of grain boundary at $\epsilon = 0$, [m^{-1}]
ρ_{net}	net dislocation density per unit length of grain boundary, [m^{-2}]
v_i	volume fraction of grain interior

v_g	volume fraction of grain boundary
σ_i	flow stress in grain interior
σ_g	flow stress in grain boundary
x	width of the grain boundary region
\bar{d}	average grain size
\bar{l}	mean intercept length
\bar{N}_L	avrage number of grain boundary intersection
\bar{d}_{eq}	average equivalent grain diameter
\bar{A}	average grain area
S_f	grain shape factor
p	grain perimeter
A	grain area
C_v	coefficient of variation of grain size
β	plane dihedral angle(PDA)
β_{SD}	standered deviation of plane dihedral angle
β_{120}	relative frequency of 120° class of PDA
β_{110}	relative frequency of 110° class of TDA
α	true dihedral angle
α_{SD}	standered deviation of true dihedral angle
α_{120}	relative frequency of 120° class of TDA
α_{130}	relative frequency of 130° class of TDA
θ, ϕ	orientation of triple edge
γ	probability of orientation of triple edge

List of Abbreviation

AR	aspect ratio
BCC	body centered cubic
CC	correlation coefficient
DSA	dynamic strain aging
EGBD	extrinsic grain boundary dislocation
EPMA	electron probe microanalyser
FCC	face centered cubic
HCP	hexagonal close packed
H-P	Hall-Petch
PDA	plane dihedral angle i.e., the angle between grain boundary segments meeting at triple points on plane of polish
SFE	stacking fault energy
SE	statistical error
TEM	transmission electron microscope
TDA	true dihedral angle i.e., the angle between grain boundary planes meeting at a common edge, known as triple edge

UTS ultimate tensile strength

VHN Vickers hardness number

Synopsis

An understanding of the mechanisms of plastic deformation is essential towards the deformation processing and strengthening of materials. A large number of fundamental studies on plastic deformation of metals have been performed on single crystals, so as to eliminate complicated effects of grain boundaries and second phase particles. Such studies provide the basic understanding of the plastic deformation of polycrystals. The commercial metal products are made up of numerous individual crystals or grains. The size of these grains and the structure of the grain boundaries play a very important role in the plastic deformation of polycrystals. The well known Hall-Petch relationship, $\sigma(\epsilon) = \sigma_0(\epsilon) + K(\epsilon)d^{-1/2}$, derived on the basis of pile-up of dislocations at grain boundaries, was the first attempt to correlate the flow stress $\{\sigma(\epsilon)\}$ of a polycrystal with grain size (d). In this relation, $\sigma_0(\epsilon)$ and K are constants at a given strain (ϵ). This relationship has been widely used in assessing plastic behaviour of polycrystals. Other relationships have also been proposed for describing the grain size dependence of flow stress. One such relationship based on a composite structure consisting of grain interior and grain boundary region, is given as $\sigma(\epsilon) = \sigma_0(\epsilon) + K(\epsilon)$.

Deviations from the Hall-Petch relation have also been reported in the literature. Various interpretations based on substructural changes were proposed to explain these deviations by different investigators. However, there is no consensus on the explanation of the deviation from the Hall-Petch relation. Generally, most researchers have attempted to correlate flow stress with mean grain size and neglected the possible influence of other microstructural parameters. For example, it has been shown by some investigators that for a given mean grain size, the samples with different grain size distribution may influence the flow stress of polycrystals. Also the different thermo-mechanical treatments applied to obtain the different

grain sizes may lead to differences in both the grain size distribution as well as the energy state of grain boundaries which can affect the flow stress in polycrystals.

Several methods have been developed for the estimation of relative energy of grain boundaries. There are a number of limitations associated with these techniques. For instance, in the methods of thermal groove and Zero creep, the original structure of the boundary may change during thermal grooving and zero creep at high temperatures and also the methods are limited to surface grain boundaries and may not be representative of the bulk material. The method based on spreading and disappearance kinetics of extrinsic grain boundary dislocations (EGBDs) in TEM during in-situ annealing is cumbersome as well as prone to error in the estimation of temperature and time of disappearance of EGBDs. On the other hand, grain boundary energies could also be related simply to the true dihedral angles (TDA) i.e., the angle between grain boundary planes meeting at a triple edge in the three dimensional structure of polycrystals. Some investigators have directly measured the TDA using TEM images, which is tedious and therefore it is not possible to obtain a statistical estimate of TDA distribution in polycrystals. However, in metallography the dihedral angles are measured as plane dihedral angles (PDA) i.e., the angle between grain boundary segments meeting at a triple point on the plane of polish. The distribution of PDA has two components: (1) variation in the TDA distribution and (2) statistical variation due to random orientation of the sectioning plane (i.e., plane of polish). The statistical variation (like random noise) leads to overshadow or hide the actual variation in the TDA. Hence such a distribution of PDA cannot be directly used in the estimation of relative energies of grain boundaries. Therefore, an appropriate statistical technique needs to be developed in order to transform the PDA distribution to TDA distribution. The measurements of PDA are relatively easy and it is possible to make a large number of measurements in a short time.

Along with the relative energy state of grain boundaries, the other geometrical changes in the grains and the variation of the hardness across a grain are important parameters in the understanding of flow stress with strain and temperature. Several dislocation models in static condition have been developed to understand the annihilation process of EGBDs

at grain boundaries and to explain the variation of flow stress with temperature. However, during deformation the situation is different because of the accumulation of EGBDs at grain boundaries with increasing strain. Therefore, a suitable model based on dislocation dynamics needs to be developed to explain the variation of flow stress with temperature.

In view of the above discussion, it is quite clear that the mean grain size alone cannot explain the flow behaviour of polycrystals. Therefore, the purpose of the present study is to examine the dependence of flow stress in polycrystals on mean grain size and the distribution of microstructural parameters such as grain size, grain shape and dihedral angles. 316L austenitic stainless steel (which is a single phase polycrystalline material over a wide temperature range) is selected as a model material for this work. The main objectives of the present study are as follows:

- Development of a statistical technique based on the principles of stereology for the transformation of experimentally measured distribution of plane dihedral angle (PD) to true dihedral angle (TDA) distribution.
- To examine and develop a mechanistic understanding of the dependence of flow stress in 316L austenitic stainless steel on grain size and other microstructural parameters such as grain shape, distribution of grain size, grain shape and dihedral angles over a wide range of temperature.
- Development of a micro-mechanistic model (based on dislocation dynamics at and in the vicinity of grain boundaries) in order to understand the effect of temperature on grain size dependence of flow stress.
- Assess the applicability of various empirical stress-strain relations and to develop an overall understanding of the strain hardening behaviour in 316L austenitic stainless steel.

The thesis is divided into six chapters.

Chapter 1 briefly discusses the importance and the limitations of the Hall-Petch relation. It also focuses on the scope and objective of this study.

Chapter 2 briefly discusses the plastic behaviour of single crystals and polycrystals. The literatures reveal that several aspects such as deviations from the Hall-Petch behaviour, estimation of the relative energy state of grain boundaries, variation of the flow stress and the Hall-Petch parameters with strain and temperature remain unresolved.

Chapter 3 describes the experimental procedures adopted in the preparation of tensile samples, tensile testing and measurements of microstructural parameters and hardness. The flat tensile samples are prepared after cold rolling of 316L austenitic stainless steel plates (as received) in successive passes and machining. These samples of two batches after annealing are tested in tension in the temperature range of room temperature to 800°C for a wide range of grain size from 2.7 μm to 64.0 μm . The microstructural characterisation of annealed and deformed samples is carried out at three different strains (5 %, 10 % and 20 %) and temperatures (room temperature, 400°C and 800°C). The grain size is measured by mean intercept length as well as grain area method. The measurements of individual grain area and perimeter are done through an image analyser to estimate the mean grain size, grain size distribution and grain shape factor. Grain aspect ratio is estimated from the measurements of linear intercept in longitudinal and transverse directions from the microstructures of the deformed specimens. The plane dihedral angles are measured directly from the micrographs. Finally the microhardness measurements are performed across the grains of annealed and deformed samples.

Chapter 4 presents the experimental results and also develops a mathematical transform to estimate the distribution of the true dihedral angles (TDA) from the experimentally measured distribution of the plane dihedral angles (PDA). Accordingly, this chapter is divided into four broad sections, viz:

- microstructural characterisation of annealed samples,

- plastic deformation at room temperature,
- plastic deformation at elevated temperature,
- estimation of true dihedral angle (TDA) distribution

The salient features are given below:

1. The distribution of the grain size and the grain shape of annealed samples of both the batches is more or less same.
2. In the temperature range of room temperature to 600°C, the Hall-Petch behaviour (for batch 1) shows two distinctly different linear regions, one in the fine grain size range ($d \leq 6 \mu\text{m}$) and the other in the coarse grain size range ($d \geq 6 \mu\text{m}$). The Hall-Petch parameter $K(\epsilon)$ is significantly higher in the fine grain region compared to that in the coarse grain region at all strains. On the other hand, the Hall-Petch intercept, $\sigma_0(\epsilon)$, is negative in the fine grain regime. Since $\sigma_0(\epsilon)$ is interpreted as the friction stress, there is no physical significance of negative $\sigma_0(\epsilon)$. Therefore, it has been concluded that the Hall-Petch relation is not valid in the fine grain region. Application of the Kocks composite model in the fine grain regime, results in positive $\sigma_0(\epsilon)$ which is comparable in magnitude to $\sigma_0(\epsilon)$ obtained in the coarse grain regime (using the Hall-Petch relation).
3. At 800°C, a single linear Hall-Petch line at a given strain with small positive value of $K(\epsilon)$ is obtained in batch 1. There is a wide scatter in the data at this temperature, and the scatter increases with strain.
4. In batch 2, a single linear Hall-Petch relation fits the data in the entire range of grain size (2.9 μm to 46.0 μm) in the temperature range of room temperature to 800°C.
5. The grain aspect ratio increases while the grain shape factor decreases with strain at room temperature and 400°C. However, at 800°C, there is no significant change observed in these parameters with strain.

- 6 The standard deviation of plane dihedral angles (PDA) increases and the relative frequency of 120° class of PDA distribution decreases with increasing strain at room temperature and 400°C . On the other hand at 800°C , the standard deviation of PDA increases slowly and relative frequency of 120° class of PDA distribution decreases in the strain range of 0 to 5 % followed by a decrease in the former and increase in the latter parameter with strain.
7. With the increase in the strain, the hardness in the grain interior as well as in the grain boundary region increases at room temperature and 400°C . However, at 800°C , the hardness in both the grain interior and in the grain boundary region increases up to 5 %, strain and thereafter it remains more or less unchanged with further straining.
8. As mentioned earlier, the relative energy state of grain boundaries of a polycrystal can be assessed by knowing the true dihedral angle (TDA) distribution. However, experimental measurements give only the plane dihedral angle (PDA) distribution. Therefore, in this chapter a mathematical transform has been developed to unfold the TDA distribution from the PDA distribution. The mathematical relations between the distribution of TDA and PDA are derived rigorously using first principles of stereology. The results obtained from this technique have been analysed in Chapter 5.

Chapter 5 contains discussion of results and also develops a dislocation model on the basis of dislocation dynamics at and in the vicinity of grain boundaries to explain the variation of flow stress with temperature. This chapter is broadly divided into four sections, viz:

- deformation at room temperature,
- deformation at elevated temperature,
- effect of temperature on flow stress,
- strain hardening behaviour.

The important findings are summarised as follows:

1. The distinctly different Hall-Petch behaviour (bi-linear) in the two regimes of grain size of batch 1 arises from different thermo-mechanical treatments employed to obtain the various grain sizes.
2. The distribution of grain size and grain shape in the samples of different average grain size remains more or less same.
3. The true dihedral angle (TDA) distribution is obtained from experimentally measured distribution of PDA, by employing the mathematical transform developed in Chapter . A significant difference observed in the distribution of TDA for samples of fine and coarse grain regimes of batch 1. In the fine grain regime the standard deviation of TDA is higher and the relative frequency of 120° class of TDA is lower in comparison to the coarse grain regime. This suggests the presence of non-equilibrium state of grain boundaries in the fine grain regime of batch 1. This has also been inferred from the results of hardness measurements.
4. Accordingly, the fine grained micro-structures may be considered as having two phases: a hard phase (mantle zone) in the vicinity of grain boundaries and a soft phase (grain interior). Kocks's composite model is more appropriate for this type of structure rather than the Hall-Petch model. By applying this model in fine grain regime in the temperature range of room temperature to 600°C , a positive value of $\sigma_0(\epsilon)$ at a given strain rate is obtained which is comparable in magnitude to $\sigma_0(\epsilon)$ obtained in the coarse grain regime (using the Hall-Petch relation).
5. The faster equilibration kinetics of the samples of batch 2 than the samples of batch 1 (due to compositional differences) leads to equilibrated grain boundaries during annealing in the entire range of grain size and hence no hard mantle zone remains even in the fine grain regime of batch 2. This leads to a single linear Hall-Petch relation in the entire range of grain size studied ($2.9\mu\text{m}$ to $46.0\mu\text{m}$) in the temperature range of room temperature to 800°C .

6. At 800°C, the samples of batch 1 also reveals a single linear Hall-Petch behaviour in the entire range of grain size due to the fact that at this temperature, the non-equilibrium grain boundaries in the fine grain regime transform to equilibrium state by the annihilation of EGBDs. However, the Hall-Petch data are highly scattered in both the batches and the scatter increases with increasing strain.
7. At 800°C, no significant change in the grain geometry with strain reveals that the main deformation mode is grain boundary sliding and grain boundary migration. Thus at 800°C, the pile-up model of Hall-Petch cannot be applied as the grain size strengthening model. The small positive value of $K(\epsilon)$ in batch 1 and the negative value in batch 2 also strongly support the above conclusion.
8. The variation of Hall-Petch parameters together with the parameters of composite relation with strain and temperature is described on the basis of geometrical changes in grains and the variation of microhardness across the grain.
9. In order to theoretically estimate the net density of dislocations in the grain boundary region, the rates of accumulation and annihilation of dislocations in the grain boundary region are estimated. At a given strain and temperature, these two rates of accumulation and annihilation of dislocations are used to obtain the net density of dislocations in the grain boundary region.
10. The general trend of variation of net dislocation density in 316L austenitic stainless steel (calculated using present model) with temperature for different grain sizes at various strains, is similar to the variation of experimental yield and flow stress.
11. In the overall experimental stress-strain curve, the Voce equation gives better fit compared to the other empirical stress-strain relations. With the increase in the temperature and the decrease in the grain size, the strain above which the dynamic recovery dominates over the strain hardening decreases.

Chapter 6 presents the conclusions of the present study and suggestions for future work.

Chapter 1

Introduction and Objectives

An understanding of the mechanism of plastic deformation and effect of various microstructural parameters on flow stress is essential towards the deformation processing and strengthening of materials. A large number of fundamental studies on the plastic deformation of metals have been performed with single crystals, so as to eliminate the complicated effects of grain boundaries and second phase particles. These studies provided basic understanding for the plastic deformation of polycrystals. The commercial metal products are made up of numerous individual crystals or grains. The size of these grains and the structure of the grain boundaries play a very important role in the plastic deformation of polycrystals.

During plastic deformation of polycrystals, both the grain boundaries and the grain interior contribute to varying extent depending upon the test condition. A reasonable mechanical properties can be achieved from the control of the grain boundaries structure and the grain size. The well known Hall-Petch relationship, $\sigma(\epsilon) = \sigma_0(\epsilon) + K(\epsilon)d^{-1/2}$ derived on the basis of pile-up of dislocations at grain boundaries, was the first attempt to correlate the flow stress $\{\sigma(\epsilon)\}$ of a polycrystal with grain size (d). In this relationship $\sigma_0(\epsilon)$ and $K(\epsilon)$ are constants at a given strain (ϵ). This relationship has been widely

used in understanding the plastic behaviour of polycrystals. Many investigators have also obtained other relationships for describing the flow stress dependence on grain size (presented in chapter 2, section 2.3.2).

Deviations from the Hall-Petch relation have been also reported in literature. Various interpretations based on substructural changes have been proposed to explain these deviations by different investigators. However, there is no consensus on the explanation of the deviations from the Hall-Petch relation. Generally, most researchers have attempted to correlate the flow stress with the mean grain size and neglected the possible influence of the distribution of microstructural parameters, such as grain size, grain shape and true dihedral angles (TDA) i.e., angle between grain boundary planes meeting at triple edge in three dimensional structure of polycrystal. These effects are discussed in chapter 2, section 2.3.3.

The energy state of grain boundaries may influence the flow stress of a polycrystal. To estimate the energy of the grain boundaries, several methods have been developed such as thermal groove [1], zero creep [2,3], spreading of the Extrinsic grain boundary dislocations (EGBDs) [4,5] and measurement of true dihedral angles (TDA) using transmission electron microscope (TEM) images [6–8]. There are a number of limitations associated with these techniques as presented in chapter 2 (section 2.3.3.1) and therefore, it is practically impossible to obtain a distribution of energy state of grain boundaries. The grain boundary energies could be simply related to the true dihedral angles (TDA) [9,10]. However, it is not feasible to experimentally measure the distribution of TDA in a polycrystal. On the other hand one can easily measure the distribution of plane dihedral angles (PDA) i.e., angle between grain boundary segments meeting at a triple point on plane of polish. However, such a distribution of PDA cannot be directly used in the estimation of relative energy of grain boundaries as discussed in chapter 2, section 2.3.3.1. Therefore an appropriate statistical technique needs to be developed in order to transform the experimentally measured distribution of PDA to TDA distribution. The measurements of PDA are relatively easy and it is possible to make a large number of measurements in a short

time.

The effect of strain and temperature on Hall-Petch parameters and flow stress is an open issue in terms of interpreting these effects. Several investigators have interpreted these on the basis of sub-structural changes during plastic deformation. Not much efforts have been put to correlate the flow stress and Hall-Petch parameters with the distribution of microstructural parameters such as grain size, grain shape, and true dihedral angle. Temperature plays a very crucial role in the plastic deformation of the polycrystals. It is now understood [11–14] that the rapid drop in the flow stress above approximately $0.5T_M$ (T_M is the melting temperature) at least in lower strain range is mainly due to the annihilation of extrinsic grain boundary dislocations (EGBDs). Several dislocation models have been developed in static condition to understand the annihilation processes of EGBDs at grain boundaries. However, during deformation the situation is different where the accumulation of EGBDs at grain boundaries occurs with increasing strain. Therefore, a suitable model based on dislocation dynamics needs to be developed in order to explain the variation of flow stress with temperature. 316L austenitic stainless steel (which is a single phase polycrystalline material over a wide temperature range) was selected as a model material for this work.

In view of the above discussion, the main objectives of this study may be listed as follows:

- Development of a statistical technique based on the principles of stereology for the transformation of experimentally measured distribution of the plane dihedral angle (PDA) to the true dihedral angle (TDA) distribution.
- To examine and develop a mechanistic understanding of the dependence of flow stress in 316L austenitic stainless steel on mean grain size, grain size and shape distribution and distribution of dihedral angles over a wide range of temperature
- Development of a micro-mechanistic model (based on dislocation dynamics at a

in the vicinity of grain boundaries) in order to understand the effects of temperature on the grain size dependence of flow stress.

- Assess the applicability of various empirical stress-strain relations and to develop an overall understanding of the strain hardening behaviour in 316L austenitic stainless steel.

Chapter 2

Plastic deformation of crystalline materials

2.1 Plastic deformation of single crystals

A large number of fundamental studies on the plastic deformation have been performed on single crystals of pure metals so as to eliminate the complicated effects of grain boundaries and the constraints imposed by neighbouring grains and second phase particles. In this section the plastic deformation behaviour of single crystals is briefly reviewed.

2.1.1 Slip systems

The principal mechanisms of plastic deformation are slip (glide), twinning and kinking. Among these, slip is the most common and important mechanism of plastic deformation for metallic crystals. The combination of a particular slip plane and a slip direction is referred to as a slip or glide system. Table 2.1 shows the main operative slip systems

Table 2.1: The main operative slip systems in three crystal structures

Crystal structure	slip plane	slip direction	Total number of slip systems
BCC	$\{110\}$ $\{112\}$ $\{123\}$	$\langle 111 \rangle$	48
FCC	$\{111\}$	$\langle 110 \rangle$	12
HCP	(0001)	$\langle 11\bar{2}0 \rangle$	3

three common crystal structures.

Schmid had shown that plastic flow begins when the shear stress resolved on the primary glide plane in the primary glide direction reaches a critical value (characteristic of the material) and independent of crystal orientation. This critical resolved shear stress (τ_0) remains more or less constant for a crystal of a given purity [15]. It is influenced by such variables as temperature, concentration of alloying elements and strain rate.

2.1.2 Stress-strain curves of metal crystals

The fundamental way to present single crystal deformation data is by plotting resolved shear stress versus shear strain. Stress-strain curves of single crystals show typically three stages of hardening (particularly distinctive in FCC crystals) as illustrated in figure 2.1. Stage 1 or easy glide is a region of low linear hardening (θ_1) while stage 2 is a second linear region with a much greater rate of work hardening (θ_2), which is frequently interrupted by the early development of stage 3 having decreasing rate of hardening (θ_3). For different metals the relative dominance of the three stages of hardening changes, and even for a given metal these three stages of hardening are influenced by various variables [16] such

as purity, crystal orientation, temperature, crystal size, shape and surface condition as discussed below.

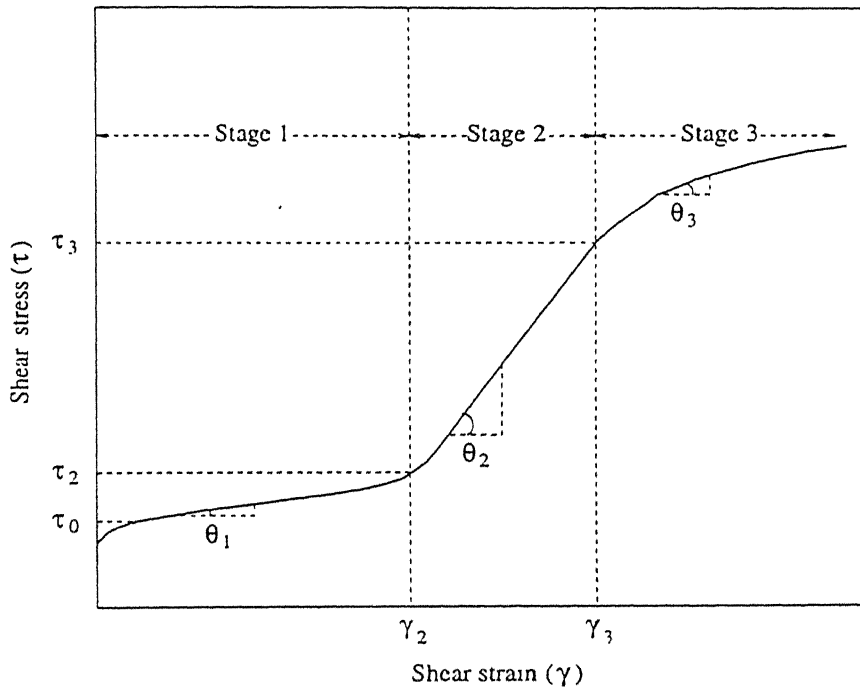


Figure 2.1: Typical stress-strain curve of a pure FCC metal single crystal.

Presence of insoluble impurities such as inclusions, even when present in low concentration can reduce and finally eliminate stage 1 hardening. On the other hand impurities which go into solid solution tend to increase the extent of stage 1 and decrease the strain hardening rate (θ_1). The extent of stage 1 decreases with increasing temperature, size of the sample, and oxide film/surface coating thickness. Orientation of crystal also affects the stage 1 hardening. Soft crystals (with orientations in the central region of stereographic triangle) are least likely to exhibit slip on more than one slip system for large part of strain and thus stage 1 is larger compared to hard orientations which lie near the corners or on the boundaries of the stereographic triangle where two or more slip systems have the same resolved shear stress.

High stacking fault energy (SFE) materials such as aluminium do not exhibit well defined stage 2 hardening while low SFE materials like copper have a well defined stage

at room temperature. Temperature has a significant effect on the duration of stage 2 hardening but the rate of hardening, other factors being constant, is very insensitive to temperature. As the temperature is increased, stage 3 becomes more pronounced and the stress-strain curve is essentially composed of stage 3. Crystal orientation, size, shape and surface condition have a negligible effect on stage 2 when compared to those observed during stage 1.

Stage 3 is much less sensitive to purity, crystal orientation, size, shape and surface condition as compared to stages 1 and 2. However, the effect of temperature is pronounced on this stage as discussed above.

2.1.3 Mechanisms of strain hardening

Strain hardening is caused by dislocations interacting with each other and with barriers such as impurities which impede their motion through the crystal lattice [17]. Hardening due to dislocation interaction is a complicated phenomena because it involves a large group of dislocations, and is difficult to specify a group behaviour in a simple mathematical way. Dislocation density increases with plastic strain through dislocation multiplication by mechanisms such as the Frank-Read type.

The earliest theory of work hardening proposed by Taylor [18,19] who assumed that many dislocations do not reach the surface of a crystal but interact elastically with other dislocations, and become anchored within the crystal forming a network. Thus the dislocation density gradually increases as deformation proceeds, and the stress necessary to move a dislocation in the presence of other dislocations is raised. A parabolic relation between shear stress(τ) and shear strain(γ) is obtained by Taylor as follows:

$$\tau = K G \left(\frac{\gamma b}{L} \right)^{1/2} \quad (2.1)$$

where, G is the shear modulus, b is the burger vector, L is the mean distance between the

dislocations in the network, $K = 1$ is for screw and $K = 2(1 - \nu)$ is for edge dislocations, and ν is the Poisson's ratio.

However, the Taylor theory is incompatible with various experimental observations relating to strain hardening. Mott [20] overcame some of the objections to Taylor's theory by replacing individual dislocation interactions by interaction between piled-up groups of dislocations against obstacles such as sessile dislocations. A dislocation pile-up consisting of n dislocations was considered as a super dislocation with the burger vector nb . Mott [20] also obtained a parabolic relation as given below:

$$\tau = \frac{G}{2\pi} \left(\frac{\gamma nb}{L} \right)^{1/2} \quad (2.2)$$

However, experimental work has shown that most single crystals do not exhibit parabolic stress-strain curves. This is the principal drawback of the above theories of work hardening.

Considering the thermally activated nature of plastic deformation, Seeger *et al.* [21] have derived an expression for the flow stress τ as a function of temperature T and strain rate $\dot{\gamma}$ as:

$$\tau(T) = \tau_G + \frac{U_0 - kT \ln \left(\frac{N A b \nu_0}{\dot{\gamma}} \right)}{V} = \tau_G + \tau_S \quad (2.3)$$

where, τ_G is an athermal component of stress which arises from the interaction of parallel dislocations on the primary slip plane, U_0 is a single rate controlling activation energy, k is a Boltzmann's constant, ν_0 is a frequency factor determined by the obstacles, V is the activation volume, N is the number of dislocations sweeping out an area (A) of the slip plane, b is the magnitude of burger vector, and τ_S is the thermal component of stress which arises from the intersection of dislocations with the forest dislocations which cut through the slip plane and other obstacles such as impurities, second phase and point defects. Hence τ_S can be represented as:

$$\tau_S = \tau_{P-N} + \tau_f + \tau_{im} + \tau_{dp} + \tau_{pd} \quad (2.4)$$

where τ_{P-N} is the resistance to dislocation movement from the crystal lattice, defined

the Peirls-Nabarro stress, τ_f is the resistance from forest dislocations, τ_m is the resistance due to interaction of dislocations with impurity atoms, τ_{dp} and τ_{pd} are the resistance due to interaction with dispersed particles of second phases and with point defects respectively.

τ_S term decreases with increase in temperature and disappears at high temperature, but the τ_G term remains unaltered as the temperature is changed. The flow stress of a metal would thus be expected to decrease rapidly with rising temperature and become independent of temperature when the temperature is raised sufficiently. The operating strain hardening mechanisms in the three stages of the stress-strain curve are considered below.

2.1.3.1 Stage 1 hardening

As only one slip system is operative in this stage, the hardening effect is low. The mean free path of dislocations is long, and a very high proportion of moving dislocations reach the surface of the crystal. Seeger and co-workers [21, 22] have attributed stage 1 hardening to long range interaction between fairly widely spaced dislocations of the primary slip system and obtained a relation for work hardening coefficient as:

$$\theta_1 = \frac{d\tau}{d\gamma} = \frac{8G}{9\pi} \left(\frac{d}{L} \right)^{3/4} \quad (2.5)$$

where, L and d are slip line length and slip line spacing, respectively.

2.1.3.2 Stage 2 hardening

The most important contribution to work hardening in face-centered-cubic metals comes from stage 2 which, like stage 1, is linear but with a much higher work hardening coefficient (θ_2) compared to (θ_1) as shown in figure 2.1. This stage begins when the slip occurs on more than one slip systems. θ_2 is relatively independent of temperature as compared to θ_1 . In this stage the interaction is considered to be between the piled-up groups of

dislocations. Further, the strong increase in flow stress in stage 2 is predominantly due to the temperature independent contribution from the stress fields of dislocations on the primary slip plane, rather than the component arising from interactions with the forest dislocations which is temperature dependent.

Observations of slip lines during stage 2 indicate that they became progressively shorter, due to increasing concentration of Lomer-Cottrell locks. The formation of Lomer-Cottrell sessile dislocations, dislocation dipoles (formed by meeting of dislocation loops gliding in closely oriented slip planes) and complex dislocation networks result in strong hardening effect in stage 2. From the hardening due to long range stresses of piled-up groups, Seeger *et al.* [21] were able to evaluate the rate of hardening in this stage as:

$$\theta_2 = \frac{d\tau}{d\gamma} = \frac{\beta G}{6\pi^2} \quad (2.6)$$

where, β is a constant $\cong 0.5$, which is close to the experimentally determined values.

As a result of slip on several slip systems, dislocation tangles begin to develop and these eventually result in the formation of dislocation cell structures consisting of regions almost free of dislocations surrounded by regions of high dislocation density. The average dislocation density(ρ) in stage 2 correlates with resolved shear stress(τ) according to the following equation:

$$\tau = \tau_0 + \alpha G b \rho^{1/2} \quad (2.7)$$

where, τ_0 is the shear stress needed to move dislocations in the absence of other dislocations and α is a numerical constant which varies from 0.3 to 0.6 for different face-centered cubic and body-centered-cubic metals.

2.1.3.3 Stage 3 hardening

Stage 3 is a region of decreasing rate of strain hardening, and it tends to occur more readily at lower stress, as the temperature is raised. Cross slip is believed to be the ma

process by which dislocations piled up at obstacles during stage 2 can escape and reduce the internal stress field. Seeger *et al.* [21] have pointed out that the beginning of stage 3 is characterised by heavy slip bands with extensive cross slip. The onset of stage 3 is dependent on the stacking fault energy (SFE) of the metals. Metals with low SFE need a high activation energy for cross-slip. Thus in order to obtain a reasonable rate of cross-slip in copper (low SFE) at room temperature, the applied stress must be very high. On the other hand, a metal such as aluminium with a high SFE will exhibit stage 3 hardening at room temperature, because the dislocations are undissociated and thus cross-slip can occur at a much lower applied stress.

2.2 Plastic Deformation of Polycrystals

The deformation of individual grains of the polycrystalline aggregate are subjected to the constraints imposed by neighbouring grains. According to Von Mises criterion, for a crystal to undergo a general change of shape by slip requires the operation of five independent slip systems. This arises from the fact that an arbitrary deformation is specified by the six components of the strain tensor, but because of the requirement of constant volume, there are only five independent strain components. Crystals which do not possess five independent slip systems are never ductile in polycrystalline form, although a small plastic strain may be possible if there is twinning or a favourable preferred orientation. Cubic metals easily satisfy this requirement, which accounts for their general high ductility. Hexagonal and other low crystal symmetry metals do not satisfy this requirement and have low ductility at room temperature in polycrystalline form.

To maintain the continuity at grain boundaries, strain in the vicinity of a grain boundary usually differs markedly from that at the center of the grain. As the grain size decreases and strain increases, the deformation becomes more homogeneous. Because of the constraints imposed by the grain boundaries, slip occurs on several systems, even at

low strains. As the grain size is reduced more of the effects of grain boundaries will be felt at the grain center. The theoretical and experimental stress-strain behaviour of a polycrystal at low temperatures are briefly considered here.

2.2.1 Computation of stress-strain curves

To understand the plastic deformation behaviour of polycrystals, it would be desirable to review various theoretical approaches to correlate the stress-strain behaviour of single crystals and polycrystals. In polycrystals the orientation factor, m (the reciprocal of Schmid factor, $\cos\phi \cos\lambda$) varies from grain to grain and thus the resolved shear stress on various slip systems also varies from grain to grain.

The first theoretical attempt to unify the behaviour was made by Sachs [23] who suggested that the individual grains in a polycrystal deform like free single crystal (i.e., by single glide). For a random aggregate of grains, he obtained the average orientation factor $\bar{m} = 2.24$ and related the tensile yield stress (σ_y) of a polycrystal to the critical resolved shear stress (τ_0), as follows:

$$\sigma_y = \bar{m} \tau_0 \quad (2.8)$$

Later this model was rationalised in a slightly modified form by Cox and Sopwith [24] Kochendorfer [25, 26] and Schwink and co-workers [27, 28].

The above approach is limited as it assumes that each grain in an aggregate behave as an unrestrained single crystal and deforms on a single slip system. This will result in the production of voids but voids are known not to open up at grain boundaries during plastic deformation, thus strain continuity must be maintained. This basic requirement was fulfilled in the theory by Taylor [29] who assumed that all the grains in polycrystal were undergoing the same homogeneous strain as the bulk material. He selected 5 slip systems out of total numbers of 12 crystallographically equivalent octahedral slip system of a face-centered-cubic (FCC) polycrystal for which least work is required in deformation.

Also he assumed that the work, $\sigma d\epsilon$, performed by a macroscopic stress (σ) in deformation ($d\epsilon$) is the sum of the works performed by the critical resolved shear stress (τ_0) in an increment of shear deformation ($d\gamma$) as follows:

$$\sigma d\epsilon = \sum_{i=1}^5 \tau_0 d\gamma_i \quad (2.9)$$

By assuming τ_0 same on each slip systems, the average orientation factor m for a polycrystal is found from equation 2.9 as follows:

$$\frac{\sigma}{\tau_0} = \bar{m} = \frac{\sum_{i=1}^5 d\gamma_i}{d\epsilon} \quad (2.10)$$

For a FCC polycrystal, Taylor calculated a value of 3.06 – 3.1 for \bar{m} (in contrast to the prediction of $\bar{m} = 2.24$ by Sachs [23]). Taylor theory had been extended [30–32] by finding the combination of slip systems that minimises the value of $\sum d\gamma_i$ and satisfy the required continuity at grain boundaries.

Kocks [33–35] discussed extensively the Taylor model and suggested that the basis of comparison should be made with single crystals which deform by multi-slip, as this deformation pattern may well be representative of the deformation that occurs in polycrystals. Such a comparison was made by Hansen [36] between the stress-strain curves of a single crystal with a tensile axis of $\langle 111 \rangle$ orientation and a polycrystalline specimen with a large grain size (figures 2.2a and 2.2b for aluminium and copper respectively). The Taylor factor ($\bar{m} = 3.06$) was used both for converting shear stress to tensile stress and shear strain to tensile strain as follows:

$$\sigma = \bar{m} \tau \quad (2.11)$$

and,

$$\epsilon = \frac{\gamma}{\bar{m}} \quad (2.12)$$

Theoretically calculated value of stress in the entire strain range is higher than experimental stress (figures 2.2a and 2.2b). The observed difference may be related to the

presence of internal stresses which are necessary in order to obtain the assumed multi-slip [36].

An alternative to the Taylor model has been proposed by Leffers [37] who considered that the pile-up stresses are generated at positions where primary slip planes meet the grain boundary and these then may be relaxed by secondary slip in the neighbouring grain. In this model (termed as modified Sachs model), the stress and the strain conversion is based respectively, on the Taylor factor ($\bar{m} = 3.06$) and Sach factor($\bar{m} = 2.03$). A better agreement between the converted single crystal curve and the experimental curve for the polycrystalline specimen is achieved (figure 2.2b).

2.2.2 Experimental stress-strain curves

Experimentally obtained tensile true stress (σ) versus true strain (ϵ) curves of metals and alloys generally have the parabolic shape, and flow stress increases with increase in strain at low temperatures. To describe the stress-strain behaviour of polycrystalline metals and alloys in uniaxial and biaxial tensile tests, the four commonly used well known empirical equations are,

$$\sigma = K_H \epsilon^{n_H} \quad (\text{Hollomon}) \quad (2.13)$$

$$\sigma = \sigma_0 + K_L \epsilon^{n_L} \quad (\text{Ludwik}) \quad (2.14)$$

$$\sigma = \sigma_s - (\sigma_s - \sigma_1) \exp(-n_v \epsilon) \quad (\text{Voce}) \quad (2.15)$$

$$\sigma = K_s (\epsilon_1 + \epsilon)^{n_s} \quad (\text{Swift/Krupskowski}) \quad (2.16)$$

where, K_H , K_L , σ_s , K_s are the strain hardening coefficients; n_H , n_L , n_v , n_s are the strain hardening exponents and σ_0 and σ_1 are the elastic limit.

Although not universally accepted, the Hollomon equation has been frequently used for aluminium and its alloys. For low carbon steels either Hollomon or Swift/Krupskowski for austenitic and high alloy steel among others the Ludwik relationship and for copper

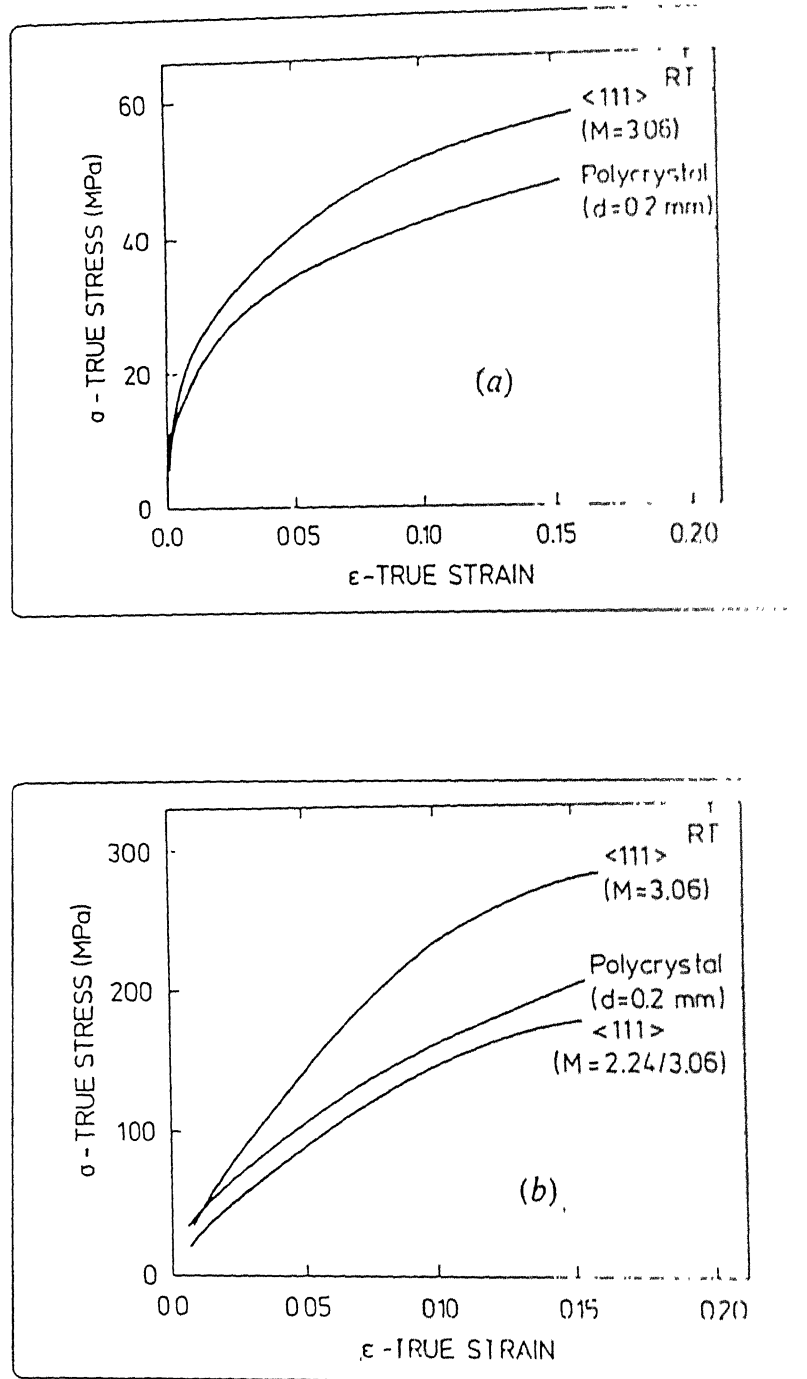


Figure 2 2: Experimental stress-strain curves at room temperature of polycrystalline specimens ($d = 0.2\text{mm}$) and theoretical stress-strain curves calculated on the basis of (a) Taylor model and (b) Taylor as well as the modified Sachs model [36].

and its alloys Voce equation is commonly used [38]. Ratke *et al.* [38] have shown from the experimentally measured values of differential n that none of the above four strain hardening equations is capable of reproducing either the measured value of differential n or of the measured strain hardening rates correctly. However it seems in many metals, the values of n vary with the amount of deformation.

Low and Garofalo [39] found that the Hollomon relation was an adequate description of the plastic flow behaviour exhibited by an 18 – 8 stainless steel. They suggested that the deviation from the Hollomon relation probably results from a phase change during deformation. Subsequently Ludwigson [40] has shown that for many stable stainless steels and the face-centered-cubic metals with low stacking fault energy, the Hollomon equation is able to describe the plastic behaviour only at higher strains. In order to account for the deviation from the Hollomon relation at low strain, Ludwigson [40] modified the Hollomon relation as:

$$\sigma = K_1 \epsilon^{n_1} + \exp(K_2 + n_2 \epsilon) \quad (2.17)$$

where, K_1 , K_2 , n_1 and n_2 are constants to describe the stress-strain behaviour of low SFE materials. It has been suggested [40] that the second term on the right hand side of equation 2.17 (dominating at lower strain) corresponds to planer slip, whereas the first term (dominating at large strains) corresponds to cross-slip and consequent cell formation.

By applying the Hollomon relation, Kashyap and Tangri [41] found three different regions in logarithmic stress-strain plots of 316L austenitic stainless steel and reported the values of n and K for these three regions. They reported a decrease in work hardening rate with increase in grain size when compared at a constant stress level, while Ulvan *et al.* [42] have observed an increase in strain hardening parameters (n and K) with the increase in grain size. The peaks/plateau in the variation of parameters of Ludwigson and Voc relations with temperature has been identified in the intermediate temperature range as one of the manifestation of dynamic strain aging [43,44]. In order to understand the work hardening behaviour, the plots of instantaneous work hardening rate $\theta = d\sigma/d\epsilon$ or $\sigma\theta$ as

function of σ have been widely used [45-47]. From these type of plots, Sivaprasad *et al.* [44] have observed accurate prediction of experimental θ at lower stress in modified austenitic stainless steel (15Cr – 15Ni – 2.2Mo – Ti) by using Ludwigson equation. However, the Voce equation follows the experimental θ values more closely at larger stress levels and also shows saturation behaviour at higher strains.

The shape of the σ versus ϵ curve and the plasticity of polycrystals depend on the type of crystal lattice, structure of crystals, grain size, temperature and strain rate. In general, the yield and flow stress of polycrystalline materials, increase with decrease in grain size. Thompson *et al.* [48] have reported a reverse trend after a certain strain level at room temperature in pure aluminium and copper, but Lloyd [49] observed a general trend of flow stress increase with decrease in grain size in pure aluminium up to large strain. He concluded that the reverse trend of Thompson *et al.*'s results, is due to the differences in texture. In general, with increase in strain rate, the flow stress increases at a constant strain level. With increase in temperature, the flow stress generally decreases and this effect is discussed below.

2.2.3 Effect of temperature on flow stress

The normalised yield (σ_y/E , E is the modulus of elasticity) and flow stress (σ_f/E) against temperature of many polycrystalline materials are distinguished by three regions as shown in figures 2.3 and 2.4. The normalised stress decreases with increasing temperature in the low temperature ($T < 0.3T_M$, T_M being the absolute melting temperature) and high temperature ($T > 0.5T_M$) regions while it is either independent or weakly dependent on temperature in the intermediate region. The first two regions up to around $0.5 T_M$ for polycrystals are similar to those of single crystals discussed in section 2.1.3. In the intermediate temperature range, the appearance of hump in the variation

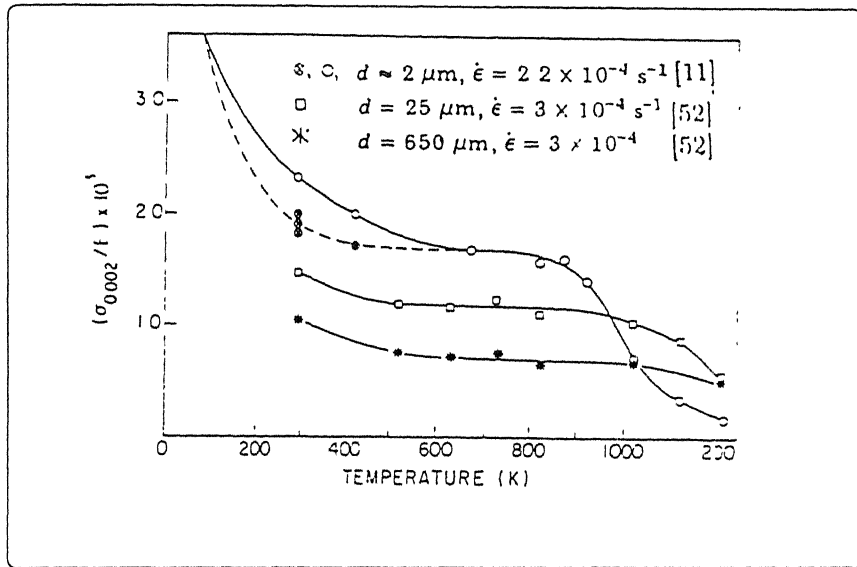


Figure 2.3: Normalised σ_y against temperature plots for micro-grained 316L austenitic stainless steel [11].

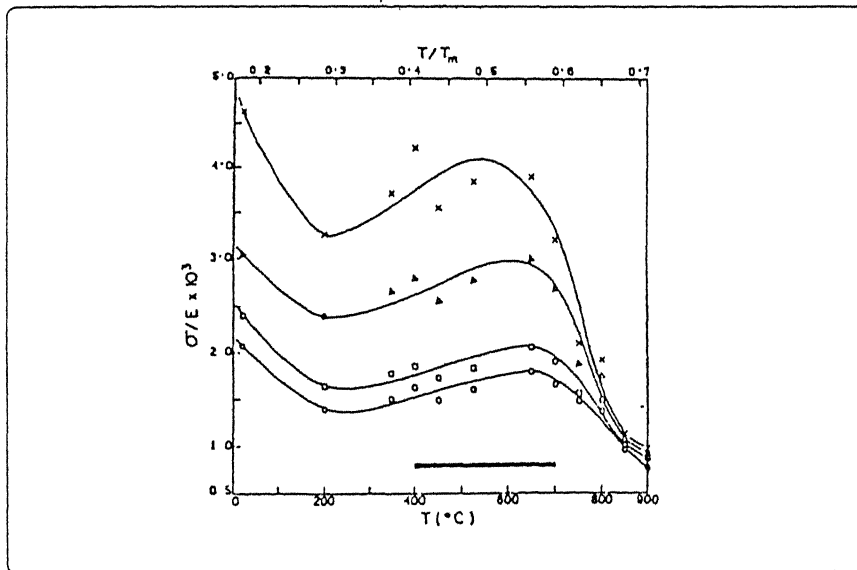


Figure 2.4: Experimentally observed variation in yield and flow stress with temperature in 316L austenitic stainless steel. The range of temperature corresponding to the jerk flow is shown by the bar [113].

of flow stress with temperature results from the dynamic strain aging (DSA) [43, 50, 51]. Mannan *et al* [52] have reported an increase in the work hardening rate with temperature for different grain sizes, and they have shown a peak at the same temperature when the flow stress starts to decrease at high temperatures. The increase in flow stress in the DSA range is considered to arise due to larger dislocation density at a given strain compared to that at other temperatures. The increase in work hardening rate in DSA range can also be correlated with the more rapid increase in dislocation density [53, 54]

The decline in work hardening rate and rapid drop in normalised flow stress above $0.5T_M$ has been attributed to precipitation of carbides [50], depleting the matrix of solutes responsible for dislocation locking as well as to dynamic recovery [51]. Others [11–14] interpreted it on the basis of annihilation of extrinsic grain boundary dislocations (EGBDs). Varin *et al.* [11] concluded from the temperature dependent yield stress plots (figure 2.3) of Mannan *et al.* [52] that the yielding, at least in the austenitic stainless steel, is strongly controlled by the grain boundaries especially for small and medium grain sizes. The main mechanism operating during the high temperature deformation is believed to be the grain boundary sliding and grain boundary migration. Thus the plastic behaviour of a polycrystal is greatly influenced by the grain size and this effect is discussed below.

2.3 Grain size effect in plastic deformation

The effect of grain size on yield and flow stress is of interest towards strengthening of materials. During deformation of polycrystalline materials both the grain boundaries and grain interiors contribute to varying extents. A reasonable mechanical properties can be achieved from the control of grain boundaries structure and grain size. First attempt in this direction was made by Hall [55] and Petch [56] to correlate the yield stress with grain size. In this section the Hall-Petch behaviour of polycrystalline materials is reviewed.

2.3.1 Hall-Petch relation

The dependence of yield and flow stress on grain size is expressed by the well known Hall-Petch relation:

$$\sigma(\epsilon) = \sigma_0(\epsilon) + K(\epsilon) d^{-1/2} \quad (2.18)$$

where, $\sigma(\epsilon)$ is the flow stress, d is the average grain size, $\sigma_0(\epsilon)$ and $K(\epsilon)$ are constants at a given strain known as Hall-Petch intercept and Hall-Petch slope respectively. The above relationship based on experimental observations is rationalised by various investigators [55–61]. $\sigma_0(\epsilon)$ is equivalent to the flow stress of a single crystal oriented for multi-slip. The term $K(\epsilon)d^{-1/2}$ relates to the resistance at the end of the slip band reaching the grain boundary. In other words $\sigma_0(\epsilon)$ is known as friction stress and $K(\epsilon)$ the grain boundary strengthening parameter. $\sigma_0(\epsilon)$ and $K(\epsilon)$ depend on the plastic strain and temperature. Equation 2.18 gives a good empirical description of the behaviour of many metals and alloys. For example, figure 2.5 shows a linear relation between yield stress and $d^{-1/2}$ for many materials [36], whereas figure 2.6 shows linear dependency of yield and flow stress with $d^{-1/2}$ of 70/30 brass [62].

Figure 2.7a shows the effect of plastic strain on the friction stress, $\sigma_0(\epsilon)$. At room temperature, $\sigma_0(\epsilon)$ monotonically increases with increasing strain [41]. The linear increase in $\sigma_0(\epsilon)$ with increasing strain had been correlated [59] with the linear stage 2 hardening observed in single crystals. The linear hardening in stage 2 is related to dislocation interactions in the absence of any recovery processes (e.g., cross slip). Sangal *et al.* [63] observed much higher value of slope ($\frac{d\sigma_0(\epsilon)}{d\epsilon}$) in 316L austenitic stainless steel as compared to theoretically predicted value from the slope of stage 2 hardening of single crystal. Hall-Petch slope $K(\epsilon)$ generally increases with increasing strain at room temperature (figure 2.7b).

The Hall-Petch constants are also dependent on the stacking fault energy (SFE) of the material. Low SFE materials such as brass [62] and 316L austenitic stainless steel [45, 52, 63] show linear dependence of $\sigma_0(\epsilon)$ with ϵ right up to necking while higher SF

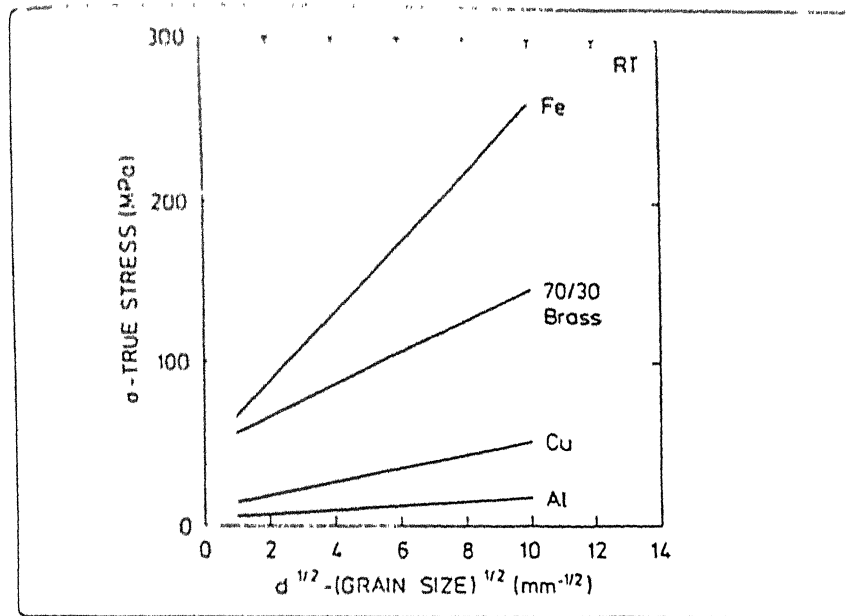


Figure 2.5: Yield stress-grain size relationship at room temperature [36].

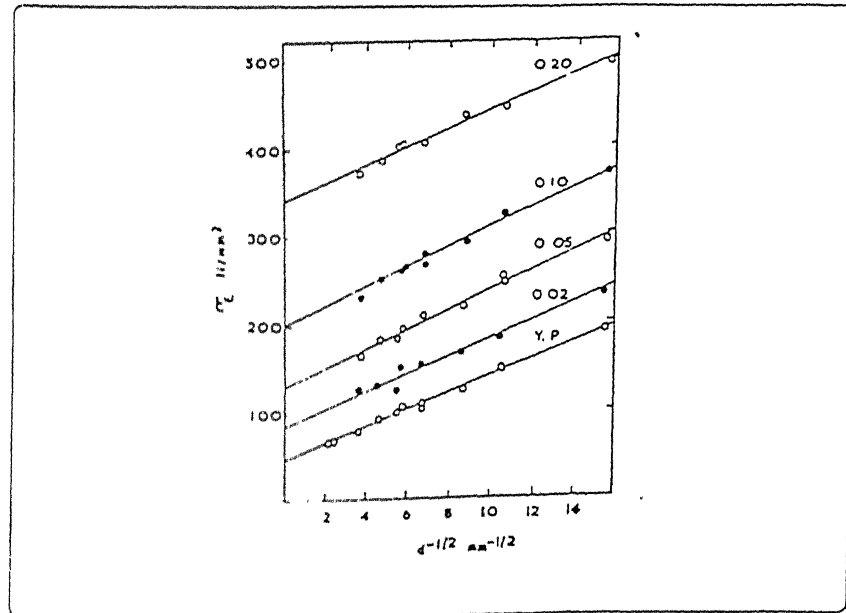


Figure 2.6: Flow stress (σ_f) dependence on grain size at various strains for 30 at. % Zn brass at room temperature [62].

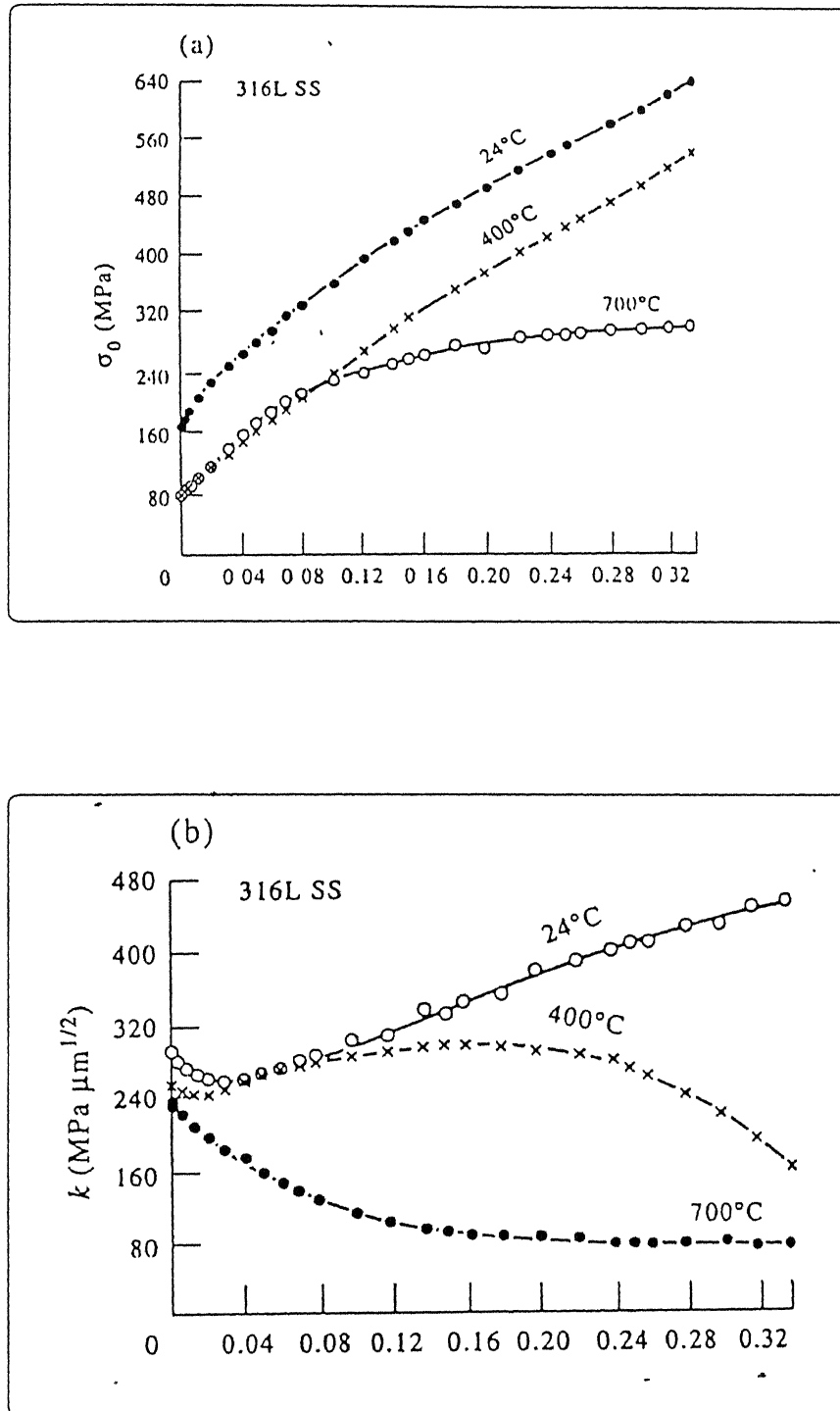


Figure 2.7: The dependence of Hall-Petch parameters (a) σ_0 and (b) K on strain [41]

materials (e.g., copper [62]) show departure from linearity at room temperature. $K(\epsilon)$ also increases with increasing strain in low SFE materials [41,52], whereas a no change [64] or decrease [62] in $K(\epsilon)$ with strain had been usually observed to be a characteristic of high SFE materials. Hall-Petch constants are strongly dependent on temperature and this effect will be discussed in a later sections.

2.3.2 Grain size strengthening models

In the Taylor model and its modifications, the effect of grain size on flow stress is not considered. An allowance for this effect was introduced by Kochendorfer [25] who suggested that the interior of the grains in polycrystalline specimens may deform like isolated single crystal and that the misfit where the grains meet might be accommodated elastically or plastically. It follows from this theory that the flow stress will depend on grain size. Several models were introduced to relate the yield and flow stress with grain size. Some of the important models are presented in the following sections.

2.3.2.1 Hall-Petch model

The original dislocation model for the Hall-Petch behaviour was based on the concept that grain boundaries act as barriers to dislocation motion. The dislocations generated from a source on slip plane will propagate and pile-up at the grain boundaries. When the stress at the tip of this pile-up exceeds some critical value (τ_c), slip is induced in the neighbouring grain. The stress (τ_c) at the tip of a pile-up of n dislocations of like sign is given by following equation:

$$\tau_c = n \tau_s \quad (2.19)$$

where, τ_s is the effective shear stress and it is taken as equal to the applied shear stress (τ) less the friction stress (τ_i) to overcome lattice resistance in dislocation motion. This can

be expressed mathematically as follows:

$$\tau_s = \tau - \tau_i \quad (2.20)$$

The number of dislocations n that can occupy a distance L along the slip plane between the source and the barrier is given by [65]:

$$n = \frac{K \pi \tau_s L}{G b} \quad (2.21)$$

where, K is a factor close to unity for a screw dislocation and $(1-\nu)$ for an edge dislocation. Taking L as equal to $d/2$, we have

$$\tau_c = \frac{\pi K (\tau - \tau_i)^2 d}{2G b} \quad (2.22)$$

or,

$$\tau = \tau_i + \left(\frac{2G b \tau_c}{\pi K d} \right)^{1/2} \quad (2.23)$$

In more simple form equation 2.23 can be written as:

$$\tau = \tau_i + K' d^{1/2} \quad (2.24)$$

In terms of normal stresses equation 2.24 is expressed as:

$$\sigma_y = \sigma_0 + K_y d^{-1/2} \quad (2.25)$$

Equation 2.25 is known as Hall-Petch relation. While σ_y is the yield stress, σ_0 and k_y are known as Hall-Petch intercept and slope, respectively. Armstrong *et al.* [59] considered the flow stress at a given strain as a function of grain size and extended equation 2.25 to include the flow stress at various strains (equation 2.18).

2.3.2.2 Forest hardening models

In this class of theories, pile-ups are disregarded and a linear relation between yield or flow stress and square root of dislocation density is taken as an established experiment

fact [66,67] and expressed by following equation:

$$\sigma_f = \sigma_0 + \alpha G b \rho^{1/2} \quad (2.26)$$

where, ρ is the average dislocation density, α is a numerical constant generally varies between 0.3 to 0.6, and σ_0 is the internal friction stress. Equation 2.26 is commonly known as the hardening equation. The first attempt to relate the dislocation density, at a given strain, to the grain size was due to Meakin and Petch [68], who assumed that the average slip distance L_s might be comparable to the grain diameter. Based on this assumption they obtained the following equation:

$$\sigma(\epsilon) = \sigma_0 + \alpha G b^{1/2} \epsilon^{1/2} d^{-1/2} \quad (2.27)$$

This differs from the usual Hall-Petch equation, since here σ_0 is independent of strain which contradicts the experimental results. Considering grain boundaries as dislocation sources, a more general model proposed by Li [69] avoids the description of the stress at grain boundaries and instead concentrates on the influence of grain size on dislocation density. For a total length of dislocations (released to the interior from grain boundary) per unit area of grain boundary, m , the dislocation density, ρ , at yielding can be calculated for a spherical grain as $\rho = 3m/d$. Combining this relation with equation 2.27 the following relation is obtained [69]:

$$\sigma_y = \sigma_0 + \alpha_1 G b (3m)^{1/2} d^{-1/2} \quad (2.28)$$

Ashby [61,70] proposed a polycrystalline strengthening model in terms of dislocations density. In this model, the deformation of each grain is separated into a uniform deformation and a local nonuniform deformation in the grain boundary region. During the uniform deformation a dislocations density (ρ^s) of statistically stored dislocations accumulates and causes work hardening within the grains, assumed to be same as in equivalent single crystal. In a grain undergoing for a uniform strain in an aggregate of grains overlaps or voids occur. These were corrected by introducing geometrically necessary dislocations

of density ρ^g [71]. The accumulation of ρ^g causes the grain size dependent part of the stress-strain curve. The ρ^g and ρ^s were calculated as follows:

$$\rho^g = \frac{c_1 \epsilon}{b d} \quad (2.29)$$

$$\rho^s = \frac{c_2 \epsilon}{b L^s} \quad (2.30)$$

where, c_1 and c_2 are constants, ϵ is the tensile strain, b is the burger vector, d is the grain size and L^s is the geometrical slip distance.

The total density of dislocations (ρ^t), in a grain may then be taken as the sum of ρ^g and ρ^s , neglecting interactions between the arrays. The following expression for the flow stress was obtained by using the hardening equation 2.26.

$$\sigma(\epsilon) = \sigma_0 + \alpha G \epsilon^{1/2} \sqrt{\frac{c_1 b}{d} + \frac{c_2 b}{L^s}} \quad (2.31)$$

The above equation shows that the flow stress at a constant strain may be a function of $d^{-1/2}(\rho^g \gg \rho^s)$ or $d^{-1}(\rho^s \gg \rho^g)$ depending upon the grain size contribution.

2.3.2.3 Composite models

The assumption by Chalmers and co-workers [72, 73] that a microscopic incompatibility zone with a width of a two micrometers may form at the grain boundary in polycrystals has led Kocks [35] to propose a composite model for polycrystalline strengthening. He considered each grain as consisting of a grain boundary rim (with a volume fraction v_g and a flow stress σ_g) and a grain interior (with a volume fraction v_i and a flow stress σ_i). By equating the forces over the whole grain with the sum of the forces on each component ($f = f_g + f_i$), the following equation was obtained:

$$\sigma = v_g \sigma_g + v_i \sigma_i \quad (2.32)$$

or,

$$\sigma = \sigma_i + (\sigma_g - \sigma_i) \left\{ \frac{4 dx - 4 x^2}{d^2} \right\} \quad (2.33)$$

where, x is the width of the grain boundary region and d is the grain size. For $d \geq x$ this equation can be written as:

$$\sigma = \sigma_i + \frac{4x(\sigma_g - \sigma_i)}{d} \quad (2.34)$$

It follows from equation 2.34 that the flow stress may vary with d^{-1} . However, a $d^{-1/2}$ relationship may also be obtained if x and σ_g are allowed to vary with d .

The composite model was further developed by Thompson and co-workers [57,74,75] by assuming the grain boundary area to be proportional to L^s/d , and obtained the following expression [74]:

$$\sigma = \sigma_0 + \left(1 - \frac{L^s}{d}\right) \frac{k_1}{L^s} + \frac{L^s}{d} k_y d^{-1/2} \quad (2.35)$$

where, L^s is the average slip length and is a function of strain and grain size, k_1 and k_y are constants. At small strains, L^s approaches d and the above equation becomes equivalent to Hall-Petch type. At increasing strain, L^s/d decreases, and thus the effect of grain size on the flow stress decreases.

Either forest hardening or composite model can be transformed into the Hall-Petch type of relationship, which is understood to be the fundamental model for grain size strengthening. The linear hardening of Hall-Petch intercept, $\sigma_0(\epsilon)$ with strain is due to the increasing stress field of already accumulated parallel pile-ups on the fresh pile-up involved in starting the next slip band in neighbouring grain [62]. The increase in dislocation density inside a grain with strain has been also observed by transmission electron microscopy [41]. The higher rate of increase in $\sigma_0(\epsilon)$ with strain compared to stage 2 hardening in single crystal was attributed to the long range stress field of extrinsic grain boundary dislocations in 316L austenitic stainless steel [63].

The increase in $K(\epsilon)$ with strain in low SFE materials can be explained from the forest hardening model of Meakin and Petch [68], where $K(\epsilon) = \alpha G b^{1/2} \epsilon^{1/2}$. In high SFE materials, the drop or no change in $K(\epsilon)$ is attributed to the development of substructures [64]. It may be pointed out that the formation of substructures implies that the initial grain size, d can no longer be used in the Hall-Petch relationship. Therefore it may

be concluded that this observed decrease in $K(\epsilon)$ with strain has no physical significance in equation 2.18. However the observed decrease in $K(\epsilon)$ at lower strain in low SFE materials like 316L austenitic stainless steel (figure 2.7b) as reported by Sangal *et al.* [63] and Kashyap *et al.* [41] cannot be explained on the above basis as no recovery process was initiated during room temperature deformation at low strains in this material. The observed initial decrease in $K(\epsilon)$ with ϵ may be due to the formation of extrinsic grain boundary dislocations (EGBDs) which act as sites of stress concentrator i.e., making it easier to generate dislocations in the vicinity of grain boundaries [63, 76]. The increase in $K(\epsilon)$ with ϵ in figure 2.7b at higher strain may be ascribed to the development of the mantle zone which hinders the propagation of dislocations through it [57, 61].

2.3.3 Effect of other microstructural parameters on flow stress

The yield and flow stress may not be only dependent on the grain size but also on other microstructural parameters, such as grain size and shape distribution, texture, and grain boundary structure. Hall-Petch relation was derived with the assumption that the stress concentration at the head of pile-ups containing large number of dislocations reaches the critical value to initiate slip in neighbouring grains. Hence this relationship may not even be used for very fine grain sizes (in nano crystalline materials), where the distance between the source at the center of grain and the grain boundary is very small. The number of dislocations in this small pile-up length may not be sufficient to initiate a dislocation source in the neighbouring grain [77].

The grain size and shape distribution play an important role in the plastic deformation of polycrystalline materials. For example, for the same mean grain size, the samples with varying grain size distribution would have varying volume fraction of grain boundaries. Since in the early stages of plastic deformation the mechanical properties of polycrystal are largely controlled by grain boundaries, varying volume fraction of grain boundaries would have an influence on these properties [78].

Texture plays an important role in the plastic deformation of polycrystals. Macher-auch [79] in his review paper has pointed out that a difference in texture may be developed due to the different mechanical and thermal treatments employed to obtain different grain sizes. This may be the possible reason for the cross over of stress-strain curves and negative values of $K(\epsilon)$ at high strains as reported by Thompson *et al.* [48].

Thompson and co-workers [48,57,75,80,81] considered that the cross over effect was an intrinsic property of polycrystal work hardening and any texture effect was overshadowed by the grain size effect. Hansen [36] in his review paper reported an increase in the volume ratio of $\langle 111 \rangle$ to $\langle 100 \rangle$ texture component during annealing of cold rolled copper in the temperature range of 400 °C to 750 °C for 10 to 20 hours to cause grain growth. The Taylor factors for the two components are 3.66 and 2.45 respectively and this texture development results in an increase in flow stress with the increase in grain size. It has been also suggested by other investigators [49,82,83] that the cross over in stress-strain curves and negative values of $K(\epsilon)$ at large strains may be an effect associated with texture. Therefore, equation 2.18 may be a valid empirical equation for the flow stress-grain size relationship in polycrystalline specimens if texture effects are accounted for.

In the grain size strengthening models, it has been implicitly assumed that grain boundary structures are similar in all samples of different grain sizes. But different thermo-mechanical treatments applied to obtain different grain sizes may result in high energy boundaries or non-equilibrium boundaries. For low annealing temperature or annealing time, the grain boundaries may remain in a non-equilibrium state after recrystallisation and grain growths as reported by Varin and Tangri [84] in an austenitic stainless steel. The lattice dislocations are easily incorporated in the grain boundaries during grain boundary migration in grain growth, and this results in a highly non-equilibrium structure of the grain boundaries. The increased thermal energy during the annealing at elevated temperatures is responsible for the rearrangement of grain boundary atoms into equilibrium state i.e., low energy configurations. Lattice dislocations can easily run-in into high angle grain boundaries during deformation, thus creating extrinsic grain boundary dislocations

(EGBDs) as shown in figure 2.8a [85]. Grain boundaries containing EGBDs possess higher energy and they can be transformed during high temperature annealing to the low energy equilibrium state by grain boundary recovery [86] as shown in figure 2.8b. It has been shown [4, 5, 12, 84, 87] that the temperature at which EGBDs disappear during in situ heating in transmission electron microscope (TEM) is significantly lower for austenitic stainless steel specimens cold rolled and annealed at relatively lower temperatures of 750 °C to 760 °C as compared to those annealed at about 1100 °C. The low temperature of disappearance of EGBDs indicates a non-equilibrium grain boundary structure, i.e., a higher grain boundary free energy.

It had been shown [13, 88] that grain boundary state has a significant effect on mechanical properties of polycrystals. Higher value of $K(\epsilon)$ in the fine grain region as compared to that in the coarse grain region in 316L austenitic stainless steel [41, 78] cannot be explained from the Hall-Petch model. Differences in the grain boundary structure may be the possible reason for above deviation. Higher free energy of grain boundaries in the fine grain region causes harder mantle zone and hence higher value of $K(\epsilon)$ as compared to that in the coarse grain region. So the relative grain boundary energy distribution in polycrystals is an important microstructural parameter in the study of plastic deformation behaviour.

2.3.3.1 Estimation of grain boundary energy distribution

Several investigators, for example Phumphery *et al.* [4, 5] and Varin *et al.* [12, 89–91] have measured the grain boundary energy by studying the spreading and disappearance kinetics of extrinsic grain boundary dislocations (EGBDs) in TEM during in-situ annealing. However the technique is cumbersome as well as prone to error in the estimation of temperature and time of disappearance of EGBDs. The value of grain boundary energy has been calculated by measurement of groove angles in the thermal groove method [1] and in the Zero creep method [2, 3]. During thermal grooving and Zero creep, the origin

structure of the boundary may change and therefore, it may not be possible to estimate the grain boundary energy distribution of the original structure. Also the methods are limited to surface grain boundaries and may not be representative of the bulk material. Grain boundary energies could also be related simply to the true dihedral angles [9, 10] i.e., the angle between grain boundary planes meeting at a triple edge in the three dimensional structure of polycrystals. Murr *et al.* [6-8] have directly measured the true dihedral angles using TEM images in which the three dimensional structure of grain boundary planes meeting at triple edges can be observed. This method of measurement is tedious and therefore it is not possible to obtain a statistical estimate of the true dihedral angle distribution in polycrystals. Cahn [92] and Goux [93] have pointed out that the true dihedral angles depend not only on the relative energy of grain boundaries but also on the torque resulting from the dependence of the energy on grain boundary orientation. Assuming that the torque term might be statistically neglected, the distribution of true dihedral angles in polycrystals can be used to infer changes in the distribution of relative energy of grain boundaries [94]. Assuming a normal distribution of grain boundary energies, Kurzydłowski [95] has related the energy distribution of grain boundary to the distribution of plane dihedral angles (i.e., the angles between grain boundary lines meeting at triple point observed in polycrystal microstructures obtained from plane of polish). The assumption of normal distribution is the main limitation of this method. The statistical distribution of true dihedral angles (TDA) may be estimated from the measured distribution of plane dihedral angles (PDA).

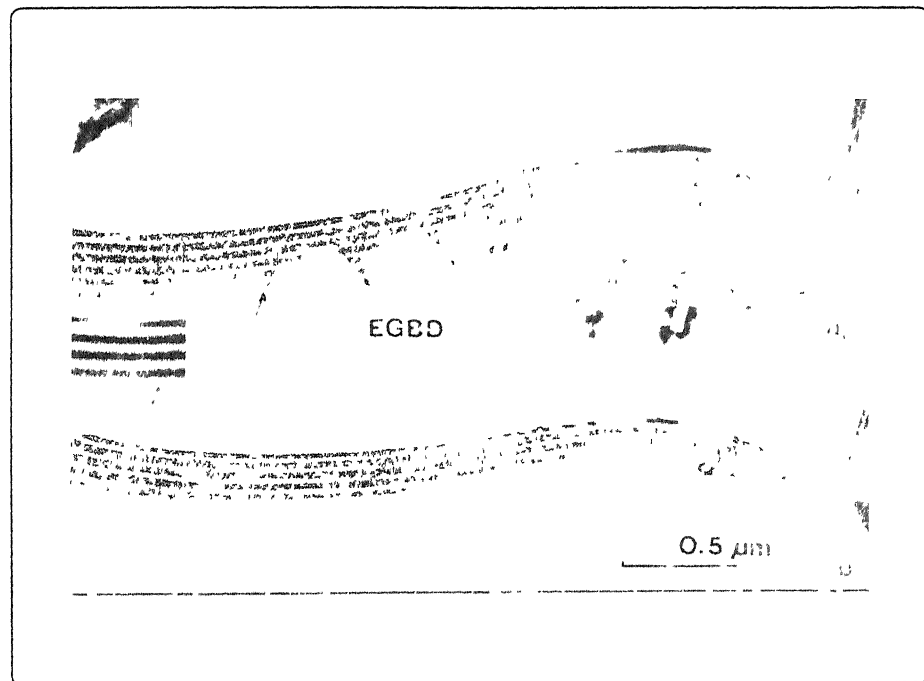


Figure 2.8: TEM micrographs: (a) showing EGBDs at grain boundary and (b) after annealing in-situ, EGBDs have disappeared [85].

2.3.4 Effect of temperature

Temperature has a very pronounced effect on the yield and flow stress of polycrystals and hence on the Hall-Petch constants. Generally the Hall-Petch intercept $\sigma_0(\epsilon)$ decreases monotonically with increasing temperature, whereas $K(\epsilon)$ decreases with increase in temperature except at intermediate temperatures where $K(\epsilon)$ shows a plateau or hump [52,88] as shown in figure 2.9. Armstrong [96] demonstrated that $\sigma_0(\epsilon)$ reflects the deformation processes in the grain interiors, while $K(\epsilon)$ reflects those in the grain boundary regions. Thus the monotonic decrease of $\sigma_0(\epsilon)$ with temperature may be attributed to decreasing lattice friction. Similarly if the general tendency for $K(\epsilon)$ to decrease with temperature is interpreted as weakening of the locking effects at grain boundaries, then the increase in $K(\epsilon)$ at intermediate temperatures may be attributed to a mechanism which contributes to additional locking at grain boundaries in this temperature range. The additional locking could occur as a result of dynamic strain aging in the grain boundary regions [41,88]. Solute segregation at grain boundaries on Cr-Mn-N austenitic stainless steel [88] may be the possible reason for dynamic strain aging at grain boundaries. Also the flow stress peaks become more pronounced at finer grain sizes is a further reason for concluding that grain boundary regions are preferred sites for dynamic strain aging [52].

From the substructural studies in 316L austenitic stainless steel, Kashyap and Tangri [41] have shown that, at intermediate temperatures (approximately 400 °C) the dislocation density in the grain interior is higher than that at room temperature, may be due to the dynamic strain aging effect. In spite of higher dislocation density at 400 °C $\sigma_0(\epsilon)$ is less than that at room temperature which reflects the dominance of thermal effect on the lattice friction. At higher temperatures (approximately 700 °C) dislocation are uniformly distributed in the grain interior, with a density less than that at 400 °C. However at higher strains, dynamic recovery is more predominant at 700 °C as compared to the substructures developed at 400 °C. This difference may result in lower $\sigma_0(\epsilon)$ at higher strains at 700 °C than those observed at 400 °C. The decrease in $K(\epsilon)$ at high

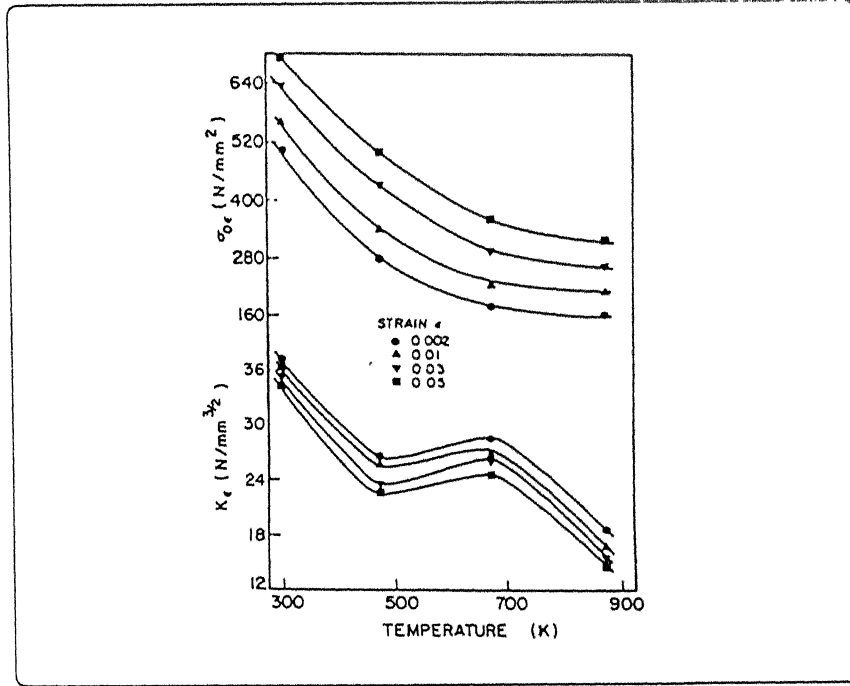


Figure 2.9: Temperature dependence of the Hall-Petch parameters [88].

temperatures is due to the cell formation which becomes easier by cross-slip and climb of dislocations.

2.3.5 Deviation from Hall-Petch relationship

Many metals and alloys clearly obey the Hall-Petch relation with some deviations [41, 49, 78, 80, 97]. Tangri and co-workers [41, 78] have observed bi-linear Hall-Petch relation in 316L austenitic stainless steel. The small grain size region shows positive deviation from the Hall-Petch plot. Sangal and Tangri [78] explained this deviation to the higher volume fraction and higher energetic state of grain boundaries which resulted in higher yield stress as compared to the extrapolated Hall-Petch plot in the similar grain size regime. Kashyap and Tangri [41] had observed higher dislocation density in the grain interior of the large grained specimens as compared to that in the fine grained specimens and hence σ_0 in the coarse grain region is higher than that in the fine grain regime. Larger accumulation of

dislocations in the mantle zone of the smaller grained specimen (increased width of mantle zone must impede further the transfer of slip from one grain to other) is responsible for higher $K(\epsilon)$ in the fine grain regime compared to the coarse grain regime.

In fine grained aluminium polycrystals, Lloyd [49] reported yield stress as inversely dependent on grain size and this relationship was found by Morris *et al.* [98]. The higher $K(\epsilon)$ value in the fine grain region obtained in the Hall-Petch plot may be due to inhomogeneous yielding and the propagation of Luder bands through the gauge length. At higher strains, $\sigma(\epsilon)$ versus $d^{-1/2}$ plot gives single linear line as observed by Kashyap *et al.* [41] in 316L austenitic stainless steel. Below 1 μm grain size in Nickel, Thompson [80] observed no change in flow stress with $d^{-1/2}$. This may be attributed to suppression of cell formation. Dislocation sources in the grain interior become rare below 1 μm . Thus the grain boundary sources are predominant in sub-micron grains. It implies that slip length is a weak function of strain and hence the fine grained materials deform entirely by boundary hardening. In copper polycrystals negative values of $K(\epsilon)$ at large strains were reported by Thompson *et al.* [48]. This deviation from the Hall-Petch relation may be an effect associated with texture [36, 49, 79, 82, 83].

Thus it seems that a single Hall-Petch relation is not able to incorporate the entire range of grain sizes. This may be due to the effect of other microstructural parameters on flow stress as discussed in section 2.3.3, which are not taken into account in Hall-Petch relationship. Also at high temperatures ($T > 0.5T_m$), the Hall-Petch behaviour is expected to break down [52, 88] since other high temperature mechanisms, such as grain boundary sliding, grain boundary migration and diffusional flow may be operative as discussed below.

2.3.6 Hall-Petch behaviour in high temperature deformation

High temperature deformation is commonly known as the working temperature above equi-cohesive temperature ($0.5T_M$, T_M is the melting temperature of the material). Below $0.5T_M$, most metals and alloys obey the Hall-Petch relationship except in some cases where deviation from the single linear relationship occurs in the fine grain region as discussed in section 2.3.5. On the other hand, Hall-Petch behaviour generally breaks down at high temperatures. For examples, the negative $K(\epsilon)$ value in Cr-Mn-N austenitic steel [88] and the excessive scatter in the $\sigma(\epsilon)$ versus $d^{-1/2}$ plots in 316L austenitic stainless steel [52] were reported. Dominance of high temperature flow mechanisms is the probable reason for break down of Hall-Petch relationship at high temperatures.

At low temperatures, intragranular dislocation slip is the important mechanism of plastic deformation, while at high temperature grain boundary sliding is an important mode of deformation and that the contribution from this mode to total strain increases with decreasing grain size. At high temperatures all the modes (intragranular dislocation slip, grain boundary sliding and diffusional flow) are known to be operative to varying degree depending on temperature and strain rate [99]. It is considered [88] that the total number of dislocations from grain boundary sources which facilitate sliding by relieving the stress concentrations developed at grain corners and other irregularities on the sliding boundary, will be proportional to the grain boundary area which is itself inversely proportional to the grain diameter. Also the diffusion distances decrease with decreasing grain size and any contribution to flow by diffusion creep will increase with decreasing grain size.

The drop in yield stress with the increase in temperature begins at a lower temperature as the grain size decreases. The samples of fine grain size exhibit lower flow stress value compared to the coarse grained samples [11]. Varin *et al.* [11] postulated that the above behaviour is due to the annihilation of EGBDs. As reported earlier, the fine grain size obtained after low temperature annealing is associated with non-equilibrium boundaries and higher free energy compared to the coarser grain size. Higher free energy of grain

boundaries assist in the spreading of EGBDs and hence they disappear at lower temperatures as compared to the coarser grain size samples. Thus at high temperatures, grain boundaries lose their barrier effect to dislocations. Accordingly, Hall-Petch relationship is not applicable at high temperatures.

2.4 Summary

Grain size is an important microstructural parameter which controls the plastic deformation behaviour of polycrystals. Before studying the effect of grain size on plastic flow, the flow stress behaviour and the strain hardening mechanism operating in the plastic deformation of single crystal must be understood. Four commonly well known strain hardening relationships were used to describe the true stress versus true strain curves of polycrystals. But none of them is able to reproduce the experimental true stress vs true strain curve in the entire strain range.

The grain size dependence of yield and flow stress of polycrystals at room temperature can be described by the well known Hall-Petch relationship. Deviation from the Hall-Petch behaviour has also been observed in some materials in the fine grain size region. The yield and flow stress may not be dependent only on the grain size but also on other microstructural parameters such as grain size and shape distribution, texture, and grain boundary structure. For the same mean grain size, samples with varying grain size distribution would have varying volume fraction of grain boundaries. This may result in a different flow stress at a given strain level. Development of texture may result in a higher flow stress of coarse grain samples as compared to that of fine grained samples at a constant strain, which contradicts the Hall-Petch relationship. In the grain size strengthening models, it had been implicitly assumed that grain boundary structure is same in all samples of different grain sizes. But different thermo-mechanical treatments applied to obtain different grain sizes may result in high energy or non-equilibrium boundaries

Grain boundary energy state plays an important role in strengthening, which must be investigated. Grain boundary energy can be estimated by several ways but all the methods suffer from various drawbacks and therefore, it is generally not possible to obtain the energy distribution of grain boundaries in polycrystals. Grain boundary energy could simply be related to the true dihedral angle. To estimate the distribution of true dihedral angles a proper technique needs to be developed.

The effect of various parameters such as strain and temperature on Hall-Petch parameters and flow stress is an open issue in terms of interpreting these effects. Several investigators have interpreted them on the basis of substructural changes during plastic deformation. Not many attempts have been made to correlate the microstructural changes such as grain size, grain shape, grain boundary energy state, etc and Hall-Petch parameters at different strains and test temperatures.

Hall-Petch relationship breaks down at high temperatures. The yield stress drop begins at a lower temperature with decreasing grain size and the samples of fine grain size show lower value of flow stress as compared to that of the samples of coarse grained. The validity of Hall-Petch relationship at different temperatures and strain may be better understood from the knowledge of the rate of generation and annihilation of EGBDs.

Chapter 3

Experimental procedure

3.1 Material

A commercially available 316L austenitic stainless steel was obtained in the form of 12.5 mm thick plates from two different sources referred to as batch 1 and batch 2. The chemical composition of the material was determined using JEOL Electron probe micro-analyser (EPMA) Super-probe model JXA - 8600MX and listed in table 3.1.

3.2 Sample preparation for tensile testing

3.2.1 Cold rolling and Machining

The procedural steps of obtaining the tensile specimens from the as received material are shown in figure 3.1. Pieces of approximately 31 mm length and 38 mm width (figure 3.1b) obtained from the as received plate (figure 3.1a) were cold rolled in successive passes to approximately 1 mm thick strip (figure 3.1c). The flat tensile specimens of dimension

Table 3.1: Chemical composition (Wt %) of commercially available 316L austenitic stainless Steel

Elements	Si	Cr	Ni	Mo	P
Batch 1	0.547	19.194	11.003	2.17	0.017
Batch 2	0.528	18.053	13.726	2.025	0.029
Elements	Cu	W	Al	C	Fe
Batch 1	0.296	0.086	0.109	0.002	Bal.
Batch 2	0.019	0.076	0.036	0.003	Bal.

as shown in figure 3.1d were obtained by machining the rolled strips after removing the cracked edges. The tensile axis of the specimens is kept parallel to the rolling direction.

3.2.2 Heat treatment

The heat treatment was carried out in a Kanthal furnace whose temperature was controlled within $\pm 2^{\circ}\text{C}$ through an Indotherm-401 temperature controller. To obtain a wide range of grain sizes, small pieces of the rolled sheet were heat treated at various temperatures (from 700°C to 1150°C) for times varying from 15 minutes to 510 minutes followed by air cooling. The tensile specimens were heat treated at suitable temperatures and for different times to obtain specific grain sizes.

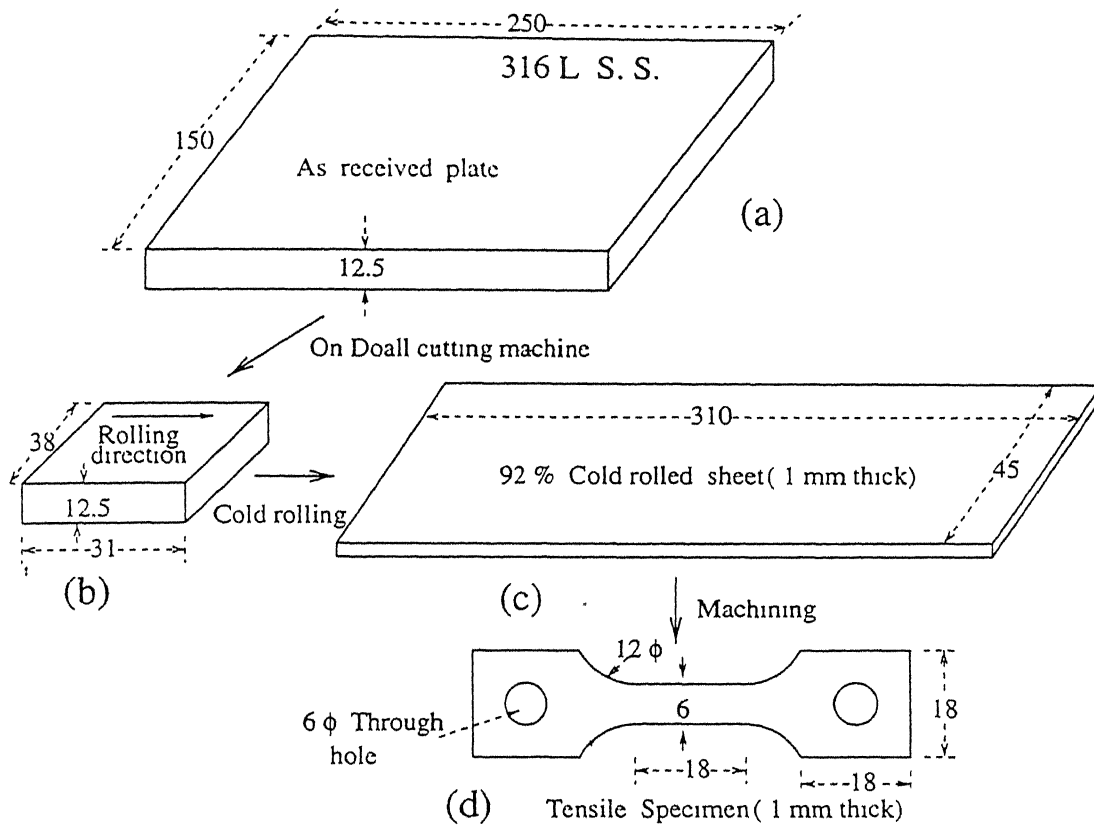


Figure 3.1: Schematic representation of operations to obtain tensile Specimens (all dimensions are in mm)

3.3 Optical and Scanning Electron Microscopy

3.3.1 Specimen preparation and examination

In order to examine the bulk microstructures, the surface layers of the samples were removed by chemical thinning using a hot solution of $50\%HCl-10\%HNO_3-5\%H_3PO_4-35\%H_2O$ [100]. The mounted samples were prepared for metallographic observation making use of standard methods of grinding and polishing. The polished metallographi samples were electrochemically etched in an electrolyte of $60\%HNO_3-H_2O$ at 1.1 Volt and current density of $0.75mA/mm^2$ for about 20 to 60 seconds [101]. This method c etching does not reveal twin boundaries. The specimens were examined by Optical an

Scanning electron (JEOL model ISI 60) microscopes.

3.3.2 Quantitative Metallography

The following quantitative metallographic measurements were carried out from various microstructures. Micrographs obtained from randomly selected areas of annealed and deformed samples were used for this purpose.

3.3.2.1 Grain size and distribution

Linear intercept and grain area methods are used for grain size measurements. More than 6 fields were randomly selected from the polished and etched surface of the annealed and deformed samples and micrographs were obtained. The mean intercept length ($\bar{l} = 1/\bar{N}_l$) is obtained in counting the number of grain boundary intersections (N_l) across a random line and the mean grain size (\bar{d}) calculated by multiplying the mean intercept length (\bar{l}) with a factor of 1.74 [102]. For some of the annealed and deformed samples, the grain size was also estimated from the two dimensional grain area measurements of more than 150 randomly selected grains using an automatic image analyser (Leitz model ASM-68K). The average equivalent grain diameter (\bar{d}_{eq}) is the diameter of a circular area equivalent to the average of measured two dimensional grain areas (\bar{A}), and can be mathematically expressed as follows:

$$\bar{d}_{eq} = \sqrt{\frac{4 \bar{A}}{\pi}} \quad (3.1)$$

In order to obtain grain size distribution in annealed samples, individual intercept lengths of more than 500 grains were measured on the randomly oriented lines across the micrographs. From the calculated equivalent grain diameters, the distribution of grains was also estimated. Percentage relative and cumulative frequency plots were made from these measurements to compare the grain size distribution in samples of different average

grain sizes of two batches.

3.3.2.2 Grain shape factor(S_F)

Grain shape factor (S_F) is defined by the following relation:

$$S_F = \frac{4 \pi A}{P^2} \quad (3.2)$$

where, A and P are the area and perimeter of an individual grain on a two dimensional plane section. The grain shape factor of more than 150 randomly selected grains of annealed and deformed samples were calculated from the measured grain area and perimeter using equation 3.2. The average of individual grain shape factors represents as the grain shape factor of an annealed or a deformed sample.

3.3.2.3 Grain aspect ratio

Grain aspect ratio is calculated from the measurement of mean linear intercepts in longitudinal and transverse directions of annealed and deformed samples. These measurements were directly made either from the polished and etched samples using a graduated eyepiece in an optical microscope or from the micrographs.

3.3.2.4 Dihedral angles

The plane dihedral angles (i.e., angle between grain boundary lines at a triple point on two dimensional plane polished section) measurements of all the three angles at a triple point were made from the traced micrographs of annealed and deformed samples. Grain boundary lines at a triple point were traced from the micrographs. More than 100 triple points were randomly selected and angles between grain boundary lines were measured. The distribution of true dihedral angles (i.e., angle between grain boundary planes meetin

at a grain edge in 3 dimensions) was estimated from these measured distribution of plane dihedral angles using a technique developed in Chapter 4. From the estimated true dihedral angle distributions, standard deviation of true dihedral angles was calculated.

3.4 Tensile testing

3.4.1 At room temperature

Tensile tests at room temperature were carried out on an Instron machine (model 1195) at a strain rate of $4.6 \times 10^{-4} s^{-1}$. From the recorded load-elongation curves, the true stress versus true strain data were calculated and results plotted. The specimens were only tested up to the maximum load in the tensile test. In order to check reproducibility of tensile data, duplicate tests were carried out on samples of each grain size. Three different grain sizes ($4.0\mu m$, $5.9\mu m$ and $29.0\mu m$) were selected from batch 2. Tensile tests were performed on these samples up to different strain levels (5 %, 10 % and 20 %) to examine the microstructural changes during deformation.

3.4.2 At elevated temperatures

A Kanthal wire wound vertical tube furnace whose temperature was controlled to within $\pm 2^{\circ}C$, was used for elevated temperature tensile testing. The specimens were tested in tension in the temperature range of $200^{\circ}C$ to $800^{\circ}C$. After attaining the required test temperature, the specimen was held there for 10 minutes and then tested at a constant cross head speed of 0.5 mm/min ($\dot{\epsilon} = 4.6 \times 10^{-4} s^{-1}$) up to the maximum load for the test temperatures below $600^{\circ}C$. The tests were continued up to fracture for test temperatures above $600^{\circ}C$. From the recorded load-elongation curves, true stress-true strain data were calculated and plotted. Some specimens were also tested on a MTS machine (model

810 12). For quantitative metallographic measurements and microstructural observations at different strain levels, tensile tests were also conducted at 400 °C and 800 °C on samples of three different grain sizes.

3.5 Hardness measurements

Vickers pyramid hardness tester was used for the hardness measurements of the annealed and deformed samples. The indentations were made using a 10 Kg load. An average of four measurements was used for this purpose. Microhardness measurements were carried out across the grains of annealed and deformed samples. A LEITZ MINILOAD 2 microhardness tester was used for this purpose. An average of five impressions was taken in this regard.

Chapter 4

Results

As mentioned in chapter 3, the commercially available 316 L austenitic stainless steel was obtained in the form of 12.5 mm thick plates from two different sources, termed as batch 1 and batch 2 respectively. These plates were cold rolled to approximately 1 mm thickness (92 % reduction) in more than 25 successive passes. To achieve a wide range of grain sizes, the cold rolled samples were annealed at different temperatures and times. The annealed samples were tested in tension at different temperatures between room temperature and 800 °C. The microstructural characterisations of annealed and deformed samples were performed in order to correlate the microstructural changes with plastic deformation. Accordingly, this chapter is broadly divided into four sections. The first three deal with the microstructural characterisation of annealed samples, and deformation behaviour at room and elevated temperatures respectively. A statistical technique based on the principles of stereology [103,104] to estimate the distribution of true dihedral angle, TDA (angle between the grain boundary planes meeting at a common edge, known as triple edge) is developed in section 4.4. This technique is further used in chapter 5 to calculate the distribution of true dihedral angles for different annealed and deformed samples of 316L austenitic stainless steels.

4.1 Characterisation of initial microstructures

The mean grain size, the distribution of size and shape of the grains, plane dihedral angle (PDA) distribution i.e., the angle between the grain boundary segments meeting at triple points on plane of polish, were evaluated. For the starting microstructures the hardness variation with annealing time at various annealing temperatures is shown in figure 4.1. Figure 4.2 shows the hardness variation with annealing temperature for various annealing times.

The variation of the average grain size (d) with annealing temperature and time are presented in figures 4.3 and 4.4 respectively. The grain size increases with increasing annealing time for a given annealing temperature. From figure 4.3, it is seen that the grain growth rate increases with annealing temperature. At a given annealing time, the grain size increases slowly with temperature in the range 800 °C to 900 °C (figure 4.4). However, above 900 °C, grain size increases at a higher rate. 90% confidence limits of the average grain size are shown as vertical bars in figures 4.3 and 4.4. For a wide range of heat treatment conditions, the measured values of hardness and the grain size are presented in table A1 of appendix A.

The deformation behaviour of samples of eight different grain sizes (2.7-64.0 μm) from batch 1 and seven (2.9-46.0 μm) from batch 2 were investigated. The microstructures of fine and coarse grained specimens of batch 1 and batch 2 are shown in figures 4.5 and 4.6 respectively. The grain size measured by two methods (linear intercept and the grain area) is shown in table 4.1. The other microstructural parameters such as grain shape factor (S_F), the coefficient of variation (SD/\bar{d}) of the grain size, the standard deviation of PDA distribution (β_{SD}) and the relative frequency of 120°(115° – 125°) class of measured PDA distribution (β_{120}) of some of the tensile samples are also included in table 4.1.

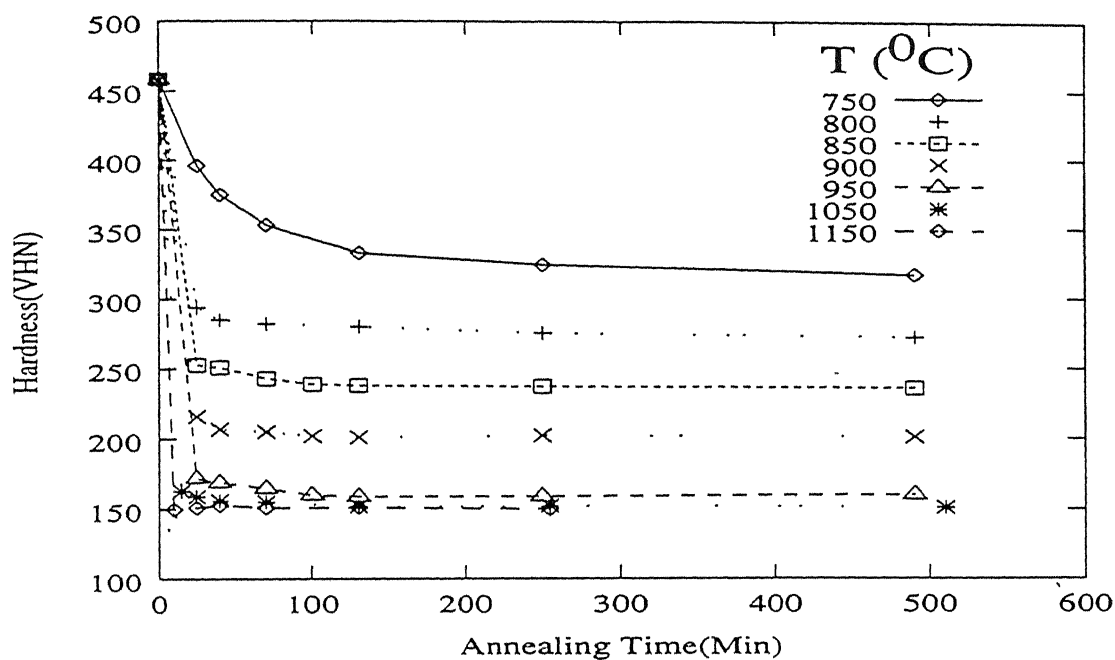


Figure 4.1: Vickers hardness vs annealing time for various annealing temperatures in batch 1.

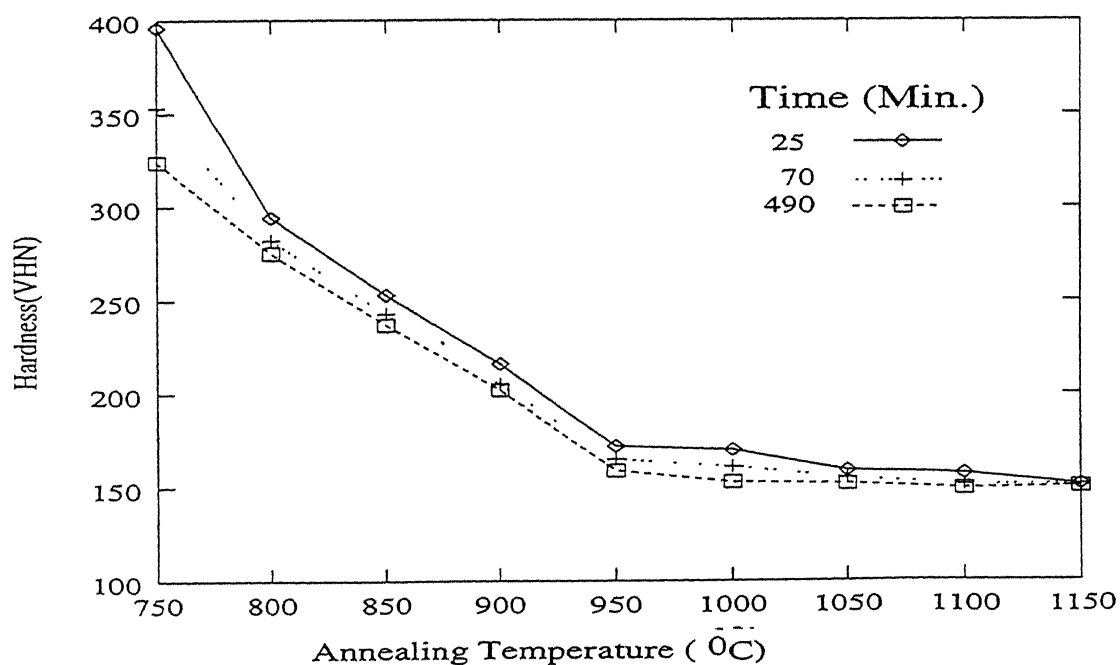


Figure 4.2: Vickers hardness vs annealing temperature for various annealing times in batch 1.

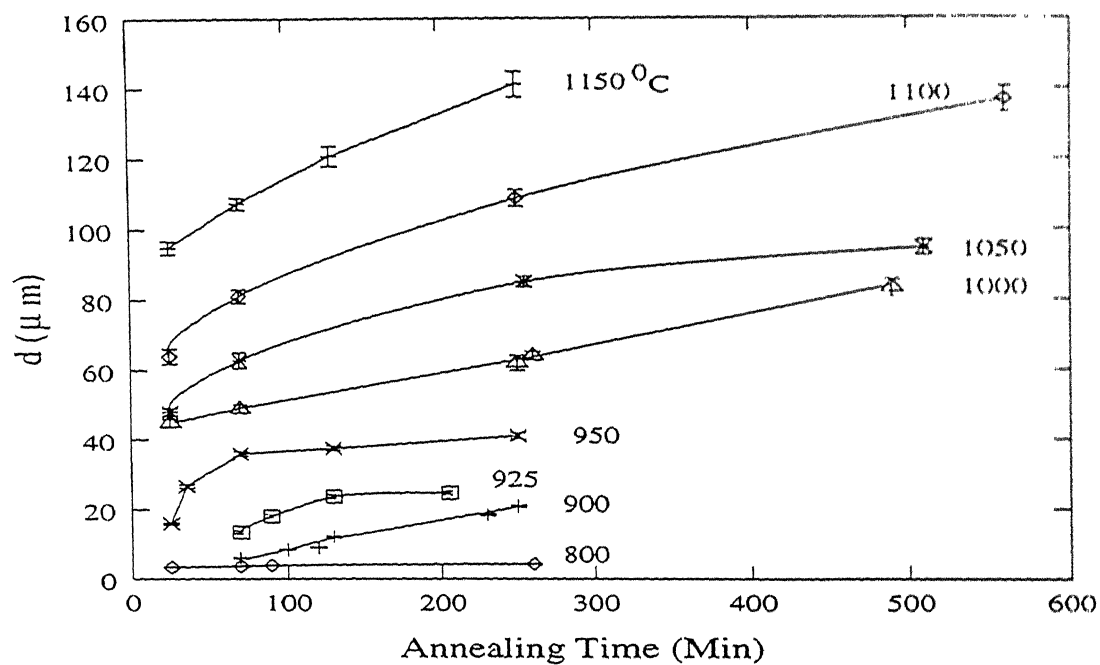


Figure 4.3: Mean grain size vs annealing time at various annealing temperatures in batch 1.

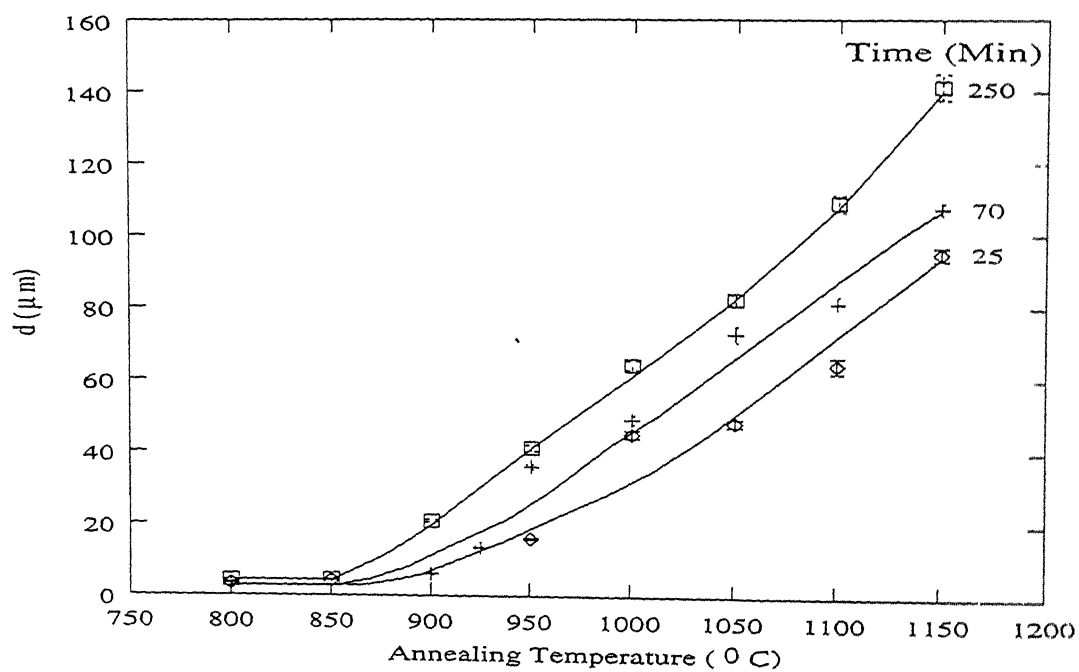


Figure 4.4: Mean grain size vs annealing temperature at various annealing times in batch 1.

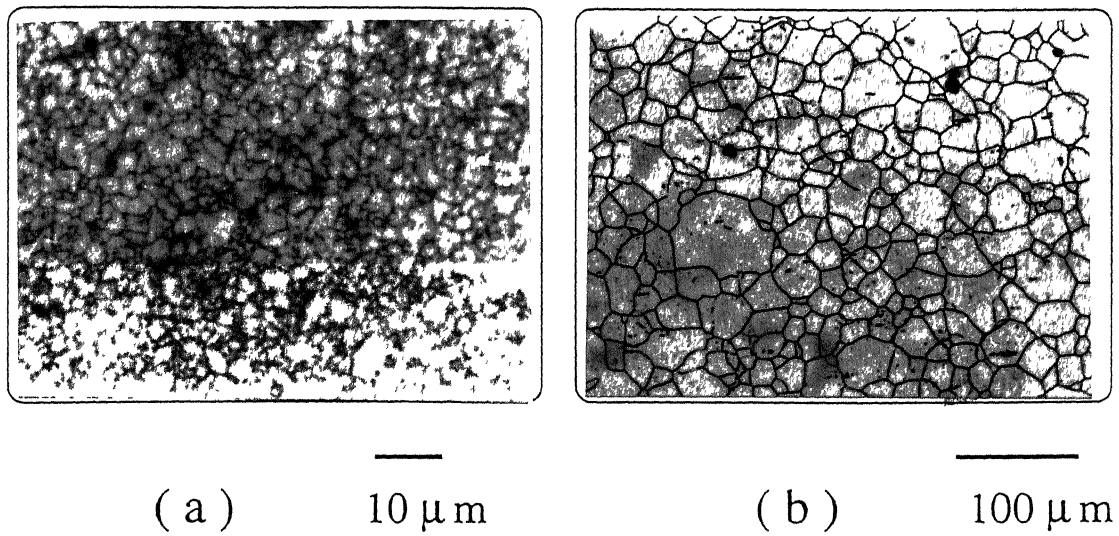


Figure 4.5: Microstructures of annealed samples of batch 1 with grain sizes: (a) $4.5\ \mu\text{m}$ and (b) $26.5\ \mu\text{m}$.

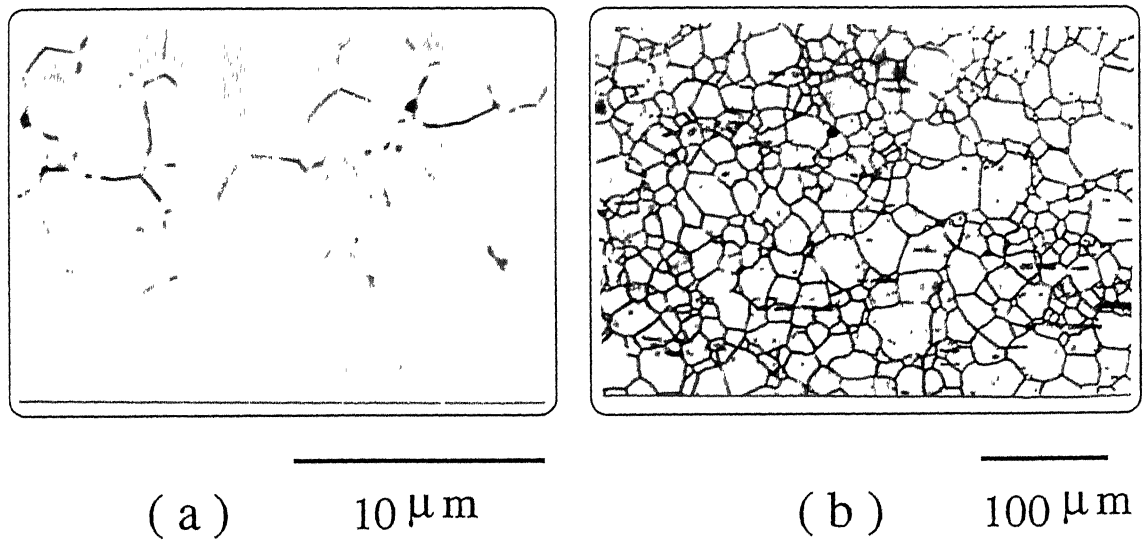


Figure 4.6: Microstructures of annealed samples of batch 2 with grain sizes: (a) $4.0\ \mu\text{m}$ and (b) $29.0\ \mu\text{m}$.

Table 4.1: Microstructural parameters of annealed samples

Batch	Annealing		d^{\dagger} (μm)	d_{eq}^* (μm)	S_F	C_V	β_{SD} (degree)	β_{120}
	T($^{\circ}\text{C}$)	Time(Min.)						
1	750	70	2.7 ± 0.06	2.8 ± 0.15	0.93 ± 0.02	0.06	18.7	0.22
1	800	90	3.9 ± 0.10	-	-	0.07	16.7	0.19
1	850	260	4.5 ± 0.30	5.1 ± 0.35	0.95 ± 0.01	0.14	15.3	0.19
1	900	70	6.0 ± 0.26	-	-	0.12	16.7	0.24
1	900	120	9.0 ± 0.37	-	-	0.12	15.7	0.28
1	900	230	18.3 ± 0.67	19.8 ± 1.72	0.93 ± 0.01	0.10	16.1	0.22
1	950	35	26.5 ± 0.80	28.1 ± 1.94	0.85 ± 0.02	0.09	16.9	0.27
1	1000	260	64.0 ± 2.09	-	-	0.09	15.1	0.23
2	750	60	2.9 ± 0.04	-	-	0.02	-	-
2	800	60	4.0 ± 0.06	4.1 ± 0.31	0.93 ± 0.02	0.04	18.0	0.26
2	850	180	5.9 ± 0.29	5.0 ± 0.33	0.91 ± 0.01	0.14	14.6	0.31
2	875	60	9.0 ± 0.35	-	-	0.11	15.6	0.25
2	900	20	15.0 ± 0.74	-	-	0.14	-	-
2	900	60	29.0 ± 1.17	27.4 ± 1.15	0.91 ± 0.01	0.11	17.3	0.29
2	950	60	45.9 ± 1.86	-	-	0.12	15.0	0.31

† by intercept method

For the purpose of comparing the size distribution of the grains in annealed samples, the frequency distributions were normalised with respect to the mean grain size. Figures 4.7a-b and 4.8a-b show the normalised, the relative and the cumulative frequency distributions for different samples. The relative frequency distributions (figures 4.7a and 4.8a) show positive skew from the normal distribution. There is no significant difference in the relative and the cumulative frequency distributions of different samples of same batch as illustrated in figures 4.7a-b and 4.8a-b. Figures 4.9a-b show the normalised, relative and cumulative frequency distributions for the samples of two batches. It can be seen from figures 4.9a-b that the relative and the cumulative frequencies of two batches also overlap. The same trend of the grain size distribution is also observed by using the individual linear intercept measurements of different samples of both the batches.

Variation of other microstructural parameters: (i) standard deviation of PDA distribution (β_{SD}), (ii) relative frequency of $120^\circ(115^\circ - 125^\circ)$ class of PDA distribution (β_{120}), (iii) grain shape factor (S_F) and (iv) coefficient of variation of grain size (C_v) as a function of mean grain size are shown in figures 4.10a-d. No significant difference is observed in the grain shape factor (S_F) and coefficient of variation (C_v) with grain size of the two batches as shown in figures 4.10c and d respectively. However, below $6\ \mu\text{m}$ grain size, the standard deviation of PDA distribution increases and the relative frequency of 120° class of PDA distribution decreases with decrease in the grain size (see figures 4.10a and b). On the other hand, above $6\ \mu\text{m}$ grain size, these parameters do not change significantly with the increase in the grain size. Figures 4.11a-d show the distribution of the relative frequency of PDA for fine and coarse grain sizes of two batches. The PDAs are distributed from 55° to 180° in both the fine and the coarse grain sizes. However, the relative frequencies of 120° and adjacent class are higher in the coarse grain size compared to that in the fine grain size as shown in figures 4.11a-d.

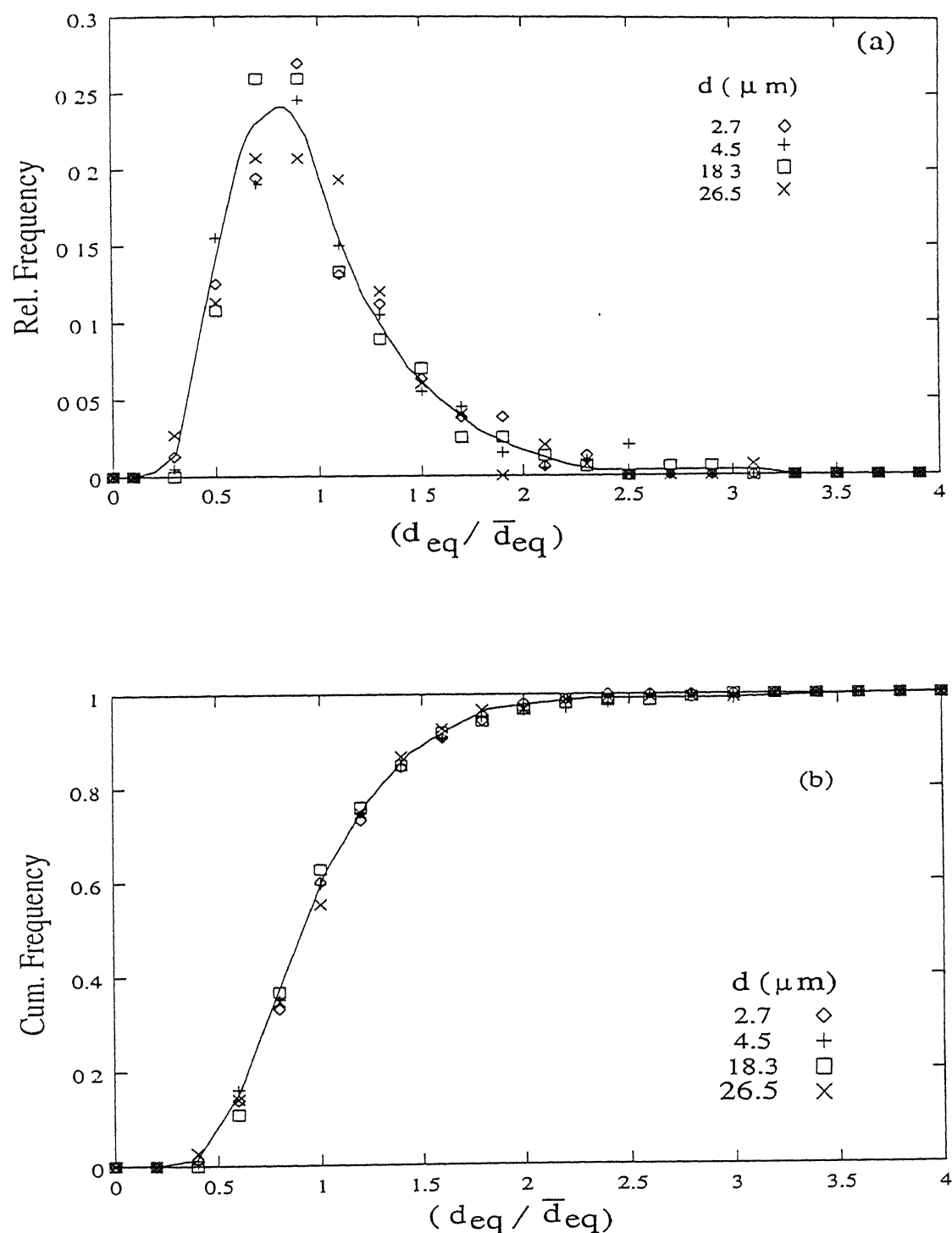


Figure 4.7: Variation of (a) relative frequency and (b) cumulative frequency with normalised equivalent grain diameter ($\frac{d_{eq}}{\bar{d}_{eq}}$) for batch 1.

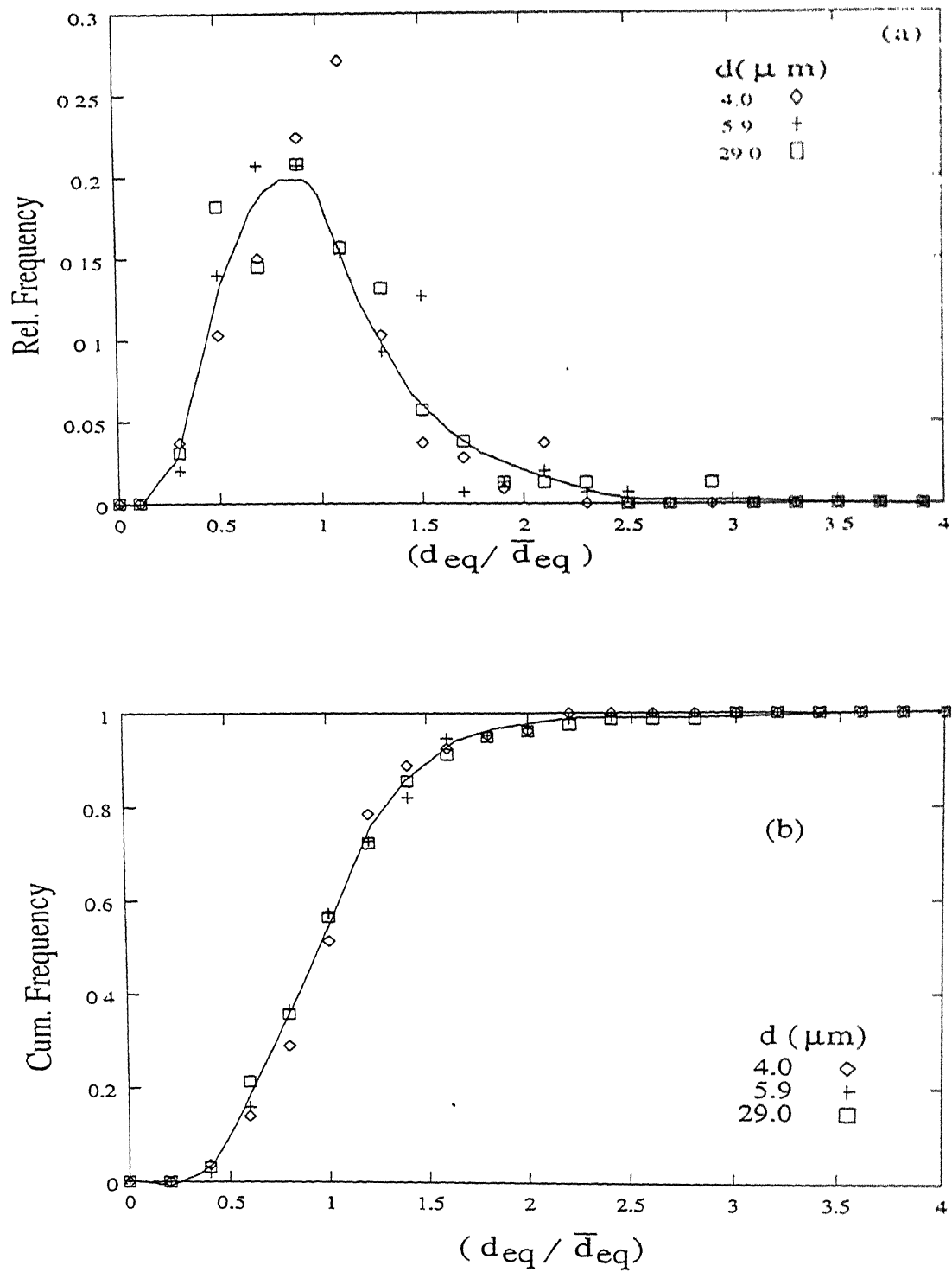


Figure 48: Variation of (a) relative frequency and (b) cumulative frequency with normalised equivalent grain diameter ($\frac{d_{eq}}{\bar{d}_{eq}}$) for batch 2.

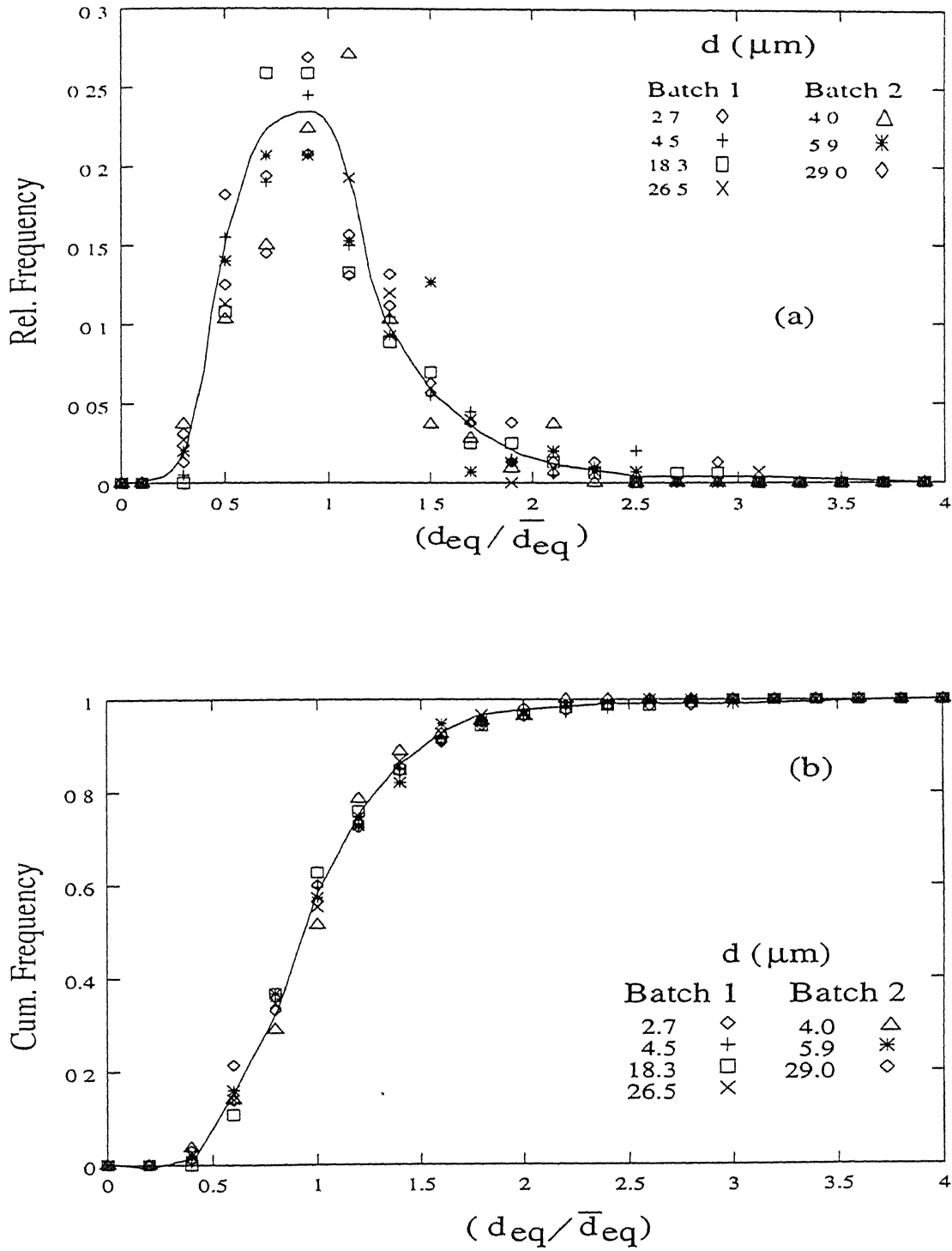


Figure 4.9: Comparison of (a) relative frequency and (b) cumulative frequency with normalised equivalent grain diameter ($\frac{d_{eq}}{\bar{d}_{eq}}$).

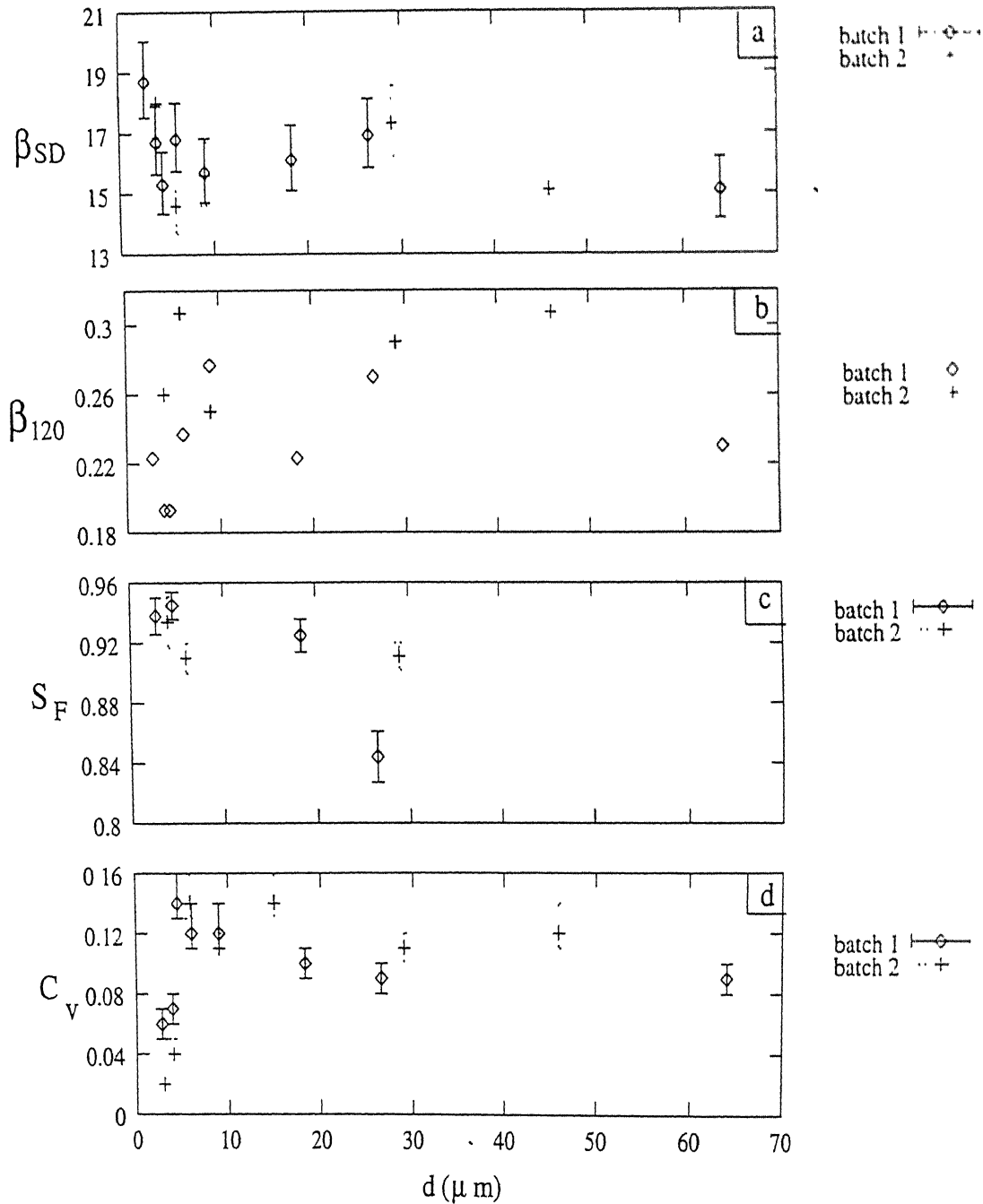


Figure 4.10: Variation of metallographic parameters: (a) standard deviation of PDA distribution (β_{SD}), (b) relative frequency of $115^\circ - 125^\circ$ class of PDA distribution (β_{120}), (c) grain shape factor (S_F) and (d) coefficient of variation of grain size (C_v) with mean grain size.

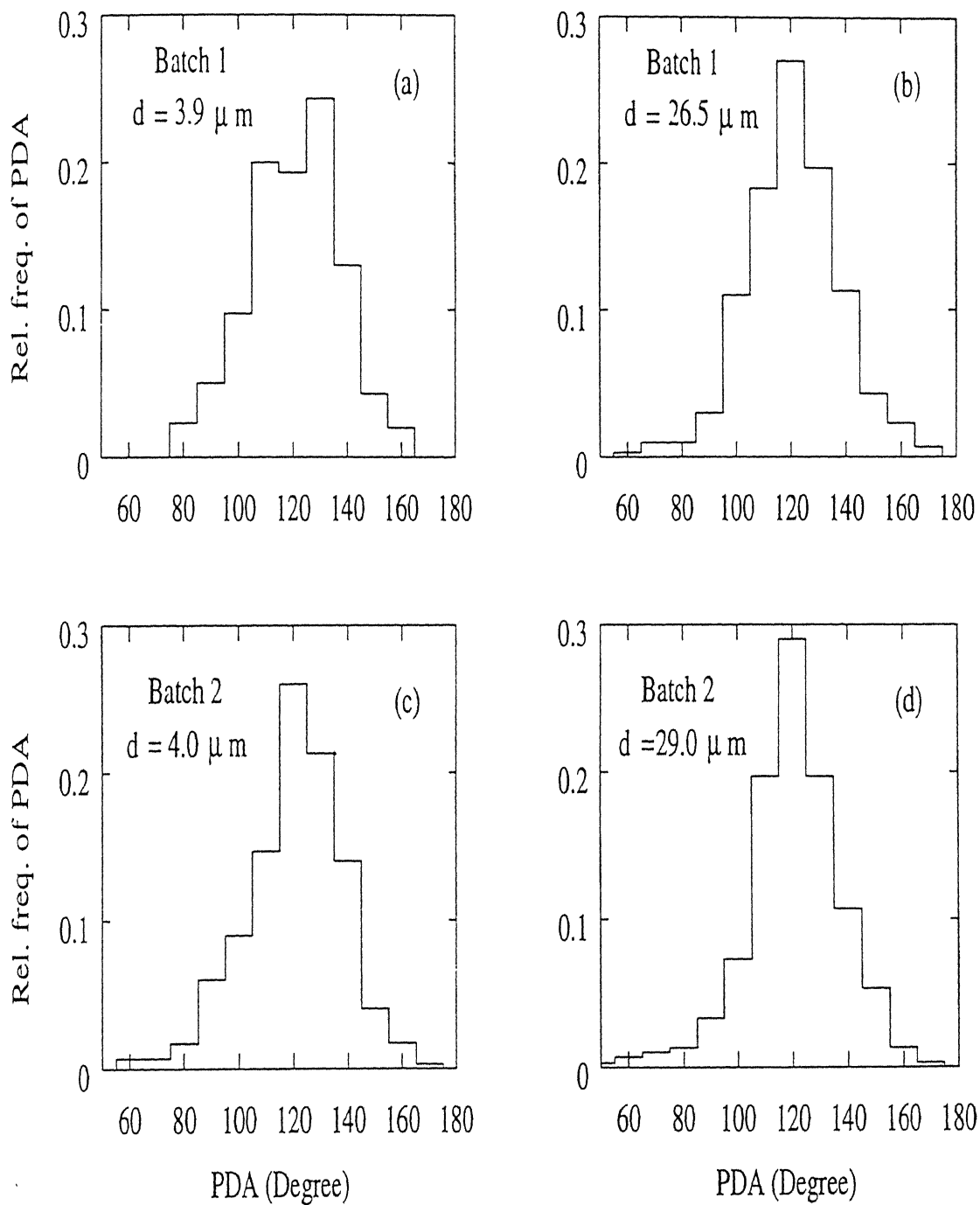


Figure 4.11: Distribution of PDAs in the annealed samples of (a) batch 1 ($d=3.9\mu\text{m}$), (b) batch 1 ($d=26.5\mu\text{m}$), (c) batch 2 ($d=4.0\mu\text{m}$) and (d) batch 2 ($d=29.0\mu\text{m}$).

4.2 Deformation at room temperature

True stress versus true strain curves for samples of various grain sizes are shown in figures 4.12 and 4.13. At a given strain level, the true stress increases with decrease in the grain size. The samples of both the batches with fine grain size show sharp yield point behaviour. For a given grain size, the samples of batch 1 show higher stress as compared to samples of batch 2 over the entire range of strain, as shown in figure 4.14. The tensile properties of samples with different grain sizes are presented in table 4.2. In general, the yield and the ultimate tensile strength decrease while the uniform elongation increases with increase in the grain size for samples of both the batches.

From the $\sigma - \epsilon$ curves of batch 1 (figure 4.12) and batch 2 (figure 4.13), the Hall-Petch plots were made as shown in figures 4.15 and 4.16 respectively at various strain levels. The Hall -Petch plots for samples of batch 1 show two distinctly different linear regimes at all strain levels (see figure 4.15). One linear region is in the fine grain size range ($d \leq 6 \mu\text{m}$) and the other in the coarse grain size range ($d \geq 6 \mu\text{m}$). The bi-linearity in Hall-Petch behaviour can be described by two separate types of equations 2.18. However, single linear Hall-Petch plots were observed at all strains for the case of batch 2, as shown in figure 4.16. For a given strain, the data for each region of batch 1 are fitted by linear regression method. The values of Hall-Petch constants $\sigma_0(\epsilon)$ and $K(\epsilon)$ were estimated from the intercept and slope of the regression line. The values of Hall-Petch parameters and coefficient of regression at various strains for the fine and the coarse grain regimes of batch 1 and for the entire grain regime of batch 2 are listed in table 4.3.

4.2.1 Hall-Petch behaviour

For batch 1 at all strain levels, $\sigma_0(\epsilon)$ in the fine grain regime is less than that of coarse

Table 4.2: Room temperature tensile properties of samples with various grain sizes.

Batch	d^* (μm)	Yield strength(MPa)	UTS (MPa)	Uniform elongation(%)
1	2.7 ± 0.06	763.1	1178.5	26.0
2	2.9 ± 0.04	490.3	1061.7	34.9
1	3.9 ± 0.10	590.1	1083.1	30.8
2	4.0 ± 0.06	436.2	1033.9	39.7
1	4.5 ± 0.30	518.3	1100.1	32.1
2	5.9 ± 0.29	381.2	990.5	39.9
1	6.0 ± 0.26	406.6	1000.5	33.5
1	$9.0 \pm .37$	376.9	960.8	35.9
2	9.0 ± 0.35	332.5	983.9	52.4
2	15.0 ± 0.74	289.2	946.6	47.6
1	18.3 ± 0.67	322.5	943.4	40.8
1	26.5 ± 0.80	299.1	938.9	51.2
2	29.0 ± 1.17	272.3	969.7	52.0
2	45.9 ± 1.86	231.4	865.1	50.7
1	64.0 ± 2.09	222.8	802.5	56.1

* by intercept method

grain regime. On the other hand, the value of $K(\epsilon)$ at a given strain in the fine grain regime is higher than that of coarse grain regime (see table 4.3). Further, it is of interest to note that $\sigma_0(\epsilon)$ in the fine grain regime is negative at lower strain levels (up to 15 %). Alternatively the true stress data for the fine grain regime are plotted against d^{-1} according to the composite model (see equation 2.34). Linear regression lines were fitted at different strain levels as shown in figures 4.17. The intercept $\{\sigma_0(\epsilon)\}$ and slope $\{K(\epsilon)\}$

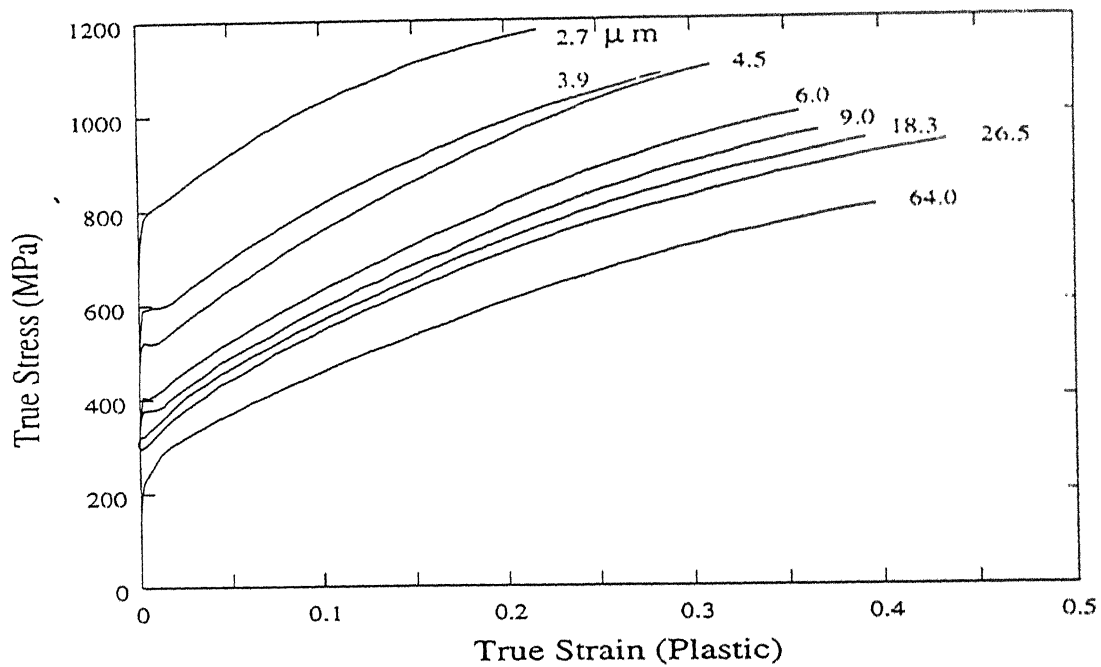


Figure 4.12: True stress-true strain curves for various grain sizes (batch 1).

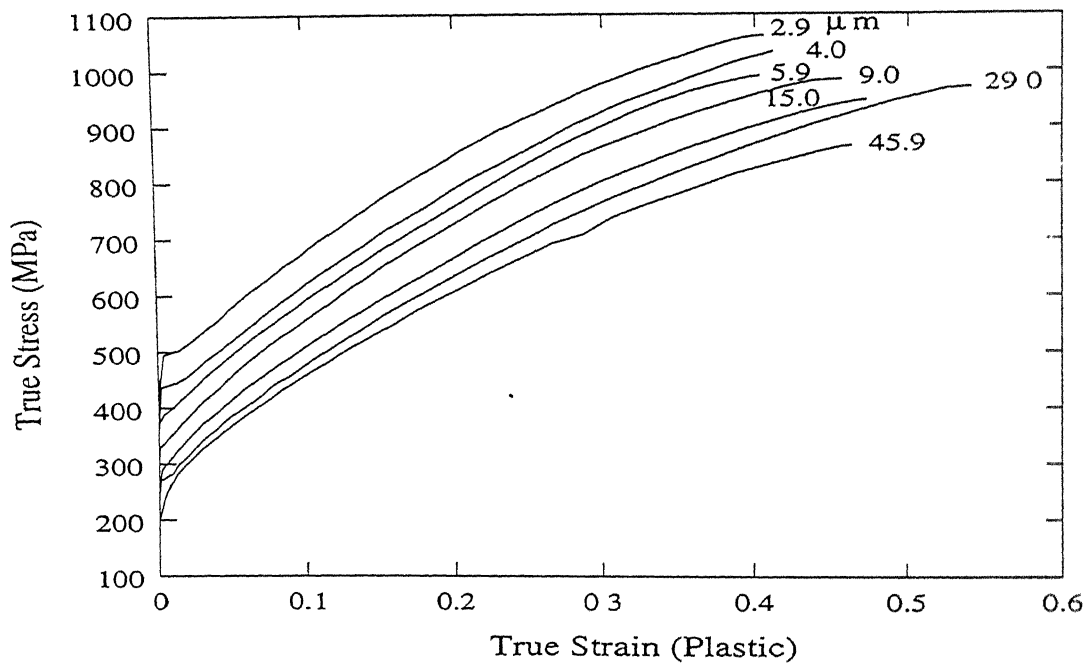


Figure 4.13: True stress-true strain curves for various grain sizes (batch 2).

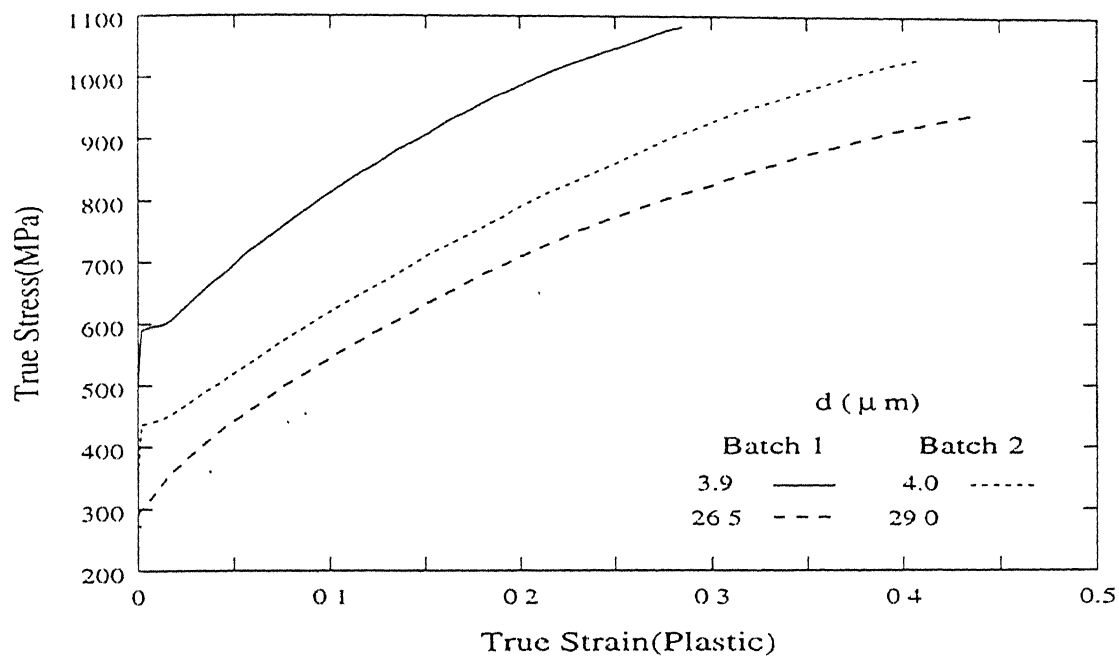


Figure 4.14: Comparison of true stress-true strain curves of batch 1 and batch 2 for different grain sizes.

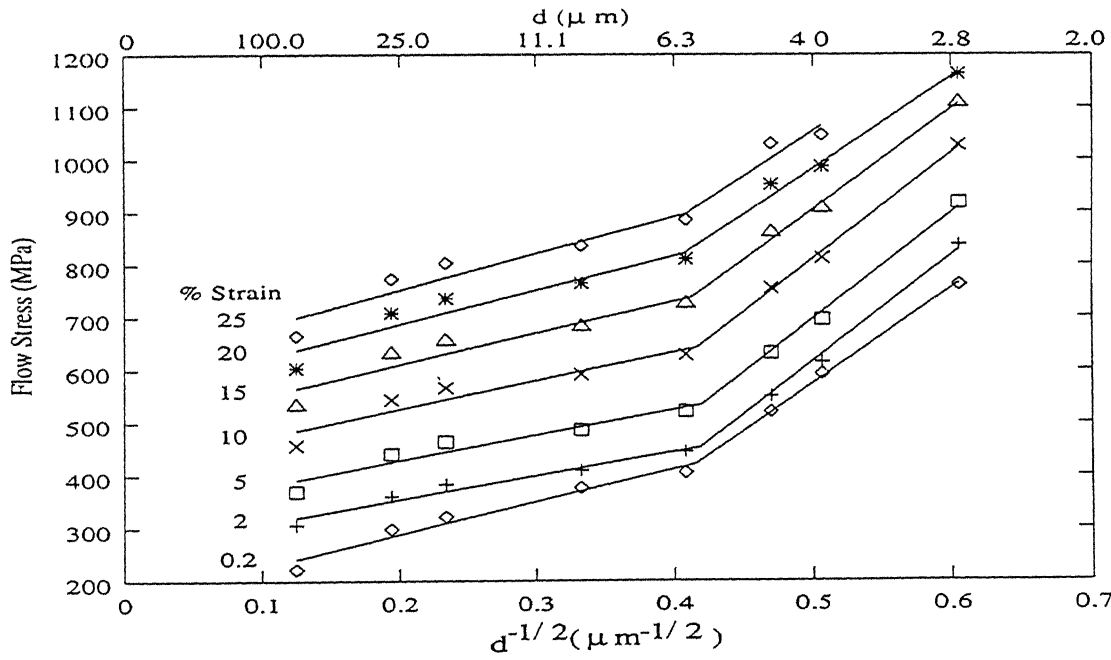


Figure 4.15: Hall-Petch plots at different strain levels (batch 1).

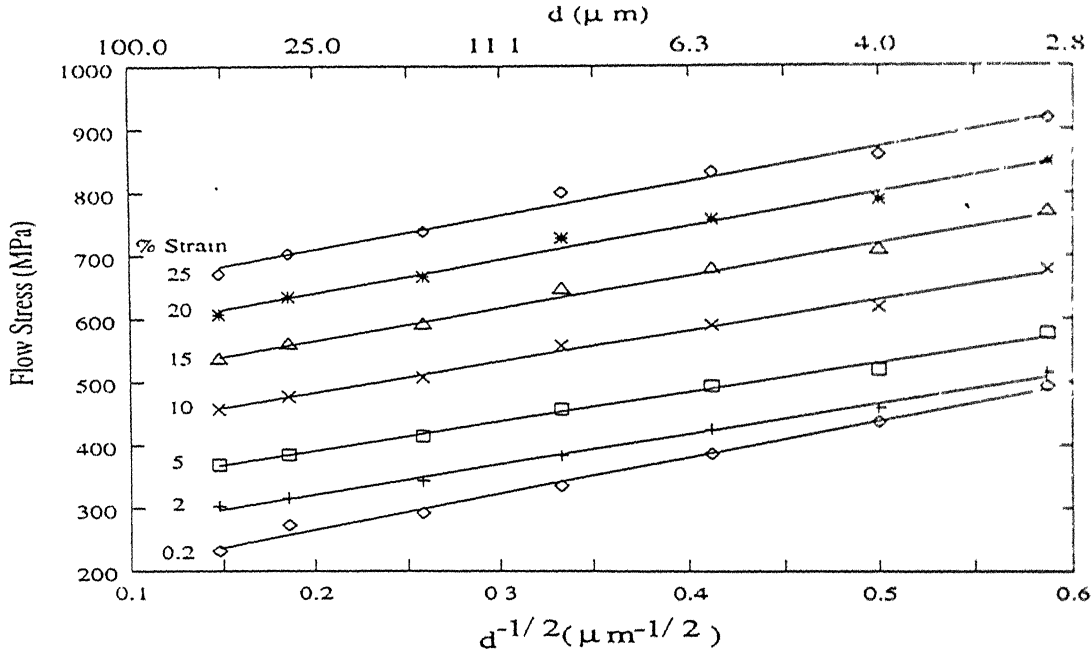


Figure 4.16: Hall-Petch plots at different strain levels (batch 2).

of these lines at different strain levels are listed in table 4.3. It may be noted that in these plots, $\sigma_0(\epsilon)$ is positive at all strain levels. The correlation coefficients of the regression lines of Hall-Petch plots and $\sigma_0(\epsilon)$ versus d^{-1} plots are also listed in table 4.3. The correlation coefficients of these two types of plots in the fine grain region of batch 1 are comparable to each other. The goodness of fit using correlation coefficient for different power of d as presented in table 4.4, depict that the Hall-Petch model is applicable in the coarse grain regime while the composite model is most suited in the fine grain regime of batch 1. Figure 4.18 shows Hall-Petch plots at several strain levels for the samples of the two batches. The stress value is higher for batch 1 than batch 2 at a given strain level, in the entire range of grain size studied. However, this difference is more significant in the fine grain regime as illustrated in figure 4.18.

4.2 Deformation at room temperature

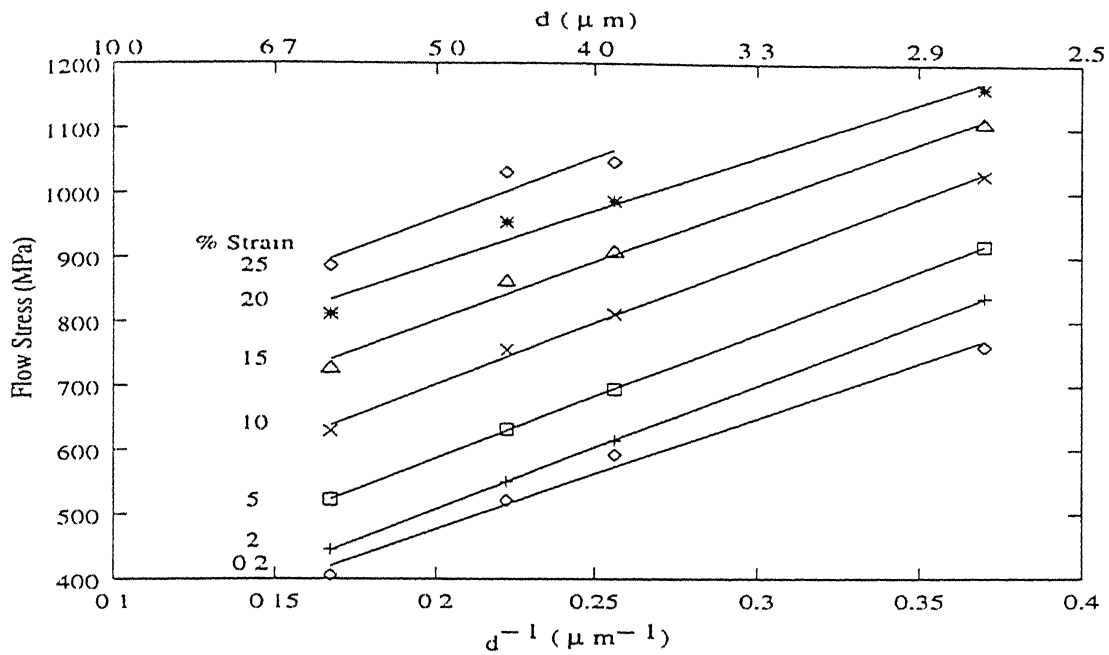


Figure 4.17: Tensile flow stress vs d^{-1} for fine grain regime of batch 1.

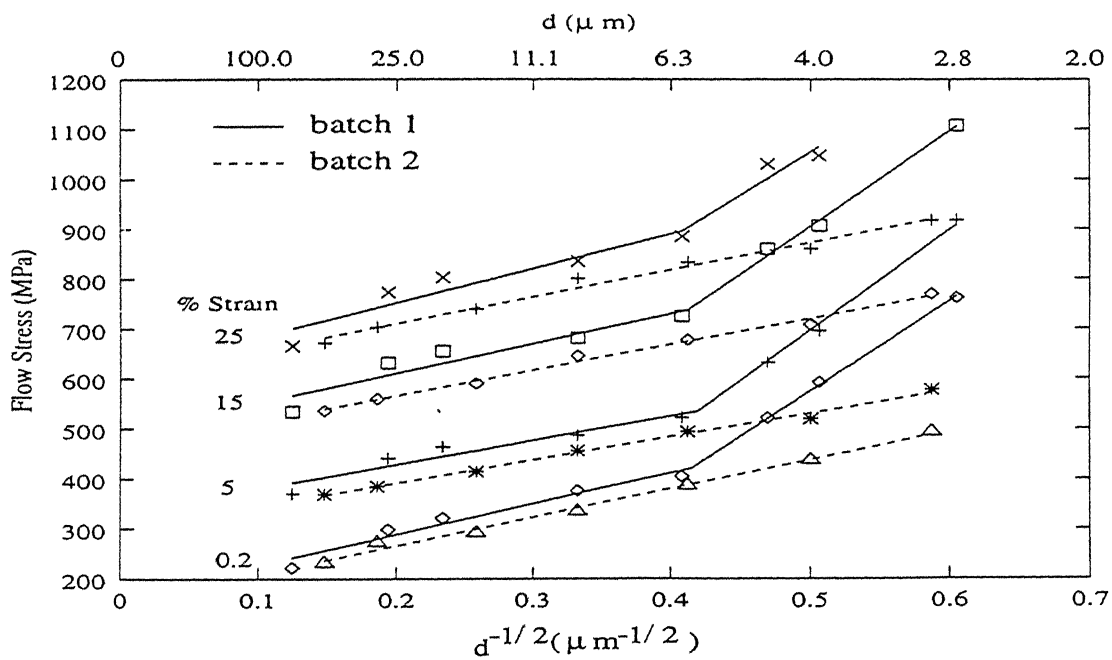


Figure 4.18: Comparison of H-P plots between batch 1 (solid lines) and batch 2 (broken lines) at different strain levels.

The variation of Hall-Petch parameters for coarse grain regime of batch 1 and the entire grain regime of batch 2 are presented in figure 4.19. In both the batches, $\sigma_0(\epsilon)$ increases parabolically with strain as shown in figure 4.19a. Figure 4.19b shows an initial decrease (up to 2 % in batch 1 and 5% in batch 2) in $K(\epsilon)$ followed by an increase with strain in both the batches. The values of $\sigma_0(\epsilon)$ and $K(\epsilon)$ of batch 1 are higher than those of batch 2, at all strains. The variation of $\sigma_0(\epsilon)$ and $K(\epsilon)$ (calculated from the σ versus d^{-1} plots at various strains) with strain for the fine grain regime of batch 1 are shown in figure 4.20. In this case $\sigma_0(\epsilon)$ is more or less unaffected up to 2 % strain followed by a parabolic increase with strain as shown in figure 4.20a. The variation of $K(\epsilon)$ with strain as depicted in figure 4.20b illustrates an initial increase up to 5 % strain followed by a decrease with increasing strain.

4.2.2 Microstructural characterisation of deformed samples

Three different grain sizes from batch 2 were selected for studying the microstructural changes during deformation. These belong to the fine ($4.0 \mu m$), the intermediate ($5.9 \mu m$) and the coarse grain ($29.0 \mu m$) regimes. The microstructures of batch 1 at different strain levels could not be characterised because of scarcity of the material. Figures 4.21a-c show the micrographs of samples deformed to different different strain levels (5 %, 10 % and 20 %). The elongation of the grains in the tensile direction can be noted from figures 4.21a-c. Plots of the standard deviation of PDA distribution (β_{SD}), the relative frequency of $120^\circ(115^\circ - 125^\circ)$ class of PDA distribution (β_{120}), the grain aspect ratio ($\frac{L}{t}$), the grain shape factor (S_F) and the coefficient of variation of grain size (C_v) versus strain are shown in figures 4.22a-e for $29.0 \mu m$ grain size samples of batch 2. Further, the microstructural parameters at different strain levels for different grain sizes are listed in table 4.5.

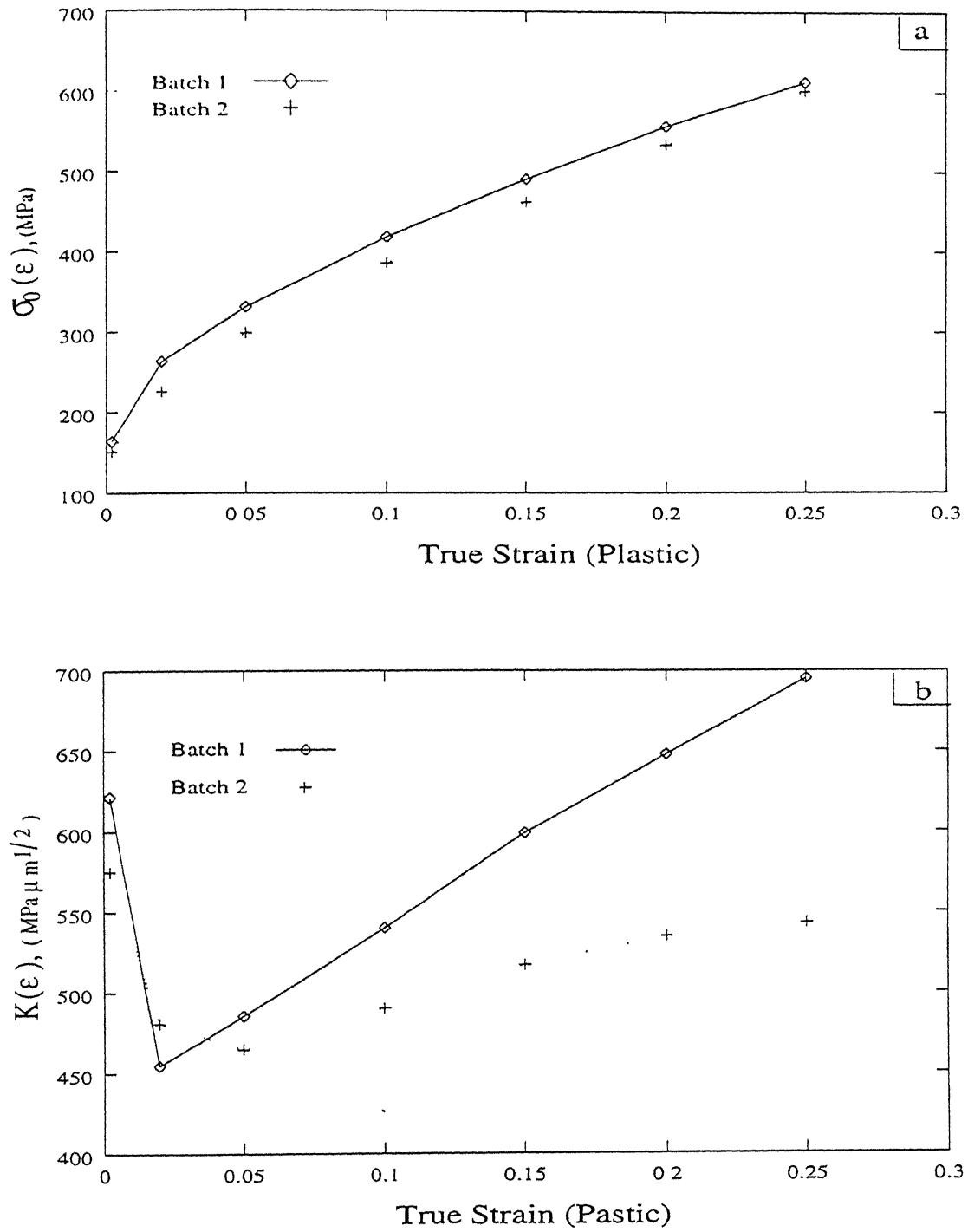


Figure 4.19: Variation of H-P parameters: (a) $\sigma_0(\epsilon)$ and (b) $K(\epsilon)$ with strain in the coarse grain regime of batch 1.

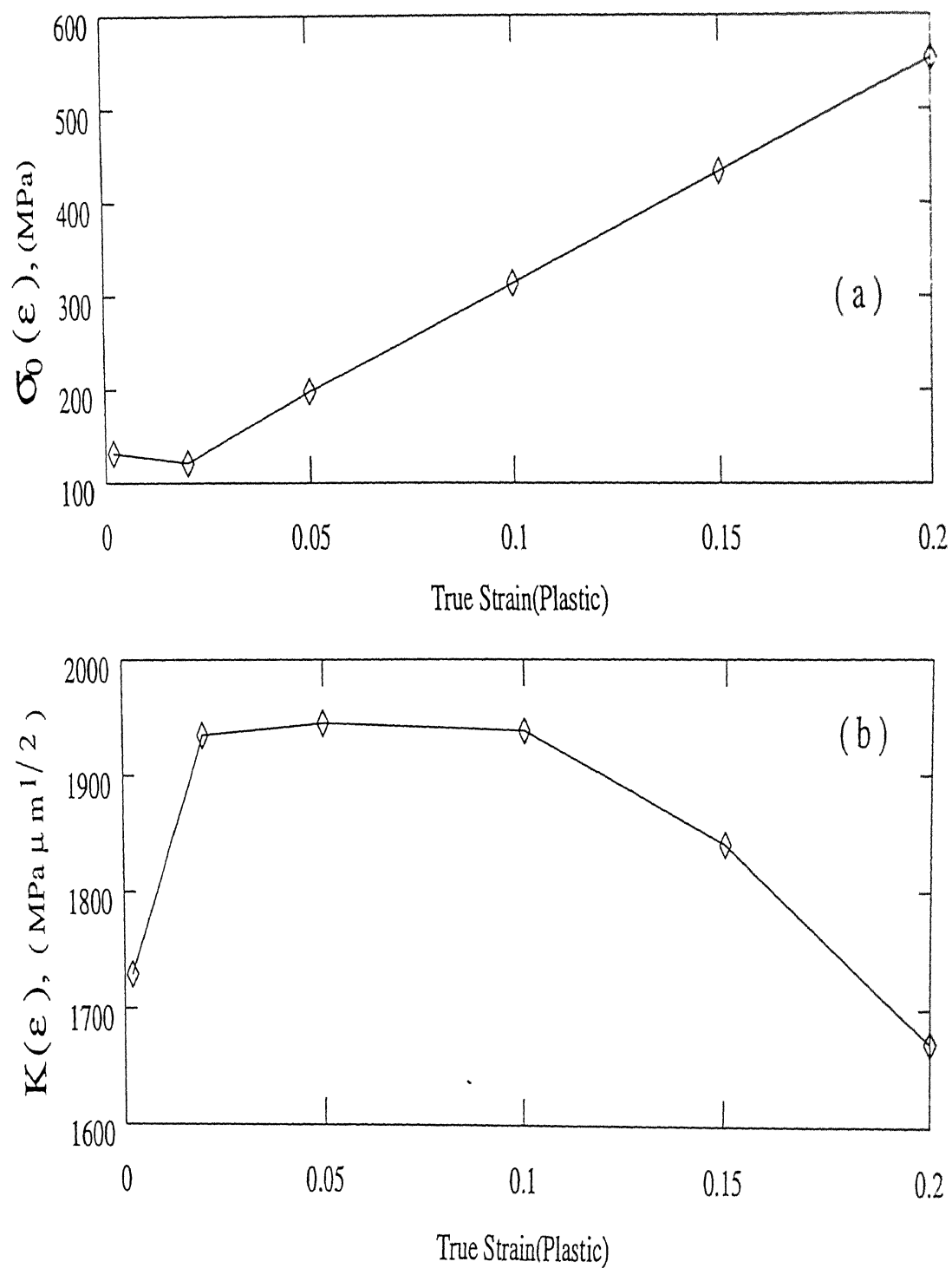


Figure 4.20: Variation of H-P parameters: (a) $\sigma_0(\epsilon)$ and (b) $K(\epsilon)$ with strain in the fine grain regime of batch 1.

Table 4.3: Values of $\sigma_0(\epsilon)$ and $K(\epsilon)$ at different strain levels.

Strain (%)	Batch 1									Batch 2		
	coarse grain regime $\sigma = \sigma_0 + Kd^{-1/2}$			fine grain regime $\sigma = \sigma_0 + Kd^{-1/2}$			fine grain regime $\sigma = \sigma_0 + Kd^{-1}$			entire grain regime $\sigma = \sigma_0 + Kd^{-1/2}$		
	$\sigma_0(\epsilon)$ (MPa)	$K(\epsilon)$ (MPa- $\mu m^{1/2}$)	CC	$\sigma_0(\epsilon)$ (MPa)	$K(\epsilon)$ (MPa- $\mu m^{1/2}$)	CC	$\sigma_0(\epsilon)$ (MPa)	$K(\epsilon)$ (MPa- μm)	CC	$\sigma_0(\epsilon)$ (MPa)	$K(\epsilon)$ (MPa- $\mu m^{1/2}$)	CC
0.2	164.0	621.4	0.978	-326.5	1804.4	0.999	131.4	1792.5	0.995	150.8	575.0	0.996
2	263.3	454.7	0.977	-383.7	2003.7	0.997	121.1	1935.0	1.000	225.6	480.8	0.997
5	330.9	485.7	0.954	-309.7	2015.1	0.998	198.3	1945.0	1.000	298.4	464.8	0.997
10	417.9	540.1	0.943	-194.6	2012.9	0.999	313.9	1938.3	0.999	385.4	490.2	0.997
15	490.2	598.9	0.941	-52.2	1915.4	0.998	432.7	1840.7	0.996	461.7	516.9	0.996
20	556.7	647.5	0.942	110.9	1744.2	0.994	553.7	1671.3	0.989	533.6	534.7	0.995
25	612.4	695.2	0.948	192.6	1723.9	0.959	579.6	1896.7	0.957	601.1	542.9	0.993

Table 4.4: Goodness of fit using correlation coefficient for different values of n in the relation, $\sigma(\epsilon) = \sigma_0(\epsilon) + Kd^{-n}$, at room temperature.

% ϵ	region	Correlation coefficient (CC) for different values of n						
		0.2	0.4	0.5	0.6	0.8	1.0	1.2
0.2	coarse	.994	.995	.995	.994	.989	.970	.894
	fine	1.000	1.000	1.000	1.000	1.000	.999	.989
5	coarse	.976	.978	.978	.976	.969	.943	.863
	fine	.994	.994	.994	.994	.996	.998	.999
10	coarse	.969	.972	.972	.969	.960	.932	.845
	fine	.997	.997	.997	.997	.998	.999	.995
20	coarse	.968	.971	.971	.968	.959	.931	.845
	fine	.995	.995	.995	.995	.995	.993	.981

The standard deviation of PDA distribution, the grain aspect ratio and the coefficient of variation of the grain size increase with strain as shown in figures 4.22a, c and e. On the other hand, the relative frequency of ideal 120° class of PDA distribution and the grain shape factor decrease with increasing strain (see figures 4.22b and d). The PDA distribution at different strain levels for the fine and the coarse grain sizes are shown in figures 4.23 and 4.24 respectively. In both cases the relative frequency distribution of PDA flattens out with increasing strain. The grain size (grain area) measured at different strain levels also included in table 4.5.

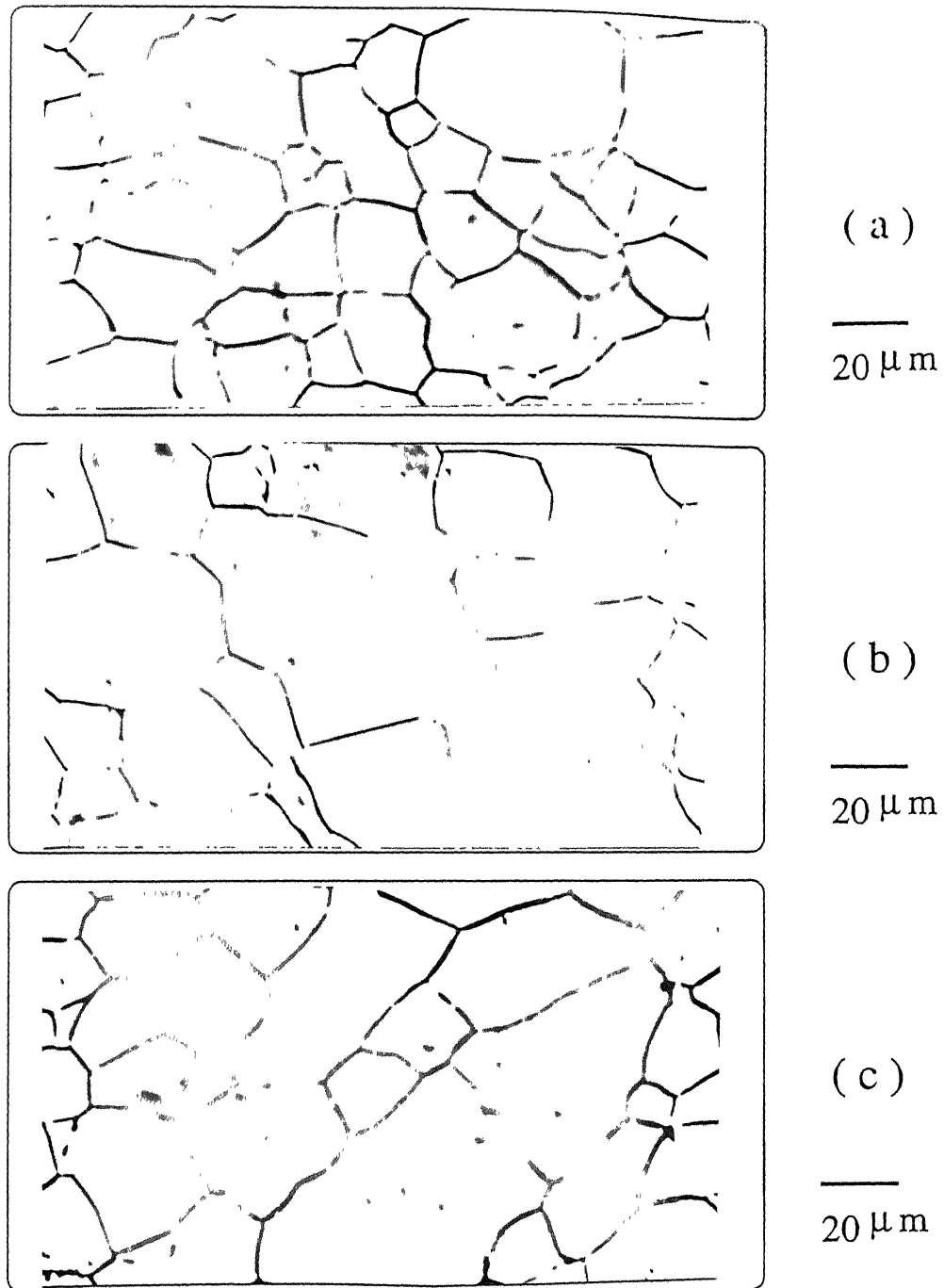


Figure 4.21: Microstructures of the samples ($d = 29.0\ \mu\text{m}$) deformed at room temperature up to the strains of (a) 5 %, (c) 10 % and (d) 20 %.

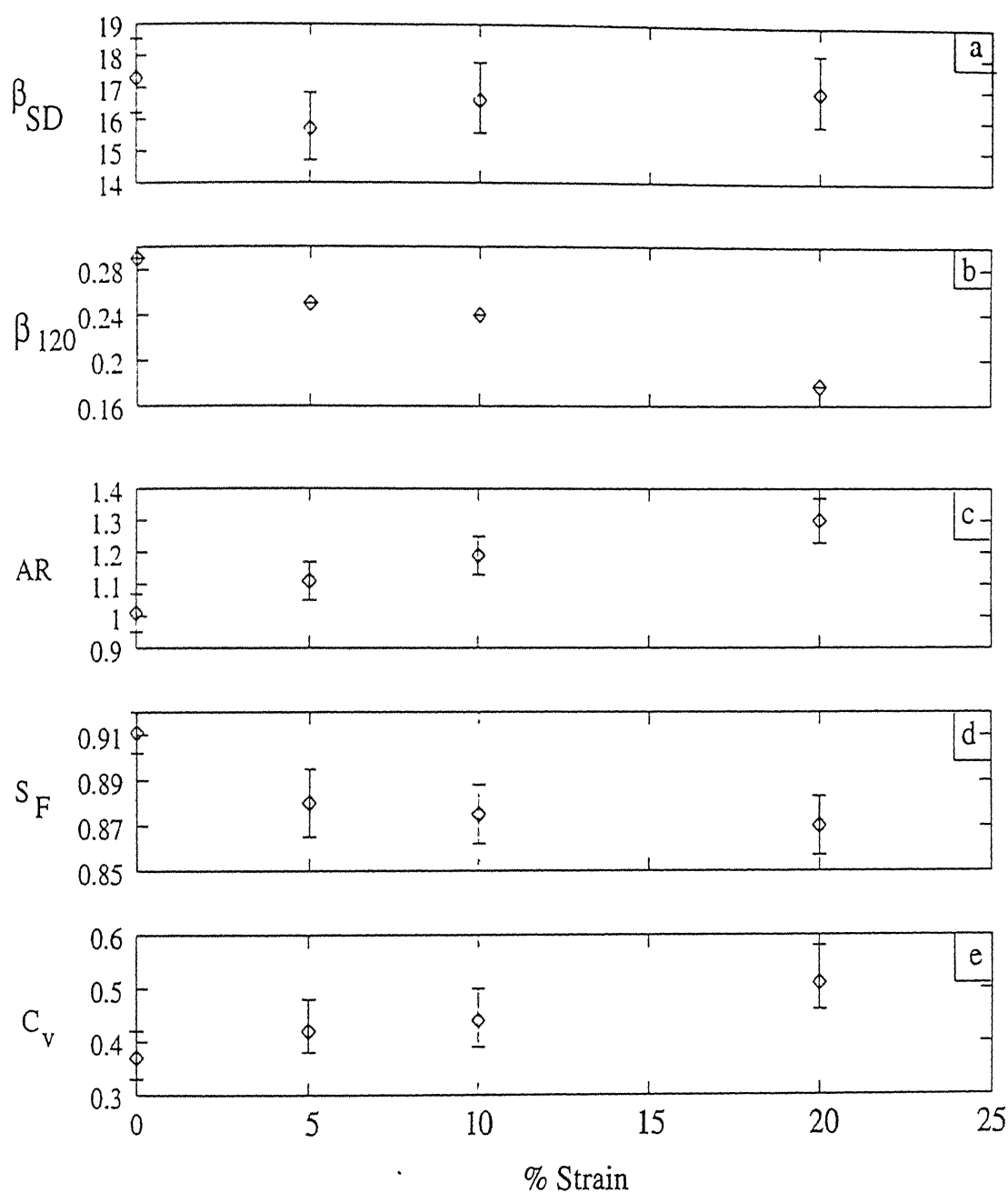


Figure 4.22: Variation of metallographic parameters: (a) standard deviation of PDA distribution (β_{SD}), (b) relative frequency of $115^\circ - 125^\circ$ degree class of PDA distribution (β_{120}), (c) grain aspect ratio (AR), (d) grain shape factor (S_F) and (e) coefficient of variation of grain size (C_v) with strain.

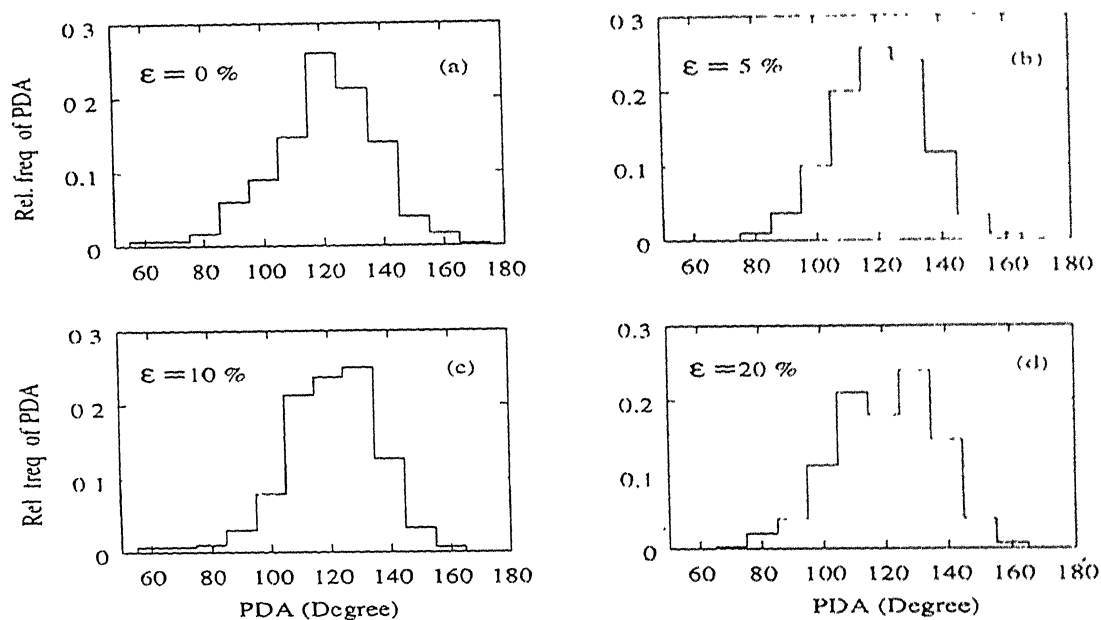


Figure 4.23: PDA distribution in the fine grain size ($d = 4.0 \mu m$) at strains: (a) 0 %, (b) 5 %, (c) 10 % and (d) 20 %.

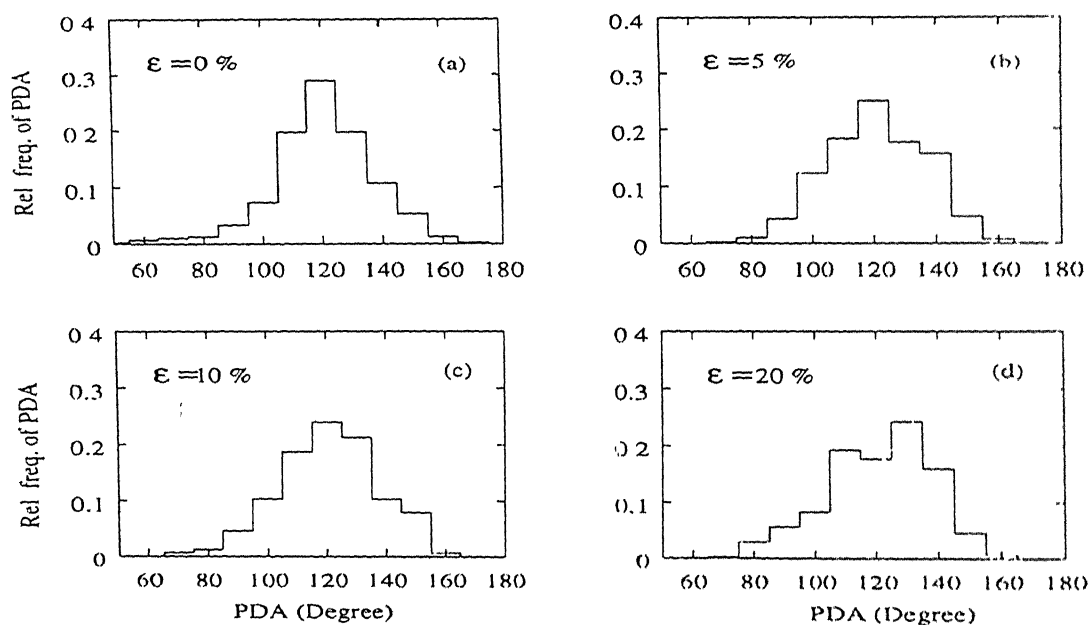


Figure 4.24: PDA distribution in the coarse grain size ($d = 29.0 \mu m$) at strains: (a) 0 %, (b) 5 %, (c) 10 % and (d) 20 %.

Table 4.5: Microstructural parameters at various strain levels for the samples of different grain sizes (batch 2).

$d (\mu\text{m})^\dagger$	$\%\epsilon$	$d_{eq}(\mu\text{m})^*$	C_V	AR	S_F	$\beta_{SD}(\text{degree})$	β_{120}
4.0 ± 0.06	0	4.1 ± 0.30	0.38	-	0.93 ± 0.02	18.0	0.26
	5	3.9 ± 0.27	0.42	-	0.89 ± 0.03	14.4	0.26
	10	3.4 ± 0.19	0.34	-	0.89 ± 0.03	15.8	0.24
	20	3.4 ± 0.19	0.34	-	0.88 ± 0.01	16.0	0.24
5.9 ± 0.29	0	5.7 ± 0.33	0.41	-	0.91 ± 0.01	14.6	0.31
	5	5.3 ± 0.22	0.40	-	0.86 ± 0.02	17.8	0.23
	10	5.6 ± 0.25	0.42	-	0.88 ± 0.01	17.2	0.23
	20	5.8 ± 0.27	0.43	-	0.86 ± 0.01	16.6	0.20
29.0 ± 1.17	0	27.4 ± 1.15	0.37	1.01 ± 0.07	0.91 ± 0.01	17.3	0.29
	5	22.9 ± 0.99	0.42	1.11 ± 0.07	0.88 ± 0.02	15.7	0.25
	10	22.3 ± 0.91	0.44	1.19 ± 0.08	0.88 ± 0.02	16.6	0.24
	20	21.0 ± 1.00	0.51	1.30 ± 0.08	0.87 ± 0.02	16.9	0.18

\dagger by intercept method

$*$ by grain area method

4.2.3 Microhardness variation in deformed samples

The microhardness measurements were performed across the selected grains after tensile testing to various strain levels. These measurements were done for two different grain sizes (18.3 and $26.4 \mu\text{m}$) of batch 1 and one coarse grain size ($29.0 \mu\text{m}$) of batch 2 and the results are presented in figures 4.25a-c. As minimum size of indentation by microhardness tester in this material was $5\text{-}6 \mu\text{m}$, the hardness variation across the grains in the fine grain regime ($d \leq 6 \mu$) could not be evaluated. In the annealed samples, there is no significant difference in microhardness between the grain boundary region and the center

of grains. However in the deformed specimens, difference between the hardness at the grain boundaries and the grain interior is quite significant as seen in figures 4.25a-c. The average microhardness increases with increasing strain for the samples of various grain sizes, as shown in figure 4.26. It may be also noted from figure 4.26 that the average microhardness decreases with increasing grain size at all strain levels for samples of both the batches. Table 4.6 shows the microhardness of samples of both batches at different strain levels.

4.3 Elevated temperature deformation behaviour

The samples of batch 1 were tested in tension at four different temperatures (200 °C, 400 °C, 600 °C and 800 °C), whereas the samples of batch 2 were tested at 400 °C and 800 °C only. The true stress versus true strain curves are shown in figures 4.27 and 4.28. In the intermediate temperature range (200 °C to 600 °C) the samples of both the batches

Table 4.6: Average microhardness values for the samples of different grain sizes at several strain levels, deformed at room temperature.

Strain (%)	Microhardness(VHN) of				
	Batch 1		Batch 2		
	d=18.3 (μm)	d=26.5 (μm)	d=4.0 (μm)	d=5.9 (μm)	d=29.0 (μm)
0	195.7 \pm 6.3	174.6 \pm 3.5	194.3 \pm 7.5	179.9 \pm 3.2	151.4 \pm 12.4
5	-	-	225.7 \pm 8.7	212.5 \pm 8.7	190.5 \pm 6.3
10	-	-	248.4 \pm 3.7	237.3 \pm 17.9	212.5 \pm 5.4
15	295.8 \pm 7.7	262.9 \pm 13.3	-	-	-
20	-	-	272.6 \pm 4.3	266.0 \pm 11.2	255.5 \pm 8.5
30	314.7 \pm 29.1	294.4 \pm 12.5	-	-	-
40	377.8 \pm 46.5	320.1 \pm 30.1	-	-	-

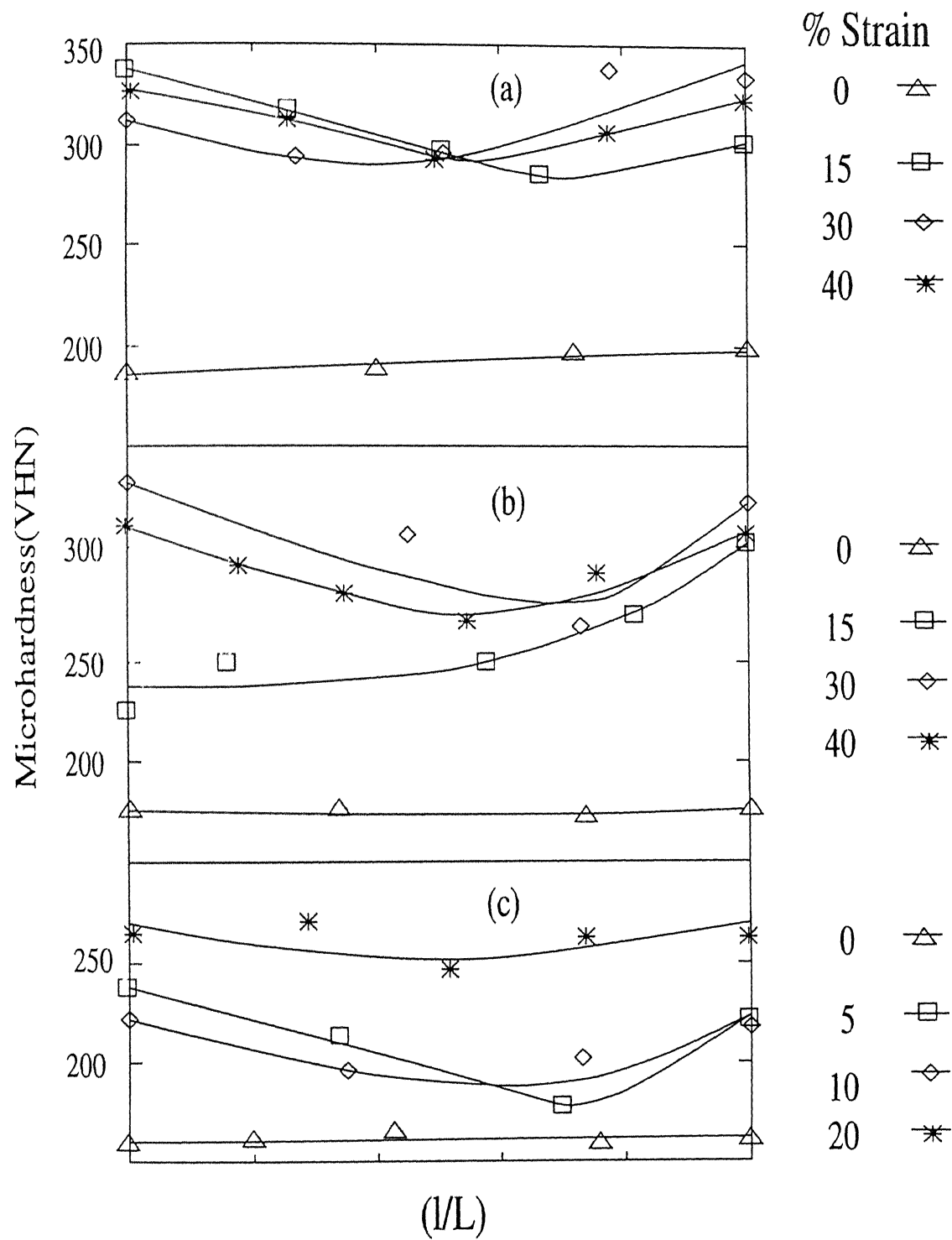


Figure 4.25: Microhardness variation at different strain levels across grains of sizes (a) $18.3 \mu m$ (batch 1), (b) $26.4 \mu m$ (batch 1) and (c) $29 \mu m$ (batch 2).

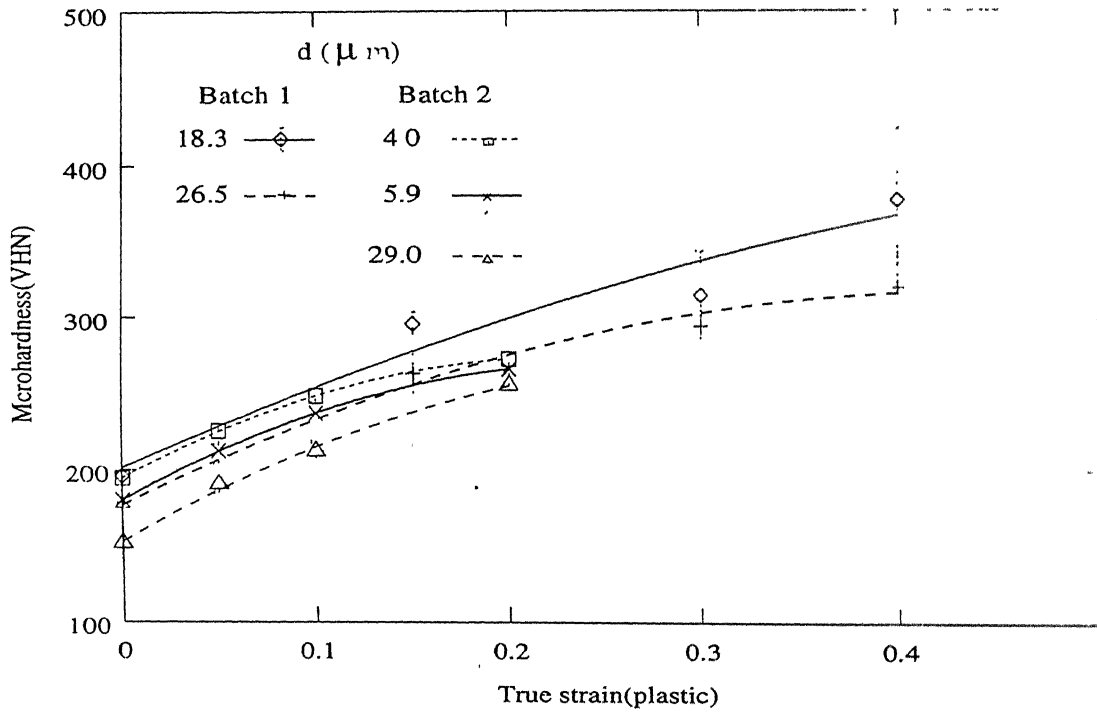


Figure 4.26: Variation of average microhardness with strain, deformed at room temperature.

exhibit jerky flow. Moreover, the jerkiness increases with temperature and grain size in this temperature range. The true stress increases with increasing strain for all the grain sizes of two batches up to the test temperature of 600 °C. On the other hand, at 800 °C, the strain hardening in the lower strain range (depending on the grain size) and subsequently the strain softening can be noted from figures 4.27d and 4.28b. Up to the test temperature of 600 °C and at a constant strain level, the true stress increases with decrease in the grain size. In general with a few exceptions, the flow stress of samples of batch 1 at 800 °C also increases with decreasing grain size at a given strain (figure 4.27d). However in samples of batch 2, the flow stress generally decreases with decreasing grain size at 800 °C (figure 4.28b).

Figures 4.29a and b show the comparison of flow stress between the samples of coarse and fine grain sizes of two batches at 400 °C and 800 °C respectively. At a given strain, grain size and temperature, the sample of batch 1 shows higher flow stress than batch 2.

However, the difference in flow stress between the two batches is not so pronounced in the coarse grain regime as compared to that in the fine grain regime of two batches at 400 °C (figure 4.29a).

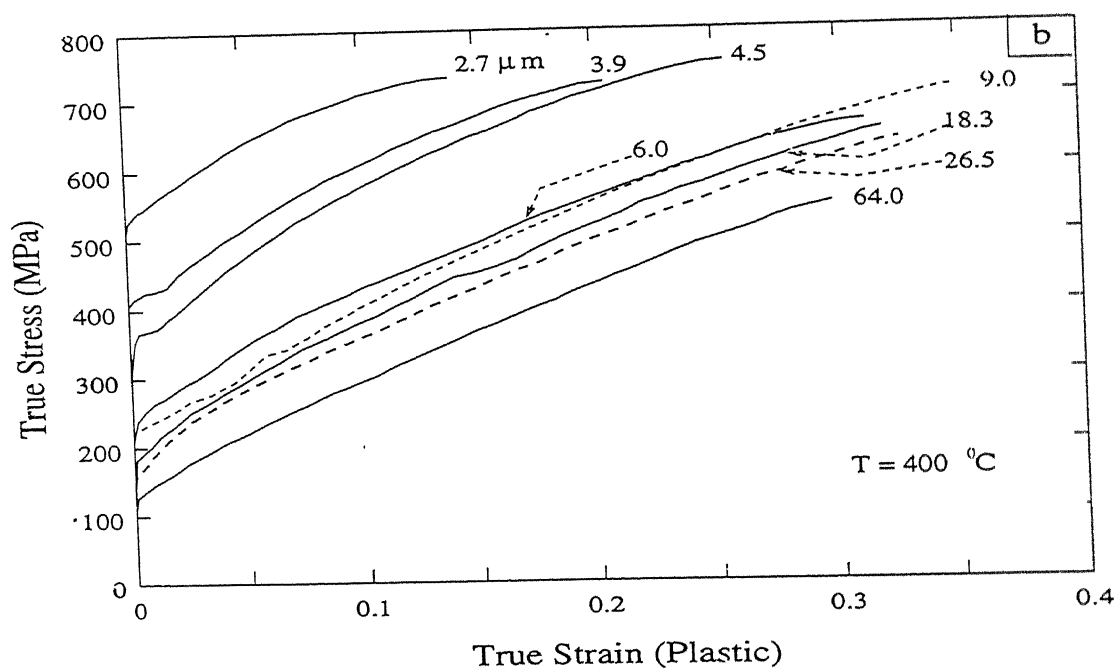
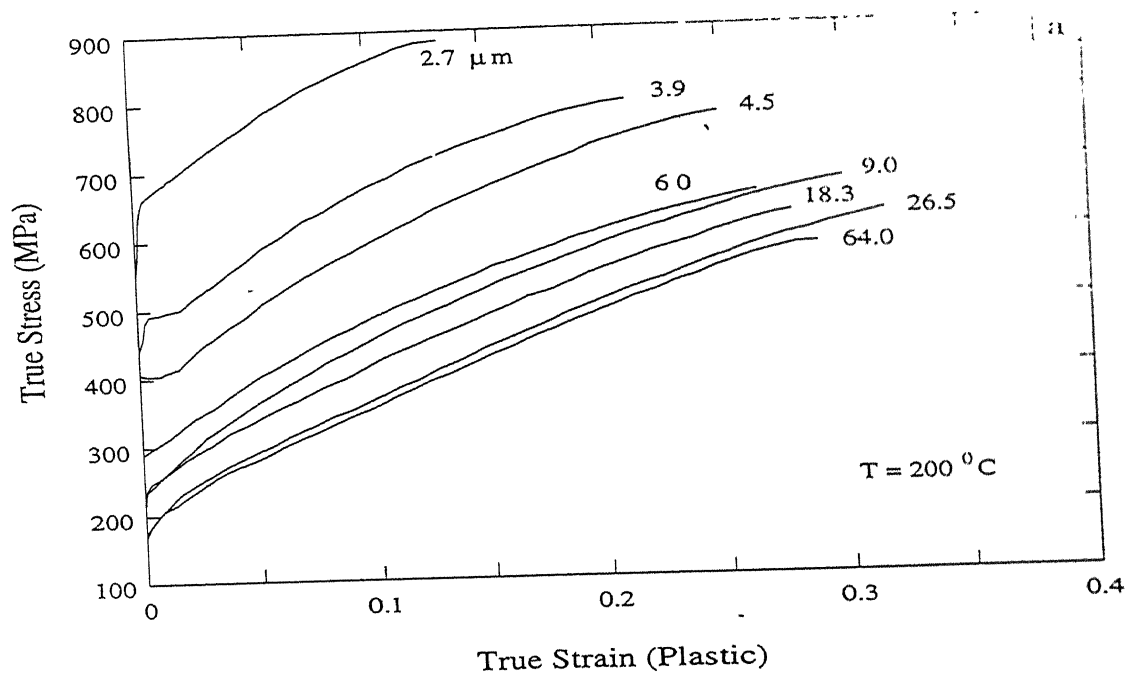
On the other hand, at 800 °C, the flow stress difference at a given strain between the coarse grain regime of two batches is significant as seen in figure 4.29b. It may also be noted from figure 4.29b that in the lower strain range the flow stress of the fine grain sample is higher than the coarse grain sample of batch 1 and the opposite trend is in batch 2. At higher strains, the flow stress of coarse grained sample is higher than the fine grained one in batch 1 and the opposite trend is in batch 2. The deformation behaviour at a given grain size for different temperatures is compared in figures 4.30 and 4.31 for batches 1 and 2, respectively. The flow stress at a given strain decreases with increase in temperature in both the fine and the coarse grained samples of two batches. These figures also illustrate that the % elongation decreases with increase in temperature up to 600 °C and thereafter it increases with increase in temperature.

The temperature dependence of flow stress normalised with respect to modulus of elasticity (E)¹ is shown in figures 4.32a-c for samples of different grain sizes at various strain levels. In the entire range of strain, the fine grain size samples show three stage behaviour with temperature. In the first stage, σ/E decreases with increasing temperature up to 400 °C. This is followed by a small increase in flow stress with temperature up to 600 °C and denoted as the second stage. In the third stage, σ/E decreases with increasing temperature as shown in figure 4.32a. On the other hand, in the coarse grain size range, the third stage is not observed at lower strains (below 2 %) and with increasing strain the third stage becomes prominent (figures 4.32b-c). The tensile properties of samples with different grain sizes at various temperatures are listed in table 4.7. At a given temperature

¹The linear relation between the modulus of elasticity (E) and temperature obtained for 316L austenitic stainless steel from the data of Garafalo [105] as:

$$E_T = 203 - 0.086T$$

where E_T is in GPa and T is in °C.



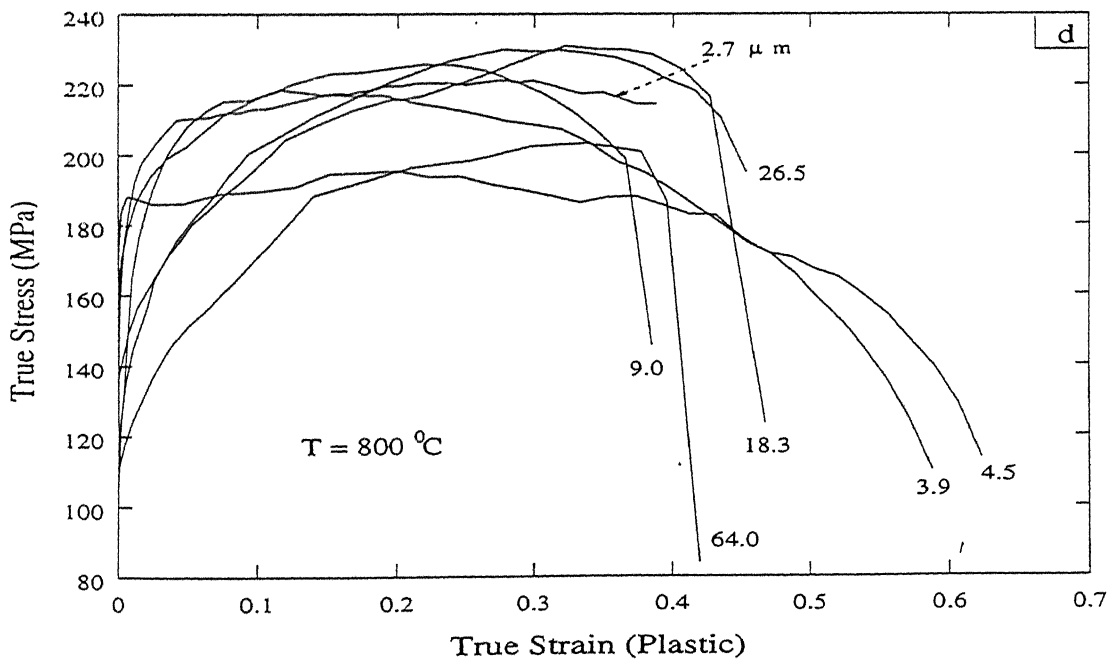
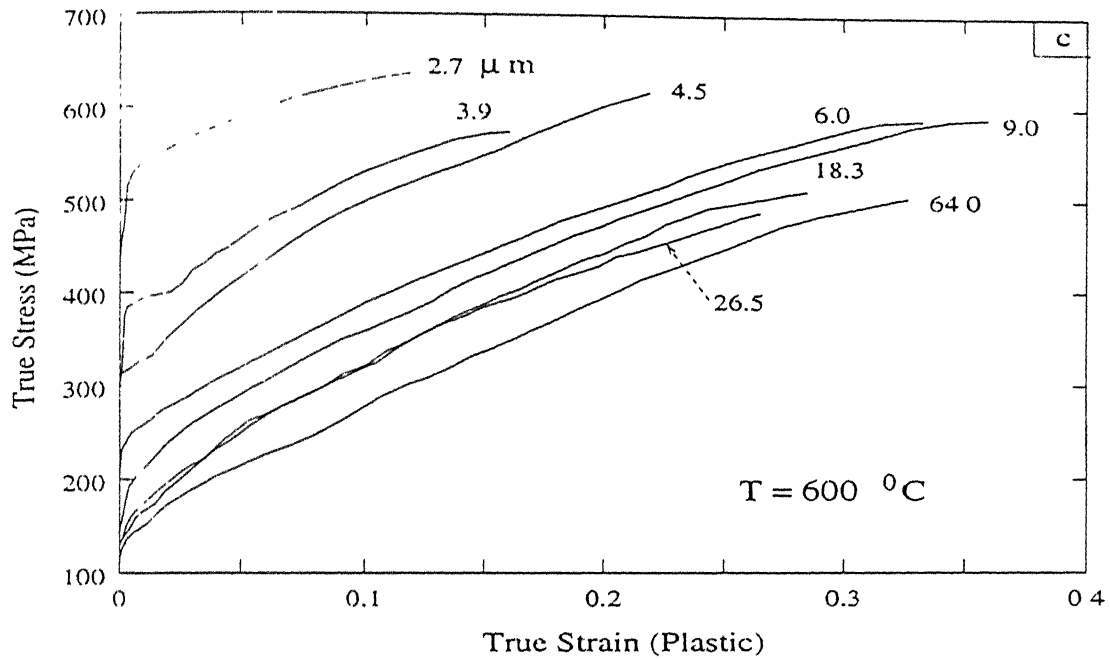


Figure 4.27: True stress-true strain curves for various grain sizes of batch 1 at temperatures: (a) $200\text{ }^{\circ}\text{C}$, (b) $400\text{ }^{\circ}\text{C}$, (c) $600\text{ }^{\circ}\text{C}$ and (d) $800\text{ }^{\circ}\text{C}$.

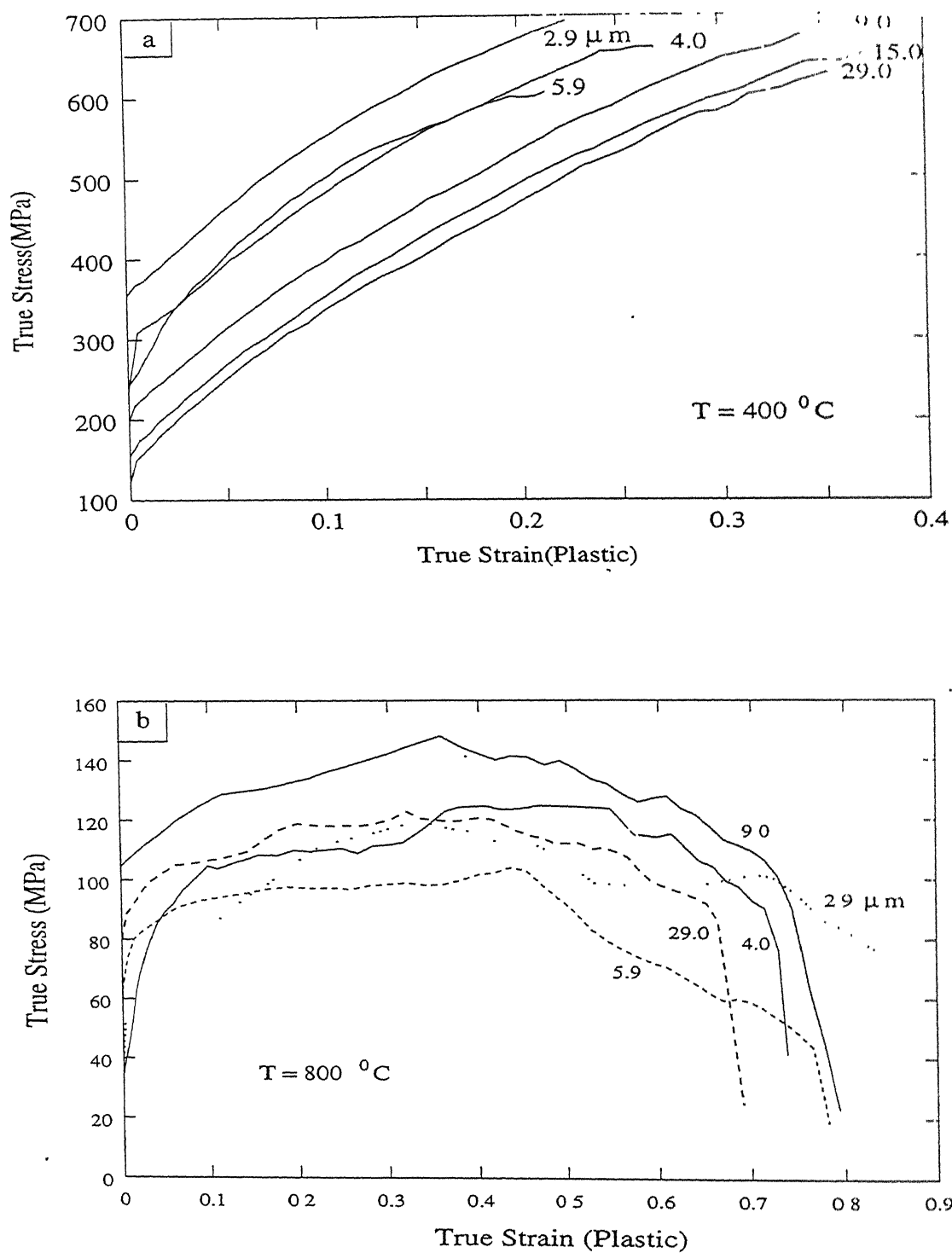


Figure 4.28: True stress-true strain curves for various grain sizes of batch 2 at temperatures: (a) 400°C and (b) 800°C .

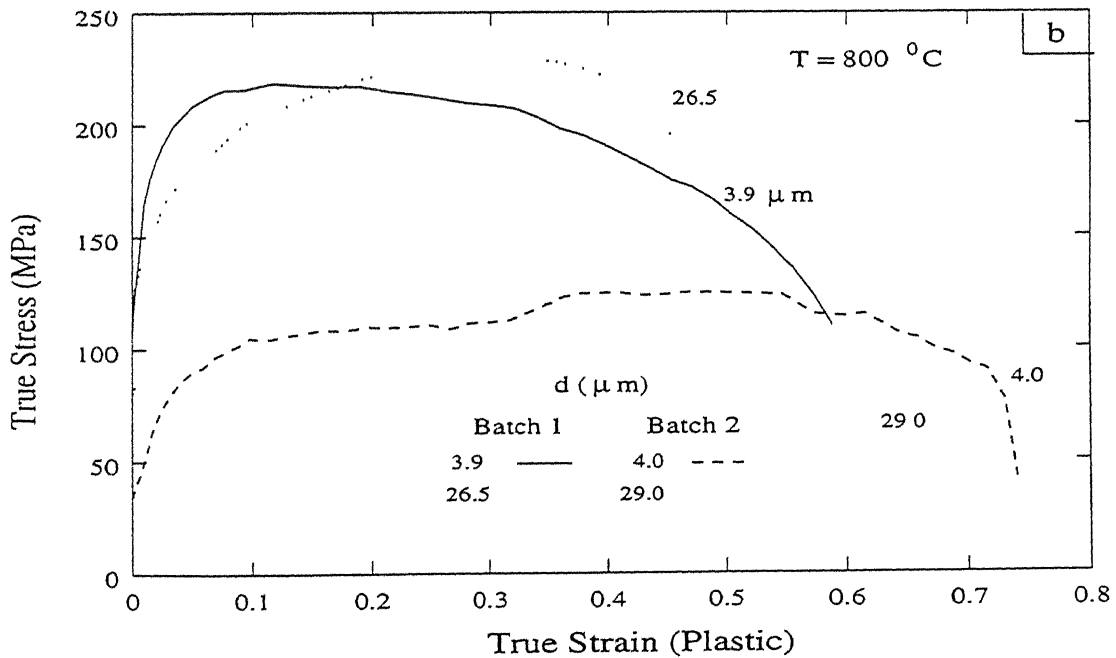
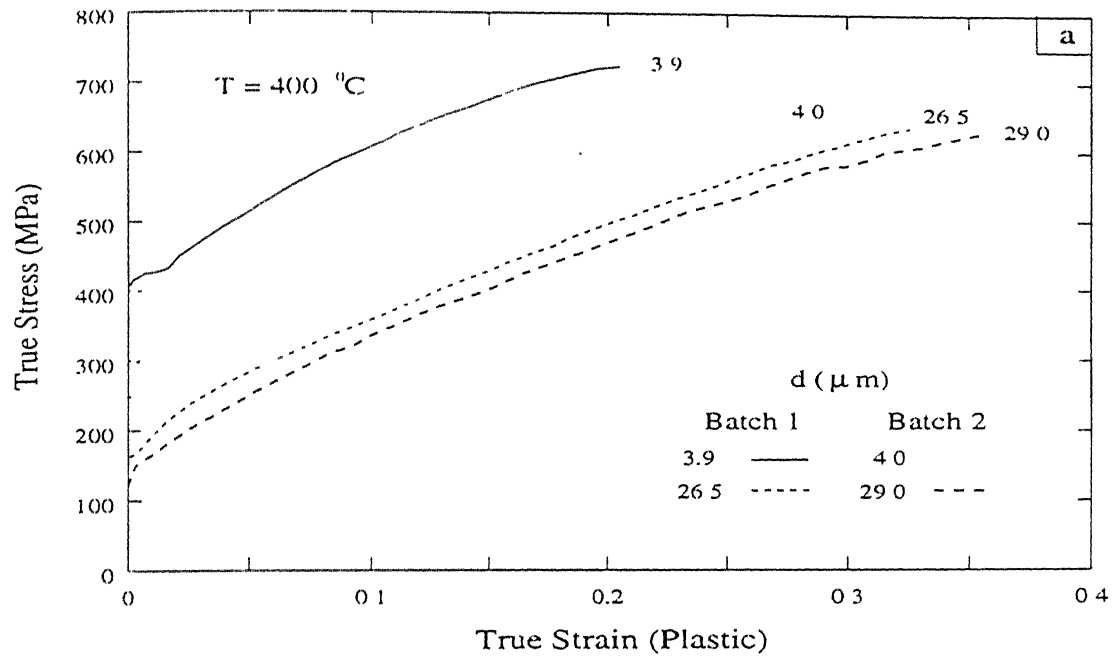


Figure 4.29: Comparison of flow stress of batch 1 and batch 2 at temperatures: (a) $400\text{ }^{\circ}\text{C}$ and (b) $800\text{ }^{\circ}\text{C}$.

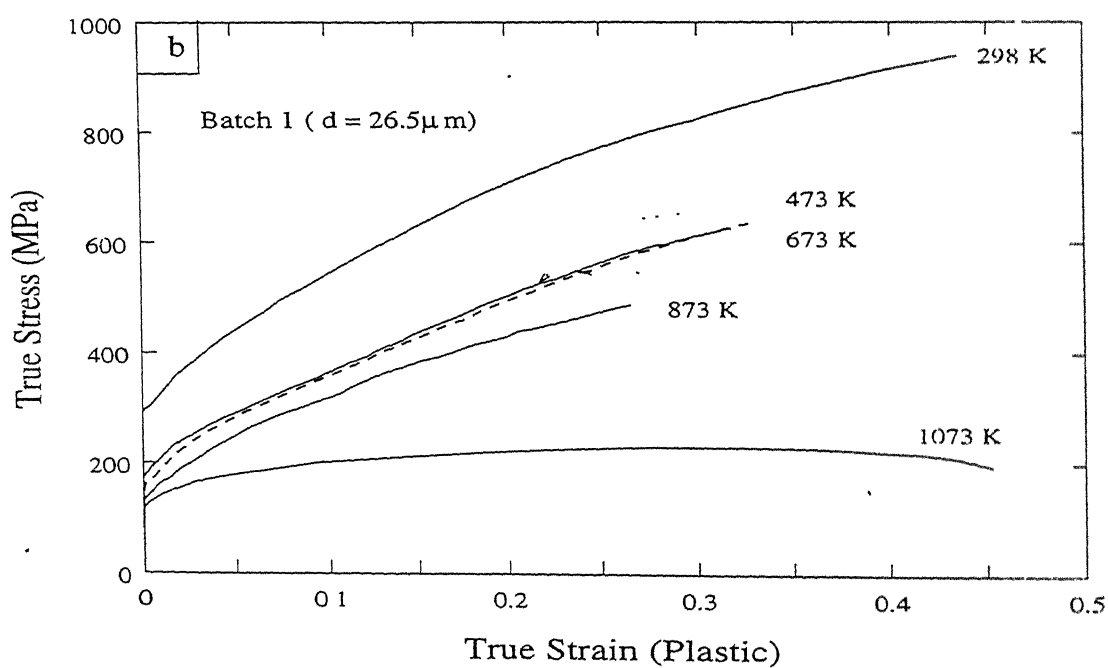
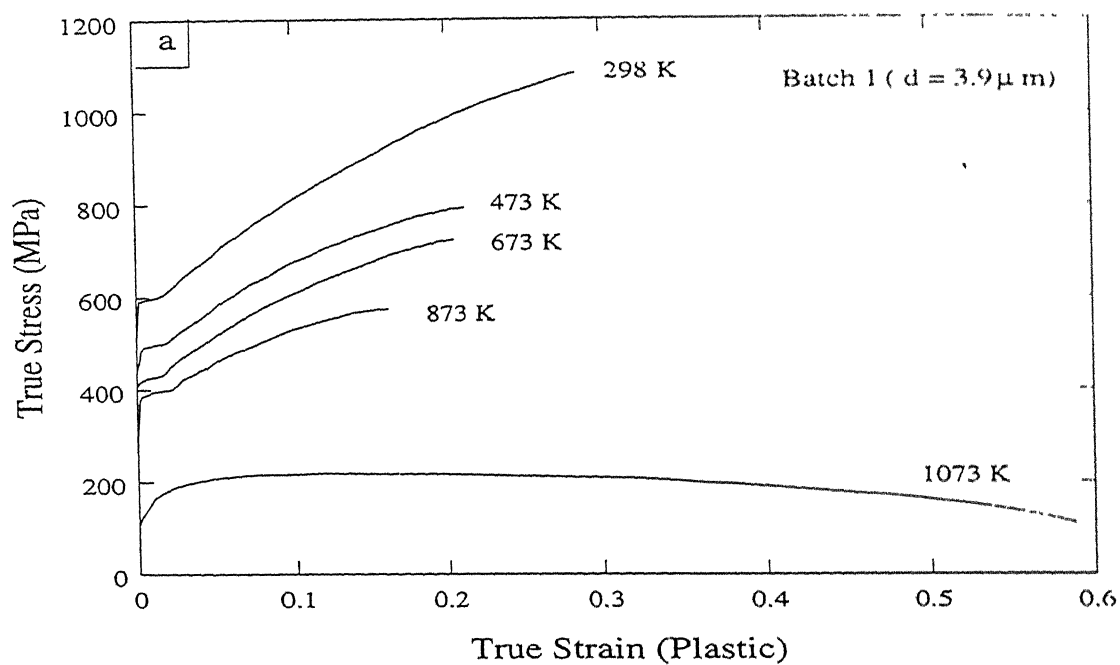


Figure 4.30: True stress-true strain curves at different temperatures (batch 1) for grain sizes: (a) $4.5 \mu\text{m}$ and (b) $26.4 \mu\text{m}$.

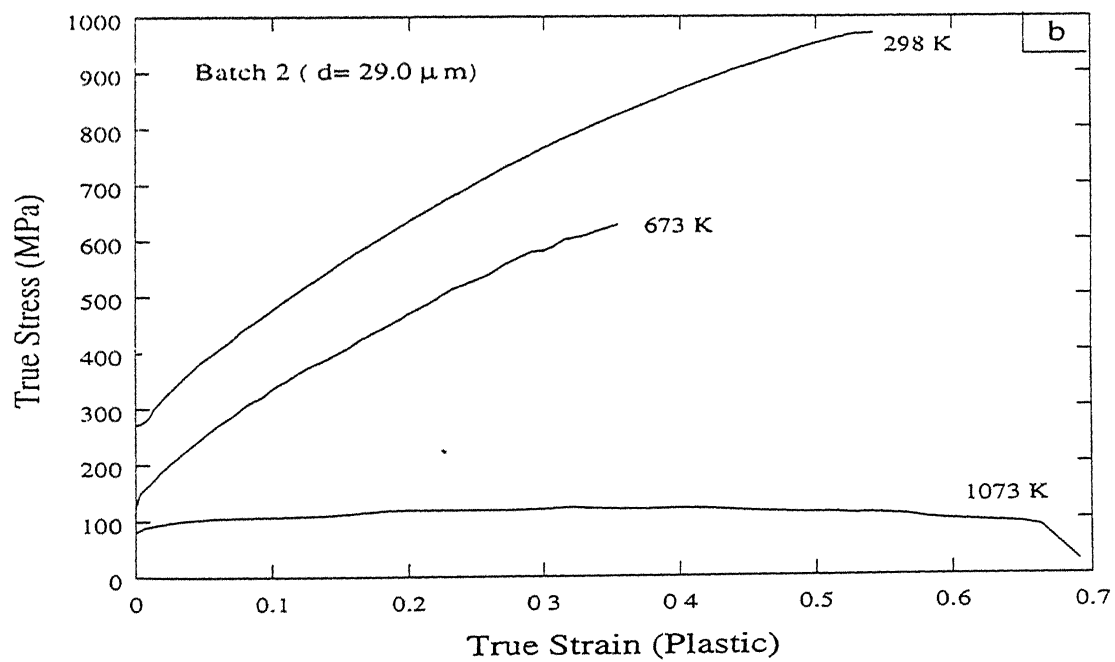
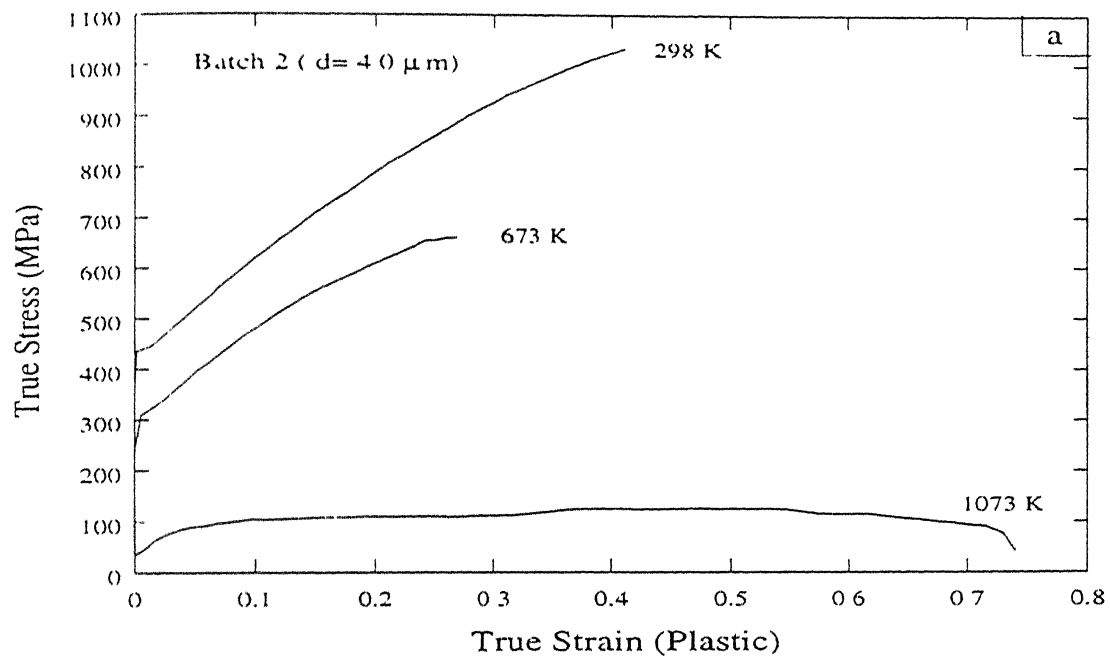
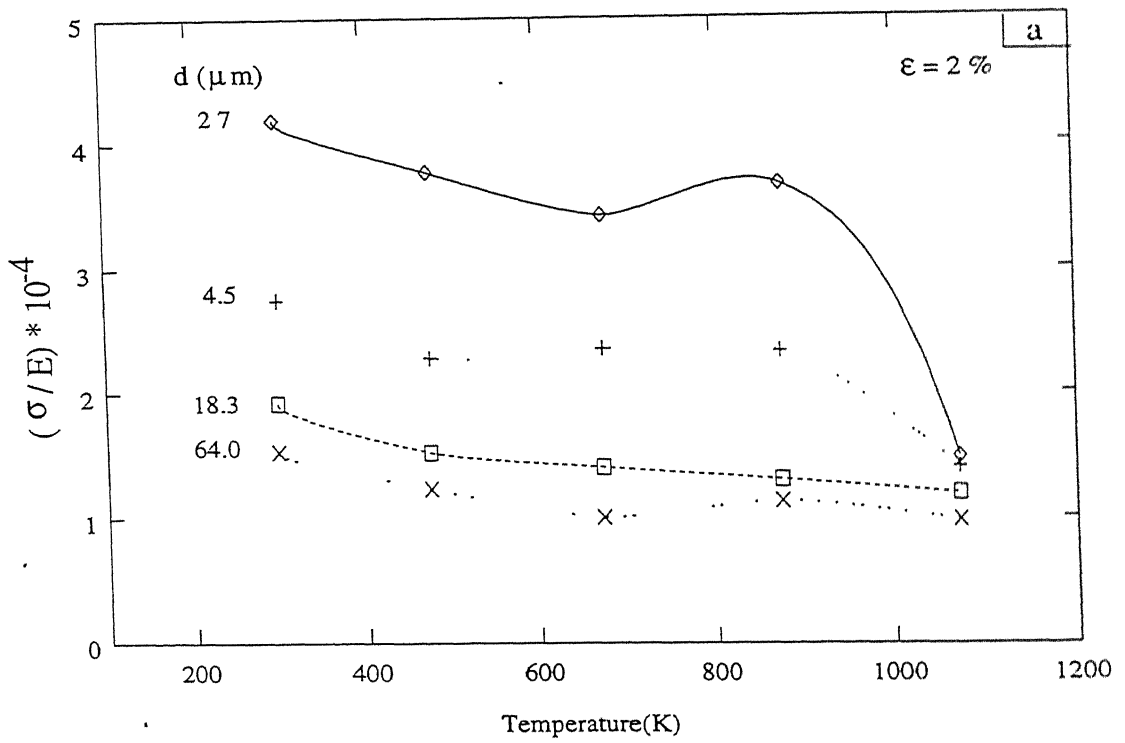
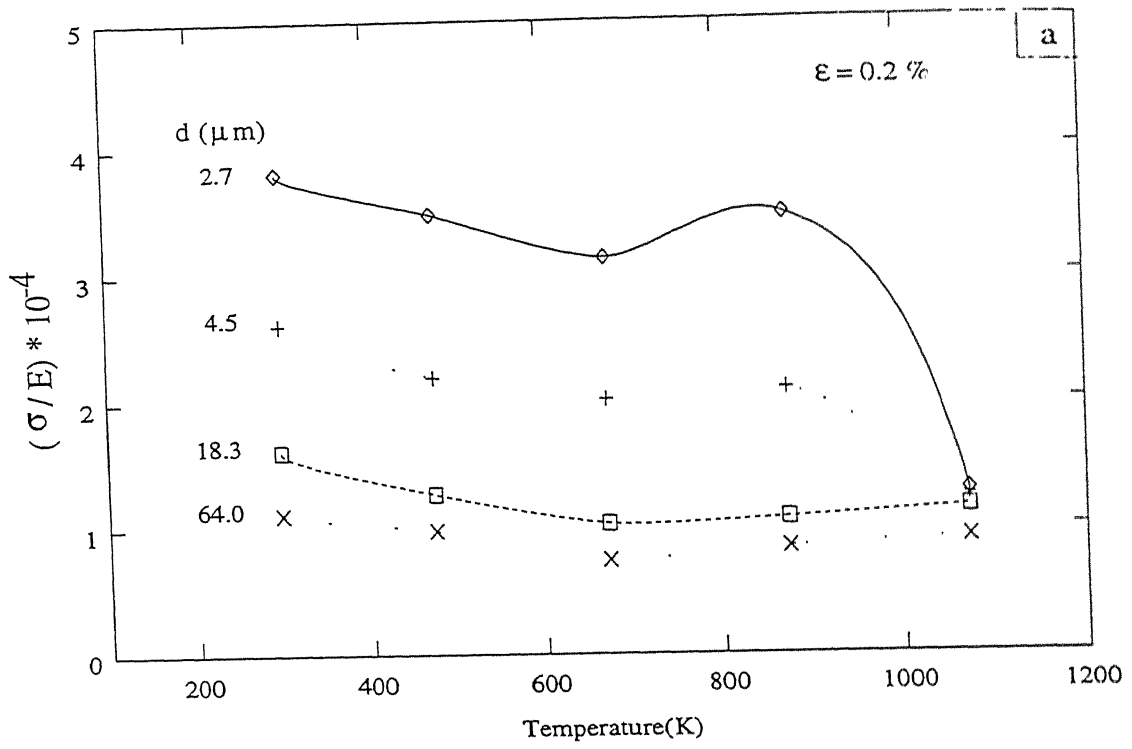


Figure 4.3I: True stress-true strain curves at different temperatures (batch 2) for grain sizes: (a) 4.0 μm and (b) 29.0 μm .



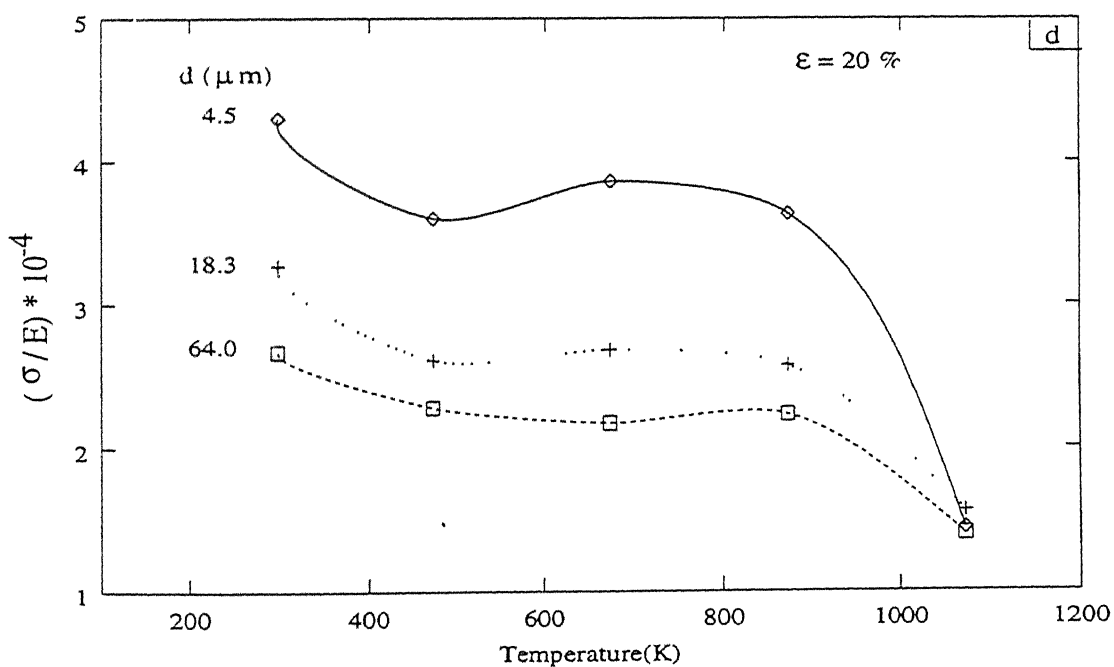
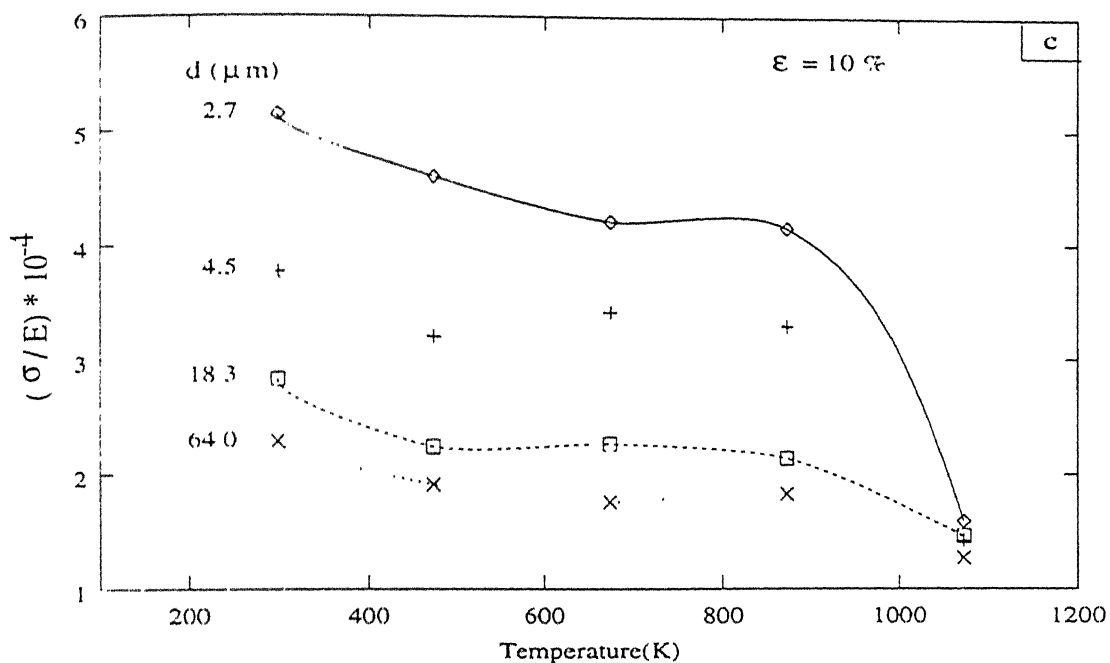


Figure 4.32: Normalised flow stress (σ/E) vs temperature (batch 1) at strains: (a) 0.2 %, (b) 2 %, (c) 10 % and (d) 20 %.

(in the range of 200 °C to 600 °C), the yield and the ultimate tensile strength increase while the % elongation decreases with the decrease in grain size. Table 4.7 shows that at 800 °C there is no systematic trend in the above parameters with the variation in the grain size. However, in general with increasing temperature the yield and the ultimate tensile strength decrease for a given grain size. On the other hand, the % elongation for a given grain size decreases up to 600 °C followed by an increase with increasing temperature.

4.3.1 Hall-Petch behaviour

The Hall-Petch plots at different temperatures were derived from the true stress-true strain curves (figures 4.27a-d and 4.28a-b) and are shown in figure 4.33 for batch 1 and in figure 4.34 for batch 2. At all strains, the batch 1 samples show two distinctly different linear Hall-Petch regimes, one in the fine grain ($d \leq 6 \mu\text{m}$) and other in the coarse grain regimes ($d \geq 6 \mu\text{m}$) over the temperature range of 200 °C to 600 °C as shown in figures 4.33a-c. At 800 °C, there is more scatter in the data and a single linear regression line is a characteristics of Hall-Petch regime at a given strain in the entire range of grain sizes studied (figure 4.33d). At elevated temperatures, the samples of batch 2 also show a single Hall-Petch regime at all strains similar to that observed at room temperature. On the other hand, at 800 °C the flow stress decreases with decrease in the grain size at all strains in batch 2 as shown in figure 4.34b.

The Hall-Petch parameters $\sigma_0(\epsilon)$ and $K(\epsilon)$ at different strain levels and temperatures are listed in table 4.8. At a given temperature and strain, $\sigma_0(\epsilon)$ is much lower in the fine grain regime as compared to the coarse grain regime of batch 1. On the other hand, $K(\epsilon)$ is much higher in the fine than the coarse grain region at a given strain. At elevated temperatures (below 600 °C) also, $\sigma_0(\epsilon)$ in the fine grain regime is negative at strains below 15 to 25 % (depending on temperature). Since negative values of $\sigma_0(\epsilon)$ do not have any physical significance, the flow stress data in the fine grain regime are plotted as a function of d^{-1} as shown in figures 4.35a-c. The σ versus d^{-1} plots yield positive intercept and

comparable correlation coefficient (CC) with the Hall-Petch regression lines. The $\sigma_0(\epsilon)$, $K(\epsilon)$ and corresponding correlation coefficients at different strains and temperatures are also included in table 4.8. The goodness of fit using correlation coefficient for different powers of d at different temperatures are presented in table 4.9. This table shows that the Hall-Petch model is applicable in the coarse grain regime while the composite model is most suited in the fine grain regime of batch 1 at temperatures of 200 °C, 400 °C and 600 °C.

Figures 4.36a and b show the comparison of Hall-Petch plots at different strain levels of two batches at 400 °C and 800 °C respectively. At 400 °C, the regression lines at different strains of two batches overlap in the coarse grain regime. However, at a given strain a significant difference is observed in the flow stress between the two batches in the fine grain regime (figure 4.36a). Figure 4.36b at 800 °C shows distinctly different Hall-Petch behaviour between the two batches. In batch 1, $K(\epsilon)$ at a given strain is positive while in batch 2 it is negative. Since negative $K(\epsilon)$ has no physical significance, Hall-Petch relation is not valid in batch 2 at 800 °C. The variation of $\sigma_0(\epsilon)$ and $K(\epsilon)$ with strain at various test temperatures for the coarse grain regime of batch 1 and for the entire grain regime of batch 2 are shown in figures 4.37a and b respectively. $\sigma_0(\epsilon)$ increases with strain at all temperatures and it decreases with increase in temperature at a constant strain level as shown in figure 4.37a. However, at lower strain range ($\epsilon \leq 5\%$), $\sigma_0(\epsilon)$ has higher value at 800 °C compared to those at 400 °C and 600 °C. Therefore the $\sigma_0(\epsilon)$ versus strain plots at 800 °C and in the lower strain range are shown as dotted lines in figure 4.37a. At the same temperature $\sigma_0(\epsilon)$ is higher in batch 1 as compared to batch 2 at all strains (figure 4.37a). It can also be noted from figure 4.37a that below 20 % strain level, $\sigma_0(\epsilon)$ in batch 1 at a given strain even at 600 °C is higher than batch 2 at 400 °C.

As discussed in section 4.2.1, at room temperature $K(\epsilon)$ decreases initially up to 2 % strain followed by an increase with strain. However, at temperatures in the range of 200 °C to 400 °C, $K(\epsilon)$ remains more or less constant at lower strains (less than 2 %).

Table 4.7: Tensile properties of the samples with different grain sizes.

Temperature (°C)	Batch	d^* (μm)	Yield strength(MPa)	UTS (MPa)	Uniform elongation(%)
200	1	2.7 ± 0.06	636.3	885.4	13.3
200	1	3.9 ± 0.10	438.8	792.9	21.2
200	1	4.5 ± 0.30	407.4	773.1	25.0
200	1	6.0 ± 0.26	289.1	657.9	26.5
200	1	9.0 ± 0.37	227.4	675.0	30.0
200	1	18.3 ± 0.67	213.1	627.6	27.9
200	1	26.5 ± 0.80	173.6	626.5	31.7
200	1	64.0 ± 2.09	168.2	580.4	28.9
400	1	2.7 ± 0.06	511.1	732.2	13.9
400	2	2.9 ± 0.04	354.6	694.0	22.6
400	1	3.9 ± 0.10	405.5	722.8	20.5
400	2	4.0 ± 0.06	269.7	660.1	26.9
400	1	4.5 ± 0.30	305.5	752.3	25.4
400	2	5.9 ± 0.29	249.2	605.0	21.4
400	1	6.0 ± 0.26	238.8	662.8	31.2
400	1	9.0 ± 0.37	226.6	709.2	34.9
400	2	9.0 ± 0.35	212.5	690.5	35.8
400	2	15.0 ± 0.74	163.3	652.6	37.4
400	1	18.3 ± 0.67	185.1	651.3	31.9
400	1	26.5 ± 0.80	165.6	635.4	32.6
400	2	29.0 ± 1.17	139.3	627.5	35.4
400	1	64.0 ± 2.09	129.2	545.4	29.8

...continued

* by intercept method

Table 4.7 (continued)

Temperature ($^{\circ}\text{C}$)	Batch	d^* (μm)	Yield strength(MPa)	UTS (MPa)	Uniform elongation(%)
600	1	2.7 ± 0.06	477.0	636.4	12.0
600	1	3.9 ± 0.10	375.6	573.0	16.1
600	1	4.5 ± 0.30	314.1	617.0	21.9
600	1	6.0 ± 0.26	237.3	588.5	33.3
600	1	9.0 ± 0.37	168.8	590.0	36.0
600	1	18.3 ± 0.67	147.1	510.6	28.5
600	1	26.5 ± 0.80	139.6	487.1	26.5
600	1	64.0 ± 2.09	130.2	503.5	32.7
800	1	2.7 ± 0.06	163.3	221.2	98.9
800	2	2.9 ± 0.04	43.2	119.1	83.9
800	1	3.9 ± 0.10	123.0	218.5	58.8
800	2	4.0 ± 0.06	37.1	124.7	74.0
800	1	4.5 ± 0.30	183.7	195.4	62.3
800	2	5.9 ± 0.29	64.2	104.0	78.3
800	1	6.0 ± 0.26	125.8	170.2	83.8
800	1	9.0 ± 0.37	170.5	225.8	38.5
800	2	9.0 ± 0.35	105.2	148.2	79.5
800	1	18.3 ± 0.67	139.1	230.0	46.7
800	1	26.5 ± 0.80	125.2	230.4	45.3
800	2	29.0 ± 1.17	82.3	122.7	69.1
800	1	64.0 ± 2.09	112.4	203.3	42.0

* by intercept method

Table 4.8: Values of $\sigma_0(\epsilon)$ and $K(\epsilon)$ at different temperatures.

Tempe- rature (°C)	Strain (%)	Batch 1										Batch 2		
		coarse grain regime $\sigma = \sigma_0 + Kd^{-1/2}$			fine grain regime $\sigma = \sigma_0 + Kd^{-1/2}$			fine grain regime $\sigma = \sigma_0 + Kd^{-1}$				entire grain regime $\sigma = \sigma_0 + Kd^{-1/2}$		
		$\sigma = \sigma_0 + Kd^{-1/2}$			$\sigma = \sigma_0 + Kd^{-1/2}$			$\sigma = \sigma_0 + Kd^{-1}$				$\sigma = \sigma_0 + Kd^{-1/2}$		
		$\sigma_0(\epsilon)$ (MPa)	$K(\epsilon)$ (MPa- $\mu m^{1/2}$)	CC	$\sigma_0(\epsilon)$ (MPa)	$K(\epsilon)$ (MPa- $\mu m^{1/2}$)	CC	$\sigma_0(\epsilon)$ (MPa)	$K(\epsilon)$ (MPa- μm)	CC	$\sigma_0(\epsilon)$ (MPa)	$K(\epsilon)$ (MPa- $\mu m^{1/2}$)	CC	
200	0.2	138.2	361.5	0.966	-441.5	1813.9	0.998	15.6	1763.5	0.994				
200	2	180.4	360.5	0.952	-456.6	1907.9	0.998	21.3	1866.5	0.999				
200	5	225.6	417.0	0.974	-391.9	1915.9	0.999	88.6	1872.1	0.999				
200	10	290.0	480.3	0.977	-295.3	1906.7	1.000	183.9	1858.7	0.998				
200	15	361.3	473.2	0.979	-249.7	1959.3	1.000	195.6	2139.7	1.000				
200	20	433.9	435.2	0.979	-153.1	1867.0	0.997	272.1	2035.0	0.995				
200	25	504.5	371.4	0.972										
400	0.2	81.9	388.0	0.979	-372.5	1494.4	0.998	4.1	1453.0	0.991	30.1	562.3	0.991	
400	2	136.0	471.1	0.963	-304.7	1452.2	0.993	66.3	1422.3	0.989	66.6	592.4	0.974	
400	5	191.2	385.6	0.940	-225.4	1428.4	0.985	141.3	1397.1	0.979	108.7	667.8	0.957	
400	10	262.6	426.9	0.949	-95.6	1337.6	0.967	251.1	1303.7	0.952	182.9	714.0	0.947	
400	15	334.3	421.3	0.942	-101.9	1500.7	0.878	157.6	2092.6	0.903	261.8	673.0	0.961	
400	20	402.1	417.9	0.933	45.1	1302.7	0.813	254.4	1905.6	0.942	352.3	573.9	0.980	
400	25	468.2	404.6	0.922							451.6	406.1	0.995	

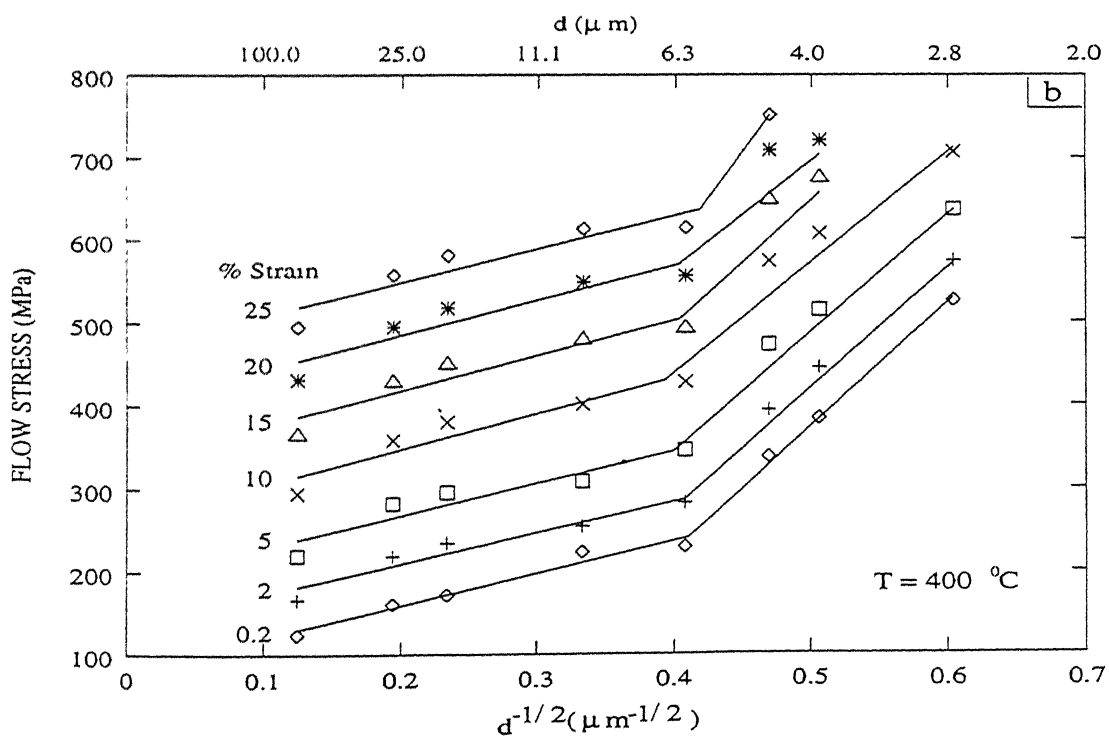
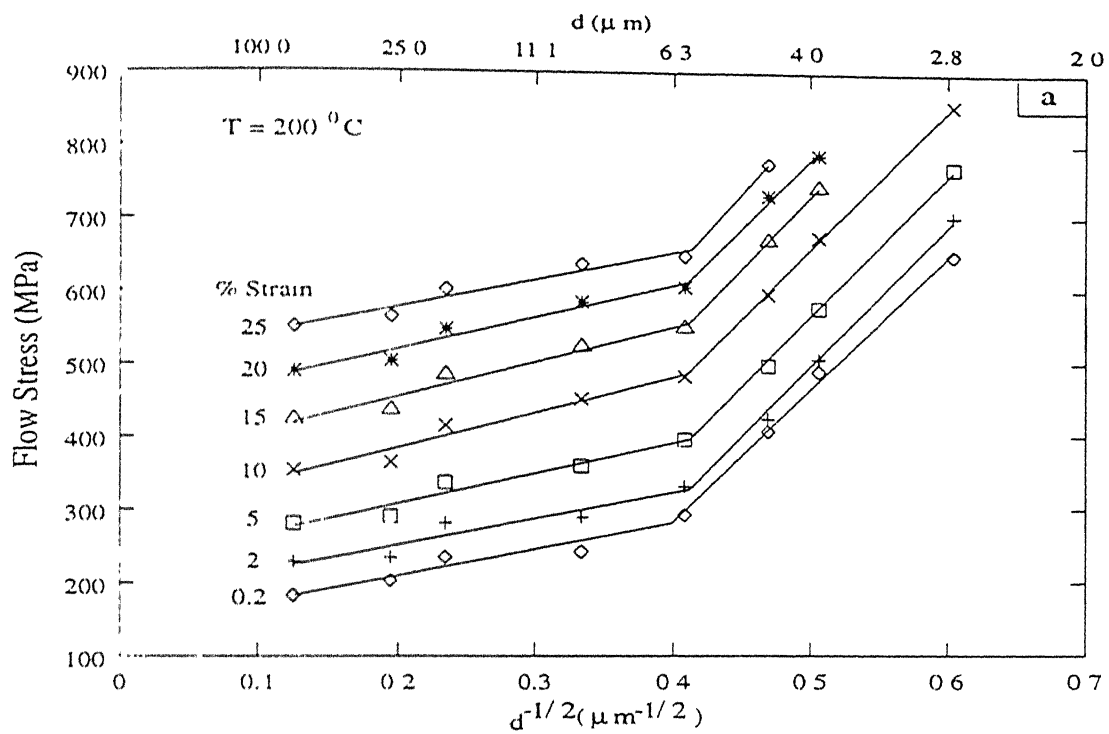
...continued

Table 4.8 (Continued)

Temperature (°C)	Strain (%)	Batch 1										Batch 2			
		coarse grain regime $\sigma = \sigma_0 + Kd^{-1/2}$				fine grain regime $\sigma = \sigma_0 + Kd^{-1/2}$				fine grain regime $\sigma = \sigma_0 + Kd^{-1}$				fine grain regime $\sigma = \sigma_0 + Kd^{-1/2}$	
		$\sigma_0(\epsilon)$ (MPa)	$K(\epsilon)$ (MPa- $\mu m^{1/2}$)	CC	$\sigma_0(\epsilon)$ (MPa)	$K(\epsilon)$ (MPa- $\mu m^{1/2}$)	CC	$\sigma_0(\epsilon)$ (MPa)	$K(\epsilon)$ (MPa- μm)	$\epsilon(\%)$	$\sigma_0(\epsilon)$ (MPa)	$K(\epsilon)$ (MPa- μm)	$\epsilon(\%)$	$\sigma_0(\epsilon)$ (MPa)	$K(\epsilon)$ (MPa- $\mu m^{1/2}$)
600	0.2	75.7	365.2	0.948	-361.4	1463.9	0.999	6.0	1429.3	0.995					
600	2	116.3	375.5	0.987	-311.1	1421.6	0.999	45.8	1393.5	1.000					
600	5	171.7	361.9	0.993	-226.5	1353.8	0.999	114.5	1317.0	0.991					
600	10	238.1	367.2	0.987	-78.2	1184.3	0.985	222.3	1143.6	0.973					
600	15	302.7	351.9	0.979	-99.0	1313.5	0.975	208.2	1458.7	0.969					
600	20	360.9	333.8	0.988											
600	25	411.8	322.9	0.993											
800	0.2	119.1	99.3	0.919									130.2	-152.0	-0.740
800	2	130.3	119.2	0.890									122.6	-98.7	-0.691
800	5	152.1	100.2	0.849									119.5	-58.8	-0.565
800	10	178.8	60.3	0.653									118.2	-31.0	-0.309
800	15	197.9	29.3	0.398									124.0	-36.1	-0.335
800	20	208.1	11.7	0.167									131.7	-49.0	-0.430
800	25	215.2	-4.1	-0.056									134.5	-52.2	-0.413

Table 4.9: Goodness of fit using correlation coefficient for different values of n in relation, $\sigma(\epsilon) = \sigma_0(\epsilon) + Kd^{-n}$ at various temperature.

Temperature ($^{\circ}C$)	% ϵ	region	Correlation coefficient (CC) for different value of n						
			0.2	0.4	0.5	0.6	0.8	1.0	1.2
200	0.2	coarse	.958	.956	.956	.958	.962	.966	.948
		fine	.999	.999	.999	.999	.999	.997	.986
	5	coarse	.967	.965	.965	.967	.971	.973	.941
		fine	.997	.997	.997	.997	.998	.999	.996
	10	coarse	.972	.971	.971	.972	.975	.976	.937
		fine	.999	.999	.999	.999	1.000	1.000	.992
	20	coarse	.978	.977	.977	.978	.980	.976	.925
		fine	.998	.998	.998	.998	.998	.997	.991
400	0.2	coarse	.989	.989	.989	.989	.987	.973	.903
		fine	.999	.999	.999	.999	.999	.997	.986
	5	coarse	.961	.964	.964	.962	.954	.930	.857
		fine	.986	.986	.986	.986	.986	.984	.974
	10	coarse	.974	.977	.977	.975	.966	.938	.850
		fine	.970	.971	.971	.971	.969	.965	.947
	20	coarse	.965	.969	.969	.966	.955	.919	.811
		fine	.823	.824	.824	.823	.819	.809	.779
600	0.2	coarse	.925	.921	.921	.924	.934	.955	.976
		fine	.997	.997	.997	.997	.998	.999	.994
	5	coarse	.990	.988	.988	.989	.992	.992	.959
		fine	.999	.999	.999	.999	.999	.998	.987
	10	coarse	.991	.991	.991	.991	.991	.983	.937
		fine	.990	.991	.991	.990	.988	.982	.959
	20	coarse	.998	.999	.999	.998	.996	.982	.919



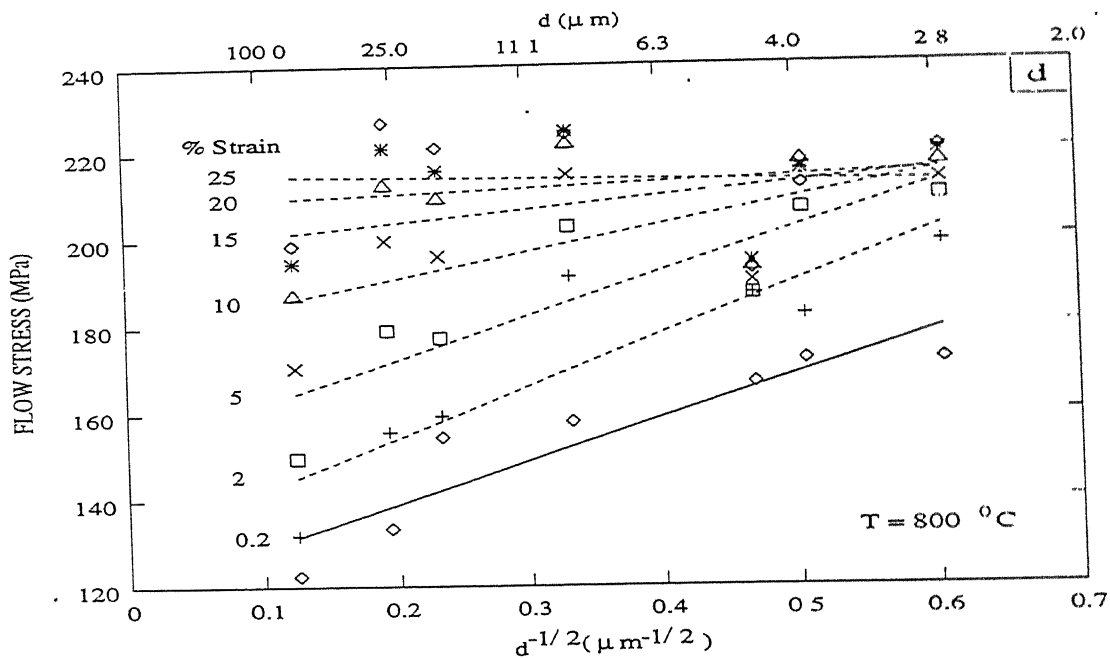
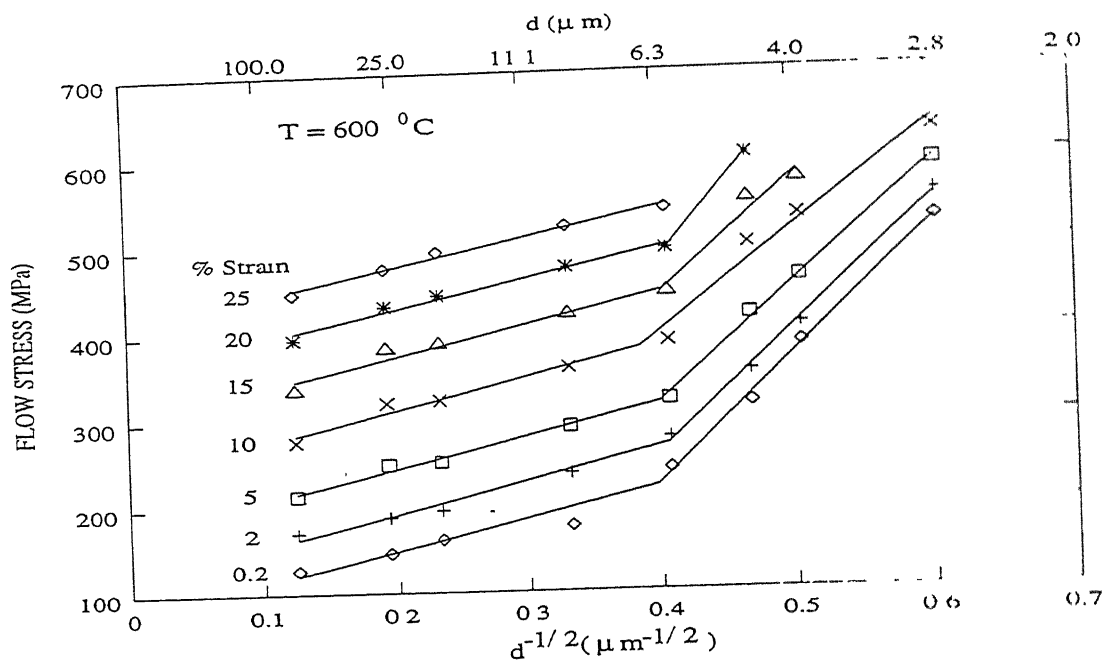


Figure 4.33: Hall-Petch plots at different strain levels (batch 1) for temperatures: (a) 200°C , (b) 400°C , (c) 600°C and (d) 800°C .

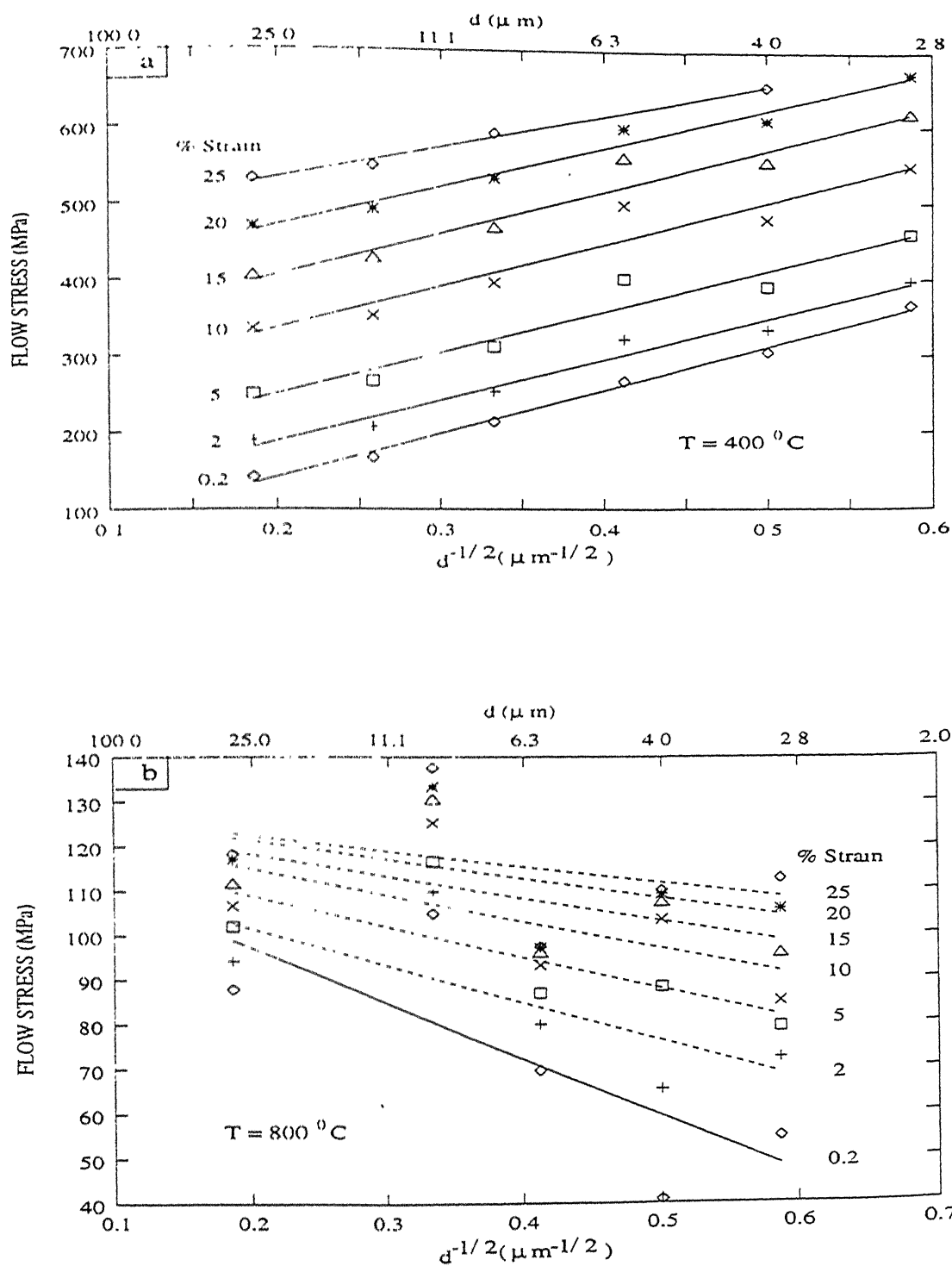
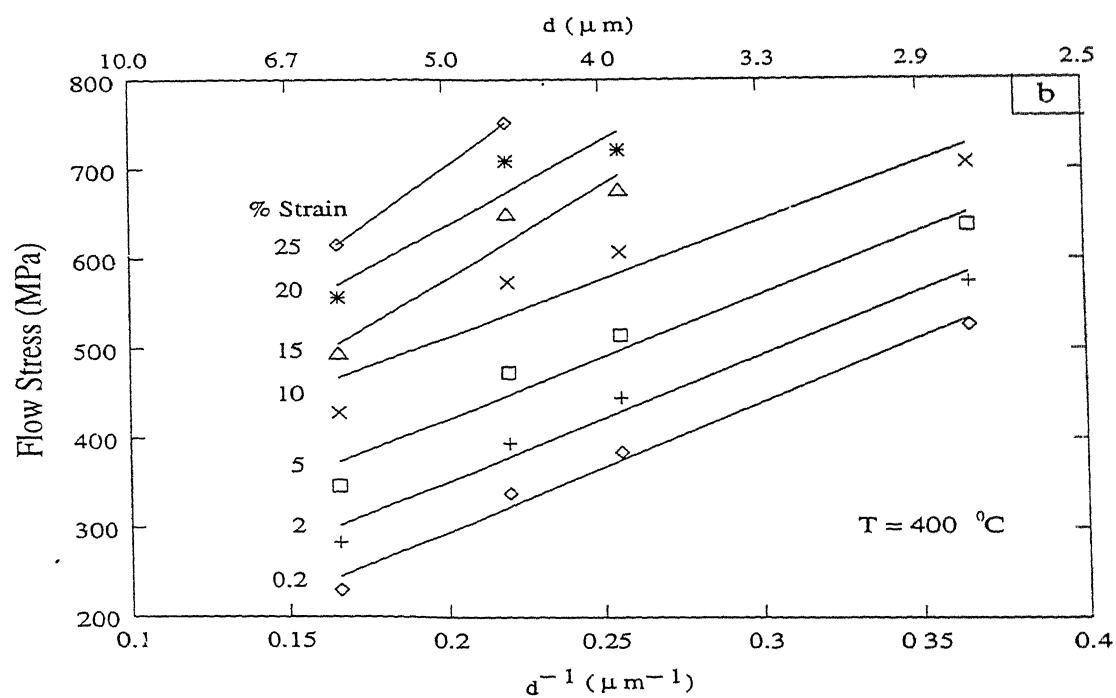
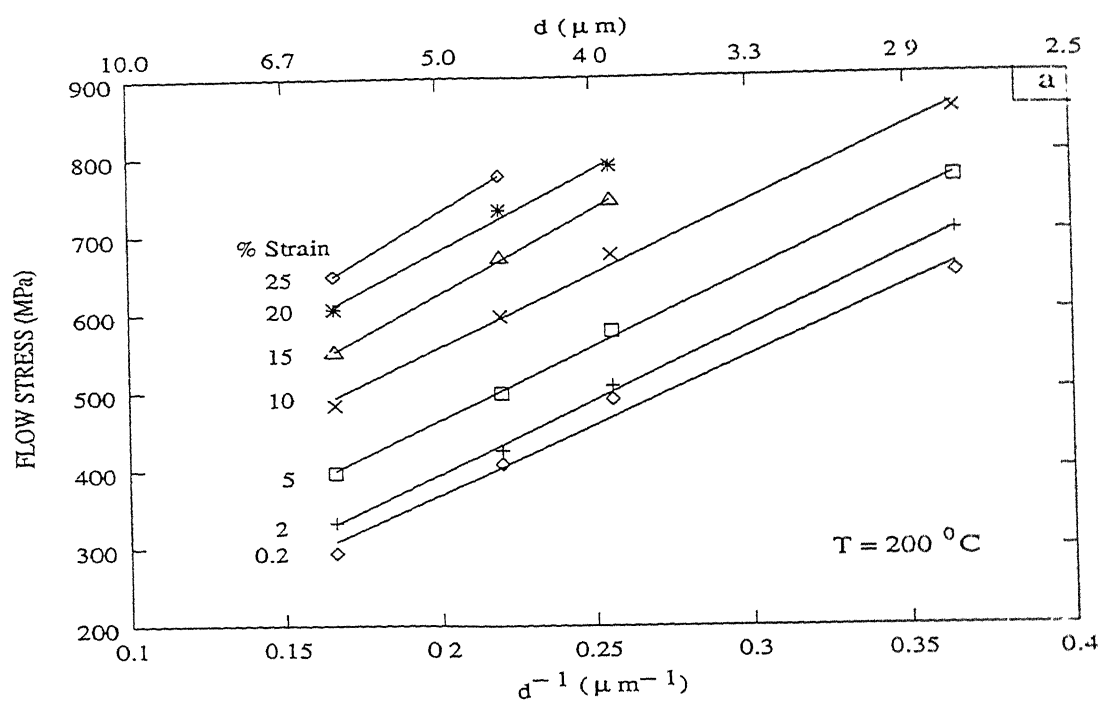


Figure 4.34: Hall-Petch plots at different strain levels (batch 2) for temperatures: (a) 400°C and (b) 800°C .



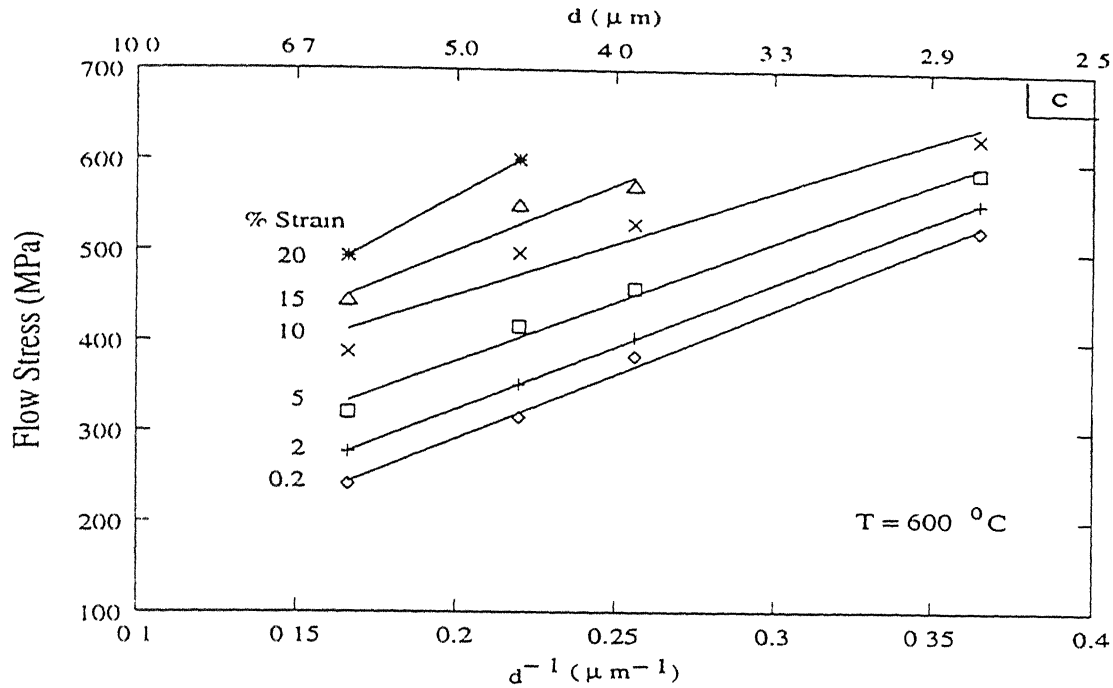


Figure 4.35: Tensile flow stress vs d^{-1} for fine grain size of batch 1 at temperatures: (a) 200 °C, (b) 400 °C and (c) 600 °C.

$K(\epsilon)$ increases in the intermediate strain range (2 to 10 %) followed by decrease with increasing strain. It can also be seen from figure 4.37b that at temperatures above 600 °C, $K(\epsilon)$ decreases with increase in strain. $K(\epsilon)$ at 800 °C is much lower than that observed at lower temperatures. The variation of $\sigma_0(\epsilon)$ and $K(\epsilon)$ in the fine grain regime of batch 1 (intercept and slope of σ versus d^{-1} plots) with strain at various temperatures are shown in figures 4.38a-b. $\sigma_0(\epsilon)$ at 200 °C and 400 °C increases parabolically with increasing strain as seen from figure 4.38a. At 600 °C, $\sigma_0(\epsilon)$ shows almost no change below 2 % strain followed by a parabolic increase with increasing strain as that observed at room temperature. At a given strain, $\sigma_0(\epsilon)$ decreases with increasing temperature (figure 4.38a). Similar to room temperature, at 200 °C, $K(\epsilon)$ increases below 5 % followed by decrease with increasing strain as depicted in figure 4.38b. It may also be noted from figure 4.38b that $K(\epsilon)$ decreases with increasing strain at higher temperatures (400 °C and 600 °C).

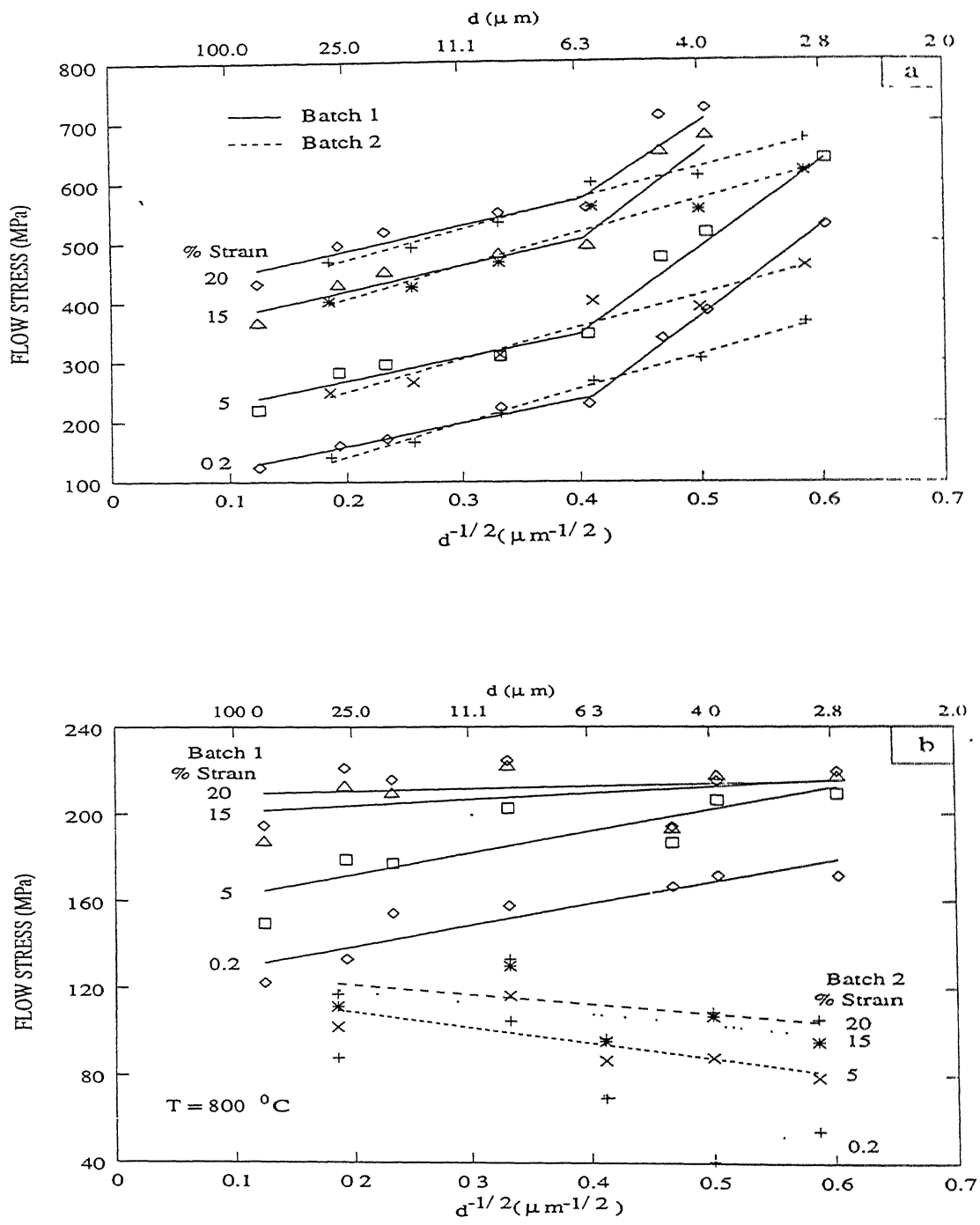


Figure 4.36: Comparison of H-P plots of batch 1 and batch 2 at different strain levels for temperatures: (a) 400°C and (b) 800°C .

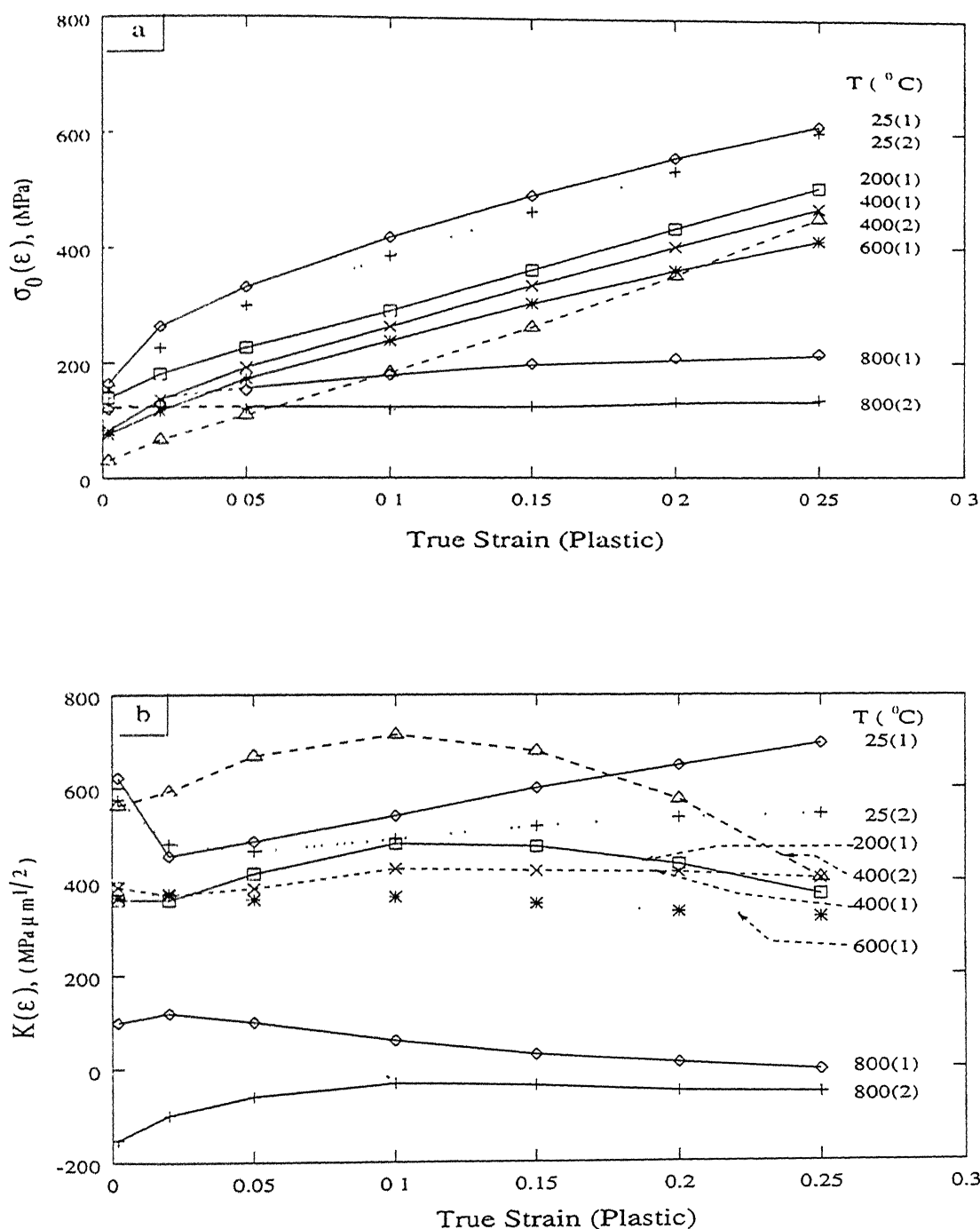


Figure 4.37: Variation of (a) $\sigma_0(\epsilon)$ and (b) $K(\epsilon)$, with strain at different temperatures in the coarse grain size region. The numbers in the brackets indicate the batch number.

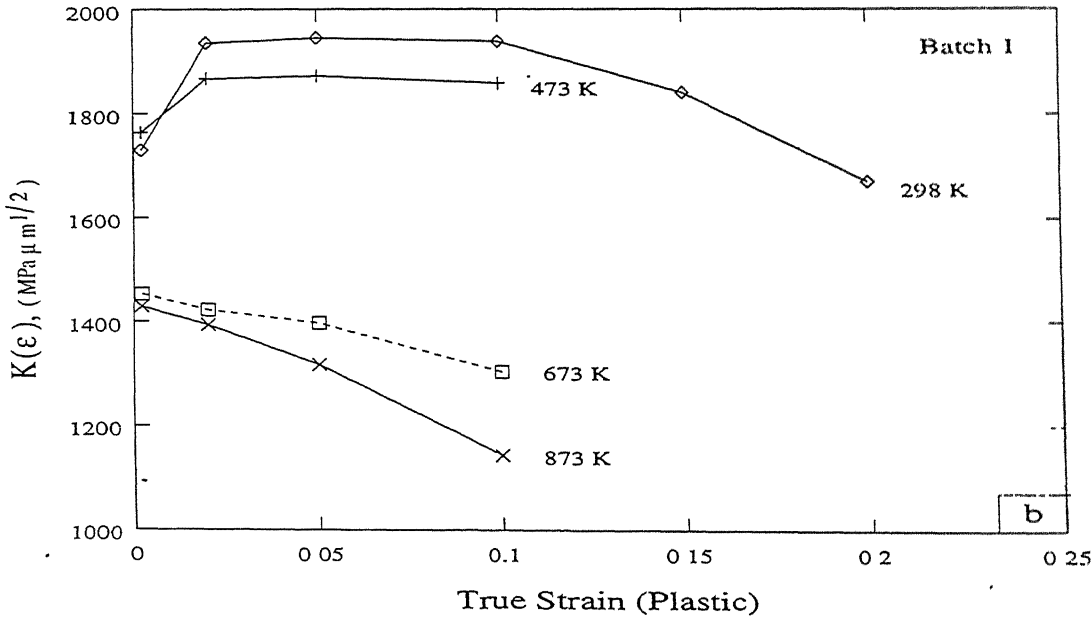
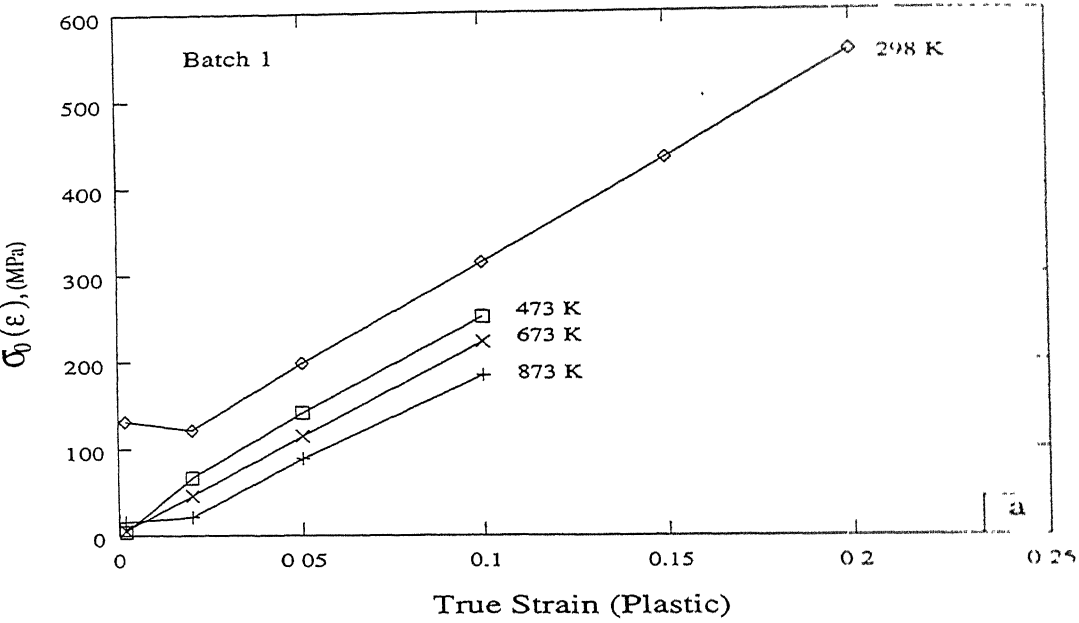


Figure 4.38: Variation of (a) $\sigma_0(\epsilon)$ and (b) $K(\epsilon)$, with strain at different temperatures in the fine grain region of batch 1.

The variation of $\sigma_0(\epsilon)$ and $K(\epsilon)$ for coarse and fine grain region of batch 1 with temperature at various strains are shown respectively in figures 4.39 and 4.40. In the coarse grain regime, the variation of $\sigma_0(\epsilon)$ with temperature at lower strains (below 10 %) shows only two stage behaviour i.e., decrease in $\sigma_0(\epsilon)$ in the first stage at lower temperatures and almost no change in second stage at higher temperatures. However at higher strains the third stage i.e., sharp drop in $\sigma_0(\epsilon)$ with temperature is also prominent as shown in figure 4.39a. On the other hand, $K(\epsilon)$ versus temperature plots at lower strains (less than 2 %) and higher strains (above 20 %) show three stage behaviour while at intermediate strains the first stage is not so prominent. Figure 4.39b shows that at all strains, a sharp drop in $K(\epsilon)$ occurs around 600 °C. In the fine grain regime, at lower strain (0.2 %), $\sigma_0(\epsilon)$ decreases till 200 °C and thereafter remains nearly constant with increasing temperature as shown in figure 4.40a. Above 0.2% strain, $\sigma_0(\epsilon)$ decreases up to 200 °C followed by a hump from 200 °C to 400 °C and subsequently again decreases beyond 400 °C. It can be seen from figure 4.40b that the variation of $K(\epsilon)$ with temperature at a given strain is opposite in trend to that observed in the variation of $\sigma_0(\epsilon)$ with temperature.

4.3.2 Microstructural characterisation of deformed samples

As discussed in section 4.2.2, three different grain sizes (4.0 μm , 5.9 μm and 29.0 μm) were selected for microstructural characterisation. The microstructures of deformed specimens at 400 °C and 800 °C in the strain range of 5 % to 20% are shown in figures 4.41 and 4.42 respectively. While elongated grains can be noted at 400 °C (figure 4.41), the grains remain more or less equiaxed for deformation at 800 °C (figure 4.42). However, the grain boundaries tend to become wavy with increasing strain at 800 °C as shown in figures 4.42a-c. The wavy type of grain boundaries are not observed at lower temperatures (figures 4.21 and 4.41). Table 4.10 lists the values of microstructural parameters at various temperatures and strains for different grain size samples of batch 2.

The variation of microstructural parameters with strain for 29.0 μm grain size samples

of batch 2 are shown in figures 4.43 and 4.44. The coefficient of variation of grain size increases with strain at 400 °C (see figure 4.43e) while at 800 °C it increases only up to 5 % and thereafter it remains more or less constant with increasing strain (figure 4.44e). In general the grain aspect ratio increases and the grain shape factor decreases with strain at 400 °C (figure 4.43c-d), as expected. At 800 °C, the grain aspect ratio increases and the grain shape factor decreases with increasing strain below 5 % strain and subsequently these parameters show no significant change with increasing strain (figures 4.44c-d). In the variation of PDA distribution with strain, the standard deviation of PDA distribution (β_{SD}) increases and the relative frequency (β_{120}) of 120th class of PDA distribution decreases at 400 °C (figures 4.43a-b). On the other hand at 800 °C, the β_{SD} increases and the β_{120} of PDA distribution decreases in the strain range of 0 to 5 % followed by an decrease in the former and increase in the later parameter with strain as shown in figures 4.44a and b respectively. The relative frequency distribution of PDA of fine ($d=4.0 \mu\text{m}$) and coarse ($d=29.0 \mu\text{m}$) grain samples at 400 °C and 800 °C are shown in figures 4.45-4.48. At 400 °C, PDA distribution flattens out with increasing strain in both fine and coarse grain samples as observed from the histograms in figures 4.45 and 4.46. On the other hand at 800 °C, the distribution of PDA remains unchanged below 5 % strain in fine grain ($d=4.0 \mu\text{m}$) regime. At an intermediate strain (10 %) it flattens and thereafter no significant change is observed in distribution (figures 4.47). However in the coarse grained ($d=29.0 \mu\text{m}$) sample at 800 °C, the flattening of distribution occurs at 5 % strain and the distribution remains unchanged with increasing strain (figures 4.48).

Table 4.10: Microstructural parameters at various temperatures and strain levels for different grain size samples of batch 2

T(°C)	d (μm) [†]	%ε	$\bar{d}_{eq}(\mu m)^*$	C _V	AR	S _F	β _{SD} (degree)	β ₁₂₀
400	4.0 ± 0.06	0	4.1 ± 0.30	0.38	-	0.93 ± 0.02	18.0	0.26
		5	4.0 ± 0.25	0.38	-	0.88 ± 0.01	15.9	0.23
		10	3.3 ± 0.19	0.35	-	0.89 ± 0.01	16.3	0.24
		20	3.6 ± 0.23	0.39	-	0.86 ± 0.01	19.0	0.16
	5.9 ± 0.29	0	5.7 ± 0.33	0.41	-	0.91 ± 0.01	14.6	0.31
		5	5.8 ± 0.27	0.43	-	0.89 ± 0.01	14.5	0.29
		10	6.0 ± 0.35	0.54	-	0.90 ± 0.02	16.4	0.25
		20	5.8 ± 0.25	0.39	-	0.89 ± 0.01	15.9	0.27
	29.0 ± 1.17	0	27.4 ± 1.15	0.37	1.01 ± 0.07	0.91 ± 0.01	17.3	0.29
		5	24.4 ± 1.12	0.49	1.07 ± 0.05	0.98 ± 0.01	15.4	0.23
		10	23.5 ± 1.16	0.53	1.18 ± 0.07	0.88 ± 0.02	16.7	0.21
		20	27.0 ± 1.29	0.51	1.26 ± 0.09	0.92 ± 0.02	17.1	0.24

...continued

[†] by intercept method^{*} by grain area method

Table 4.10 (continued)

T(°C)	d (μm) [†]	%ε	$\bar{d}_{eq}(\mu m)^*$	C _V	AR	S _F	β _{SD} (degree)	β ₁₂₀
800	4.0 ± 0.06	0	4.1 ± 0.30	0.38	-	0.93 ± 0.02	18.0	0.26
		5	3.3 ± 0.19	0.35	-	0.87 ± 0.01	15.9	0.29
		10	3.3 ± 0.22	0.40	-	0.88 ± 0.01	15.7	0.22
		20	3.2 ± 0.19	0.37	-	0.86 ± 0.03	14.4	0.25
	5.9 ± 0.29	0	5.7 ± 0.33	0.41	-	0.91 ± 0.01	14.6	0.31
		5	6.4 ± 0.34	0.49	-	0.86 ± 0.01	18.5	0.20
		10	5.8 ± 0.24	0.37	-	0.89 ± 0.01	15.6	0.28
		20	5.6 ± 0.23	0.37	-	0.88 ± 0.03	17.9	0.19
	29.0 ± 1.17	0	27.4 ± 1.15	0.37	1.01 ± 0.07	0.91 ± 0.01	17.3	0.29
		5	28.7 ± 1.39	0.52	1.14 ± 0.09	0.85 ± 0.02	18.8	0.21
		10	25.2 ± 0.81	0.38	1.17 ± 0.09	0.90 ± 0.01	17.7	0.22
		20	26.2 ± 1.10	0.45	1.15 ± 0.07	0.89 ± 0.01	15.9	0.27

† by intercept method

* by grain area method

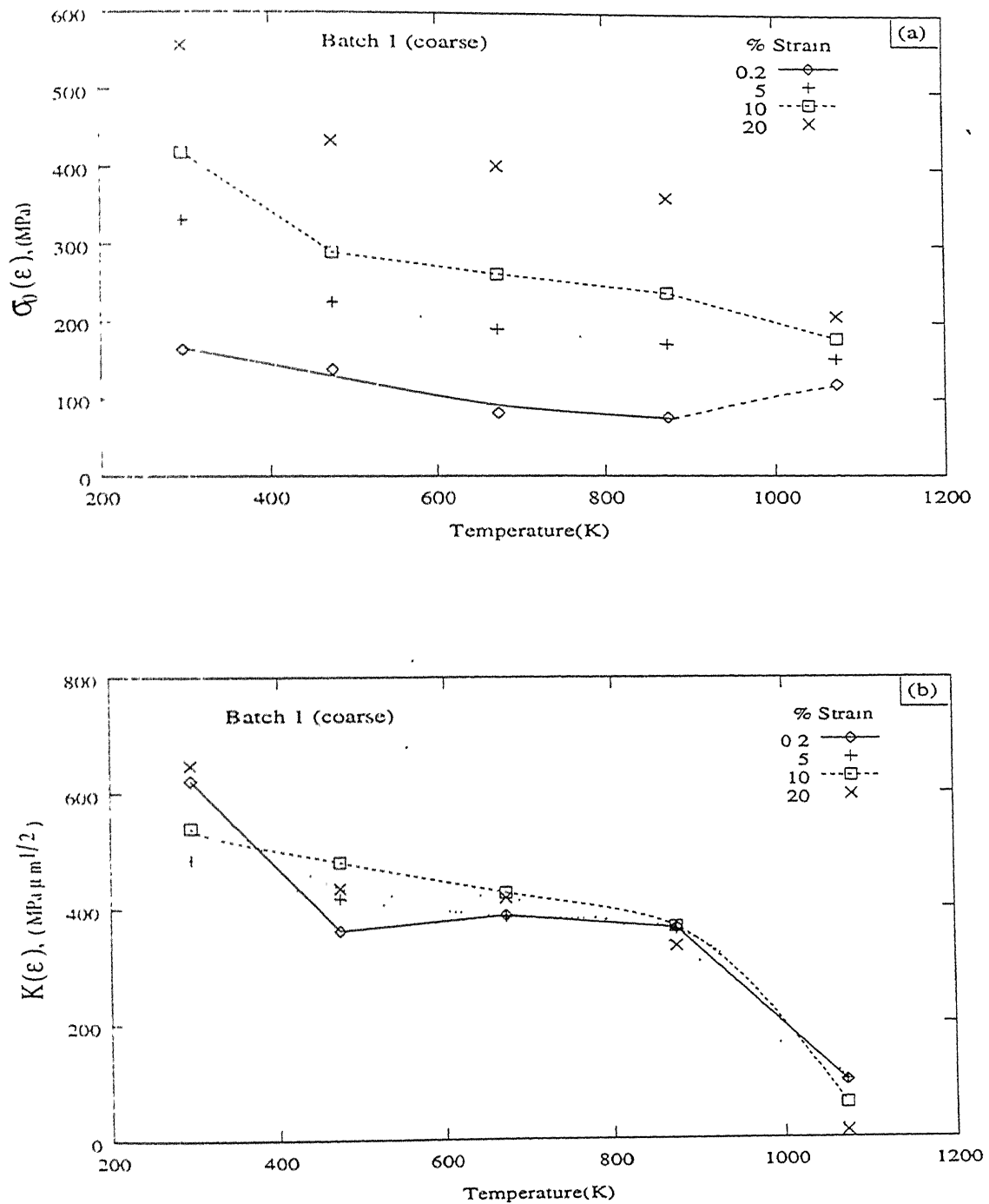


Figure 4.39: Variation of (a) $\sigma_0(\epsilon)$ and (b) $K(\epsilon)$, with temperature at various strain levels in the coarse grain regime of batch 1.

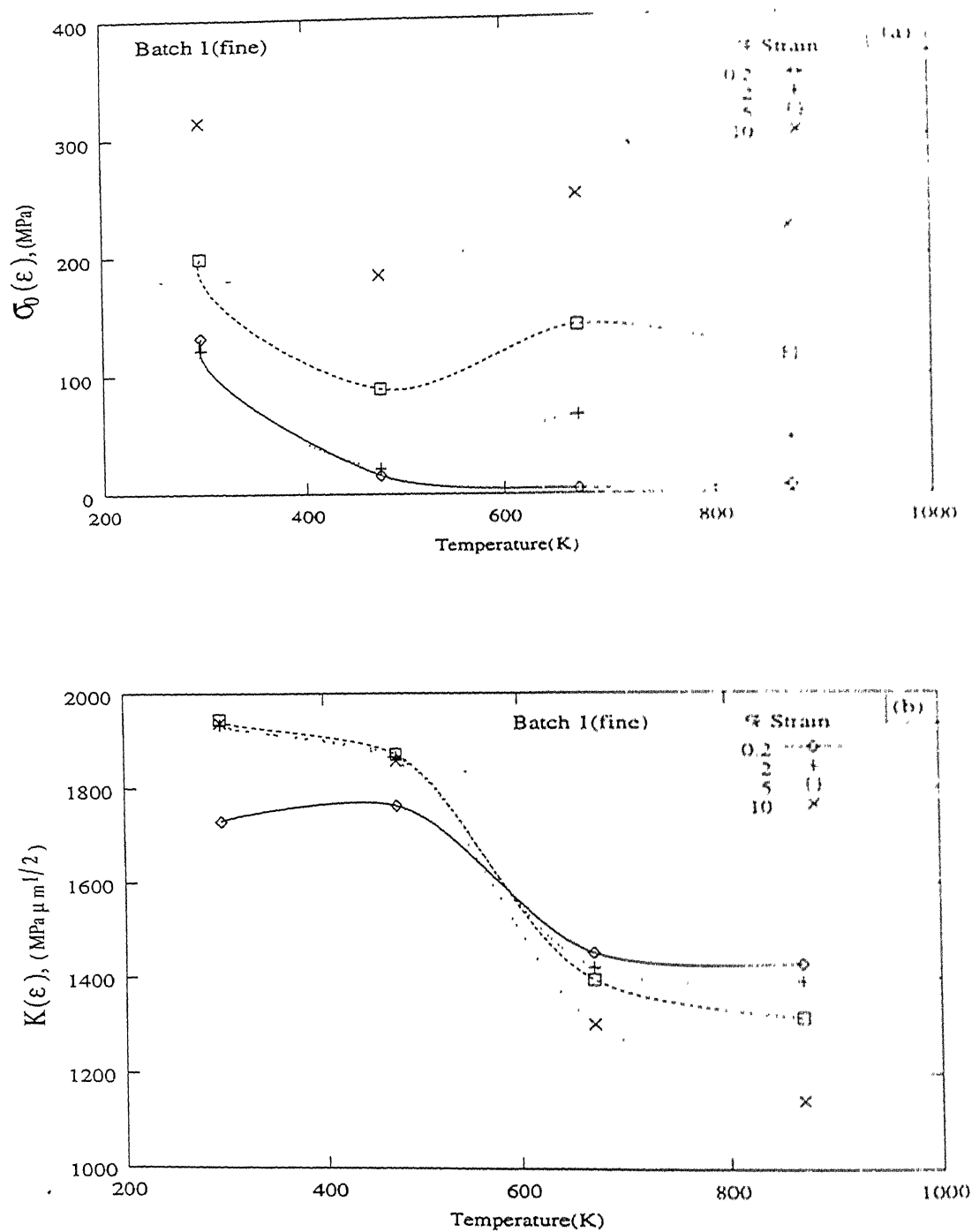


Figure 4.40: Variation of (a) $\sigma_0(\epsilon)$ and (b) $K(\epsilon)$, with temperature at various strain levels in the fine grain regime of batch 1.

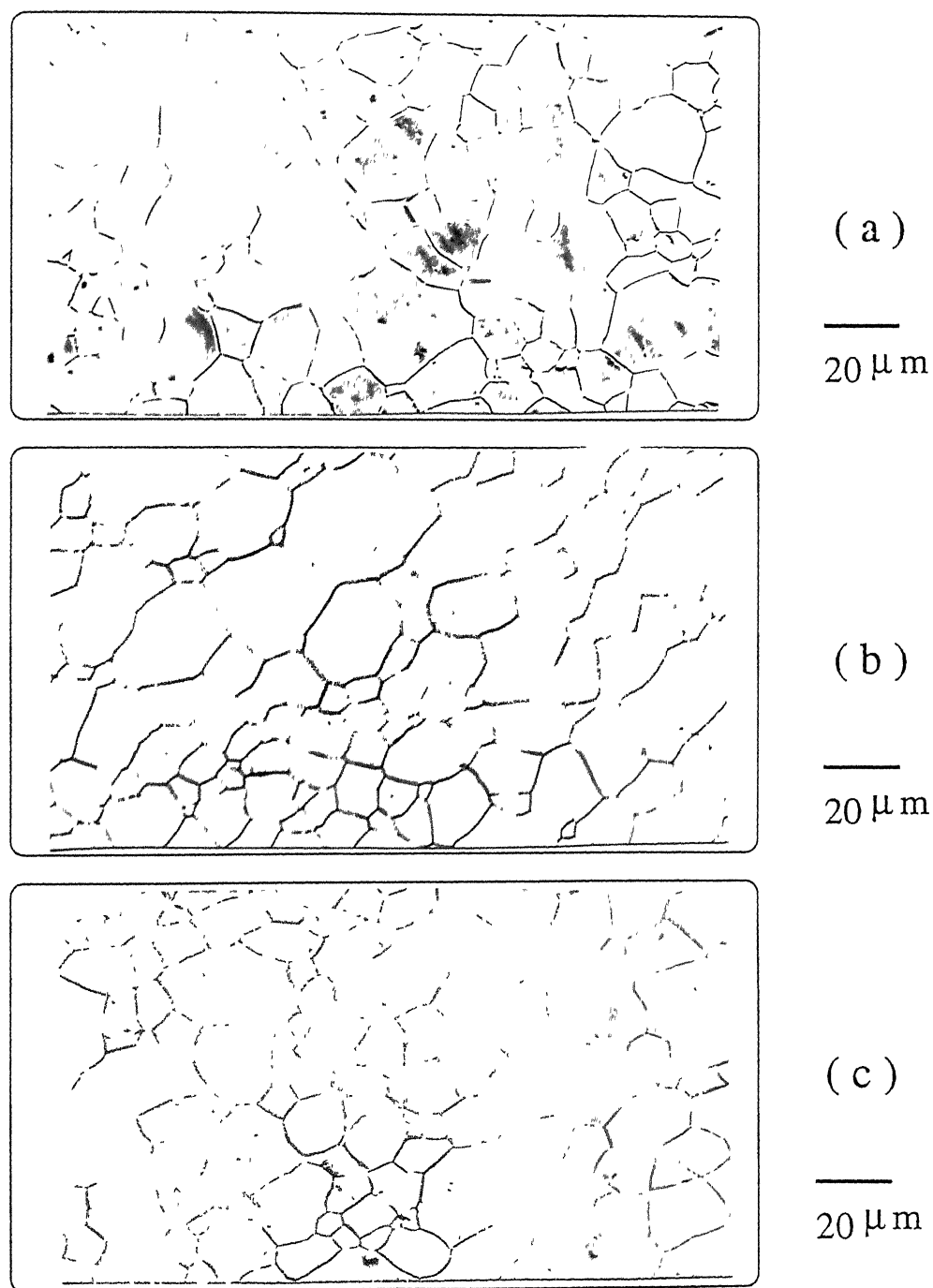


Figure 4.41: Microstructures of the samples ($d = 29.0\mu\text{m}$) deformed at 400°C up to the strains of (a) 5 %, (b) 10 % and (c) 20 %.

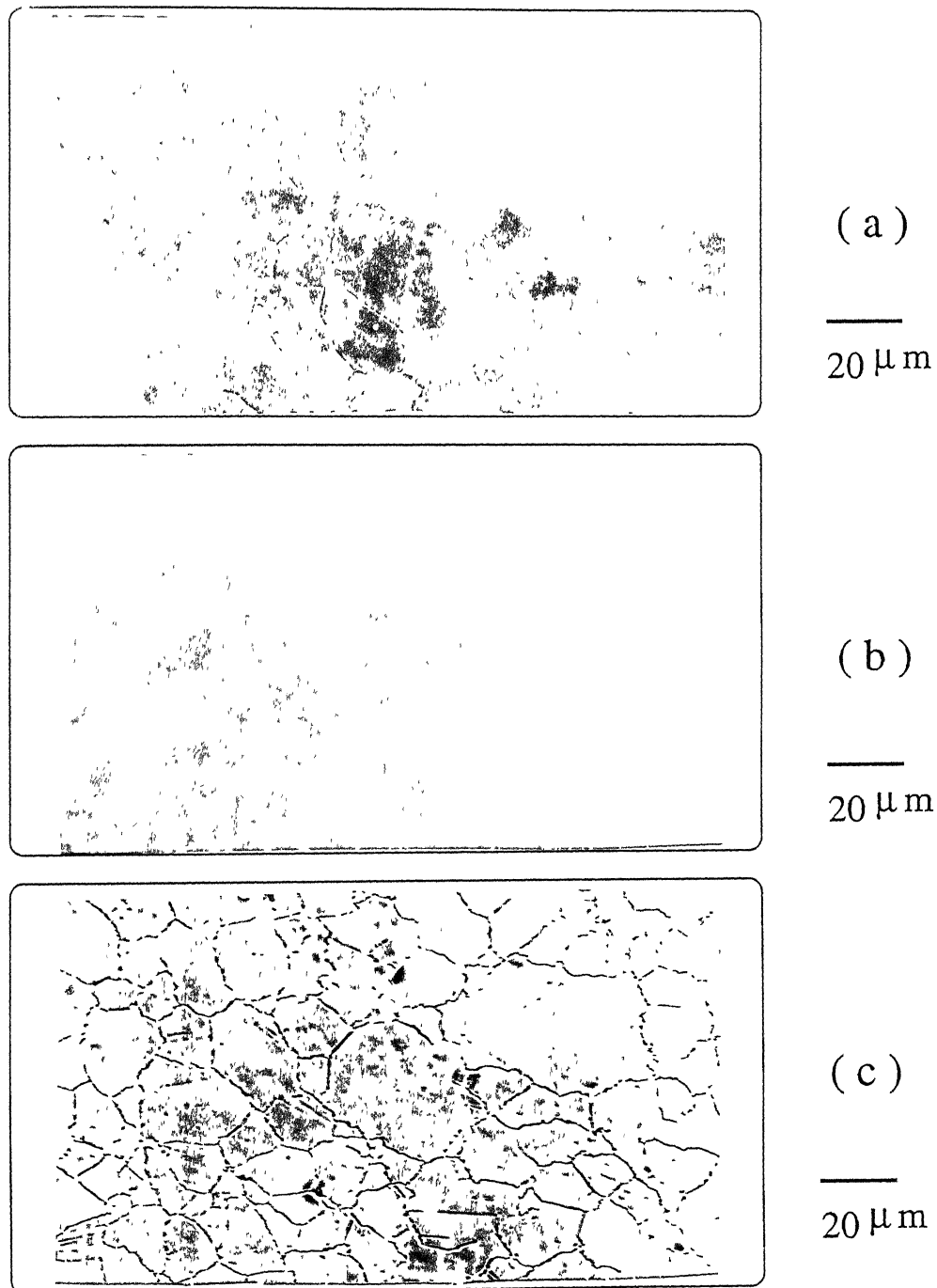


Figure 4.42: Microstructures of the samples ($d = 29.0\mu\text{m}$) deformed at 800°C up to the strains of (a) 5 %, (b) 10 % and (c) 20 %.

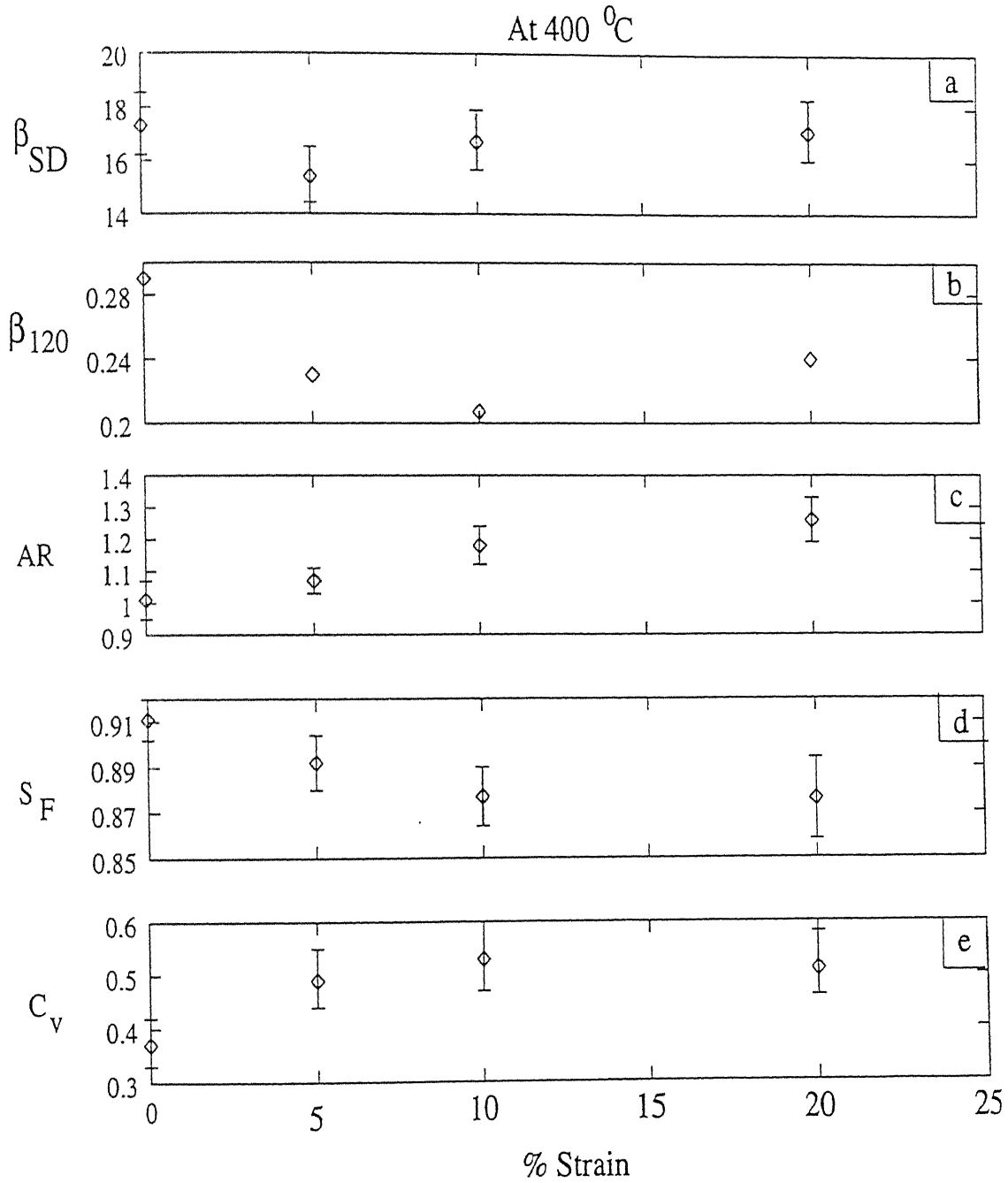


Figure 4.43: Variation of metallographic parameters: (a) standard deviation of PDA distribution (β_{SD}), (b) relative frequency of 115° – 125° class of PDA distribution (β_{120}), (c) grain aspect ratio (AR), (d) grain shape factor (S_F) and (e) coefficient of variation of grain size (C_v) as a function of strain at 400 °C for $d = 29.0\mu m$.

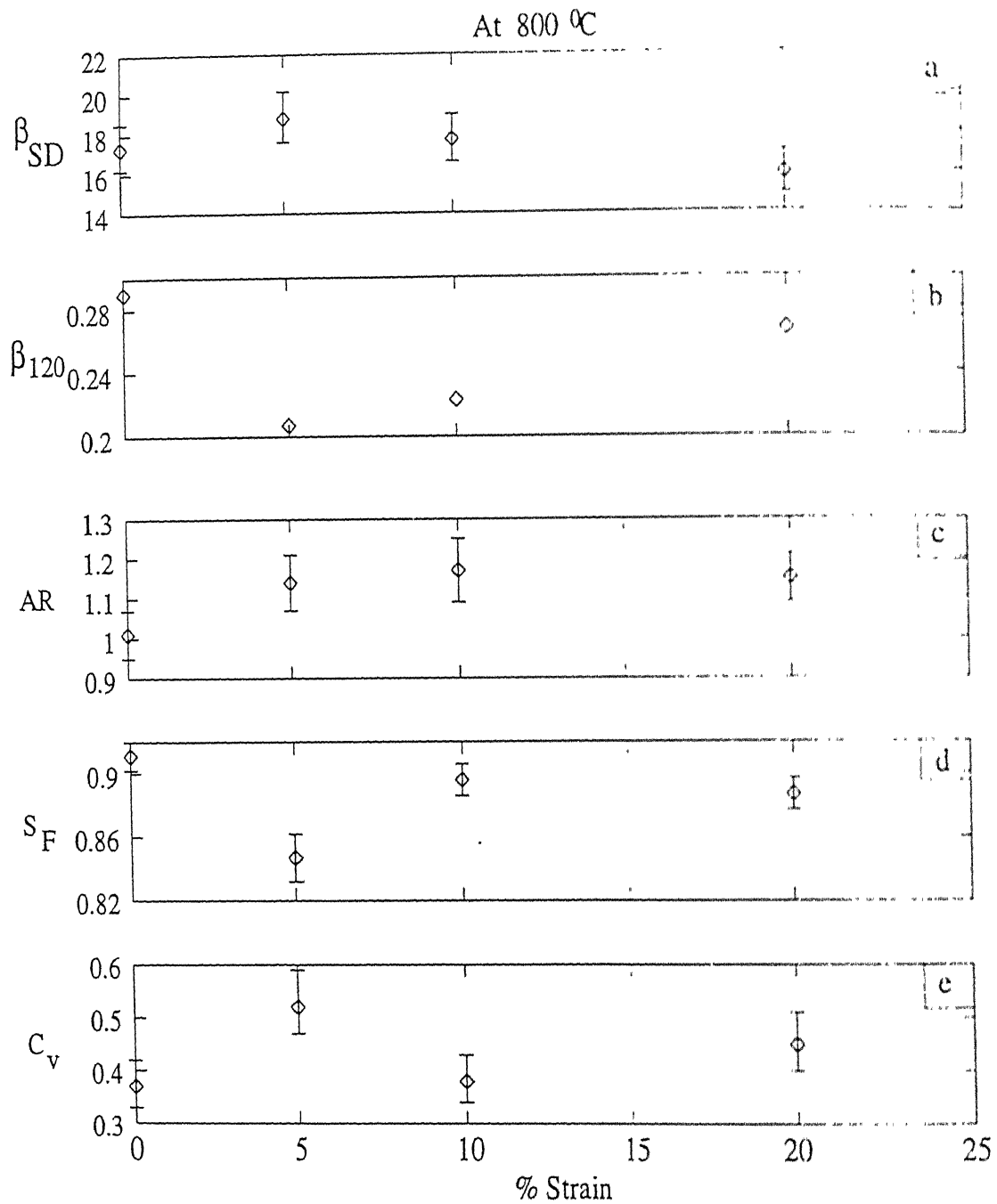


Figure 4.44: Variation of metallographic parameters: (a) standard deviation of PDA distribution (β_{SD}), (b) relative frequency of 115° – 125° class of PDA distribution (β_{120}), (c) grain aspect ratio (AR), (d) grain shape factor (S_F) and (e) coefficient of variation of grain size (C_v) as a function of strain at 800 °C for $d = 29.0\mu m$.

4.3 Elevated temperature deformation behaviour

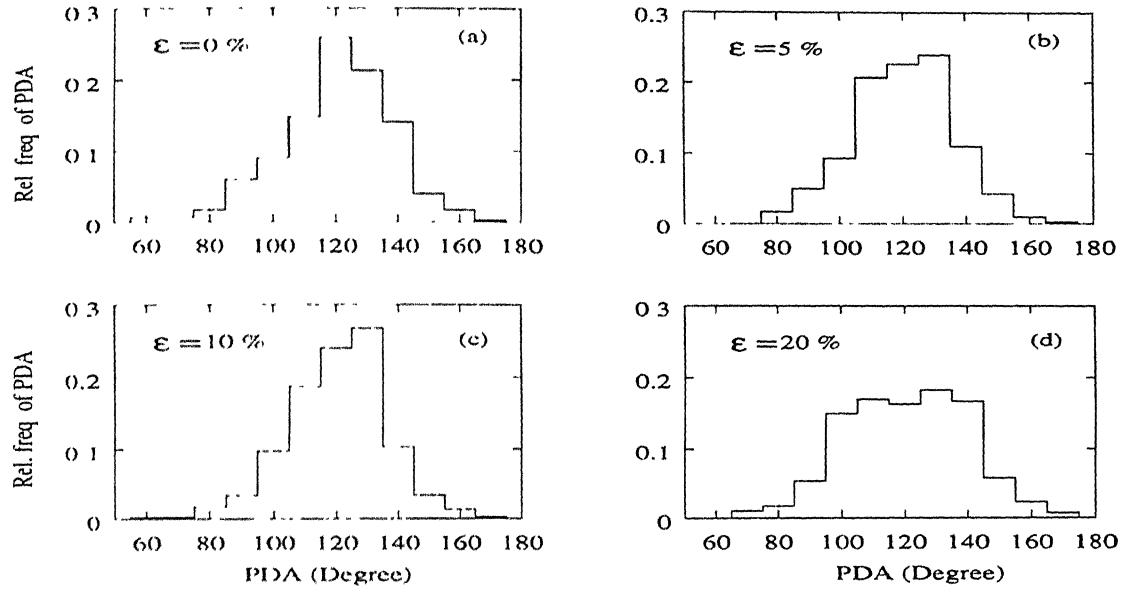


Figure 4.45: PDA distribution at 400°C in the fine grain size ($d = 4.0 \mu m$) at % strains: (a) 0, (b) 5, (c) 10 and (d) 20.

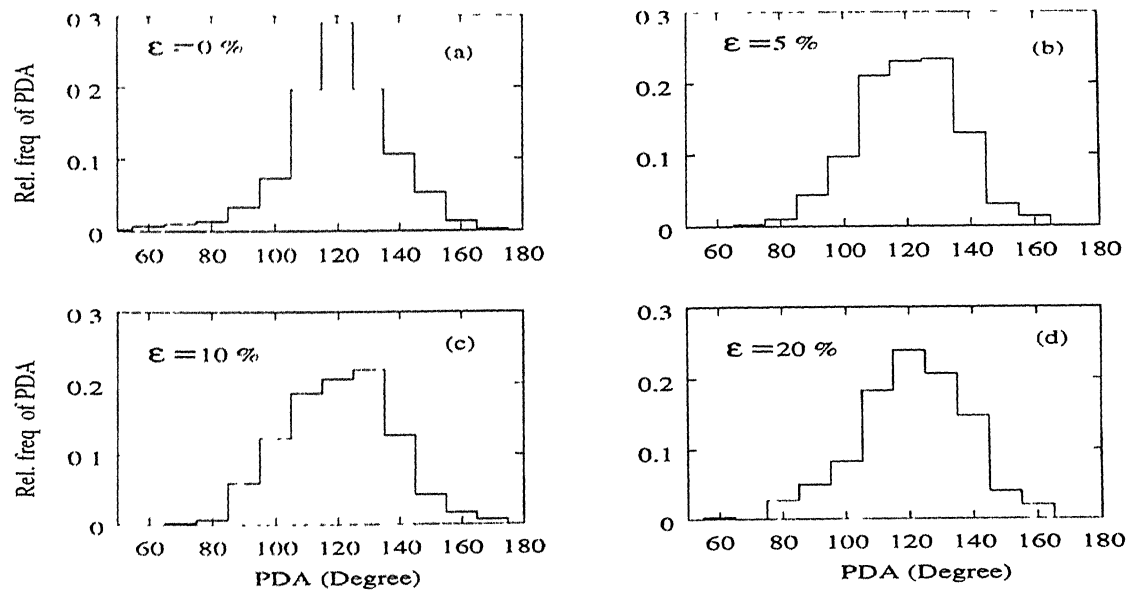


Figure 4.46: PDA distribution at 400°C in the coarse grain size ($d = 29.0 \mu m$) at % strains: (a) 0, (b) 5, (c) 10 and (d) 20.

Figures 4.49 to 4.51 show the variation of microstructural parameters with temperature for 29.0 μm grain size at different strain levels (5 %, 10 % and 20 %). At 5 % strain, C_v , grain aspect ratio, and β_{SD} increase while S_F and β_{120} of 120 $^\circ$ class of PDA distribution decrease with increasing temperature as shown in figures 4.49. At intermediate strain (10 %), the microstructural parameters are nearly independent of test temperature (figure 4.50). However at higher strains (20 %), C_v , grain aspect ratio, and β_{SD} decrease while S_F and β_{120} of 120 $^\circ$ class of PDA distribution increase with temperature as depicted in figures 4.51. The nature of variation in microstructural parameters with temperature at 20 % strain is the opposite of that observed at lower strain (5 %). This transformation is gradual since at intermediate strain (10 %), these parameters show more or less no change with temperature.

4.3.3 Microhardness variation in deformed samples

Figures 4.52a and b show the variation of microhardness through selected grains in annealed and deformed samples of average grain size 29 μm at 400 $^\circ\text{C}$ and 800 $^\circ\text{C}$ respectively. As mentioned in section 4.2.3, the microhardness value is nearly the same in the grain interior and at the grain boundaries in annealed samples. However, with increasing strain, the microhardness value increases both inside and at the grain boundaries as shown in figure 4.52a at 400 $^\circ\text{C}$. The difference between the microhardness at the grain boundaries and the grain interior is maximum at low strain (5 %). This difference in the microhardness values between the grain boundary and the grain center decreases with increasing strain as seen from figure 4.52a. On the other hand at 800 $^\circ\text{C}$, this difference is same at all strains as seen in figure 4.52b. At 800 $^\circ\text{C}$, no significant difference is observed in microhardness at a selected position in a grain above 5 % strain as illustrated in figure 4.52b. The variation of microhardness through grains at different temperatures at 5 %, 10 % and 20 % strain levels are presented in figures 4.53a-c. At 5 % strain, the microhardness distribution

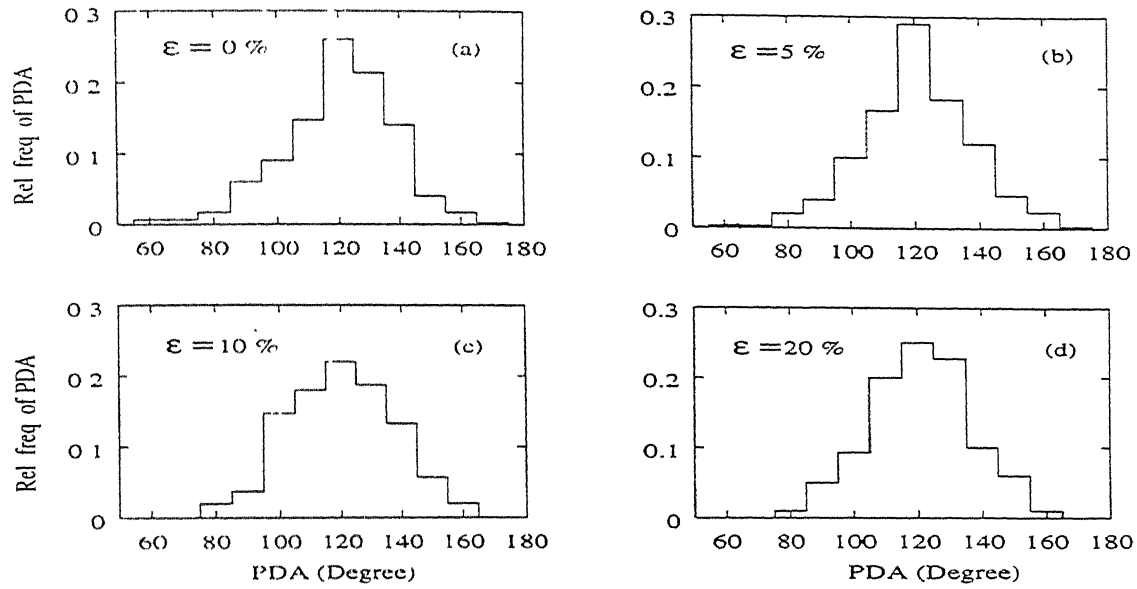


Figure 4.47: PDA distribution at 800°C in the fine grain size ($d = 4.0 \mu\text{m}$) at % strains: (a) 0, (b) 5, (c) 10 and (d) 20.

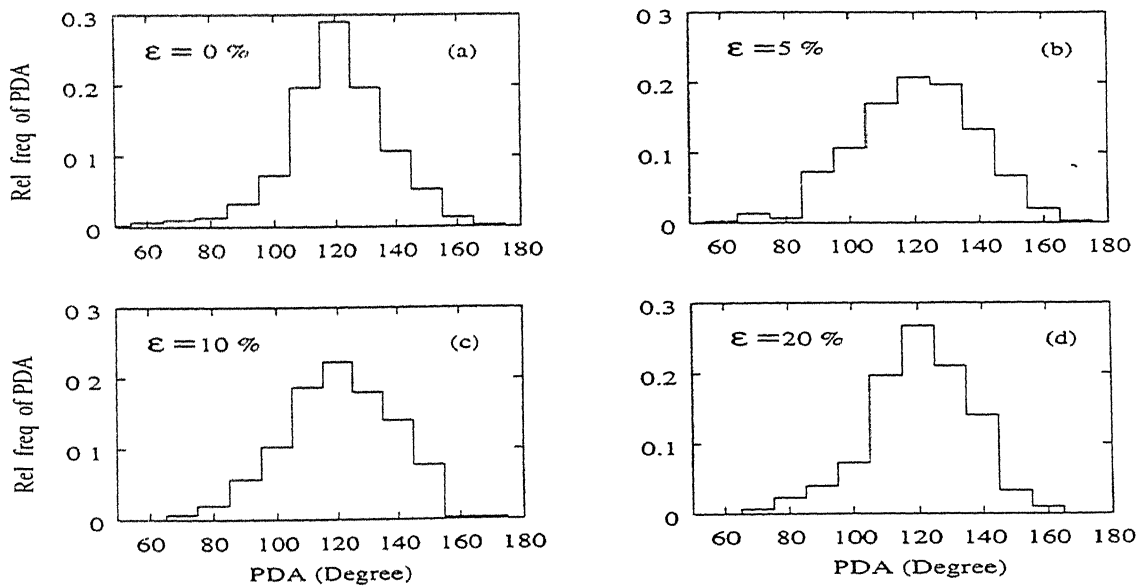


Figure 4.48: PDA distribution at 800°C in the coarse grain size ($d = 29.0 \mu\text{m}$) at % strains: (a) 0, (b) 5, (c) 10 and (d) 20.

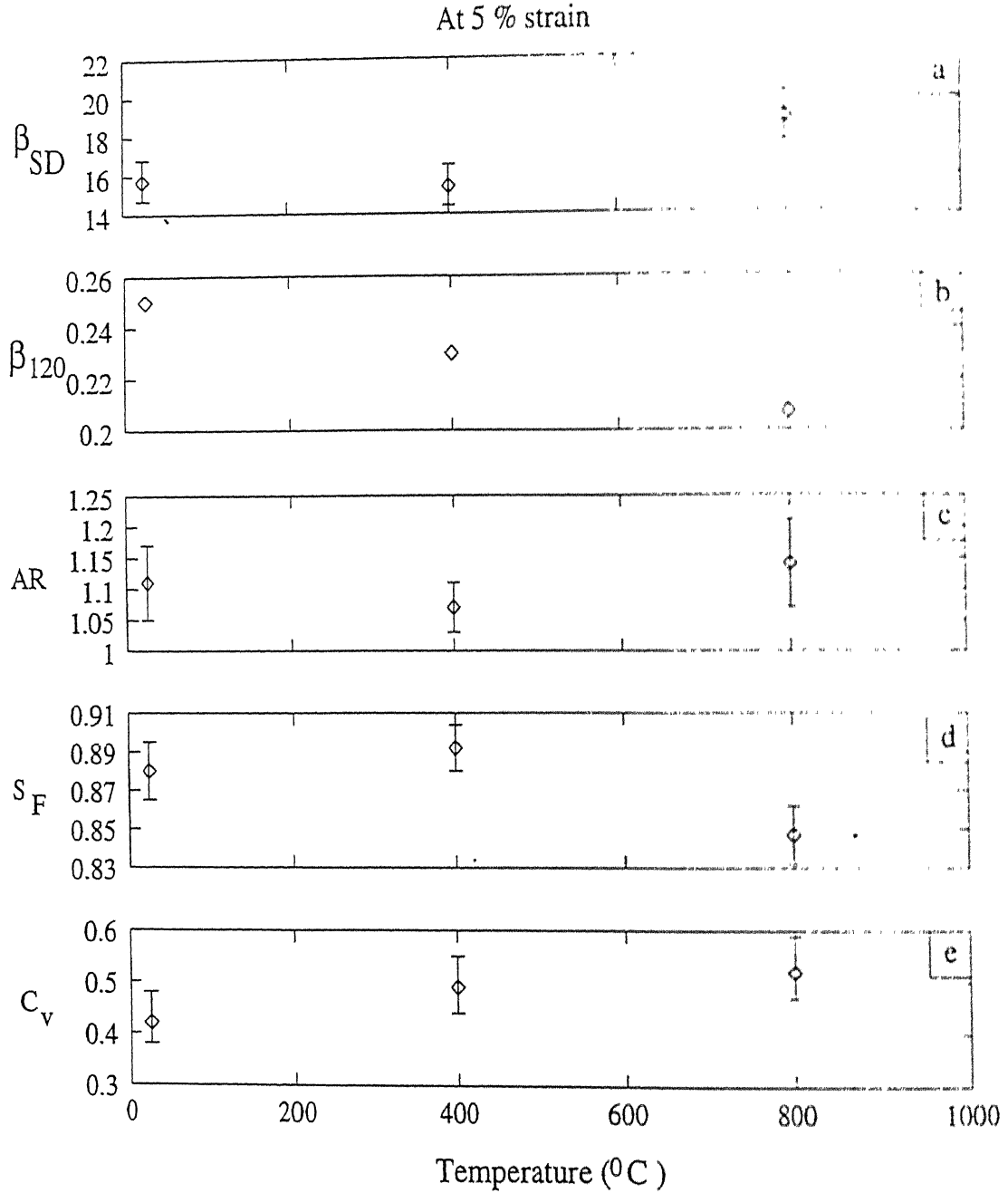


Figure 4.49: Variation of metallographic parameters: (a) standard deviation of PDA distribution (β_{SD}), (b) relative frequency of $115^\circ - 125^\circ$ class of PDA distribution (β_{120}), (c) grain aspect ratio (AR), (d) grain shape factor (S_F) and (e) coefficient of variation of grain size (C_v) as a function of temperature at 5 % strain for $d = 29.0 \mu m$.

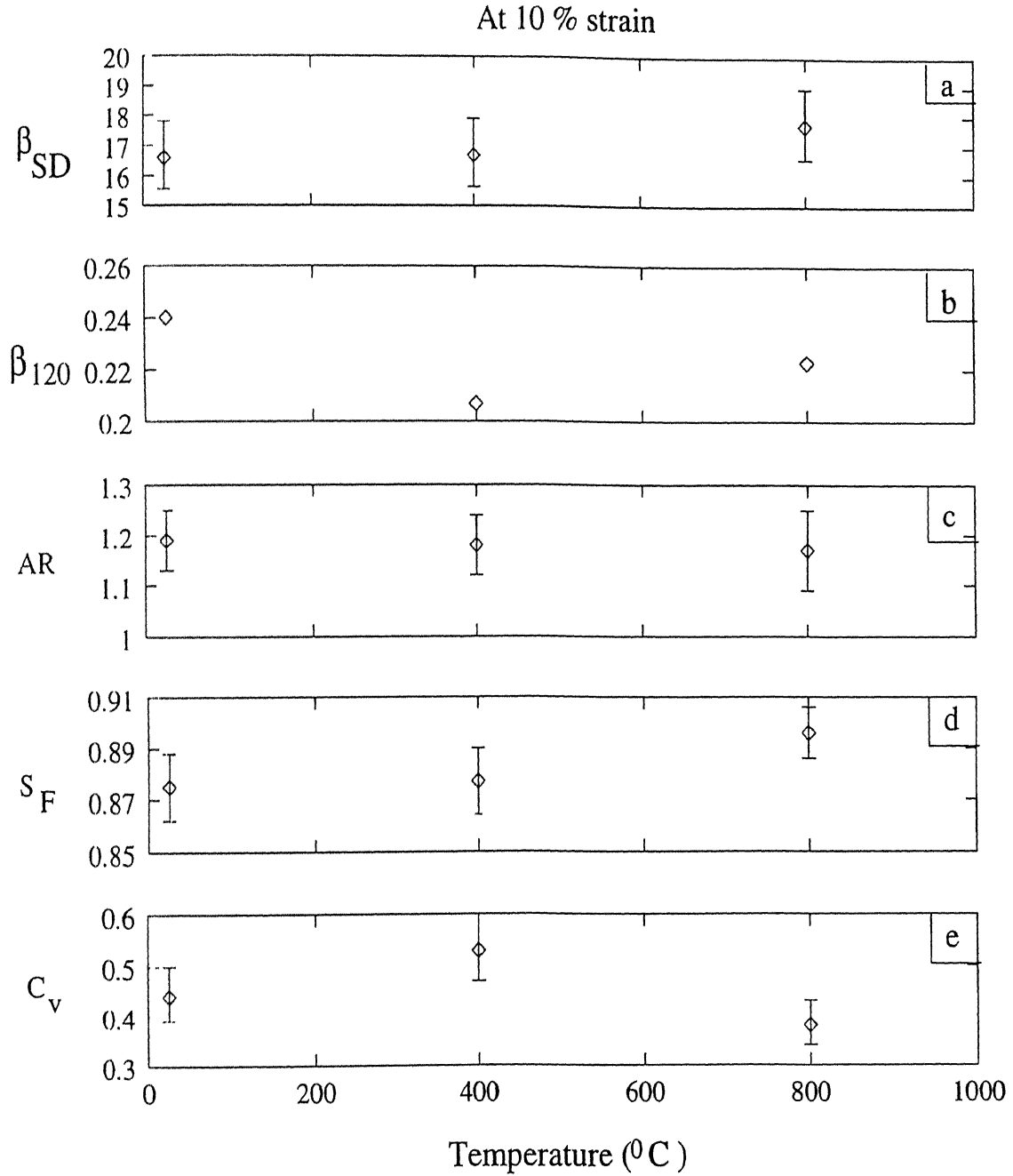


Figure 4.50: Variation of metallographic parameters: (a) standard deviation of PDA distribution (β_{SD}), (b) relative frequency of 115° – 125° class of PDA distribution (β_{120}), (c) grain aspect ratio (AR), (d) grain shape factor (S_F) and (e) coefficient of variation of grain size (C_v) as a function of temperature at 10 % strain for $d = 29.0 \mu m$.

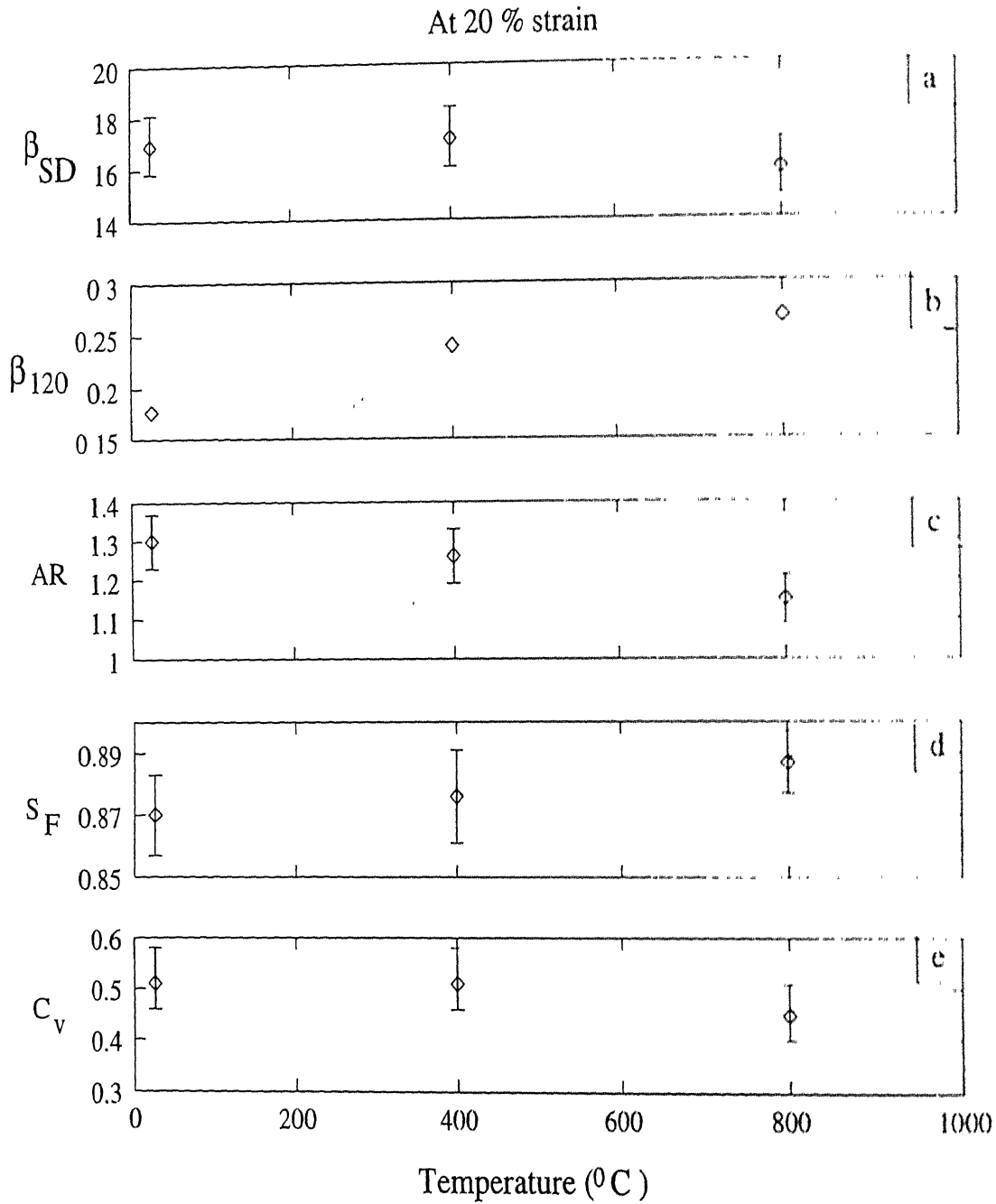


Figure 4.51: Variation of metallographic parameters: (a) standard deviation of PDA distribution (β_{SD}), (b) relative frequency of 115° – 125° class of PDA distribution (β_{120}), (c) grain aspect ratio (AR), (d) grain shape factor (S_F) and (e) coefficient of variation of grain size (C_v) as a function of temperature at 20 % strain for $d = 29.0 \mu m$.

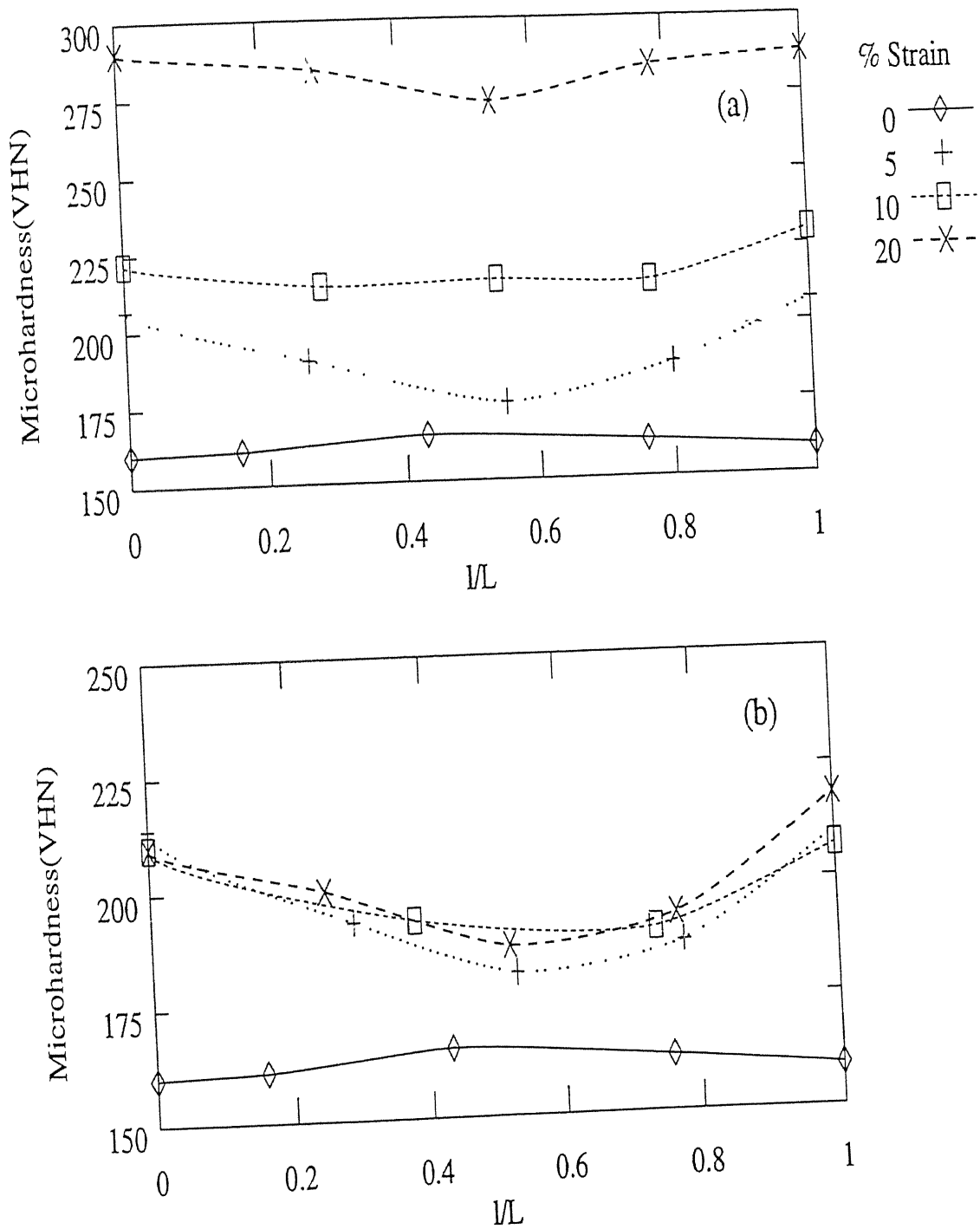


Figure 4.52: Microhardness variation across grains, $d = 29 \mu\text{m}$ (batch 2) at different strain levels for temperatures: (a) 400°C and (b) 800°C .

and values at a given position at different temperatures is more or less same (figure 4.53a). Above 5 % strain, the microhardness at different position in a grain is highest at 400 °C and lowest at 800 °C as depicted in figure 4.53b-c. However, the difference between the microhardness values at a given position at different temperatures increases with increasing strain (figures 4.53a-c).

The variation of microhardness with strain at different temperatures is shown in figure 4.54a and with temperature at various strain levels is shown in figure 4.54b. Microhardness increases at all temperatures with increasing strain. Below 5 % strain, the rate of increase in microhardness at all temperatures is same. However, as compared to the lower temperatures, the rate of decrease is faster above 5 % strain at 800 °C. At all strain levels, the microhardness increases with temperature (below 400 °C) and thereafter it decreases with increasing temperature as depicted in figure 4.54b. The values of microhardness at various strains and temperatures for samples of batch 2 with 29.0 μm are listed in table 4.11.

Table 4.11: Average microhardness values at different temperature and strain for batch 2 (d=29 μm).

Strain (%)	Microhardness(VHN) of Batch 2(d = 29 μm) at		
	298 K	673 K	1073 K
0	151.4 \pm 12.4	151.4 \pm 12.4	151.4 \pm 12.4
5	190.5 \pm 6.3	204.3 \pm 9.5	198.6 \pm 9.0
10	212.5 \pm 5.4	225.9 \pm 9.1	199.9 \pm 7.1
20	255.5 \pm 8.5	282.1 \pm 7.4	203.4 \pm 9.7

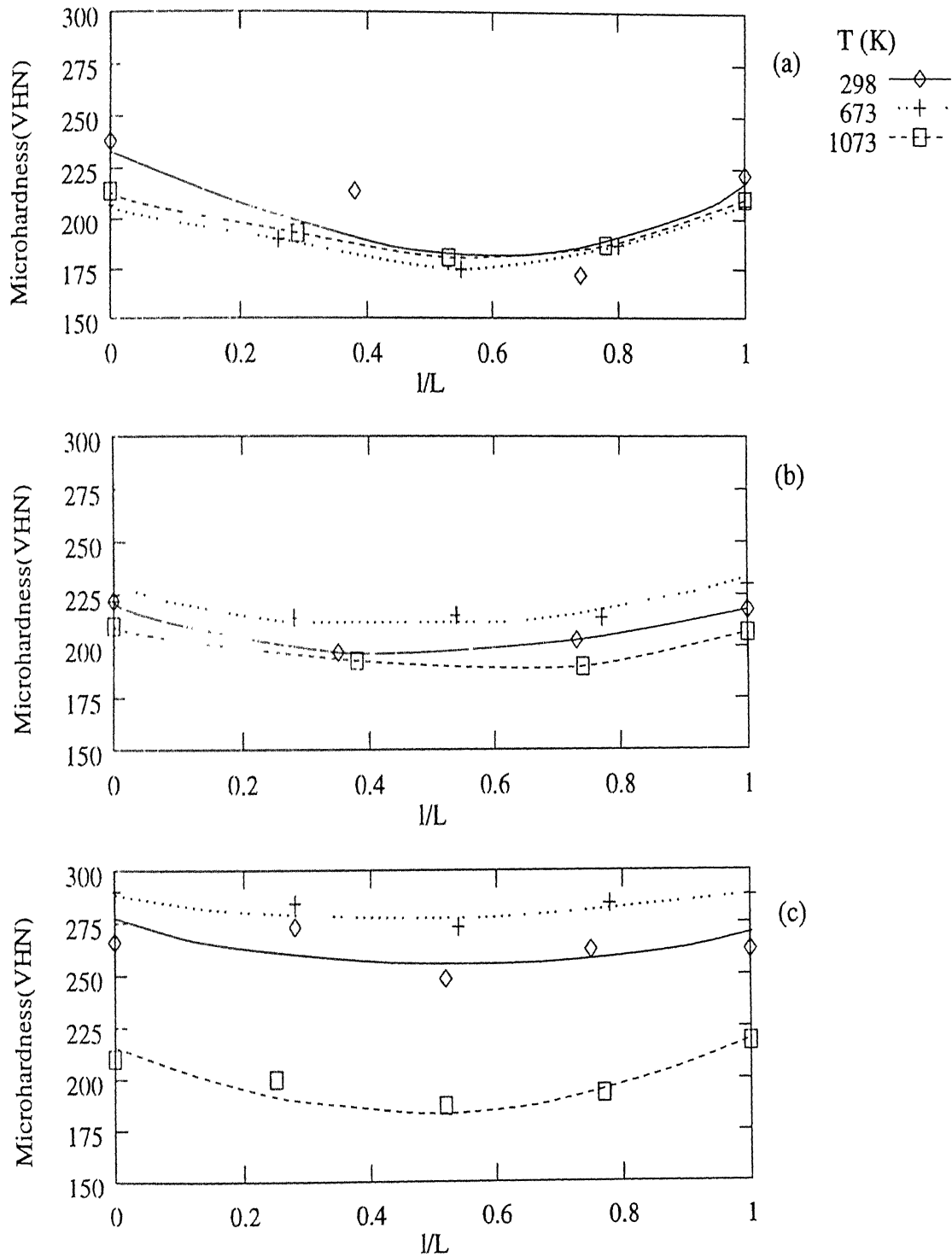


Figure 4.53: Variation of microhardness across grains ($d = 29 \mu m$) at different temperatures for strains: (a) 5 % , (b) 10 % and (c) 20 %.

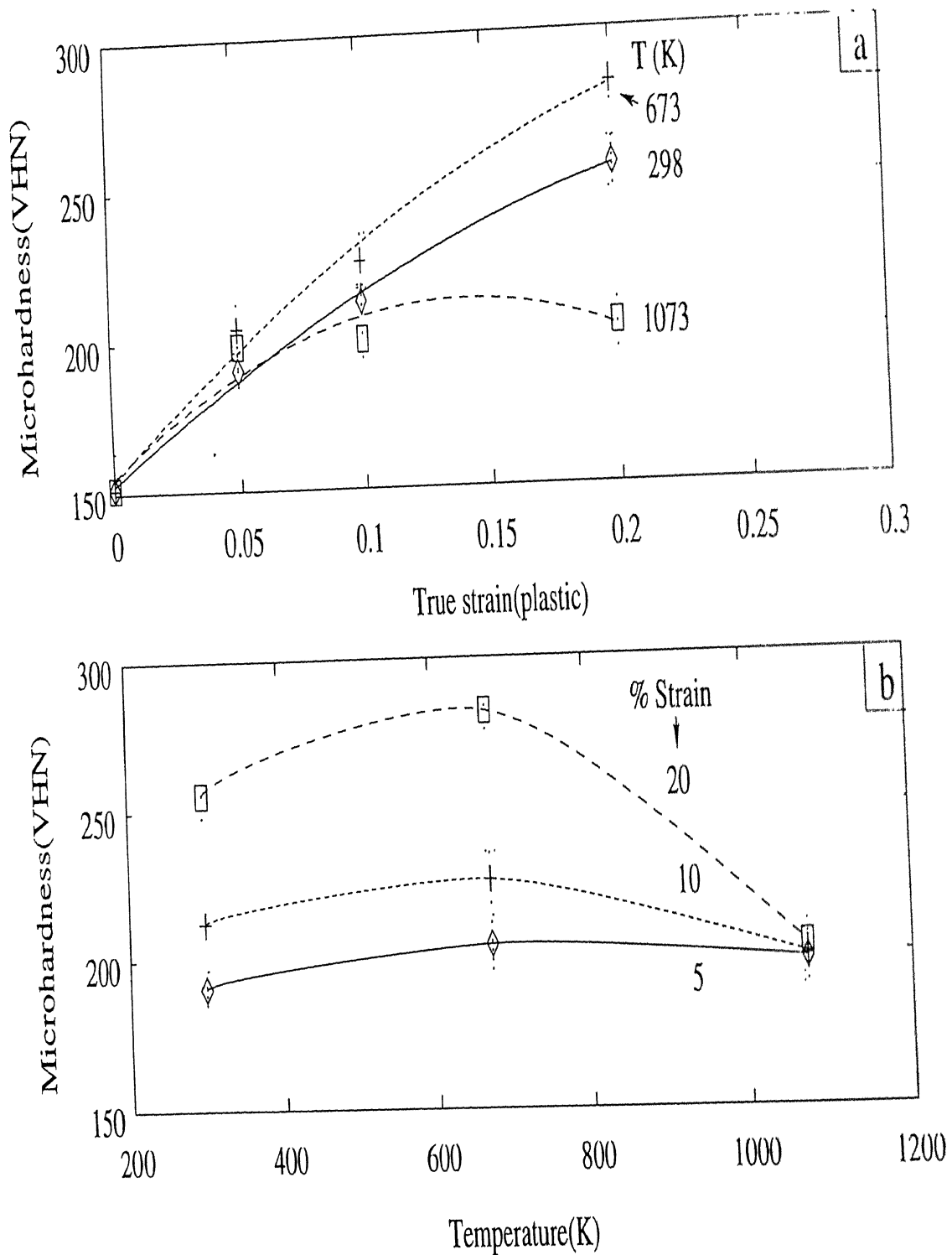


Figure 4.54: Variation of microhardness (a) with strain and (b) with temperature in the sample of 29.0 μm grain size.

4.4 Estimation of true dihedral angle (TDA) distribution

In a polycrystal the grain boundaries may have different values of energy, which may lead to the difference in distribution of TDA (angle between the grain boundary planes meeting at a common edge, known as triple edge). As discussed in chapter 2 (section 2.4) the TDA can be measured [6–8] in transmission electron microscope (TEM). However, it is very cumbersome and not practical to estimate the statistical distribution of TDA through TEM. In the practice of metallography, the dihedral angles are measured as plane dihedral angles (PDA) between the grain boundary segments meeting at a triple point. In a polycrystal, the triple edges are randomly oriented with respect to the plane of polish. Therefore, the distribution of plane dihedral angles (PDA) has two components: (1) variation in the TDA distribution and (2) statistical variation due to random orientation of the sectioning plane. The statistical variation (like random noise) tends to overshadow or hide the actual variation in the TDA distribution. Hence such a distribution of PDA cannot be directly used for the calculation of the relative energy of the grain boundaries. On the other hand, these surface measurements are relatively easy and it is possible to make a large number of measurements in a short time. Therefore, in the following sections, a transformation procedure is developed to unfold the distribution of true dihedral angles from the measured distribution of plane dihedral angles.

4.4.1 Relation between TDA and PDA

Figure 4.55 shows a randomly oriented triple edge sectioned by the plane of polish, P . The true dihedral angle between grain boundary planes A and B is α and the corresponding grain boundary segments a and b make a plane dihedral angle of β on the plane of polish as shown in figure 4.55. The triple edge is parallel to the Z -axis and the grain boundary plane A is in the XZ plane. The orientation of the plane of polish is described by the

orientation of the plane normal (denoted by \hat{n}) in terms of angles ϕ and θ in spherical co-ordinates. The unit vectors \hat{r}_1 and \hat{r}_2 are normal to the grain boundary planes A and B respectively. Let \vec{a} and \vec{b} be the vectors parallel to the grain boundary segments a and b respectively.

From figure 4.55, the vectors \hat{r}_1 , \hat{r}_2 and \hat{n} can be expressed as follows:

$$\hat{r}_1 = \hat{j} \quad (4.1)$$

$$\hat{r}_2 = -\sin\alpha \hat{i} + \cos\alpha \hat{j} \quad (4.2)$$

$$\hat{n} = \sin\theta \cos\phi \hat{i} + \sin\theta \sin\phi \hat{j} + \cos\theta \hat{k} \quad (4.3)$$

Since \vec{a} is the line of intersection of planes A and P , while \vec{b} is the line of intersection of the planes B and P , \vec{a} and \vec{b} can be represented by the following cross-products:

$$\vec{a} = \hat{r}_1 \times \hat{n} \quad (4.4)$$

and

$$\vec{b} = \hat{r}_2 \times \hat{n} \quad (4.5)$$

From equations 4.1 to 4.5, \vec{a} and \vec{b} may be expressed in the following form,

$$\vec{a} = \cos\theta \hat{i} - \sin\theta \cos\phi \hat{k} \quad (4.6)$$

and,

$$\vec{b} = \cos\alpha \cos\theta \hat{i} + \sin\alpha \cos\theta \hat{j} - \sin\theta \cos(\phi - \alpha) \hat{k} \quad (4.7)$$

β , the plane dihedral angle, can be expressed as:

$$\cos\beta = \frac{\vec{a} \cdot \vec{b}}{|\vec{a}| |\vec{b}|} \quad (4.8)$$

The terms in equation 4.8 can be obtained from equations 4.6, 4.7 and 4.8:

$$\vec{a} \cdot \vec{b} = (\cos\theta \hat{i} - \sin\theta \cos\phi \hat{k}) \cdot (\cos\alpha \cos\theta \hat{i} + \sin\alpha \cos\theta \hat{j} - \sin\theta \cos(\phi - \alpha) \hat{k})$$

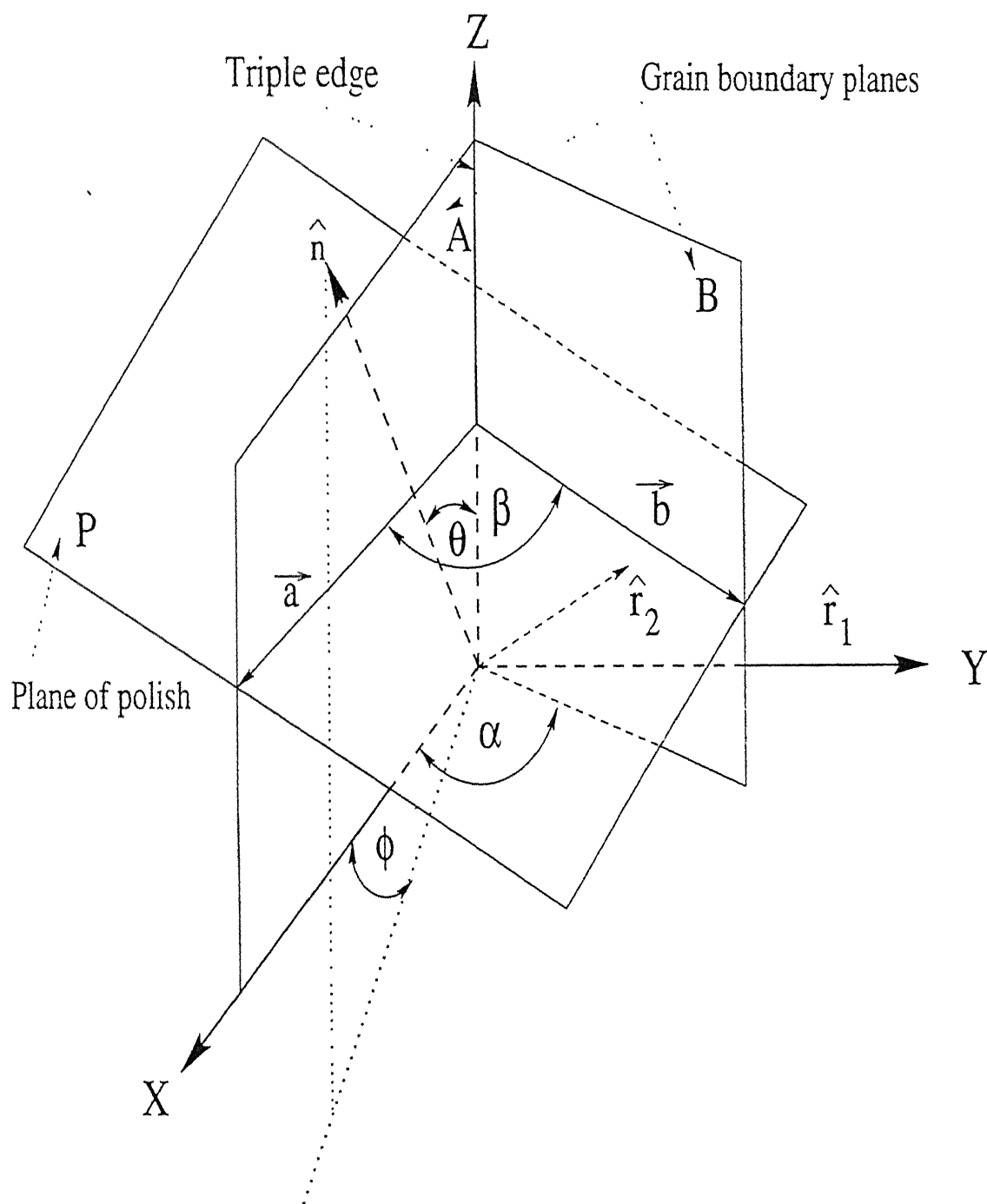


Figure 4.55 A random section through two grain boundary planes meeting at an angle of α . The normal to the plane of section makes an angle θ with the Z- axis and the projection of the normal on the XY- plane makes an angle ϕ with the X- axis. The line of intersection of grain boundaries on plane of polish makes an angle β .

or

$$\vec{a} \cdot \vec{b} = \cos^2\theta \cos\alpha + \sin^2\theta \cos\phi \cos(\phi - \alpha) \quad (4.9)$$

$$|\vec{a}| = \sqrt{\cos^2\theta + \sin^2\theta \cos^2\phi} = \sqrt{1 - \sin^2\theta \sin^2\phi} \quad (4.10)$$

$$|\vec{b}| = \sqrt{\cos^2\alpha \cos^2\theta + \sin^2\alpha \cos^2\theta + \sin^2\theta \cos^2(\phi - \alpha)} = \sqrt{1 - \sin^2\theta \sin^2(\phi - \alpha)} \quad (4.11)$$

Thus, from equations 4.8 to 4.11, the following expression can be obtained ²

$$\cos\beta = \frac{\cos^2\theta \cos\alpha + \sin^2\theta \cos\phi \cos(\phi - \alpha)}{\sqrt{(1 - \sin^2\theta \sin^2\phi)(1 - \sin^2\theta \sin^2(\phi - \alpha))}} \quad (4.12)$$

It is seen from equation 4.12 that if $\theta = 0^\circ$ then $\beta = \alpha$, as would be expected. However, for any given value of α , β can vary from 0° to 180° depending upon the orientation of the plane of polish.

4.4.2 Probability of intersection of a triple edge with plane of polish

In figure 4.56, the orientation of the normal to the plane of polish is given by θ and ϕ and the triple edge is kept parallel to Z-axis. By an appropriate transformation of axes, the normal to the intersection plane can be made parallel to the Z-axis. As a result the triple edge will now have an orientation given by θ and ϕ as shown in figure 4.56. This figure shows a triple edge of length l within a cube of unit dimensions and the sectioning plane (which is parallel to XY plane after the transformation of axes) can randomly cut the cube at any height. It is clear from this figure that the probability of cutting a triple edge is given by

$$P_1 = \frac{\text{projected length of triple edge on the Z-axis}}{\text{length of cube edge}} = l \cos\theta \quad (4.13)$$

²Equation 4.12 reduces to the relation reported (without derivation) by Harker and Parker [106] by changing the orientation of the axes to that taken by them

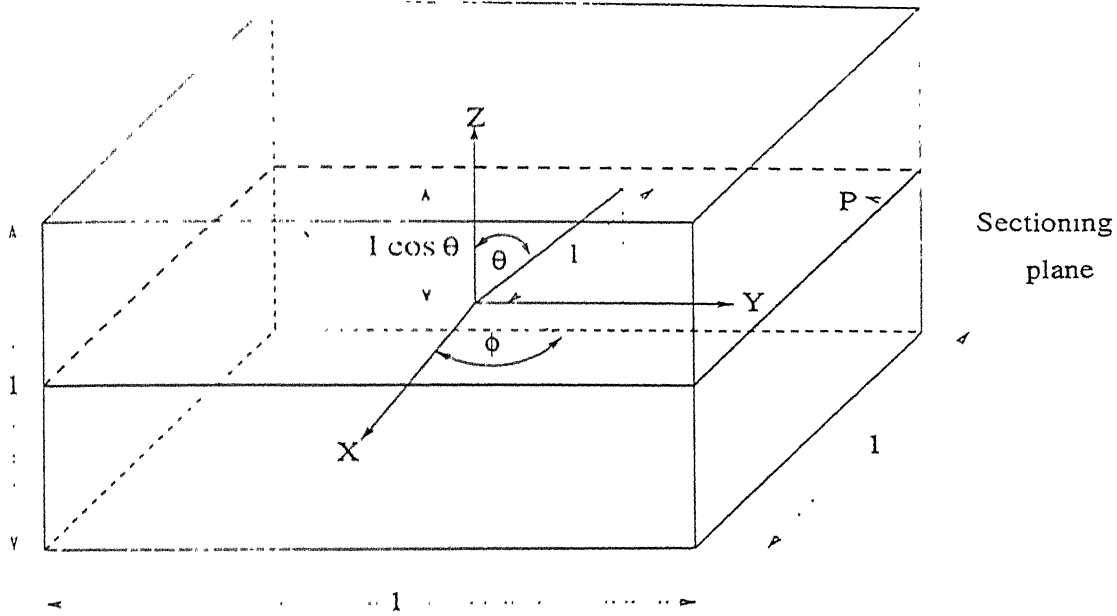


Figure 1.56: A triple edge in an unit cube and the sectioning plane is parallel to the XY -plane

It may be noted that the probability is independent of ϕ . This is because on changing ϕ the triple edge merely rotates about the Z -axis without altering the projected length. Since the triple edge can have any random orientation θ and ϕ , the average probability of intersection is given by

$$P_2 = \frac{\text{average projected length}}{\text{length of cube edge}} = \frac{l}{\pi/2} \int_0^{\pi/2} \cos \theta d\theta = \frac{2l}{\pi} \quad (4.14)$$

4.4.3 Distribution of plane dihedral angles when all the true dihedral angles are 120°

A distribution of plane dihedral angles, β , will now be obtained for the case when all the true dihedral angles are 120° (i.e., the ideal case). This arises due to the random orientations of the plane of polish with respect to the grain boundary planes. Probability

of a random orientation (θ and ϕ) is given by (see appendix B):

$$P(\theta, \phi) = \frac{\sin\theta d\phi d\theta}{4\pi} \quad (4.15)$$

where, $P(\theta, \phi)$ is the probability that the orientation lies in the range θ to $\theta + d\theta$ and ϕ to $\phi + d\phi$. ϕ varies from 0 to 2π and θ varies from 0 to π . The general technique of Monte-Carlo simulation was employed to determine the distribution. A description of the technique is given below.

A large number of plane dihedral angles were generated by simulating intersections between the plane of polish and randomly oriented triple edges. For this purpose the random orientations of θ and ϕ may be generated by using equation 4.15. On examining equation 4.15, it is clear that ϕ is uniformly distributed over the interval 0 to 2π . Now from equation 4.15, the probability of orientation (say γ) lying between 0 to θ and 0 to 2π may be expressed as:

$$\gamma = \frac{1}{4\pi} \int_0^\theta \int_0^{2\pi} \sin\theta d\phi d\theta \quad (4.16)$$

or,

$$\cos\theta = 1 - 2\gamma \quad (4.17)$$

Since γ is the probability of orientation which may vary from 0 to 1. It is clear from equation 4.17 that $\cos\theta$ is uniformly distributed over -1 to +1 (i.e., θ distributed over 0 to π). Let the plane dihedral angle distribution be divided into M classes of size interval $\Delta\beta$ over the angular range of 0 to π . Thus the distribution of plane dihedral angles were obtained by adopting the following procedure.

- (a) The orientation of plane of polish is randomly selected ($\theta = 0$ to π and $\phi = 0$ to 2π). A uniform random number between 0 to 2π is generated to obtain ϕ . Another uniform random number between -1 to +1 is generated to obtain $\cos\theta$.
- (b) To check whether the above selected orientation of plane of polish with respect to triple edge will intersect the selected triple edge or not. For this purpose, consider

unit volume in which triple edges of known length l are randomly oriented. Let the plane of polish, P bisect the unit volume as shown in figure 4.57.

Let the Z co-ordinate of one end of triple edge be q , which may randomly vary from 0 to 1 (see figure 4.57). The projected Z co-ordinate of second end of triple edge in Z direction will be, $r = q + l \cos \theta$, where θ has its usual meaning as mentioned above. The triple edge will be intersected by the plane of polish (which is located at a height of 0.5 unit):

1. if $q \leq 0.5$ and $r \geq 0.5$, or
2. $q \geq 0.5$ and $r \leq 0.5$.

(c) For a selected orientation of triple edge, which can be intersected by the plane of polish, PDA is calculated using equation 4.12.

(d) The computed PDA is added in the respective class

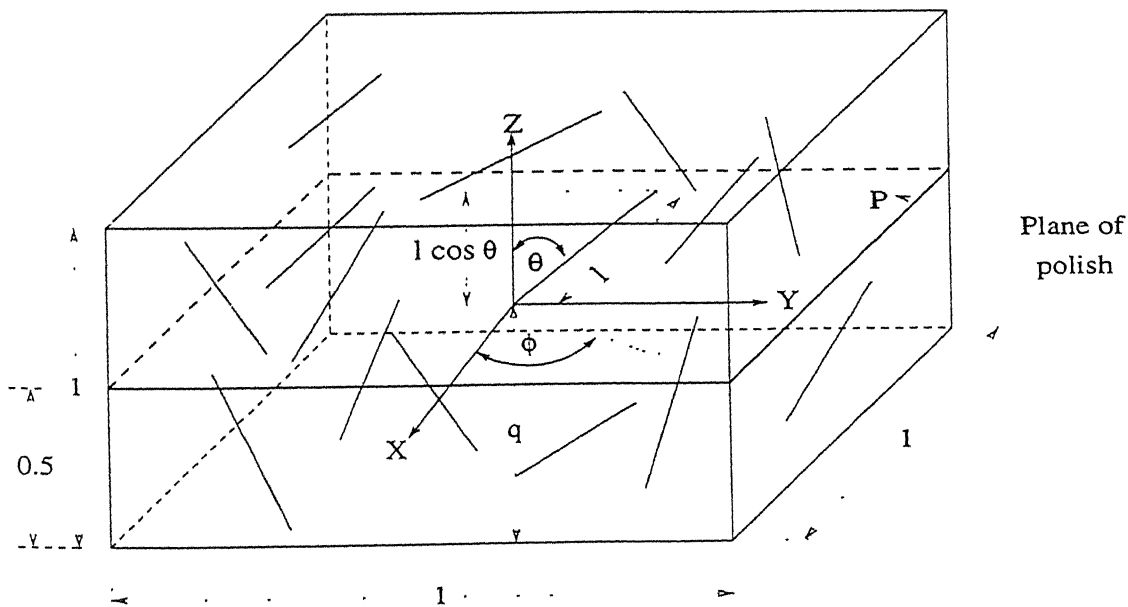


Figure 4.57: Randomly oriented triple edges in an unit cube and sectioning plane is parallel to the XY -plane.

- (e) Procedures (a) to (d) is repeated for at least 10,000 random orientations (θ , ϕ) and random positions (q) of the triple edges.
- (f) The relative frequency distribution of each class of PDA is obtained by dividing the number in each class with sum total of intersection of triple edges by the plane of polish.

For $M = 17$ ($\Delta Q = 10^\circ$), figure 4.58 shows the histogram of plane dihedral angle distribution obtained from the intersection of a polycrystal whose all the true dihedral angles are of 120° (ideal case). It is clear from figure 4.58 that the plane dihedral angles are distributed in the entire range from 0° to 180° . However, the relative frequency of 120° ($115^\circ - 125^\circ$) class of PDA distribution is maximum (0.362) and standard deviation of PDA distribution is 21.7.

The above analysis is not just limited to the ideal case (i.e., all the true dihedral angles are 120°) but it can easily be applied to obtain a distribution of plane dihedral angles from

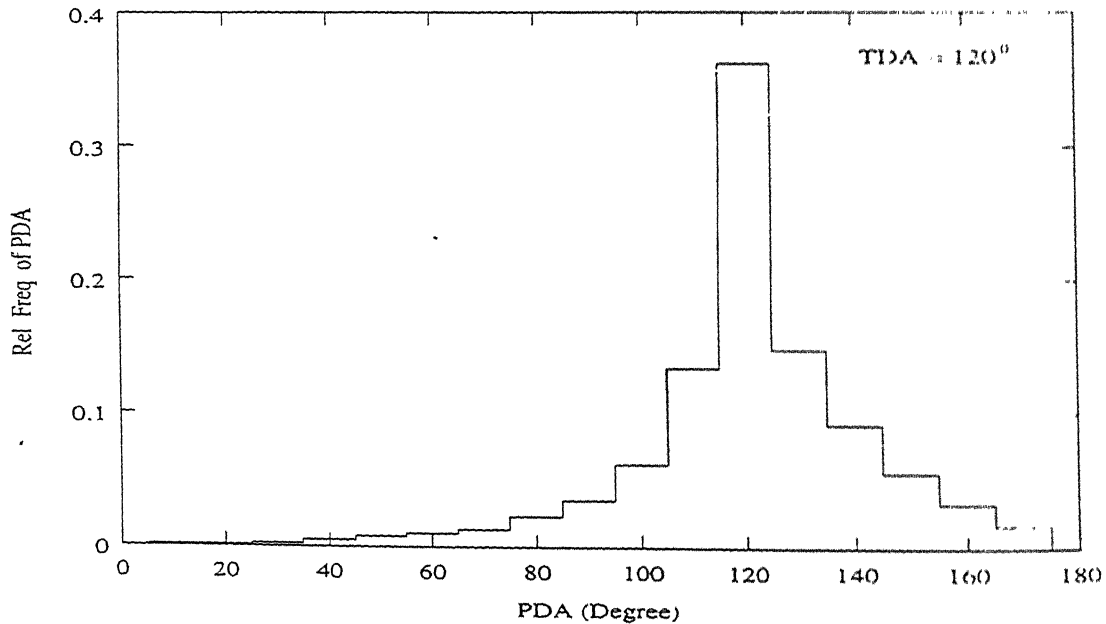


Figure 4.58: The distribution of PDAs for 120° TDA (ideal case).

any constant value of the true dihedral angle. For example, figure 4.59a and b show the histograms of PDA distribution obtained for 110° and 130° angles of TDA respectively.

It may be noted from the above histograms (figures 4.58 and 4.59a-b) that the plane dihedral angle class corresponding to the maximum relative frequency is same as the true dihedral angle. Table 4.12 shows the relative frequencies of a few classes of PDA distribution and standard deviation of PDA distribution for different values of TDA. The relative frequency of 120° class of PDA distribution decreases and subsequently the standard deviation of PDA distribution increases with decrease or increase in the TDA value from 120° as shown in table 4.12. It may also be observed that the relative frequencies of other classes (e.g., 110° or 130°) increases with increasing or decreasing value of TDA from 120° .

4.4.4 Distribution of plane dihedral angles obtained from a distribution of true dihedral angles

Table 4.12: Relative frequencies of different class of PDA distribution and standard deviation of PDA distribution, obtained from different values of TDA.

TDA (Degree)	Relative frequencies of PDA class							STD (PDA)
	90	100	110	120	130	140	150	
100	0.148	0.314	0.145	0.077	0.046	0.036	0.022	31.4
110	0.065	0.142	0.336	0.141	0.085	0.054	0.031	25.3
120	0.035	0.062	0.134	0.362	0.148	0.092	0.056	21.7
130	0.017	0.038	0.052	0.131	0.395	0.160	0.095	22.0
140	0.009	0.012	0.030	0.052	0.119	0.435	0.183	26.2

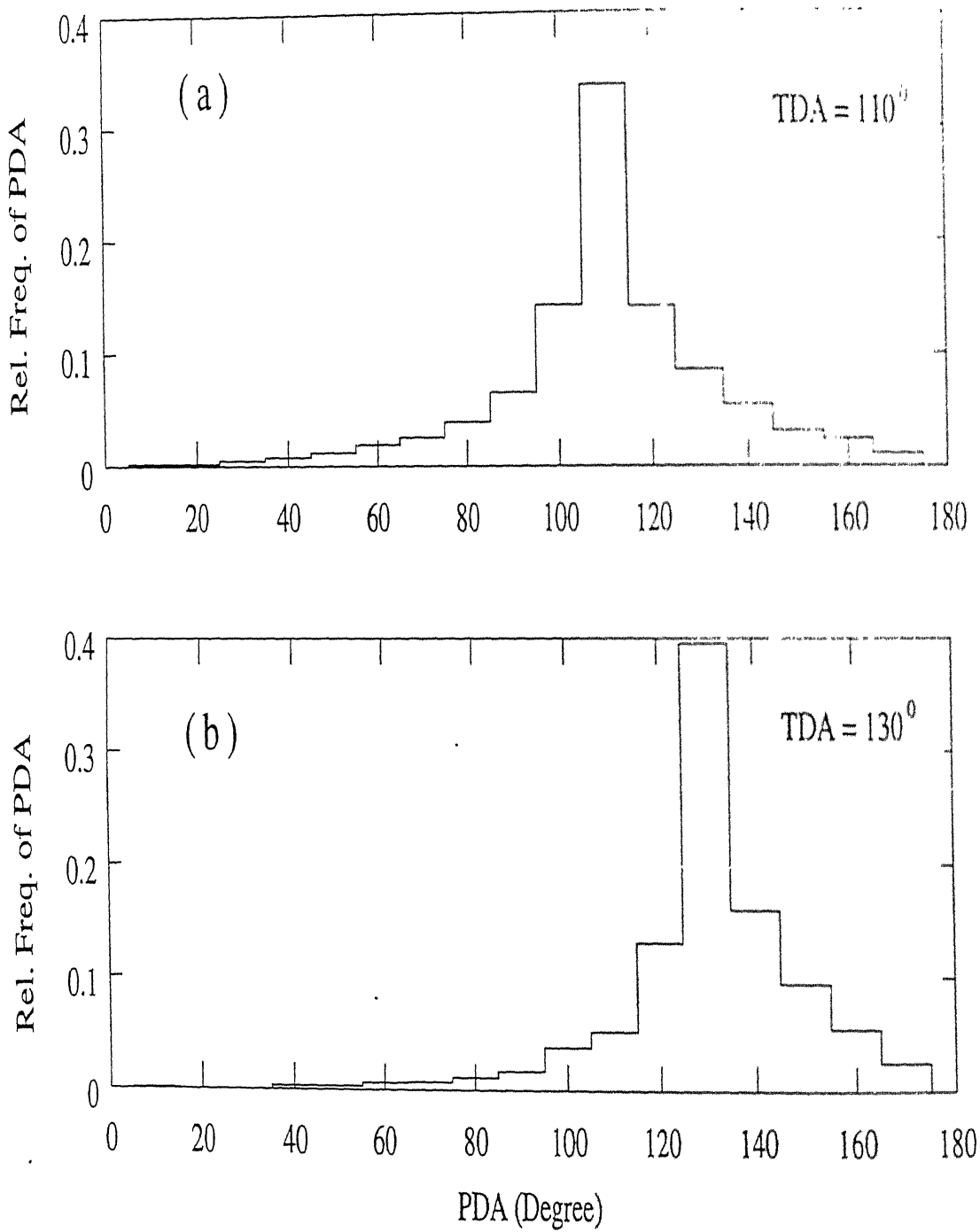


Figure 4.59: The distribution of PDA for TDAs: (a) 110° and (b) 130°.

In general the real polycrystals are likely to consist of a distribution of true dihedral angles. This distribution of true dihedral angles can be assumed to be subdivided into classes of small size intervals. Now each class considered independently, will generate a distribution of plane dihedral angles. The overall distribution of plane dihedral angles will then be the weighted sum of the individual distributions obtained from each class of true dihedral angles. The weights will be simply related to the numerical density (i.e., number per unit volume) of each true dihedral angle class.

Let the true dihedral angle distribution be divided into M classes of size interval $\Delta\alpha$ over the angular range 0 to π . Thus the j_{th} class covers an angular range of $(j-1)\Delta\alpha$ to $j\Delta\alpha$. N_{Vj} denotes the number per unit volume (or numerical density) of grain boundary plane pairs which make an angle between $(j-1)\Delta\alpha$ to $j\Delta\alpha$. Now consider the plane dihedral angle distribution to be also divided into M classes of size interval $\Delta\beta$ (where, $\Delta\beta = \Delta\alpha$) over the angular range of 0 to π . N_{Ai} denotes the number of grain boundary segment pairs, making an angle between $(i-1)\Delta\beta$ to $i\Delta\beta$, per unit area of the plane of polish. All the classes of true dihedral angles will contribute to each class of plane dihedral angles. Let $N_{A_{ij}}$ be the individual contribution to the i^{th} class of PDA from the j^{th} class of TDA. The individual contribution $N_{A_{ij}}$ can be expressed as:

$$N_{A_{ij}} = P_2 a_{ij} N_{Vj} \quad (4.18)$$

where, P_2 is the probability of cutting a triple edge (given by equation 4.14) and a_{ij} is the probability of obtaining the PDA in class (range: $(i-1)\Delta\beta$ to $i\Delta\beta$) from j_{th} class of true dihedral angle. P_2 is obtained from equation 4.14 by assuming an average triple edge length l . The coefficient a_{ij} is simply the frequency of the i_{th} class of PDA distribution obtained from the Monte-Carlo simulation procedure discussed in the previous section. The computer programme used for the calculation of coefficients a_{ij} is presented in appendix C. In this computer programme a NAG library routine is used to generate the random orientation and random value of true dihedral angle from a selected class. Substituting P_2 from equation 4.14 in equation 4.18, the total number of grain boundary segment pairs per unit area, N_{Ai} , can be expressed as the sum of the contribution from

all the true dihedral angle classes:

$$N_{A_i} = \sum_{j=1}^M N_{A_{ij}} = \frac{2l}{\pi} \sum_{j=1}^M a_{ij} N_V; \quad (4.19)$$

By dividing both sides in equation 4.19 with $\sum_{k=1}^M N_{A_k}$ (i.e., total number of grain boundary segment pairs at triple points per unit area, N_A).

$$y_i = \frac{2l}{\pi} \sum_{j=1}^M a_{ij} \frac{N_{V_j}}{\sum_{k=1}^M N_{A_k}} = \frac{N_{A_i}}{\sum_{k=1}^M N_{A_k}} \quad (4.20)$$

where y_i is the relative frequency (probability) of i^{th} class of PDA. Since the total number of grain boundary segment pairs per unit area of plane of polish will be equal to the product of P_2 and the total number of the grain boundary plane pairs at triple edge (N_V). It can be expressed as:

$$N_A = \sum_{k=1}^M N_{A_k} = \frac{2l}{\pi} N_V \quad (4.21)$$

Thus from equations 4.20 and 4.21, the relative frequency of i^{th} class of plane dihedral angle may be expressed as follows:

$$\sum_{j=1}^M a_{ij} x_j = y_i \quad (4.22)$$

where x_j is the relative frequency of j^{th} class of TDA in polycrystal. Equation 4.22 results M linear simultaneous equations for i and j varying from 1 to M , with M unknown relative frequencies of TDA ($x_1, x_2, x_3, \dots, x_M$), as follows:

$$a_{11}x_1 + a_{12}x_2 + a_{13}x_3 + \dots + a_{1M}x_M = y_1$$

$$a_{21}x_1 + a_{22}x_2 + a_{23}x_3 + \dots + a_{2M}x_M = y_2$$

$$a_{M1}x_1 + a_{M2}x_2 + a_{M3}x_3 + \dots + a_{MM}x_M = y_M$$

4.4.5 Transformation of plane dihedral angle distribution to true dihedral angle distribution

The above M linear equations with M unknowns can easily be solved by using standard numerical methods. Using the Monte-Carlo procedure outlined in section 4.4.3, tables of coefficients, a_{ij} , can be generated for given values of class widths of TDA and PDA distributions. Such tables can be used directly for the calculation of TDA distribution. Table 4.13 is such table which includes the computed values of a_{ij} for $i = j = 17$ and is used in the present investigation to unfold the TDA distribution from the measured distribution of PDA. In table 4.13, the first and the last classes of TDA and PDA have class width of 15° , while rest of the other classes have class width of 10° . The columns in the table gives the relative frequencies (i.e., a_{ij}) of the PDA distribution for a given value of TDA.

The Gauss elimination method was applied to solve for the unknowns x_j (i.e., frequencies of TDA distribution) in the above linear simultaneous equations 4.22 for a given (or measured) distribution of PDA. It was observed in many cases that a few values of the relative frequencies of TDA (x_j) were negative. In context of the relative frequencies, negative x_j has no physical significance. The negative values are observed mainly in those cases of TDA class, in which the actual values of the relative frequencies are close to zero, as shown in table 4.14 for $M = 17$. Table 4.14 shows the true dihedral angle distribution from the distribution of plane dihedral angles measured on the plane of polish for 316L austenitic stainless steel annealed at temperature of 950°C for 35 minutes. The PDAs were measured manually from the micrograph, which may lead to some error in PDAs and may be responsible for observed negative values of TDA frequencies by Gauss elimination method.

In order to eliminate the above problem, equations 4.22 were solved by using an optimization technique [107, 108] with the constraint that all the relative frequencies of TDA

must be greater than or equal to zero. Let us assume the measurement error in y_i is Δ_i , then the equation 4.22 in appropriate form may be written as follows

$$\sum_{j=1}^M a_{ij} x_j = y_i + \Delta_i \quad (4.23)$$

or,

$$\Delta_i = \sum_{j=1}^M a_{ij} x_j - y_i \quad (4.24)$$

Δ_i may be positive or negative depending upon the error in measurements of PDAs. The total sum of square of Δ_i ($i=1$ to M) can be expressed as a function F as:

$$F = \sum_{i=1}^M \Delta_i^2 \quad (4.25)$$

or,

$$F = \sum_{i=1}^M \left(\sum_{j=1}^M a_{ij} x_j - y_i \right)^2 \quad (4.26)$$

Equation 4.26 was solved by minimising F under the constraints that all $x_j \geq 0$.

In the present investigation, NAG library routine was used for the optimization (the method is briefly presented in appendix C). The programme, presented in appendix D, uses the quasi-Newton algorithm for finding a minimum of a function $F(x_1, x_2, \dots, x_M)$, subject to bounds on the independent variables x_1, x_2, \dots, x_M , using function values only.

For a measured PDA distribution of annealed samples of 316L austenitic stainless steel (second column of table 4.14), the above optimization programme calculated the distribution of TDA (see fourth column of table 4.14). The TDA distribution obtained by this method has no negative values. Therefore, the above optimization method can be used to estimate the distribution of TDA in polycrystal from the corresponding measured distribution of PDA. The relative energy distribution of the grain boundaries can also be assessed from the estimated distribution of TDA.

Table 4.13: Computed values of the coefficients a_{ij} .

PDA distribution(a_{ij}) for different value of TDA																	
PDA	10	20	30	40	50	60	70	80	90	100	110	120	130	140	150	160	170
0-15	.91	.26	.09	.05	.02	.01	.01	.01	.00	.00	.00	.00	.00	.00	.00	.00	.00
15-25	.08	.55	.25	.11	.05	.03	.02	.01	.01	.01	.00	.00	.00	.00	.00	.00	.00
25-35	.01	.13	.42	.20	.10	.07	.03	.03	.01	.01	.00	.01	.00	.00	.00	.00	.00
35-45	.00	.03	.14	.37	.20	.10	.06	.03	.02	.01	.01	.00	.00	.00	.00	.00	.00
45-55	.00	.01	.05	.14	.35	.18	.08	.05	.03	.02	.01	.00	.00	.00	.00	.00	.00
55-65	.00	.01	.02	.06	.14	.32	.15	.08	.04	.03	.01	.01	.01	.00	.00	.00	.00
65-75	.00	.00	.01	.03	.05	.13	.32	.16	.09	.05	.03	.01	.01	.00	.00	.00	.00
75-85	.00	.00	.01	.01	.03	.06	.14	.31	.14	.07	.05	.02	.01	.01	.00	.00	.00
85-95	.00	.00	.00	.01	.01	.04	.07	.14	.29	.14	.06	.04	.02	.01	.00	.00	.00
95-105	.00	.00	.00	.01	.01	.03	.03	.07	.15	.29	.15	.06	.03	.02	.01	.00	.00
105-115	.00	.00	.00	.00	.01	.01	.03	.04	.08	.15	.31	.13	.05	.02	.01	.00	.00
115-125	.00	.00	.00	.00	.00	.01	.02	.03	.04	.09	.16	.33	.14	.06	.02	.00	.00
125-135	.00	.00	.00	.00	.01	.01	.01	.02	.03	.05	.09	.18	.36	.14	.05	.01	.00
135-145	.00	.00	.00	.00	.00	.01	.01	.01	.03	.04	.06	.08	.18	.40	.13	.03	.00
145-155	.00	.00	.00	.00	.00	.00	.01	.01	.01	.02	.03	.06	.10	.21	.45	.13	.01
155-165	.00	.00	.00	.00	.00	.00	.00	.00	.01	.01	.02	.03	.05	.09	.21	.56	.06
165-180	.00	.00	.00	.00	.00	.00	.00	.00	.00	.01	.01	.01	.03	.04	.10	.26	.92

Table 4 14: Relative frequencies of measured PDA distribution and calculated TDA distribution by Gauss elimination and optimisation methods of 316L austenitic stainless steel sample annealed at 950°C and 35 Minutes.

Angles (Degree)	Relative frequencies of		
	measured PDA	calculated TDA	
		By Gauss elimination method	By Optimisation method
0-15	.000	.001	.000
15-25	.000	-.001	.000
25-35	.000	-.001	.000
35-45	.000	-.001	.000
45-55	.000	-.003	.000
55-65	.003	-.021	.000
65-75	.010	.016	.000
75-85	.010	-.054	.000
85-95	.030	-.087	.000
95-105	.110	.152	.000
105-115	.183	.274	.285
115-125	.270	.583	.572
125-135	.197	.157	.143
135-145	.113	.066	.000
145-155	.043	-.064	.000
155-165	.023	-.009	.000
165-180	.007	-.003	.000

Chapter 5

Discussion

In the previous chapter the experimental results on the plastic deformation behaviour of 316L austenitic stainless steel over a wide range of grain size (2.7 to 64 μm) and temperature (room temperature to 800 $^{\circ}\text{C}$) were presented. As already mentioned the 316L austenitic stainless steel was obtained from two different sources (referred to as batch 1 and batch 2) for this study. The principal aim of the present study was to analyse the effect of grain size and other microstructural parameters on the tensile flow stress (especially Hall-Petch behaviour) over a wide temperature range. The microstructural parameters other than grain size include the grain size and shape distribution, and the distribution of true dihedral angles (TDA). The flow stress dependence on temperature is discussed in the context of extrinsic grain boundary dislocations (EGBDs) by establishing a semi-quantitative model. Further, the applicability of strain hardening laws in the tensile deformation behaviour of 316L stainless steel was analysed. Accordingly this chapter is divided into four different sections. The first two sections deal with the plastic deformation behaviour at room and elevated temperatures, respectively. The third section establishes a semi-quantitative model of density of EGBDs during deformation to study the variation of flow stress with temperature. The fourth and last section examines the applicability of strain hardening laws in modeling the deformation behaviour.

5.1 Deformation at room temperature

5.1.1 Hall-Petch behaviour

The results of this study on the Hall-Petch behaviour (for batch 1) show two distinctly different linear regions at all strains (see figure 4.15). It is clear from figure 4.15 that one linear region is in the fine grain size range ($d \leq 6 \mu\text{m}$) and the second region is in the coarse grain size range ($d \geq 6 \mu\text{m}$). The values of Hall-Petch intercept $\sigma_0(\epsilon)$ and slope $K(\epsilon)$ for both the fine and the coarse grain regions are listed in table 4.3. It is seen that the Hall-Petch parameter $K(\epsilon)$ is significantly higher in the fine grain regime compared to that of the coarse grain regime at all strains. On the other hand, $\sigma_0(\epsilon)$ is negative in the fine grain regime. Since there is no physical significance of negative $\sigma_0(\epsilon)$, it appears that the Hall-Petch relation (equation 2.18) is not valid in the fine grain regime. As mentioned in the previous chapter, the fine grain regime can be characterised in terms of the flow stress versus inverse of grain size relation (equation 2.34). The values of the parameters $\sigma_0(\epsilon)$ and $K(\epsilon)$ (in equation 2.34) thus obtained from figure 4.17 are shown in table 4.3. It may be noted that the intercept $\sigma_0(\epsilon)$ is positive and $K(\epsilon)$ is much lower than that observed in the Hall-Petch relation. The physical significance of the two parameters of equation 2.34 vis-a-vis the parameters of the composite relation will be discussed later. An analysis of the goodness of fit, using the correlation coefficient for different powers of d by regression analysis presented in tables 4.4 show that the Hall-Petch model (σ vs $d^{-1/2}$) is valid in the coarse grain regime and the composite model (σ vs d^{-1}) is appropriate in the fine grain regime of batch 1.

The distinctly different behaviour in the two regimes of grain size may arise from different thermo-mechanical treatments employed to obtain various grain sizes. As table 4.1 shows, the fine grain sizes were obtained by annealing the cold rolled (92%) samples at temperatures below 900°C and the coarse grain sizes were obtained by annealing the cold rolled samples at or above 900°C . These thermo-mechanical treatments may pro-

duce differences in the annealed microstructures (such as, high energy grain boundaries) of various samples. Such differences could be evaluated by experimental measurement of certain microstructural parameters other than grain size, as discussed in chapter 2 (section 2.3.3). The parameters used to characterise the microstructures of annealed samples are grain size, grain size and shape distribution and distribution of true dihedral angles (TDA). From the results of microstructural characterisation of annealed samples presented in previous chapter, the following observations can be reiterated.

- The normalised relative and cumulative frequency plots (figures 4.7 through 4.9) show no significant difference in the grain size distribution in the two linear regions. The figures also depict no significant difference in the grain size distribution of batch 1 and batch 2 samples.
- The average grain shape factor (S_F) and the average grain aspect ratio (AR) remain more or less unaltered in the entire grain size range for both the batches as shown in figure 4.10c and table 4.2 respectively. These results indicate that the grain shape distribution is nearly same in the annealed samples of the two batches.
- The relative frequency of 120° class of the plane dihedral angle distribution shows a decrease with decreasing grain size in the fine grain regime of batch 1, while in the coarse grain regime it remains nearly constant with grain size (figure 4.10b). Correspondingly the standard deviation of plane dihedral angles also increases with decreasing grain size in the fine grain regime and remains nearly constant in the coarse grain regime as shown in figure 4.10a. For further analysis the true dihedral angle (TDA) distribution has been calculated from the measured plane dihedral angle (PDA) distribution for different annealed grain sizes using the methodology presented in chapter 4, section 4.4. The results of the analysis are shown in figure 5.1. The standard deviation of true dihedral angles was also calculated for different grain sizes and are presented in figure 5.2a. The relative frequencies of different classes of TDA are shown in figures 5.2b-d. The estimated TDA distribution shows

a significant difference in the fine and the coarse grain regimes of batch 1 (figure 5.1a-b). The standard deviation of TDA increases with decreasing grain size in the fine grain region of batch 1, whereas the standard deviation of TDA in the coarse grain region is more or less constant (figure 5.2a). The relative frequency of $120^\circ(115-125^\circ)$ class of TDA decreases while that of other classes of TDA such as, $110^\circ(105-115^\circ)$ and $130^\circ(125-135^\circ)$ increases with decreasing grain size in the fine grain regime. In the coarse grain regime there is no substantial change observed in the relative frequencies of different classes of TDA with decreasing grain size (figure 5.2b-d). In batch 2, the TDA distributions remain nearly same in the entire range of grain size as shown in figures 5.1c-d and 5.2a-d. On comparing PDA and TDA distribution, it is clear that the changes in the TDA distribution is much more significant.

As discussed in chapter 2, with increasing coefficient of variation of grain size i.e., the spread of grain sizes, the surface area of grain boundaries per unit volume increases. This increase in surface area of grain boundaries per unit volume can result in a higher flow stress at a given strain [78]. But the present results as discussed above show no significant difference in the grain size and shape distributions in the entire range of grain sizes studied. Therefore the significantly different Hall-Petch behaviour in the fine and the coarse grain regimes cannot be explained simply on the basis of grain size and shape distributions. However, the above differences in the Hall- Petch behaviour may be explained on the basis of variation of TDA distribution in the two regimes of grain sizes.

At equilibrium all the three grain boundaries meeting at a triple edge have same energies. This state results in the equal values of all the three TDAs (i.e., 120°) at a triple edge. As the equilibrium state is approached the standard deviation of TDA tends towards zero and the relative frequency of 120° class of TDA approaches the value of 1.0. The present results show higher standard deviation of TDA distribution and lower relative frequency of 120° class of TDA in the fine grain regime of batch 1 as compared to

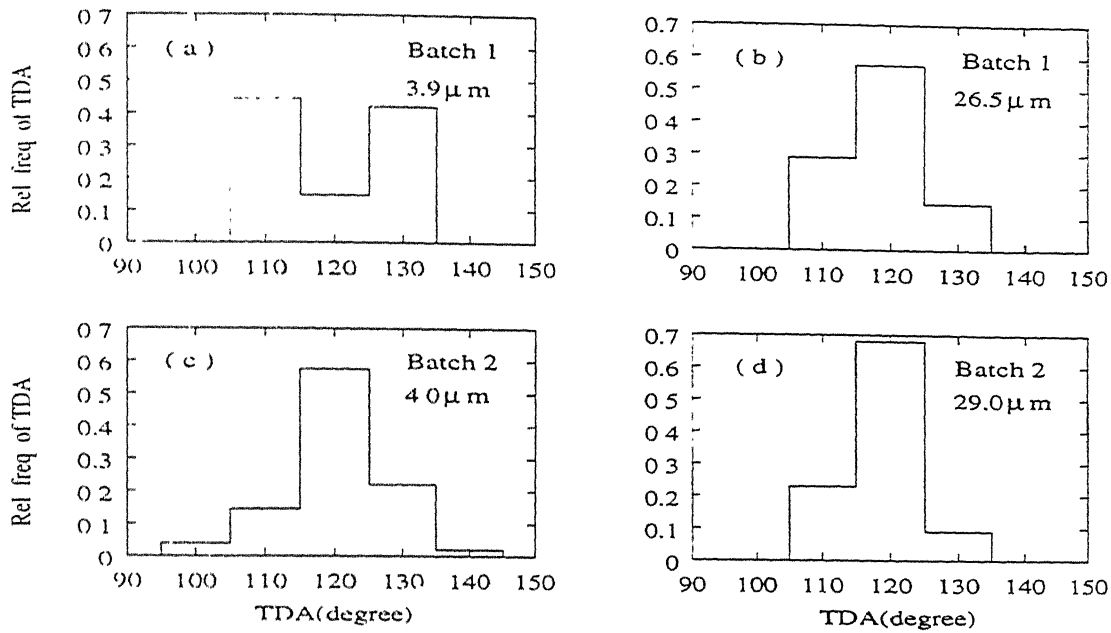


Figure 5.1: Distribution of TDAs, in annealed samples of batch 1 with grain sizes (a) 3.9 μm and (b) 26.5 μm and in annealed samples of batch 2 with grain sizes (c) 4.0 μm and (d) 29.0 μm .

the coarse grain regime. This illustrates the higher energy or non-equilibrium state of grain boundaries in the fine grain regime as compared to the coarse grain regime. As discussed in chapter 4 (section 4.4), the higher energy state of grain boundaries (more non-equilibrium boundaries) corresponds to higher stress field. This stress field arises due to the presence of high density of extrinsic grain boundary dislocations (EGBDs). These EGBDs accumulate during the process of grain growth. Due to the lower annealing temperature employed to get the fine grain sizes, these EGBDs are unable to annihilate. On the other hand, the higher annealing temperature employed to produce the coarse grain sizes leads to the annihilation of EGBDs and hence equilibrium grain boundaries. The annealing behaviour will be discussed later in more detail.

The region of high stress field near the grain boundaries can be considered as a hard mantle zone due to the presence of high density of EGBDs and lattice dislocations in the vicinity of grain boundaries [13,14]. In the coarse grain regime, the grain boundaries

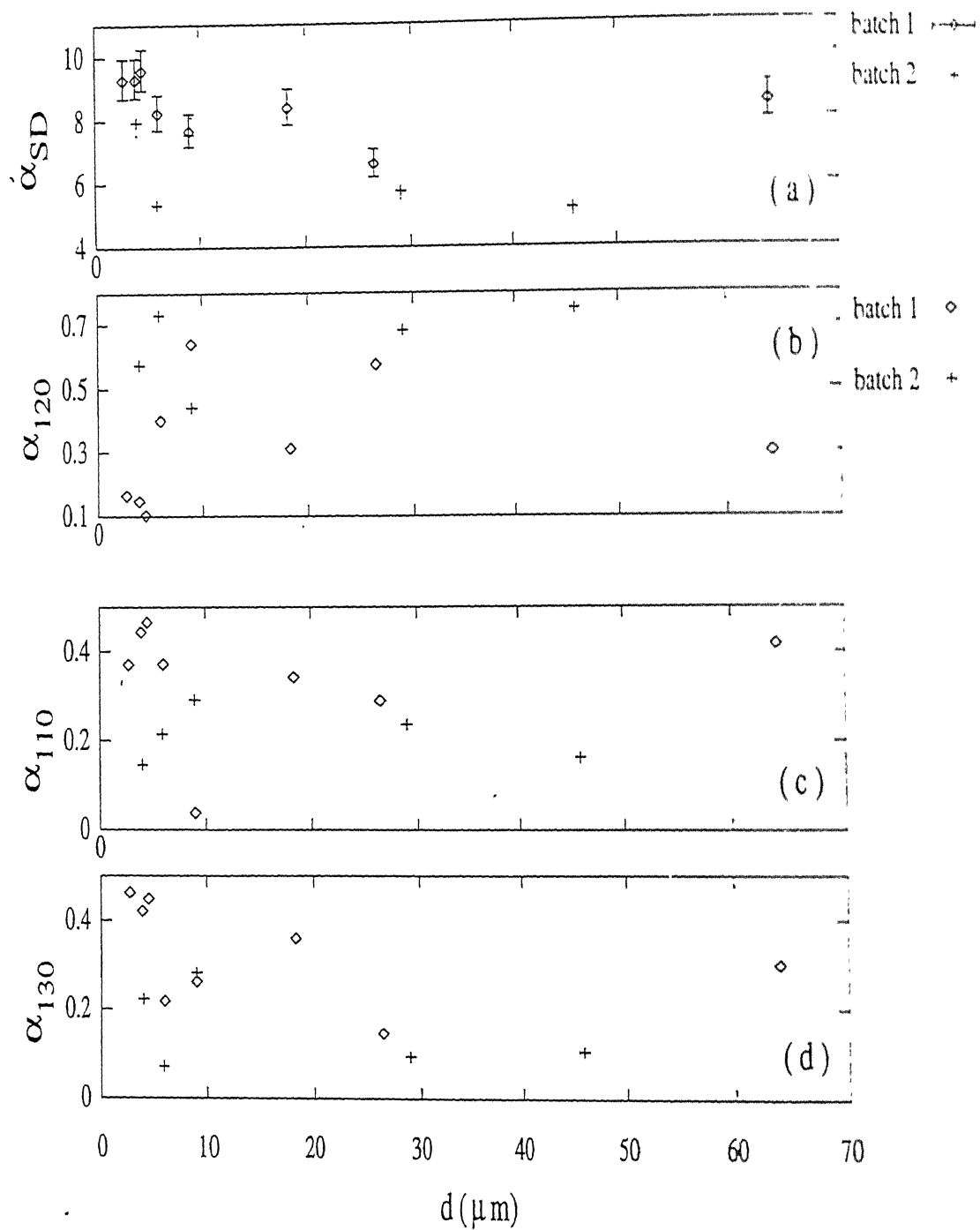


Figure 5.2: Variation of different parameters of TDA distribution: (a) standard deviation (b) relative frequency of 120° class (c) relative frequency of 110° class and (d) relative frequency of 130° class with grain size.

are in equilibrium state (low standard deviation of TDA and higher relative frequency of 120° class of TDA), and hence no mantle zone is expected to develop. Sangal *et al.* [78] also reported a higher standard deviation of plane dihedral angles (PDA) in the fine grain regime than the coarse grain regime. As already discussed in chapter 4 (section 4.4), the PDA distribution has two components: (1) variation in the TDA distribution and (2) statistical variation due to random orientation of the sectioning plane. The statistical variation (like random noise) tends to overshadow or hide the actual variation in the TDA. In the present investigation a mathematical method was developed (presented in chapter 4, section 4.4) and was used to transform the PDA distribution to TDA distribution. In this process the statistical component was eliminated. Therefore, the differences in the TDA distribution as a function of grain size are much more significant than in the case of PDA distribution.

The grain growth rate appears to be very sluggish below 900°C as depicted in figures 4.3 and 4.4. These figures also indicate an abrupt increase in grain growth rate at or above 900°C . During grain growth, the migrating grain boundaries sweep up the lattice dislocations in their vicinity. These dislocations are termed as extrinsic grain boundary dislocations (EGBDs). As discussed above, the presence of high density of EGBDs results in higher energy i.e., non-equilibrium grain boundaries. For annihilation of these EGBDs high thermal energy is required to facilitate the high temperature processes such as cross-slip and climb. Lower temperature annealing will not be able to provide sufficient thermal energy for annihilation of EGBDs by these processes. Since lattice (or bulk) diffusion is required for the equilibration of grain boundaries [86, 89], the kinetics of equilibration is relatively slow at lower temperatures. Thus, different grain boundary segments may be at varying stages of equilibration, leading to a distribution of grain boundary energy levels. Therefore, at a triple edge the three grain boundaries may not possess the same energy (as would be expected if all of them had been equilibrated). Consequently the angles between grain boundary segments will not be 120° (see chapter 4, section 4.4).

As discussed above the coarse grain sizes were obtained by thermal treatment at or

above 900°C where the grain growth rates are very high compared to those observed at annealing temperatures below 900°C . The rapid grain growth rate suggests that the process of reduction in the energy of grain boundaries is faster in this regime of grain size as compared to those in the fine grain regime. Above 900°C , the faster diffusion reduces the grain boundary energy by annihilation of EGBDs. These equilibrated grain boundaries result in a lower standard deviation of TDA and higher relative frequency of ideal 120° class as discussed above. Hence the samples with the coarse grain size may be considered to be free from the mantle zone unlike the case of samples with fine grain size.

Accordingly the fine grained microstructures may be considered as having two phases: a hard phase (mantle zone) in the vicinity of grain boundaries and a soft phase (grain interior). Kocks composite model is more appropriate for this type of structure rather than the Hall-Petch model. This model (as discussed in chapter 2, section 2.3) considers each grain as consisting of a grain boundary rim (with a volume fraction v_g and a flow stress σ_g) and a grain interior (with a volume fraction v_i and a flow stress σ_i). Considering the force equilibrium over the whole grain, Kocks [35] derived the σ vs $d^{-1/2}$ relation (equation 2.34). The intercepts of the plots based on equation 2.34 at all strains are positive for samples of batch 1 in the fine grain regime. The goodness of fit using correlation coefficients of these plots are also comparable with those found in the Hall-Petch plots (see table 4.3). The intercept and slope of these plots can be expressed as:

$$\sigma_0 = \sigma_i \quad (5.1)$$

and,

$$K = 4x(\sigma_g - \sigma_i) \quad (5.2)$$

The different terms in the above equations have been already defined in chapter 2, section 2.3.

$\sigma_0(\epsilon)$ obtained from the σ vs $d^{-1/2}$ plots in the fine grain regime (132 MPa at yield stress) is close to the value obtained in the coarse grain regime by Hall-Petch plots (164 MPa at yield stress). However, the values of $K(\epsilon)$ in the fine grain regime (1730 MPa μm at yield

stress by composite plot) is much higher than those observed in the coarse grain region (622 MPa $\mu m^{1/2}$ at yield stress by Hall-Petch plot). Kashyap *et al.* [41] also observed two linear regions in the Hall-Petch plots in 316L austenitic stainless steel. Kashyap *et al.* [41] calculated the average values of $\sigma_0(\epsilon)$ and $K(\epsilon)$ by fitting a single regression line over the entire range of grain size at all strains. However they observed bi-linear Hall-Petch plots up to 5 % strain levels at room temperature and up to 2 % strains at higher temperatures. Their data was analysed in the present work by considering two regimes of grain sizes at different temperatures and strain levels. The results of the analysis is shown in figure 5.3a. $\sigma_0(\epsilon)$ was found to be small (59 MPa at yield stress) at room temperature and negative (-45 MPa at yield stress) at a higher temperature (400 °C). Thus it appears that the negative Hall-Petch intercept in the fine grain regime is not uncommon. The application of Kocks composite model (equation 2.34) in the fine grain regime of the data of Kashyap *et al.* [41] is shown in as a plot of σ versus d^{-1} in figure 5.3b. This figure shows the $\sigma_0(\epsilon)$ value of 177 MPa (at yield point) is comparable to the Hall-Petch intercept in the coarse grain regime of 200 MPa (at yield point). Thus by applying the Hall-Petch model in the coarse grain regime and the composite model in the fine grain regime, a more or less same value of $\sigma_0(\epsilon)$ is obtained. Since $\sigma_0(\epsilon)$ represents the flow stress in the grain interior, this appears to be reasonable. However, the $K(\epsilon)$ value at a given strain remains higher in the fine grain regime than the coarse grain regime.

The microhardness data across grains of annealed samples in the coarse grain regime (see figure 4.25a-b) shows no significant difference between the grain boundary and grain interior regions. This observation suggests that the coarse grains are free from hard mantle zone and the grain boundaries are in an equilibrium state. The minimum diagonal size of indentation by microhardness tester in this material was observed to be of 5-6 μm . Therefore it was not possible to measure the hardness variation across grains in the fine grain regime ($d \leq 6 \mu$). However, figure 4.2 shows significant differences in the average hardness of two regimes of grain sizes. The hardness remains more or less constant in the coarse grain regime (annealed at or above 900 °C), whereas it abruptly increases in the fine grain regime (annealed at temperatures below 900 °C) with decreasing grain size.

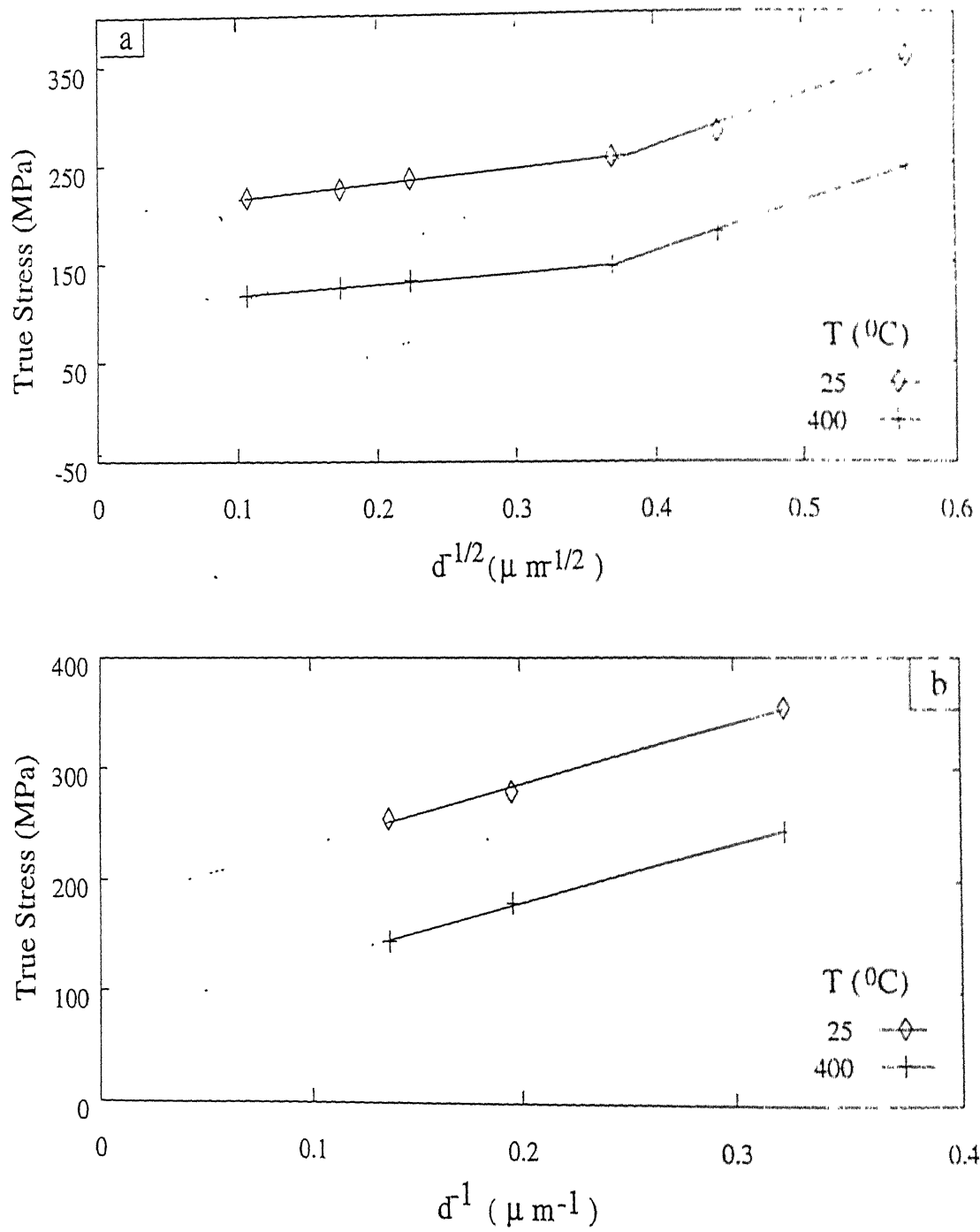


Figure 5.3: Reanalysis of Kashyap *et al.* [41] data: (a) $\sigma(\epsilon)$ vs $d^{-1/2}$ and (b) $\sigma(\epsilon)$ vs d^{-1} in the fine grain regime.

The value of $\sigma_0(\epsilon)$ at yield point is comparable in the fine and in the coarse grain regimes. This difference in hardness between the coarse and fine grain regimes is likely to be due to the differences in hardness at or in the vicinity of grain boundaries. Therefore it is reasonable to conclude that in annealed condition the fine grained samples exhibit a hard mantle zone in the vicinity of grain boundaries while in the coarse grain regime, the grains are free from any hard mantle zone in batch 1.

The Hall-Petch relation is found to be obeyed in most of the polycrystalline materials except for a few deviation [41, 49, 78, 80, 97]. The differences in the values of $\sigma_0(\epsilon)$ and $K(\epsilon)$ between the two regimes of grain sizes is considerably higher in the present investigation as compared to those reported by Kashyap *et al.* [41]. This may be due to the thermo-mechanical treatment employed to obtain fine grain size; it resulted in a comparatively hard mantle zone in the present investigation. Lloyd [49] attributed the bi-linearity in aluminium alloys to the inhomogeneous yielding in the fine grain regime ($d \leq 3\mu\text{m}$) and fitted $\sigma(\epsilon)$ vs d^{-1} relationship as originally proposed by Morris *et al.* [98]. The inhomogeneous yielding (propagation of Luder bands) in aluminium alloys is attributed to the shortage of mobile dislocations caused by the absence of easily operated dislocation sources. The bi-linearity observed in the present investigation in 316L austenitic stainless steel cannot be explained on the above basis as no inhomogeneous yielding was observed. Thompson *et al.* [48] reported deviation from the Hall-Petch relation in pure copper. The texture development during annealing may be the possible reason for deviation from the Hall-Petch relation in copper [83].

The batch 2 samples show a single linear Hall-Petch plot at a given strain in the entire range of grain size (2.9 to 46 μm) as shown in figure 4.16. However, figures 4.14 and 4.18 show a significant difference in the flow stress and Hall-Petch behaviour between the samples of two batches. For a constant grain size, the batch 1 depicts higher flow stress value than batch 2 in the entire range of strain studied (figure 4.14). In the Hall-Petch plots, the batch 2 shows a single linear line at a given strain in the entire range of grain size while batch 1 reveals two linear regions (figure 4.18). There is a substantial difference in

the Hall-Petch behaviour of two batches, especially in the fine grain regime (figure 4.18). In the microstructural characterisation of annealed samples of two batches, the grain size and shape distribution can be noted to be similar (figures 4.9a-b and 4.10c). However there is a significant difference observed in the distribution of true dihedral angles (TDA) as the standard deviation of TDA (figure 5.2a) and the relative frequencies of different classes of TDA (figures 5.2b-d) demonstrate. The batch 1 shows higher standard deviation of TDA and lower class frequency of 120° class of TDA than those of batch 2 in the entire range of grain sizes and this difference is more pronounced in the fine grain regime of two batches. Thus it appears that, even the fine grain sizes obtained in batch 2 are having an equilibrium grain boundaries.

Considering the annealing characteristics of the two batches, a given grain size is obtained at a lower annealing temperature in batch 2 than batch 1. For example, to obtain grain size of $29\ \mu\text{m}$ at the same annealing time (60 minutes), the required annealing temperatures are 950°C and 900°C for batches 1 and 2 respectively. In general the faster grain growth occurs in batch 2 than in batch 1. Therefore, the kinetics of equilibration of grain boundaries is probably faster in batch 2 than in batch 1. This leads to an equilibrated grain boundary state (without the presence of any mantle zone) for the entire grain size range from $2.9\ \mu\text{m}$ to $46\ \mu\text{m}$ for the samples of batch 2. The electron probe micro-analyser (EPMA) results (table 3.1) show that batch 2 has higher Ni, Mn and lower C, Si and Cr content than batch 1. The stacking fault energy (SFE) increases with the increase in Ni and Mn [109-111] and decrease in C, Si and Cr content [109,111,112]. The increase in SFE, decreases the width of extended dislocations and hence the cross-slip of dislocations become easier. Thus, the addition of a solute which increase the SFE is expected to decrease the yield and flow stress. If SFE is decreased, the opposite trend may be observed. In the present investigation, due to the above compositional differences the samples of batch 2 have a higher SFE than the samples of batch 1. These SFE differences may lead to a higher equilibration kinetics of grain boundaries due to the easy cross-slip even at a lower temperature in batch 2 than in batch 1. The above

compositional differences may also lead to a higher yield and flow stress in batch 1 than batch 2. The C and Mo tend to increase the lattice parameter in austenitic stainless steel as reported by Ohkubo *et al.* [109] and thereby an increase in yield and flow stress may follow. The difference in the yield and flow stress in the samples of two batches is much more pronounced in the fine grain regime due to the combined effect of compositional differences and hard mantle zone in the vicinity of grain boundaries in batch 1.

5.1.2 Effect of strain on Hall-Petch parameters

As discussed above the two regions of grain size of batch 1 demonstrate distinctly different Hall-Petch behaviour. In the coarse grain regime the well known Hall-Petch behaviour and in the fine grain regime the composite model are applicable. In the following section the effect of strain on Hall-Petch parameters is discussed separately for the two regions of grain sizes.

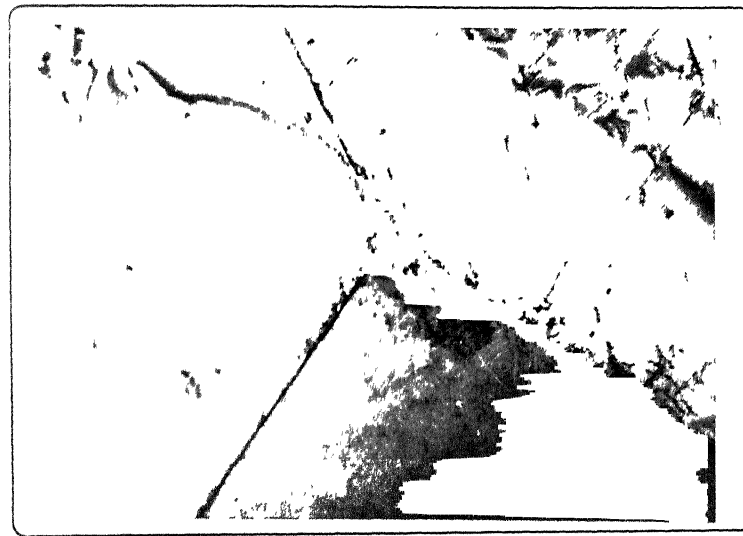
5.1.2.1 Coarse grain regime

Figure 4.19a shows a parabolic increase in $\sigma_0(\epsilon)$ with strain. Kashyap *et al.* [41] also reported a parabolic increase in $\sigma_0(\epsilon)$ with strain. $\sigma_0(\epsilon)$ value of 160 MPa obtained in the present investigation at yield point is close to the value of 200 MPa reported by Kashyap *et al.* [41]. The increase in $\sigma_0(\epsilon)$ with strain is ascribed to the resistance for the movement of dislocations in the grain interior. The increased work-hardening in the grain interior is also confirmed by the increase in microhardness in the grain interior with increasing strain as shown in figures 4.25a-c. This shows that with increasing strain the dislocation density in the grain interior increases. The substructural studies on 316L stainless steel by Kashyap *et al.* [41] also indicate the increase in dislocation density in the grain interior with increasing strain (figures 5.4a-b). This is in agreement with the above conclusion. Meakin and Petch [62] observed linear increase in $\sigma_0(\epsilon)$ with strain in α - brass. They

formulated a linear relation between $\sigma_0(\epsilon)$ and strain on the basis of back stress exerted by accumulated parallel pile-ups on a fresh pile-up involved in starting the next slip band. However the present result and that of Kashyap *et al.* [41] for 316L stainless steel indicated a parabolic increase in $\sigma_0(\epsilon)$ with strain.

$\sigma_0(\epsilon)$ at a given strain may be interpreted as the flow stress of a single crystal oriented for multiple slip. $\sigma_0(\epsilon)$ in Hall-Petch plots at a given strain is the stress value at $d^{-1/2} = 0$ i.e., the flow stress of a single crystal. The flow stress of a f.c.c. single crystal oriented for multiple slip also has a parabolic variation with strain. Kashyap *et al.* [41] attributed the parabolic behaviour of $\sigma_0(\epsilon)$ versus strain to the formation of dislocation tangles on the basis of their TEM observations (figure 5.4b). The $\sigma_0(\epsilon)$ versus strain in batch 2 also shows a parabolic increase in $\sigma_0(\epsilon)$ with strain and the $\sigma_0(\epsilon)$ at a given strain was found to be lower than batch 1. This may be due to the higher Ni and Mn, and lower Cr, C and Si content in the samples of the batch 2 than the batch 1. The compositional differences may result in a higher flow stress in batch 1 than those in batch 2 at a given strain [109]. Figure 4.19b shows an initial decrease (up to 2 % in batch 1 and 5% in batch 2) in $K(\epsilon)$ followed by an increase with strain in both the batches. An examination of the results of microstructural characterisation of deformed samples presented in chapter 4 (section 4.2.2) reveals the following observations.

- The grain size (d) and coefficient of variation of grain size (C_v) show statistically no significant change with increasing strain, as shown in table 4.5 and figure 4.22e respectively.
- The grain aspect ratio (AR) increases whereas the grain shape factor (S_F) decreases with increasing strain (figure 4.22c-d).
- With increasing strain, the relative frequency of 120° class of PDA distribution decreases (figure 4.22b) and correspondingly the standard deviation of PDA distribution increases (figure 4.22a). Significant differences are observed in the calculated



5 μm (a)



5 μm (b)

Figure 5.4: TEM micrographs of the samples of 316L austenitic stainless steel ($d = 86.7\mu\text{m}$) deformed at room temperature up to strains of (a) 2 % and (b) 34 % [41].

true dihedral angle distribution with increasing strain (see figures 5.5 and 5.6). The relative frequency of the ideal configuration (i.e., 120° class of TDA) decreases with strain. On the other hand the relative frequencies of other classes of TDA distribution such as 110° and 130° are seen to increase with strain in the samples of different grain sizes, as shown in figure 5.7b-d. This resulted in an increase in the standard deviation of TDA distribution with increasing strain (see figure 5.7a).

The above results of grain size and coefficient of variation reflect that the grain size and shape distribution remain more or less constant with increasing strain. This is to be expected, since at room temperature no grain boundary migration occurs. The decrease in grain shape factor and increase in grain aspect ratio imply that the grains elongate with increasing strain as can also be seen in deformed microstructures (figures 4.21a-c). This is due to the deformation of samples by mainly intragranular dislocation slip mode. The increase in standard deviation of TDA and decrease in relative frequency of 120° class with increasing strain indicate a shift of the grain boundaries towards a more non-equilibrium state. Accordingly the grain boundary regions become harder with increasing strain. The microhardness data (see figure 4.25a-c) also supports this hypothesis.

The decrease in $K(\epsilon)$ at lower strain may be attributed to the accumulation of extrinsic grain boundary dislocations (EGBDs) at grain boundaries [63]. Prior to deformation, the microstructures of annealed samples in the coarse grain regime are expected to consist of equilibrated grain boundaries. This was concluded from the TDA distribution (see section 5.1.1). At small strains the trapped lattice dislocations interact with the grain boundaries resulting in the formation of EGBDs as shown in figure 2.8a. The EGBDs act as stress concentrators [63] and lead to a significant decrease in the stress required to generate dislocations in the grain boundary region. The density of the sites of stress concentration is equal to the density of EGBDs [63]. Since the density of EGBDs increases with increasing plastic strain, the density of potential sites where dislocations can be generated also increases with increasing strain. Thus $K(\epsilon)$ which is a function of the stress required to generate dislocations would decrease with increasing strain. Kashyap

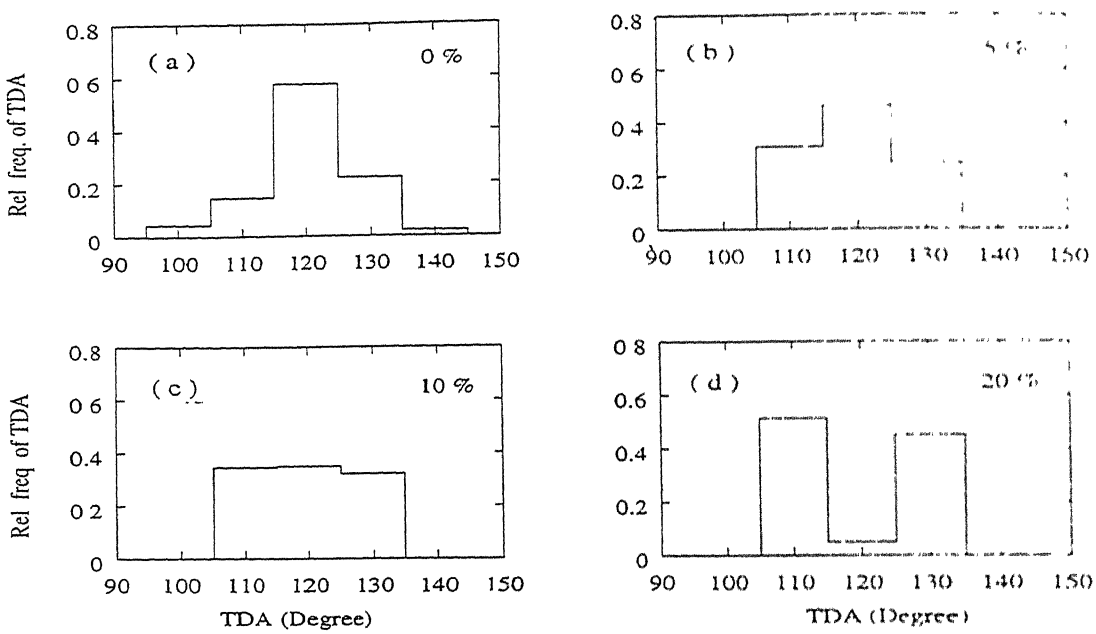


Figure 5.5: TDA distributions in samples of grain size, $d = 4.0 \mu\text{m}$, in batch 2 at various % strains: (a) 0 (b) 5 (c) 10 and (d) 20.

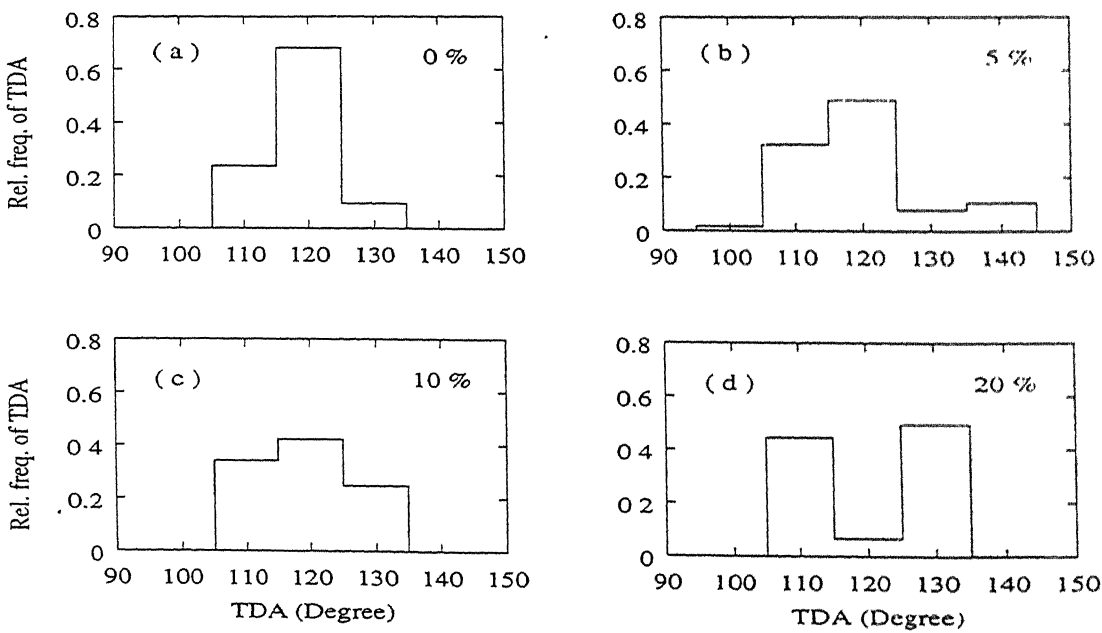


Figure 5.6: TDA distributions in samples of grain size, $d = 29.0 \mu\text{m}$, in batch 2 at various % strains: (a) 0 (b) 5 (c) 10 and (d) 20.

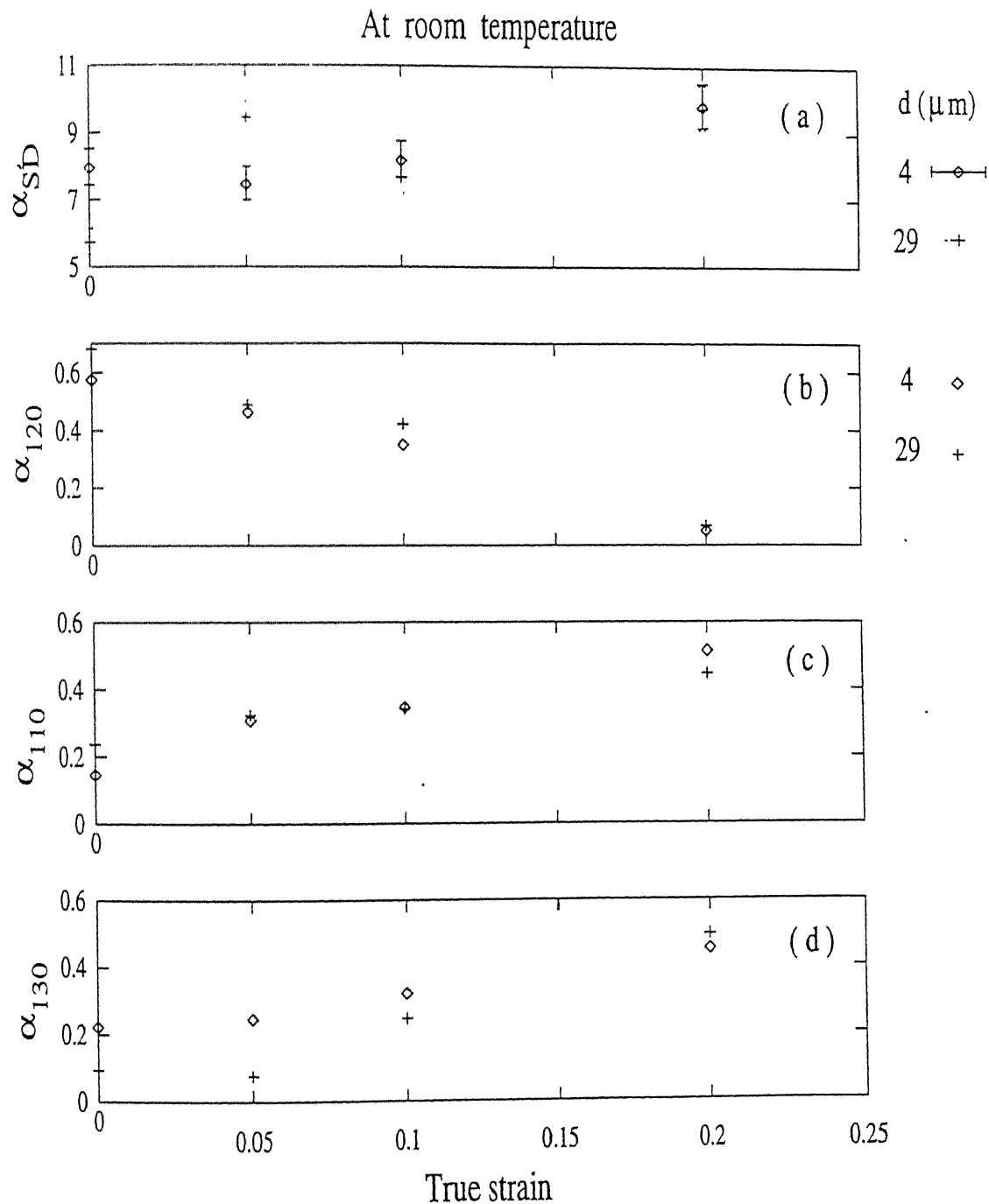


Figure 5.7: Variation of different parameters of TDA distribution: (a) standard deviation (b) relative frequency of 120° class (c) relative frequency of 110° class and (d) relative frequency of 130° class for different grain sizes with true strain.

et al. [41] and Sangal *et al.* [63] also observed a decrease in $K(\epsilon)$ at lower strain and they interpreted it on the basis of accumulation of EGBDs as discussed above.

The increase in $K(\epsilon)$ with strain after the initial fall can be interpreted on the basis of increasing resistance to the propagation of dislocations in the grain boundary region. The accumulation and interaction of EGBDs at grain boundaries transform the grain boundaries to a higher energy or non-equilibrium state. This may result in the formation of a mantle zone in the vicinity of grain boundaries. The variation of TDA distribution and microhardness results as discussed above supports the above statements. Thus the resistance to the propagation of dislocations through the hard mantle zone increases with increasing strain. If $K(\epsilon)$ is identified with the average grain boundary resistance to plastic flow, then this increased width of mantle zone causes further resistance to slip transfer from one grain to the other and thus $K(\epsilon)$ increases with increasing strain. Ashby [61] and Thompson *et al.* [74] explained the increase in $K(\epsilon)$ with strain on the basis of increased density of geometrically necessary dislocations near the grain boundaries. Others [27, 59, 62] also interpreted the increase in $K(\epsilon)$ with strain in terms of the intragranular intersection hardening which arises from the grain size dependence of the dislocation density.

5.1.2.2 Fine grain regime

As discussed earlier the composite model is applied to this region of grain size of batch 1 which yielded the σ versus d^{-1} relationship (equation 2.34). The variation of $\sigma_0(\epsilon)$ (equation 5.1) and $K(\epsilon)$ (equation 5.2) with strain is discussed below.

$\sigma_0(\epsilon)$ is more or less unchanged up to 2% strain followed by parabolic increase with increasing strain as shown in figure 4.20a. Above 2 % strain, the strain hardening rate decreases with strain. The substructural study on this material by Kashyap *et al.* [41,113] shows a lower rate of increase of dislocation density in the grain interior at low strains

(up to 2 %) in the fine grain regime (see figure 5.8a) relative to the coarse grain regime (see figure 5.4a). Hence the $\sigma_0(\epsilon)$ in the fine grain regime remains more or less unchanged with strain at low levels. The parabolic increase in $\sigma_0(\epsilon)$ above 2% strain level may be attributed to the increase in dislocations density inside the grain with increasing strain, as shown in figures 5.8a-b. At higher strain the dynamic recovery is more predominant and it leads to the formation of dislocation cell structure (see figure 5.8b).

The variation of $\sigma_0(\epsilon)$ with strain may be compared to the stress-strain curve of a single crystal oriented for multiple slip as discussed in the previous section. In this range of grain size the rate of increase of $\sigma_0(\epsilon)$, $\{d\sigma_0(\epsilon)/d\epsilon\}$, at a given strain is high compared to that obtained in the coarse grain regime. This is attributed to the high back stress of the accumulated dislocations in the hard mantle zone of fine grain regime.

The variation of $K(\epsilon)$ with strain as shown in figure 4.20b demonstrates an initial increase in $K(\epsilon)$ up to 5 % strain followed by a decrease with increasing strain. A comparison of the variation of $K(\epsilon)$ with strain in the coarse and in the fine grain regimes (see figures 4.19b and 4.20b) indicates opposite trends. The initial increase in $K(\epsilon)$ with strain may be attributed to the increasing resistance to the mobility of dislocations in the grain boundary region. As already discussed in section 5.1.1 the grain boundary regions in the fine grain regime have the hard mantle zone even in annealed condition. This hard mantle zone hinders the propagation of dislocations and hence $K(\epsilon)$ increases with increasing strain due to the intragranular intersection hardening as suggested by Meakin and Petch [62]. The presence of hard mantle zone in the fine grain regime is the possible reason for much higher $K(\epsilon)$ value in this region than in the coarse grain region. The decrease in $K(\epsilon)$ at higher strains may be ascribed to the dominance of dynamic recovery over strain hardening near the grain boundary region as suggested by Jago *et al.* [114] and the substructural study of Kashyap *et al.* [41] (shown in figure 5.8b). Due to the presence of high stress field near grain boundary region (Kocks parameter, $K(\epsilon) = 1945 \text{ MPa } \mu\text{m}$ at 5% strain), the dynamic recovery and cell formation starts at a lower strain leading to a decrease in $K(\epsilon)$ at higher strains.

In the coarse grain regime the grain boundaries have lower stress field even at high strains (Hall-Petch parameter, $K(\epsilon)$ at 25 % strain is $695 \text{ MPa } \mu\text{m}^{1/2}$) as compared to those observed in the fine grain regime (Hall-Petch parameter, $K(\epsilon)$ even at yield point is $1808 \text{ MPa } \mu\text{m}$). Therefore, in the coarse grain regime the dynamic recovery in grain boundary region may not be so dominant as in the fine grain regime. Hence $K(\epsilon)$ increases with increasing strain above 2 % strain in the coarse grain regime while it decreases above 5 % strain in fine grain regime. Meakin and Petch [62] also observed a parabolic increase in $K(\epsilon)$ up to 10 % strain followed by a decrease thereafter in high zinc brasses which have high SFE. The initial increase was attributed to the intragranular intersection hardening. However with increasing strain the eventual formation of dislocation networks near the grain boundaries may supply unlocked sources that allow easier generation of a new slip band and so lower $K(\epsilon)$ at higher strain. This formation of dislocation networks near the grain boundaries is more favourable in the fine grain regime of the presently studied material due to the non-equilibrium state of grain boundaries and high stress field.

In conclusion it can be stated that the present study shows distinctly two different regions of grain sizes having different Hall-Petch intercept and slope at all strains. However Kashyap *et al.* [41] only reported bi-linearity up to 5% strain level and the transition grain size is more or less same as observed in the present investigation. This different Hall-Petch behaviour in the two regions of grain size is the result of differences in the energy state of grain boundary regions. The TDA distribution and the hardness measurement confirm the presence of a hard mantle zone in the samples of fine grain size of batch 1. The Composite model and the well known Hall-Petch model are applicable in the fine and the coarse grain regimes of batch 1 samples. On the other hand, the Hall-Petch relation is valid over the entire range of grain size in the samples of batch 2. At a given strain and grain size, the batch 1 shows higher flow stress value as compared to batch 2. This may have its origin in their compositional variations. The difference in flow stress is more pronounced in the fine grain regime due to the combined effect of compositional differences and energy state of grain boundaries. The variation of $\sigma_0(\epsilon)$ with strain in both the regions shows more or



(a)



(b)

Figure 5.8: TEM micrographs of the samples of 316L austenitic stainless steel ($d = 5.0\mu\text{m}$) deformed at room temperature up to strains of (a) 2 % and (b) 24 % [113].

less similar behaviour as in single crystals oriented for multi-slip. However the variation of $K(\epsilon)$ with strain shows opposing trends in the two regimes of grain sizes.

5.2 Deformation at elevated temperature

5.2.1 Hall-Petch behaviour

Hall-Petch behaviour (for batch 1) in the temperature range from 200 °C to 600 °C show two distinctly different linear regions at all strains, as shown in figures 4.33a-c. This is similar to the Hall-Petch behaviour observed at room temperature (see figure 4.15). The transition grain size between the two regimes remains same (6 μm) over the entire temperature range from room temperature to 600 °C. The scatter in the Hall-Petch data increases with increasing temperature and strain as can be observed from the Hall-Petch plots and regression coefficients presented in table 4.8. The values of the Hall-Petch parameters $\sigma_0(\epsilon)$ and $K(\epsilon)$ for both the fine and the coarse grain regimes at different temperatures and strains are listed in table 4.8. Over the entire temperature range from room temperature to 600 °C, the Hall-Petch parameter $K(\epsilon)$ is significantly higher at a given strain in the fine grain regime as compared to that in the coarse grain regime (see table 4.8). Below 20% strain, the Hall-Petch parameter $K(\epsilon)$ varies approximately from 1300 to 1960 MPa $\mu m^{1/2}$ in the fine grain regime. In the coarse grain regime, $K(\epsilon)$ varies approximately in the range, 320 to 480 MPa $\mu m^{1/2}$. $\sigma_0(\epsilon)$ in the above temperature range (room temperature to 600 °C) is approximately in the range of 75 to 560 MPa. However, $\sigma_0(\epsilon)$ in the fine grain regime over the temperature range from 200 °C to 600 °C and strain range of 0.2 to 20 % is negative as may be seen from table 4.8. It may be recalled that a similar observation i.e, negative $\sigma_0(\epsilon)$ values in the strain range of 0.2 to 15 % was also made at room temperature, as shown in table 4.3. An analysis of the Hall-Petch data of Kashyap *et al.* [41] presented in figure 5.3a also shows negative value of $\sigma_0(\epsilon)$ (-40 MPa at 0.2 % strain) and higher $K(\epsilon)$ value in the fine grain regime than the coarse grain regime

at 400 °C.

As discussed in section 5.1.1, since $\sigma_0(\epsilon)$ represents the flow stress of a single crystal, the negative values of $\sigma_0(\epsilon)$ has no physical significance. Therefore it may be concluded that the Hall-Petch relation is not valid in the fine grain regime in the temperature range from room temperature to 600 °C. As already mentioned in chapter 4 that the fine grain regime in the temperature range from room temperature to 600 °C can be modeled using equation 2.34 (flow stress dependence on inverse of grain size). Figures 4.35a-c show the linear plots of flow stress versus inverse of grain size at three different temperatures, 200 °C, 400 °C and 600 °C. The physical significance of the σ versus $d^{-1/2}$ relation (equation 2.34) has already been discussed. The values of $\sigma_0(\epsilon)$ and $K(\epsilon)$ (constants in equation 2.34) thus obtained are also included in table 4.8. $\sigma_0(\epsilon)$, (which is the flow stress of a single crystal) in this case is positive over the entire range of temperature and strain considered. An analysis of the goodness of fit, using the co-relation coefficient for different powers of d by regression analysis presented in tables 4.4 and 4.9 show that the Hall-Petch model (σ vs $d^{-1/2}$) is valid in the coarse grain regime and the composite model (σ vs d^{-1}) is valid in the fine grain regime of batch 1, over the temperature range from room temperature to 600 °C.

The samples of batch 2 at 400 °C show a single linear Hall-Petch plot at a given strain in the entire range of grain size (2.9 to 46 μm) as illustrated in figure 4.34a. This observation is analogous with the room temperature Hall-Petch behaviour in batch 2. The values of $\sigma_0(\epsilon)$ and $K(\epsilon)$ at different strains are included in table 4.8. It may be noted from table 4:8 that at a given strain and at a temperature of 400 °C, the value of $K(\epsilon)$ is higher and $\sigma_0(\epsilon)$ is lower in batch 2 than in batch 1. Figure 4.36a compares the Hall- Petch behaviour between the two batches at 400 °C. It may be noted from figure 4.36a that the flow stress values in the coarse grain regime of two batches are comparable to each other. On the other hand in the fine grain regime the flow stress of batch 1 is significantly higher than batch 2. The annealing characteristic of the two batches, as already discussed in section 5.1.1, is significantly different. The rapid grain growth characteristic observed in

batch 2 relative to batch 1 (arising due to compositional differences) leads to equilibrated structure of grain boundaries even in the fine grain regime of batch 2. However, in the case of batch 1 the sluggish grain growth behaviour below 900°C leads to the non-equilibrium grain boundaries in the fine grain regime.

As suggested earlier, the samples with different thermo-mechanical treatments can lead to grain boundaries with varying energy states. These variations in the energy states result in differences in the experimentally measurable parameters: the true dihedral angle distribution and microhardness profile across grains. Annealed samples of fine grain regime of batch 1 shows higher standard deviation of true dihedral angles (figure 5.2a) and lower relative frequency of the 120° class of true dihedral angle distribution (figure 5.2b) as compared to the observation in the coarse grain regime. This illustrates that the existence of non-equilibrium grain boundaries in the fine grain regime as compared to that in the coarse grain regime (discussed in detail in section 5.1.1). The non-equilibrium grain boundaries in the fine grain regime leads to a hard mantle zone which consists of dislocations at grain boundaries: extrinsic grain boundary dislocations (EGBDs) and lattice dislocations in the vicinity of grain boundaries. While in the case of the coarse grain regime, the polycrystalline samples are expected to be free from a hard mantle zone due to the fact that they were subjected to higher annealing temperatures. The presence of hard mantle zone in the fine grain regime of batch 1 is also confirmed from the microhardness profile across grains and hardness measurement of annealed samples. However, in batch 2, there is no significant difference observed in the true dihedral angle distribution and microhardness profiles in the two regimes of grain sizes. This indicates an absence of a hard mantle zone in the entire range of grain sizes considered and thereby leads to a single linear Hall-Petch plot in batch 2.

The dynamic strain aging (DSA) behaviour is observed in both the batches in the temperature range of 200°C to 600°C . At 400°C , the value of $K(\epsilon)$ in batch 2 is higher than that observed in the coarse grain regime of batch 1. The higher Ni, Mn and lower C, Si and Cr content (see table 3.1) in batch 2 than batch 1 leads to higher stacking fault

energy (SFE) [109–112]. The higher SFE may results in a decrease in flow stress with increasing temperature due to easy cross-slip. On the other hand, the dynamic strain aging increases the flow stress due to the locking of mobile dislocations. The C and N atoms in the lattice lock the dislocations in dynamic strain aging (DSA) range. These elements preferably segregate near the grain boundaries. Thus the grain boundary region is the preferential site for DSA, as also suggested by Kutumba Rao *et al.* [88]. Therefore, higher C content in batch 1 would lead to a greater degree of DSA. As a consequence, $K(\epsilon)$ in batch 1 should be higher than in batch 2 at 400 °C. However, figure 4.37b shows the opposite trend of higher $K(\epsilon)$ in batch 2 than in batch 1 at a given strain at 400 °C. The reason for this discrepancy is not clear. One possible reason may be related to the compositional difference in other interstitial solute atoms such as nitrogen. However, Nitrogen analysis could not be carried out as the standard is not available in Electron Probe micro-analyser (EPMA). With decreasing grain size in the coarse grain regime, the difference in flow stress between the two batches decreases as illustrated in figure 4.36a. However, the presence of a hard mantle zone prior to deformation in the samples of fine grain size of batch 1 leads to much higher $K(\epsilon)$ value than that of batch 2. This results in an overall higher flow stress in batch 1 than in batch 2 in the fine grain regime.

The hard mantle zone in the grain boundary region and the soft grain interior in the fine grain regime of batch 1 leads to the applicability of Kocks composite model rather than the Hall-Petch model. The presence of hard mantle zone in the fine grained annealed samples of batch 1 is responsible for much higher values of $K(\epsilon)$ in this regime as compared with the coarse grain regime. This high value of $K(\epsilon)$ is found up to the test temperature of 600 °C, as shown in table 4.8. According to Valiev *et al.* [115] and Grabski *et al.* [116], the extrinsic grain boundary dislocations (EGBDs) or trapped lattice dislocations (TLDs) create the so called non-equilibrium grain boundaries of the first order. At the same time these EGBDs are stable only at relatively low temperatures ($< 0.5T_M$, where T_M is the melting temperature). As shown by various investigators [4,5,87,116–120] during in-situ annealing of thin foils in the transmission electron microscope (TEM) the EGBDs spread out and

their images disappear at high temperatures. The observation of the spreading process is interpreted as core widening [4,116-119]. It is also suggested that the EGBDs dissociate into structural grain boundary dislocations with smaller burger vectors [121-123]. Darby *et al.* [121] suggested that for random high angle grain boundaries the burger vectors of structure EGBDs are vanishingly small and for that reason such dislocations cannot be observed in TEM. The driving force for this process is the decrease in the elastic energy of EGBDs. However, such a process can explain only the disappearance of the EGBD contrast in TEM but not the complete annihilation of EGBDs which would require the value of the total burger vector to go to zero. Thus, on completion of above stage, grain boundaries are still in a non-equilibrium state (referred to as non-equilibrium grain boundaries of the second order [116,124]) having residual stresses associated with partially relaxed EGBDs. This was confirmed in various investigations [12,14,63,116,124]. Further reduction of the excess energy due to the presence of residual stresses of partially relaxed EGBDs occurs at high temperature by the rearrangement and annihilation of EGBDs which finally leads to the equilibrium grain boundary structure [13,116,121,124,125].

In the 316L austenitic stainless steel, the spreading of EGBDs occurs below 600°C ($0.53T_M$) as reported by Varin *et al.* [158,159], whereas annihilation of EGBDs takes place at temperatures higher than 600°C , as calculated by Sangal *et al.* [13] and Varin *et al.* [12]. This was also experimentally deduced by the observed drop in yield stress in 316L austenitic stainless steel on annealing for short time [14]. Thus it is concluded that the high $K(\epsilon)$ values observed in the fine grain regime of the batch 1 in the temperature range from room temperature to 600°C is due to the non-equilibrium structure of the grain boundaries and consequently a hard mantle zone.

At 800°C , both the batches exhibit single linear Hall-Petch behaviour in the entire range of grain sizes studied at a given strain as shown in figures 4.33d and 4.34b. The data exhibits wide scatter which increases with strain. The values of correlation coefficient of regression lines above 5% is less than 0.7, as shown in table 4.8. Thus it is difficult to obtain a meaningful Hall-Petch analysis at strains higher than 5%. Accordingly the

result of regression analysis for strains greater than 0.2% is indicated by dashed lines in figures 4.33d and 4.34b. $\sigma_0(\epsilon)$ and $K(\epsilon)$ values obtained from the linear regression at different strains for both the batches are listed in table 4.8. The values of the Hall-Petch parameter $K(\epsilon)$ are significantly lower than those observed at lower temperatures. For example, in batch 1 at a strain of 0.2%, the value of $K(\epsilon)$ is $99.0 \text{ MPa } \mu\text{m}^{1/2}$ at 800°C , whereas at the lower temperature of 600°C , the values of $K(\epsilon)$ are $1464 \text{ MPa } \mu\text{m}^{1/2}$ (from Hall-Petch plot) and $1430 \text{ MPa } \mu\text{m}$ (from σ versus d^{-1} plot) in the fine grain regime and in the coarse grain regime the value of $K(\epsilon)$ is $365 \text{ MPa } \mu\text{m}^{1/2}$ (from Hall-Petch plot). This indicates that the strengthening effect of grain boundaries is considerably reduced. However values of $\sigma_0(\epsilon)$ at low strains at 800°C are comparable to those obtained at 600°C for both the batches. $\sigma_0(\epsilon)$ obtained from the composite relation in the fine grain regime of batch 1 at 600°C is much lower than that observed at 800°C . For example, at a strain of 0.2%, the value of $\sigma_0(\epsilon)$ is 119 MPa at 800°C , while at 600°C , the value of $\sigma_0(\epsilon)$ is 6 MPa (from composite relation) in the fine grain regime and in the coarse grain regime the value of $\sigma_0(\epsilon)$ is 76 MPa (from Hall-Petch plot). This demonstrates that at 800°C the maximum resistance to flow is from the grain interior while at lower temperatures the grain boundaries give maximum resistance to flow at lower strains.

Figure 4.36b compares the Hall-Petch behaviour of two batches at 800°C . The Hall-Petch analysis of the data at 800°C shows that the Hall-Petch parameter $K(\epsilon)$ has small positive value in batch 1 and negative in batch 2 over the entire strain range. In other words, the flow stress slowly increases in batch 1 and decreases in batch 2 with decreasing grain size. The negative value of Hall-Petch parameter $K(\epsilon)$ at 800°C in an austenitic stainless steel containing 21Cr-14Mn-0.68N-0.12C, is also reported by Kutumba Rao *et al.* [88]. It has been considered [52, 88, 94] that at higher temperature above $0.5 T_M$, the main deformation mode is the grain boundary sliding and migration. Thus the pile-up model of Hall-Petch is not applicable at 800°C . Also cross-slip is easier at 800°C , and it leads to the formation of cell and subgrains at lower strains. The cell boundaries act as a barrier to movement of mobile dislocations. Thus the cell formation diminishes the

importance of the grain boundaries in controlling the flow stress. Therefore, it may be more appropriate to analyse the flow stress in terms of cell size together with grain size. The higher SFE of batch 2 as compared to batch 1 leads to the more easy cross-slip of dislocations in batch 2. Consequently cell formation is much easier in batch 2 than in batch 1 and hence Hall-Petch breaks down at a lower strains at 800°C in batch 2 than in batch 1.

5.2.2 Effect of strain on Hall-Petch parameters

It has been demonstrated in the above sections that in the case of batch 1, Hall-Petch model describes the flow stress dependence on grain size in the coarse grain regime ($> 6\mu\text{m}$) and the Kocks composite model is applicable in the fine grain regime ($< 6\mu\text{m}$) in the temperature range of room temperature to 600°C . While in the case of batch 2 the Hall-Petch model is valid over the entire grain size range (from $2.9\mu\text{m}$ to $46.0\mu\text{m}$) in the above temperature range. At 800°C the flow stress dependence on grain size is substantially different in both the batches. The values of Hall-Petch parameter $K(\epsilon)$ in batch 1 are positive, while they are negative in batch 2. Both the batches illustrate wide scatter in data around the regression line above 5% strain level. In the following sections the effect of strain on the parameters, $\sigma_0(\epsilon)$ and $K(\epsilon)$ is discussed separately in the two grain size regimes.

5.2.2.1 Coarse grain regime

Figure 4.37a shows the variation of $\sigma_0(\epsilon)$ with strain at different temperatures. In the temperature range of room temperature to 600°C , $\sigma_0(\epsilon)$ increases parabolically with strain in both the batches. At 800°C , the increase in $\sigma_0(\epsilon)$ with strain is very small as compared to lower temperatures. The variation of Hall-Petch parameter $K(\epsilon)$ with strain at different temperatures for both the batches is shown in figure 4.37b. In the

temperature range of 200°C to 400°C , $K(\epsilon)$ remains more or less constant in the strain range of 0 to 2% strain in batch 1. On further straining, $K(\epsilon)$ increases up to 10% strain and subsequently decreases with increasing strain. However, above 400°C , there is a slight increase in $K(\epsilon)$ up to 2% strain followed by gradual decrease with increasing strain. On the other hand, in batch 2, $K(\epsilon)$ at 400°C increases in the strain range of 0 to 10% and thereafter decreases with increasing strain. At 800°C , $K(\epsilon)$ in batch 2 is negative and it becomes less negative with increasing strain.

In order to understand the variation of the Hall-Petch parameters $\sigma_0(\epsilon)$ and $K(\epsilon)$ with strain, it is worthwhile to examine the geometrical changes in the microstructures through the variation of some of the metallographic parameters (e.g., standard deviation of plane dihedral angle distribution, relative frequency of 120° class of plane dihedral angle distribution, grain aspect ratio, grain shape factor and coefficient of variation of grain size) with strain. Figure 4.43 shows the variation of the microstructural parameters with strain at intermediate temperature of 400°C and several important observations can be noted from it. The coefficient of variation of grain size remains nearly constant with increasing strain (figure 4.43e). Grain size calculated using grain area method at different strain levels (presented in table 4.10) also shows no significant change with strain. No significant change in grain size and grain size distribution with strain suggest the absence of dynamic recrystallisation and grain growth during deformation at 400°C . The microstructure of specimens deformed at 400°C in figures 4.41a-c also show no evidence of recrystallisation.

The grain aspect ratio increases considerably while the grain shape factor (S_F) decreases slightly with increasing strain as illustrated in figures 4.43c and d respectively. This implies that the grains elongate with increasing strain as is also confirmed from the microstructures as shown in figures 4.41a-c. These variations in grain aspect ratio and grain shape factor may be interpreted as the dominance of intragranular dislocation slip without any measurable grain boundary sliding and grain boundary migration. This is in agreement with the investigation of Kurzydowski *et al.* [94] which were also based on the grain geometry changes such as standard deviation of mean intercept length (σ_l),

mean normalised standard deviation of intercept length (σ_l/l) and ratio of maximum grain diameter to equivalent grain diameter (d_{max}/d_{eq}).

The relative frequency of the 120° class of the plane dihedral angle distribution shows a decrease with increasing strain (figure 4.43b). Correspondingly the standard deviation of plane dihedral angle distribution increases with increasing strain as shown in figure 4.43a. For further analysis the true dihedral angle distribution has been calculated from the measured plane dihedral angle distribution at different strain levels using the methodology presented in chapter 4 (section 4.4). The results of the analysis are shown in figures 5.9 and 5.10. The standard deviation of true dihedral angles together with the relative frequencies of different classes of true dihedral angles at different strains are presented in figures 5.11a-d. The true dihedral angle distribution spreads out up to 10 % strain and correspondingly the standard deviation also increases in this strain range. Beyond 10 % strain the spread in the true dihedral angle distribution reduces gradually with increasing strain leading to a small decrease in the standard deviation. The relative frequency of 120° class of true dihedral angle distribution decreases in the strain range between 0 to 10 % followed by slight increase with increasing strain (figure 5.11b). On the other hand, the relative frequencies of 110° and 130° classes of true dihedral angle distribution are observed to increase up to 10 % strain followed by a gradual decrease with increasing strain (figures 5.11c-d). Thus it may be concluded that below 10 % strain the grain boundaries shift towards a non-equilibrium state (due to accumulation of EGBDs) with increasing strain. However, above 10 % strain the decrease in standard deviation and increase in relative frequency of 120° class suggests a partial recovery of non-equilibrium grain boundaries.

The dependence of Hall-Petch parameters $\sigma_0(\epsilon)$ and $K(\epsilon)$ on strain at 400°C can be understood from the above results. The increase in $\sigma_0(\epsilon)$ with strain at a given temperature can be ascribed to the increased resistance for the movement of dislocations in the grain interior. The increased resistance is due to the increase in the density of dislocations in the grain interior and the long range stress field associated with EGBDs (discussed in section 5.1.2). On the basis of the observed geometrical changes (grain aspect ratio, grain

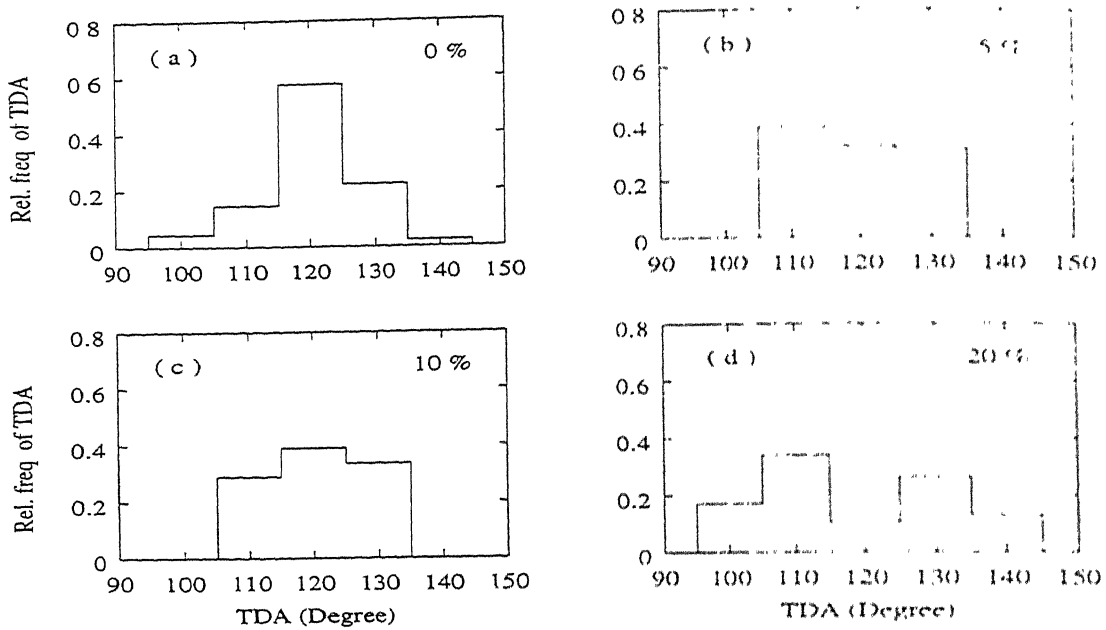


Figure 5.9. TDA distributions in the samples of batch 2 with grain size, $d = 4.0 \mu\text{m}$, deformed at 400°C up to various % strains: (a) 0 (b) 5 (c) 10 and (d) 20.

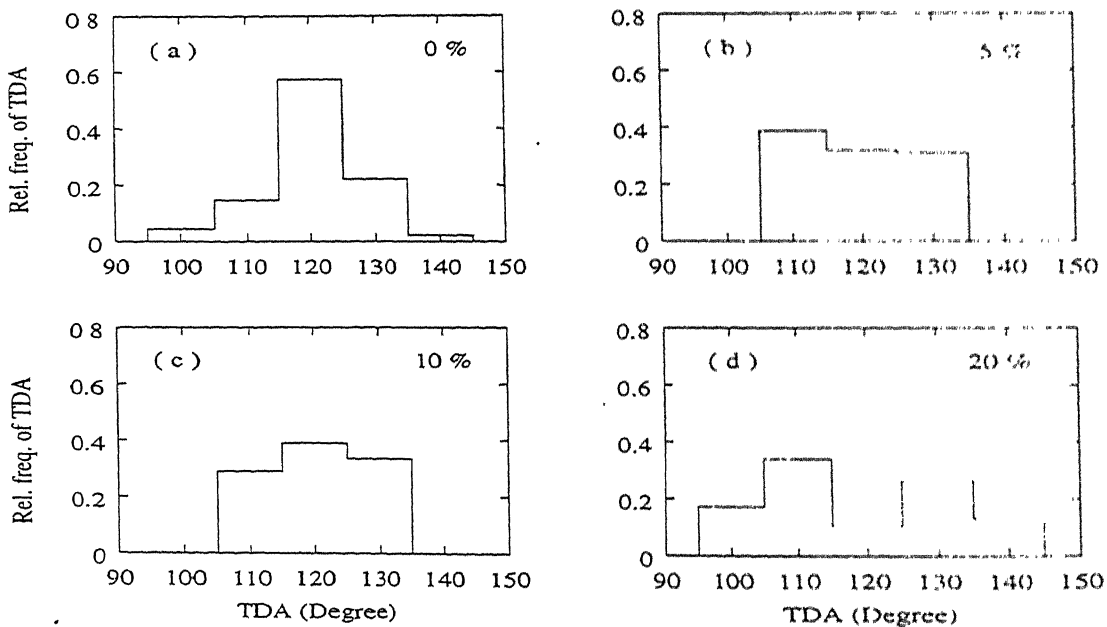


Figure 5.10: TDAs distribution in the samples of batch 2 with grain size, $d = 29.0 \mu\text{m}$, deformed at 400°C up to various % strains: (a) 0 (b) 5 (c) 10 and (d) 20.

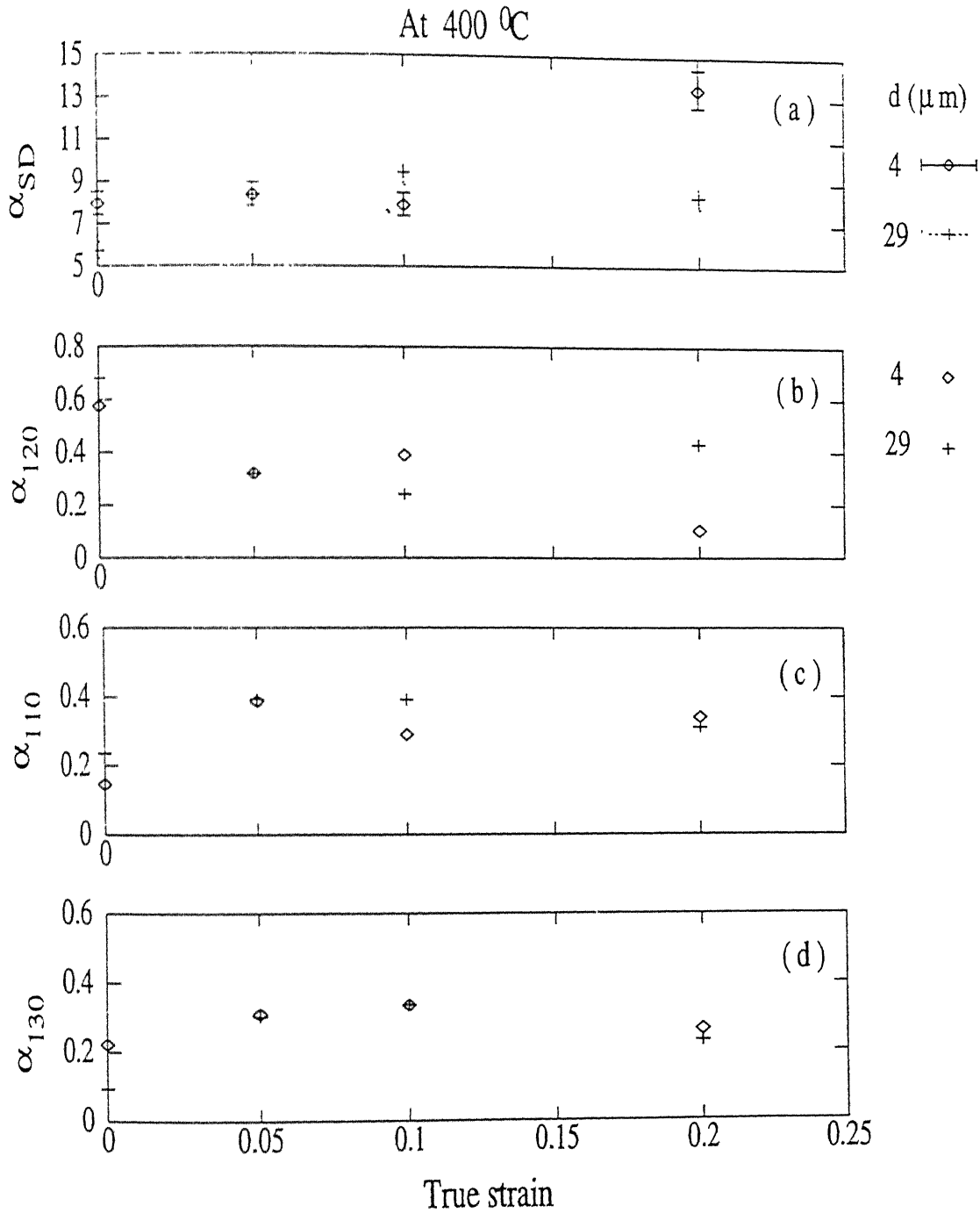


Figure 5.11: Variation of different parameters of TDA distribution: (a) standard deviation (b) relative frequency of 120° class (c) relative frequency of 110° class and (d) relative frequency of 130° class with strain for different grain sizes at 400 °C.

shape factor and true dihedral angles distribution) in the microstructure as a function of strain at 400°C , it is concluded that in the intermediate temperature range (200°C to 600°C) the dislocation density in the grain interior as well as in the grain boundary region increases with strain. This is also supported by the microhardness results presented in figures 4.52a, and 4.54a. The hardness of both the grain interior and grain boundary region increases with increasing strain as illustrated in figure 4.52a. Correspondingly the average microhardness increases with increasing strain at 400°C (figure 4.54a). It may be seen from figures 4.53a-c that for samples deformed beyond 5 % strain, the microhardness profile across grains is higher at 400°C as compared to room temperature. This can be explained on the basis of dynamic strain aging which occurs in the temperature range of 200°C to 600°C . Due to locking of dislocations by solute atoms, the dislocation density at 400°C can be expected to increase at higher rate than at room temperature. This conclusion is in agreement with the substructural observations of Kashyap *et al.* [41] in the same material as shown in figures 5.4b and 5.12b. In spite of higher dislocation density in grain interior at 400°C , $\sigma_0(\epsilon)$ is lower than that at room temperature. This reflects the dominance of thermal effect on the lattice flow. The thermal energy aids the movement of dislocations in overcoming barriers and thus leads to a lower value of $\sigma_0(\epsilon)$.

The variation of the Hall-Petch parameter $K(\epsilon)$ with strain as shown in figure 4.37b, can also be correlated to the microstructural changes with strain. Initially below 2 % strain there is no significant change in $K(\epsilon)$ with increasing strain at 400°C . This can be interpreted as a combined effect of accumulation of EGBDs and dynamic strain aging. It was suggested by Sangal *et al.* [63] that the presence of EGBDs at grain boundaries leads to increase in the density of potential sites where dislocations can be generated. Thus $K(\epsilon)$ which is a function of stress required to generate dislocations would decrease with increasing density of EGBDs and (as discussed in section 5.1.1), $K(\epsilon)$ initially decreases with strain at room temperature. However, in the temperature range between 200°C to 600°C , the dynamic strain aging increases the stress required to propagate slip across grain boundaries. Also the dynamic strain aging is suggested to occur more favourably

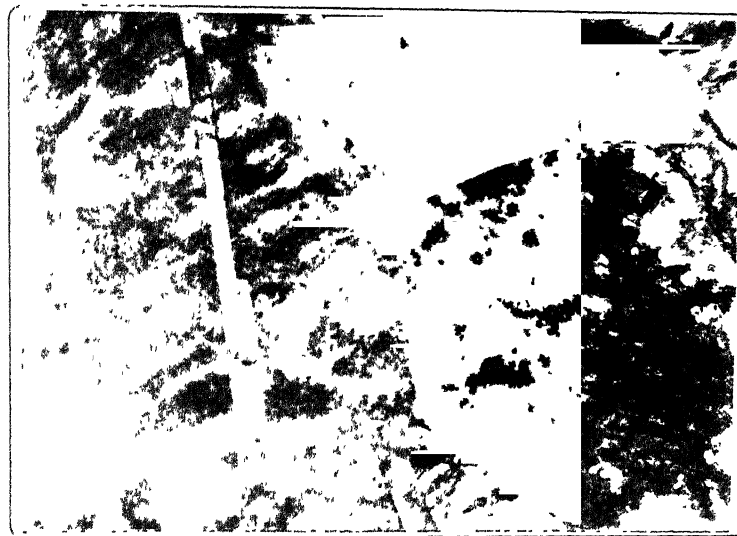
in the grain boundary region [52, 88]. On the basis of humps in the flow stress versus temperature curve, it was concluded that dynamic strain aging is more pronounced in small grain regime [52, 88]. Thus the combined effect of EGBDs and dynamic strain aging leads to only a small change in $K(\epsilon)$ below 2 % strain in the temperature range from 200 °C to 600 °C. With increasing temperature, the drop in $K(\epsilon)$ below 2 % strain decreases as seen from figure 4.37b. The increase in jerkiness in the load elongation curves with increasing temperature in the temperature range of 200 °C to 600 °C reflects the increasing influence of dynamic strain aging. Thus the dominance of dynamic strain aging over EGBDs accumulation leads to decreased drop in $K(\epsilon)$ below 2% strain with increasing temperature.

With increasing strain the density of dislocations in the grain boundary region increases. The microhardness results (figure 4.52a) also illustrate the increase in hardness in grain boundary region with increasing strain at 400 °C. This increased dislocation density hinders in the propagation of slip across grain boundary region. The combined effect of increased dislocation density and dynamic strain aging leads to an increase in $K(\epsilon)$ with strain at 400 °C. The observed decrease in $K(\epsilon)$ beyond 10% strain is attributed to the onset of dynamic recovery processes which become favourable in the grain boundary region due to a substantial increase in dislocation density. The recovery processes lead to the formation of cell structure by the rearrangement and annihilation of dislocations. The formation of cell structure at higher strain is confirmed from the TEM observation of Kashyap *et al.* [41] as shown in figure 5.12b. It is to be noted that beyond 10% strain there is no significant change in the true dihedral angle distribution observed. This is a significant observation as it suggests that no further changes in the energy state of grain boundaries took place due to simultaneous accumulation and annihilation of dislocations. Therefore, with increasing temperature the recovery processes start at lower strain. This results in a decrease in the strain, corresponding to the maximum $K(\epsilon)$, with temperature (see figure 4.37b).

Considering the variation of microstructural parameters with strain at 800 °C in the

coarse grain regime, no significant change in the grain size (see table 4.10) and the grain size distribution (figure 4.44e) are observed at different strain levels. This implies that even at 800°C grain growth and dynamic recrystallisation do not occur during plastic deformation. Below 5% strain, the grain aspect ratio increases whereas the grain shape factor decreases with strain. However, above 5% strain, there is no significant change observed in these parameters with increasing strain as seen from figures 4.44c-d. The micrograph (figures 4.42a) at 5% strain show elongated grains as well as some curved or bulged grain boundary segments. The elongation of grains suggests that intragranular dislocation slip is the dominant mode of deformation. Beyond 5% strain, bulging in grain boundaries becomes increasingly prominent (figures 4.42b-c) while there is no significant change observed in the grain aspect ratio and grain shape factor with increasing strain (figures 4.44c-d). Hence the contribution of grain boundary sliding and migration to overall deformation of the polycrystal can no longer be neglected. The increase in grain interior and grain boundary hardness and correspondingly average microhardness below 5% strain and subsequently no significant change in hardness values as presented in figures 4.52b and 4.54a also support the above conclusion.

The relative frequency of 120° class of the plane dihedral angle distribution decreases up to 5% strain and subsequently increases with increasing strain (figure 4.44b). Accordingly the standard deviation of plane dihedral angle distribution increases followed by decrease beyond 5% strain (figure 4.44a). The above trend can be seen much more clearly in the case of the distribution of the true dihedral angles (see figures 5.15a-b). The spread (around 120° class) in the distribution increases with increasing strain up to 5% strain (see figures 5.13a-b and 5.14a-b). In the same strain range the standard deviation also increases (figure 5.15a). While for strains greater than 5% strain, the spread as well as the standard deviation decreases with increasing strain. The relative frequency of 120° class of true dihedral angle distribution decreases in the strain range of 0 to 5% strain followed by



10 μm (a)



5 μm (b)

Figure 5.12: TEM micrographs of the samples of 316L austenitic stainless steel deformed up to 34 % strains at 400 °C with grain sizes: (a) 5.1 μm and (b) 86.7 μm [41].

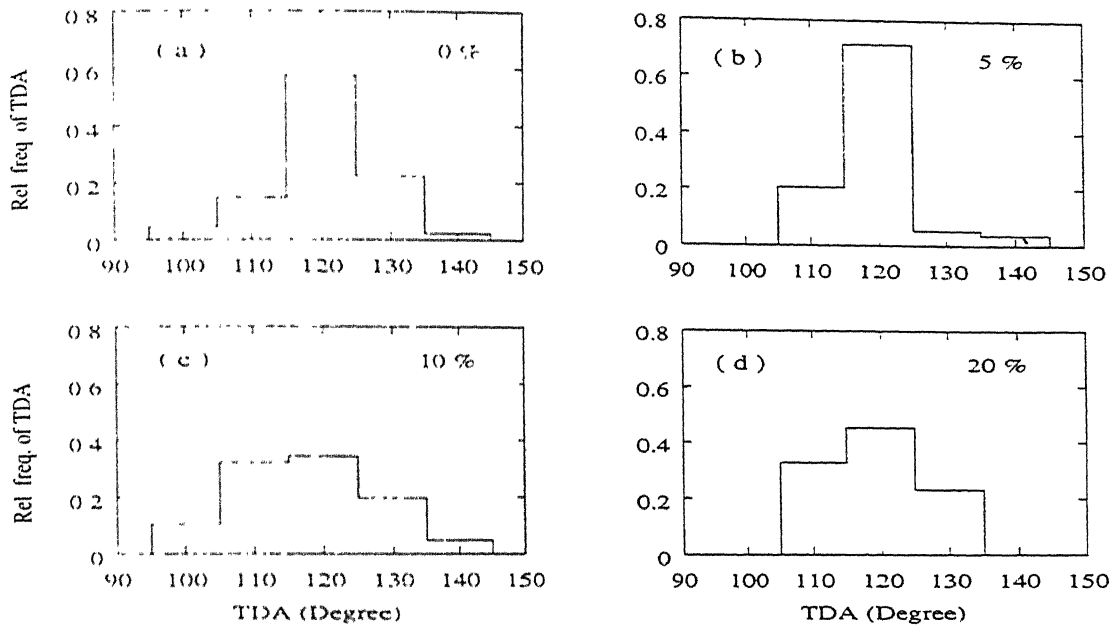


Figure 5.13: TDA distributions in the samples of batch 2 with grain size, $d = 4.0 \mu\text{m}$, deformed at 800°C up to various % strains: (a) 0 (b) 5 (c) 10 and (d) 20.

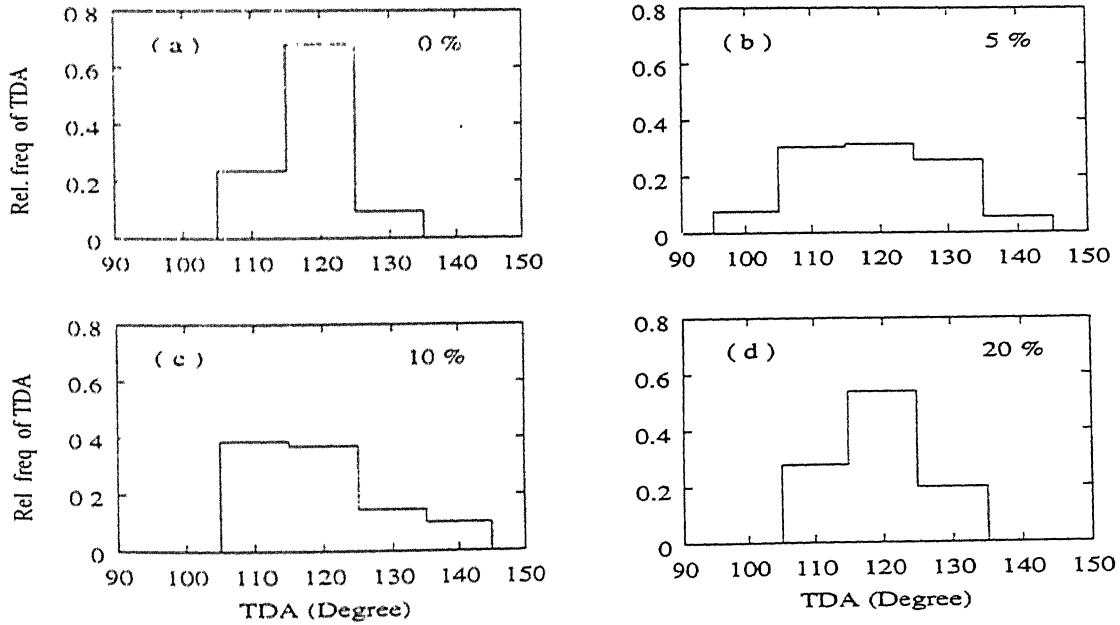


Figure 5.14: TDA distribution in the samples of batch 2 with grain size, $d = 29.0 \mu\text{m}$, deformed at 800°C up to various % strains: (a) 0 (b) 5 (c) 10 and (d) 20.

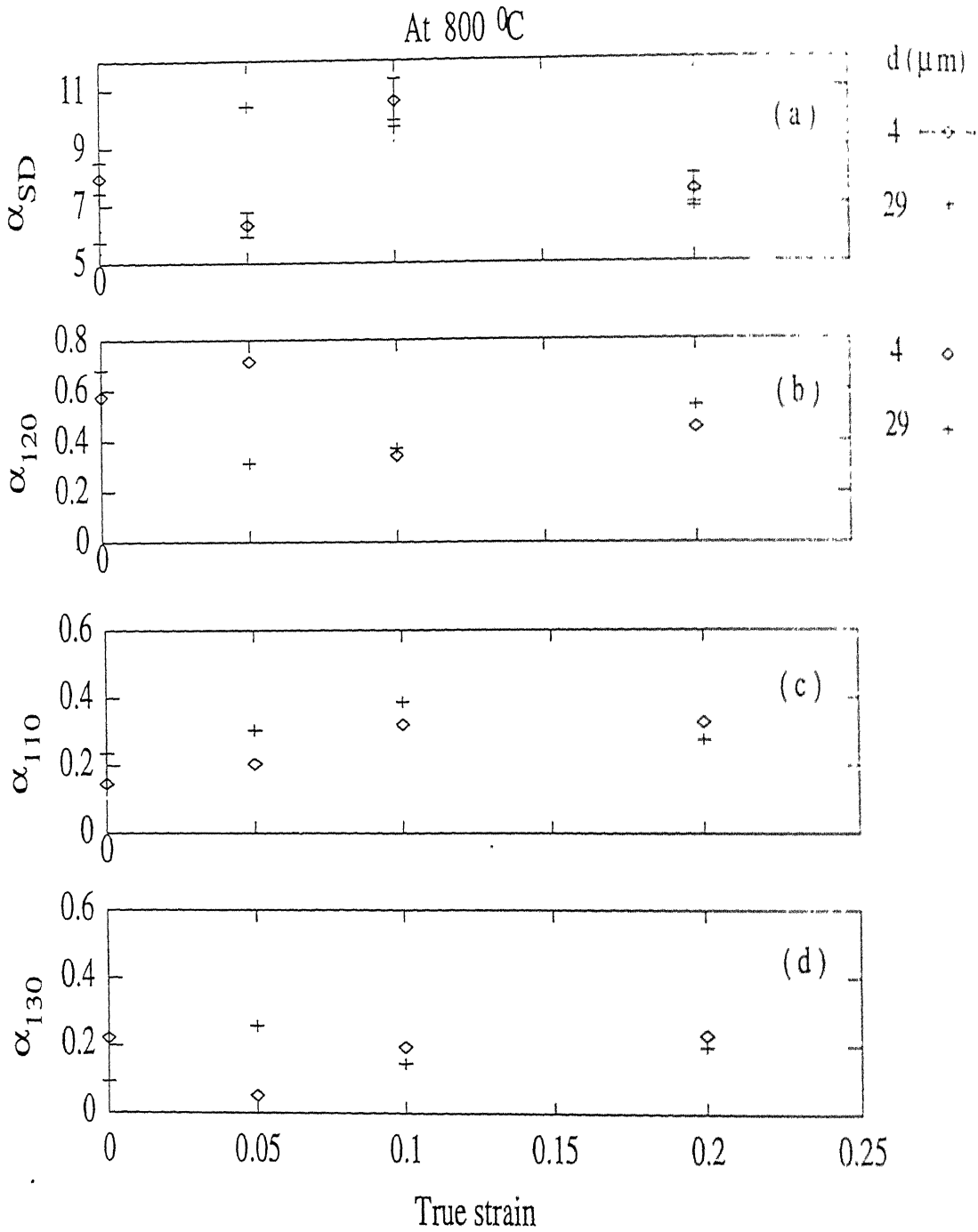


Figure 5.15: Variation of different parameters of TDA distribution: (a) standard deviation (b) relative frequency of 120° class (c) relative frequency of 110° class and (d) relative frequency of 130° class with strain for different grain sizes at 800 °C.

an increase with increasing strain (figure 5.15b). Similarly the relative frequencies of 110° and 130° classes of true dihedral angle distribution are observed to increase below 5% strain and decrease with increasing strain for strains greater than 5 % (figures 5.15c-d). The above variations in the true dihedral angle distribution below 5 % strain at 800°C suggest that the grain boundaries transform from equilibrium to non-equilibrium structure. However above 5 % strain, the increase in 120° peak of true dihedral angle distribution (figure 5.15b) leads to the conclusion that there is a decrease in the energy state of grain boundaries. This can be achieved by recovery processes at grain boundaries such as annihilation of EGBDs. This is in agreement with the microhardness results (figures 4.52b) which show increase in hardness in the grain boundary region up to 5 % strain and thereafter no significant change with increasing strain.

The variation of $\sigma_0(\epsilon)$ and $K(\epsilon)$ with strain at 800°C can now be explained on the basis of the above discussion. The values of $\sigma_0(\epsilon)$ below 5 % strain at 800°C is slightly higher than that at 400°C and 600°C . However above 5 % strain $\sigma_0(\epsilon)$ is significantly lower than the corresponding value at 600°C as shown in figure 4.37a. The load elongation curves at 800°C also show the jerky behaviour in the lower strain range. Thus the presence of dynamic strain aging in the lower strain range and the dominance of intragranular dislocation slip leads to a more or less comparable dislocation density that would be expected at 400°C and 600°C at lower strains. This is in agreement with the substructural observations of Kashyap *et al.* [41]. On the basis of the grain geometry changes, it is expected that the contribution of grain boundary sliding and migration becomes important to the overall deformation of the polycrystalline samples. Above 5% strain, the onset of the annihilation of EGBDs would occur leading to a decrease in the long range stress field associated with EGBDs. This subject will be considered in greater detail in section 5.3. The TEM observation of Kashyap *et al.* [41] also show the formation of cell structures in the grain interior (figure 5.16b). The formation of cells as well as reduction in long range stress field of EGBDs at 800°C result in a lower value of $\sigma_0(\epsilon)$ as compared to that observed at 600°C .

The Hall-Petch parameter $K(\epsilon)$ at 800°C at a given strain is much lower than that observed at other lower temperatures, as shown in figure 4.37b. $K(\epsilon)$ increases slightly up to 2 % strain and beyond 2 % strain, $K(\epsilon)$ decreases with increasing strain in batch 1. In the range of small strains (up to 5% strain) the observed changes in the true dihedral angle distribution and the hardness in the grain boundary region (as discussed earlier in this section) suggest the accumulation of EGBDs leading to a decrease in $K(\epsilon)$. On the other hand, dynamic strain aging would tend to increase in $K(\epsilon)$. Thus the small increase in value of $K(\epsilon)$ with strain in the strain range of 0 to 2 % is probably due to a more dominant effect of dynamic strain aging over the effect of accumulation of EGBDs. However, above 2 % strain the formation of cell structures and the onset of the annihilation of EGBDs leads to a decrease in $K(\epsilon)$ with increasing strain.

The variation of $\sigma_0(\epsilon)$ with strain in batch 2 also demonstrates a parabolic increase at 400°C and a gradual increase at 800°C , as shown in figure 4.37a. The behaviour of the variation $\sigma_0(\epsilon)$ with strain is similar in both the batches at a given temperature. However, at a given strain and temperature, $\sigma_0(\epsilon)$ in batch 2 is lower than batch 1. As discussed in section 5.2.1, this difference between the two batches can be understood in terms of the effect of alloying elements (C, Cr, Ni, Mn, etc.) on the stacking fault energy and interstitial strengthening. The dependence of Hall-Petch parameter $K(\epsilon)$ on strain in batch 2 shows similar variation at 400°C as observed in batch 1 (figure 4.37b). However, the value of $K(\epsilon)$ at a given strain in batch 2 at 400°C is higher than that in batch 1. This has been discussed in section 5.2.1 in terms of the effect of alloying elements on dynamic strain aging. On the other hand in batch 2 at 800°C , $K(\epsilon)$ is negative and becomes less negative with increasing strain as illustrated in figure 4.37b. Because of the negative value of $K(\epsilon)$, the Hall-Petch relation is not valid for batch 2 at 800°C for the entire strain range. The higher SFE of batch 2 probably leads to cell formation at a much smaller strain as compared to batch 1. It has been shown by many investigators [41, 52, 88, 126–128] that the grain size in the Hall-Petch relation should be replaced by cell size.



5 μm (a)



2 μm (b)

Figure 5.16: TEM micrographs of the samples of 316L austenitic stainless steel deformed up to 34 % strains at 700 °C with grain sizes: (a) 5.1 μm and (b) 86.7 μm [41].

5.2.2.2 Fine grain regime

As already discussed in section 5.2.1, the Hall-Petch model is invalid in the fine grain regime ($< 6\mu\text{m}$) of batch 1 in the temperature range of room temperature to 600°C . It has also been shown that the Kocks composite model describes the flow stress dependence on grain size in the fine grain regime at temperatures in the range of room temperature to 600°C . A detailed discussion of the significance of the Kocks parameters $\sigma_0(\epsilon)$ (equation 5.1) and $K(\epsilon)$ (equation 5.2) is given in section 5.1.1. In the temperature range of 200°C to 600°C , the fine grain ($2.7\mu\text{m}$) sample exhibits a maximum strain of up to 13 % only. Therefore, the discussion on the variation of $\sigma_0(\epsilon)$ and $K(\epsilon)$ with strain is limited to the strain range of 0 to 10 %.

Figure 4.38a shows the variation of $\sigma_0(\epsilon)$ with strain at different temperatures. $\sigma_0(\epsilon)$ shows more or less linear variation with strain at all temperatures. As already discussed in section 5.1.1, a hard mantle zone is expected to exist prior to deformation in the vicinity of grain boundaries. At a given strain the maximum contribution on flow stress is from the grain boundary region compared to grain interior region. Thus dynamic recovery is favourable at a given temperature and strain in the grain boundary region and almost nil in the grain interior region. This leads to the linear increase in $\sigma_0(\epsilon)$ with strain in the fine grain regime. This is in agreement with the substructural study of Kashyap *et al.* [41] as shown in figures 5.12a-b. However at higher temperature (700°C), the subgrain formation is also observed at higher strain in fine grains (figure 5.16a).

The variation of the Kocks parameter $K(\epsilon)$ with strain at different temperatures is shown in figure 4.38b. At 200°C , $K(\epsilon)$ increases rapidly below 2 % and thereafter remains nearly constant with increasing strain. This is similar to the variation observed at room temperature. As discussed in section 5.1.2, the presence of hard mantle zone prior to deformation leads to increase in $K(\epsilon)$ even in lower strain range. This presence of hard mantle zone (i.e., a large density of dislocations) in the grain boundary region leads to the early formation of cell and subgrain structure by dynamic recovery. This

interpretation is in agreement with the TEM studies of Kashyap *et al.* [41] and Jago *et al.* [114]. The occurrence of dynamic recovery is responsible for decrease in $K(\epsilon)$ above 2 % strain at 200 °C. At higher temperatures e.g., 400 °C and 600 °C, the combined effect of temperature and the dislocations stress field in the grain boundary region results in faster recovery. This leads to an increase in the rate of decrease in $K(\epsilon)$ with temperature and also for temperature greater than 200 °C, $K(\epsilon)$ decreases with increasing strain starting from yield point.

5.2.3 Effect of temperature on Hall-Petch parameters

The variation of Hall-Petch parameters $\sigma_0(\epsilon)$ and $K(\epsilon)$ as a function of temperature in the regime where Hall-Petch relation is valid (i.e., coarse grain regime in the temperature range from room temperature to 600 °C and the entire grain size range at 800 °C) are shown in figures 4.39a and b respectively. In the fine grain size range up to 6 μm (the flow stress is described by the composite model), the variation of the parameters of Kocks model, $\sigma_0(\epsilon)$ and $K(\epsilon)$ as a function of temperature are shown in figures 4.40a and b respectively. The physical significance of $\sigma_0(\epsilon)$ in both the Hall-Petch and composite models is identical, i.e., $\sigma_0(\epsilon)$ represents the flow stress of single crystal. $K(\epsilon)$ is a grain boundary strengthening parameter. It may be observed from figure 4.39a that the general behaviour of $\sigma_0(\epsilon)$ versus temperature is analogous to the well known behaviour of flow stress versus temperature in single crystals. In the following sections the effect of temperature on the parameters $\sigma_0(\epsilon)$ and $K(\epsilon)$ is discussed separately in the two regimes of grain sizes.

5.2.3.1 Coarse grain regime

Just as in the case of single crystals, $\sigma_0(\epsilon)$ versus temperature also shows a two stage behaviour at lower strain and a three stage behaviour at higher strain (figure 4.39a). In the first stage (temperature range of room temperature to 200 °C), $\sigma_0(\epsilon)$ decreases rapidly

and thereafter in the second stage (temperature range of 200°C to 800°C) at lower strains (0 to 5%) $\sigma_0(\epsilon)$ remains more or less constant. However, above 600°C , there is a small increase in $\sigma_0(\epsilon)$ for 0.2 % strain, as shown in figure 4.39a as dotted lines. At higher strains (beyond 5%) the second stage extends from 200°C to 600°C . The onset of stage 3 occurs beyond 600°C for higher strains.

The nature of $\sigma_0(\epsilon)$ versus temperature curves can be explained on the basis of Seeger's theory for the variation of flow stress with temperature in single crystals. According to the theory the flow stress for a single crystal has two components:

$$\tau = \tau_G + \tau_S \quad (5.3)$$

where τ_G is the temperature independent contribution to the flow stress, which arises from the elastic interactions between dislocations; τ_S is the temperature dependent contribution to the flow stress and is the stress necessary for the mobile dislocations to cut through a dislocation forest. Forest cutting is a thermally activated process and the activation energy decreases linearly with applied stress. As a consequence, τ_S should also decrease linearly with temperature at a given strain or stress. Beyond a certain temperature, the contribution from τ_S would vanish and therefore from equation 5.3, τ becomes temperature independent. Thus the decrease in $\sigma_0(\epsilon)$ in the first stage may be predominantly¹ due to the linear decrease in τ_S with temperature. The gradual decrease in $\sigma_0(\epsilon)$ with temperature in the second stage is primarily due to the decrease in τ_G because of the decrease in shear modulus with temperature. This is confirmed from the variation of $\sigma_0(\epsilon)/E$ with temperature which shows almost no decrease with temperature in the second stage as depicted in figure 5.17a. Further, the relaxation of EGBDs in this temperature range (as discussed in section 5.2.2) may also result in a decrease in $\sigma_0(\epsilon)$ with temperature. However the dynamic strain aging (DSA) which occurs in this temperature range leads to an increase in $\sigma_0(\epsilon)$ with temperature. Therefore these two effects (EGBDs relaxation and DSA) on $\sigma_0(\epsilon)$ may neutralise each other.

¹In polycrystals, other factors, such as, the long range stress field of non-equilibrium grain boundaries, also have an effect on $\sigma_0(\epsilon)$ as discussed in section 5.1.1

Below 5% strain, as already discussed in section 5.2.2, intragranular dislocations slip is the important deformation mechanism over the temperature range from room temperature to 800 °C. This has been concluded from the grain geometry changes and microhardness profile across grains. The variation of metallographic parameters with temperature at 5% strain show comparatively higher grain aspect ratio and lower grain shape factor at 800 °C than at lower temperatures as illustrated in figures 4.49c-d. Thus at lower strain due to the dominance of dynamic strain aging and intragranular dislocation slip mode over other mode of deformation at 800 °C, leads to a more or less comparable dislocation density with that expected at lower temperatures. This interpretation is in agreement with the TEM study of Kashyap *et al.* [41]. The variation of average microhardness with temperature below 5% strain also shows a small increase in hardness with increasing temperature. Therefore, in the temperature range from room temperature to 800 °C, $\sigma_0(\epsilon)$ does not reveal stage 3 or rapid drop at strain below 5%.

The drop in $\sigma_0(\epsilon)$ with temperature for strains above 5% in stage 3 cannot be explained on the basis of the above discussion. However it can be interpreted on the basis of high temperature recovery processes. Above 600 °C, the formation of cell structure at higher strains involves the rearrangement and annihilation of dislocations, the activation of climb processes and annihilation of EGBDs at grain boundaries. The annihilation of EGBDs at grain boundaries leads to a decrease in back stress on mobile dislocations. These processes leads to a rapid drop in $\sigma_0(\epsilon)$ at higher strains (above 5%) beyond approximately 600 °C as shown in figure 4.39a.

For strains higher than 5%, the nature of the variation of the metallographic parameters (grain shape factor and grain aspect ratio) with temperature is gradually reversed. This can be seen from figures 4.50a-e (at 10% strain) and 4.51a-e (at 20% strain). Above 5% strain, the increase in microhardness at intermediate temperature (400 °C), as shown in figures 4.53b-c and 4.54b, arises due to the effect of dynamic strain aging (discussed in section 5.2.2). The rapid drop in hardness in the higher temperature region coupled with the observed grain geometry changes indicates that with increasing strain the de-

formation mechanism shifts from intragranular dislocation slip to grain boundary sliding and migration. The occurrence of faster recovery processes as mentioned above at higher strains leads to a rapid drop in $\sigma_0(\epsilon)$ at higher temperatures.

The variation of the Hall-Petch parameter $K(\epsilon)$ with temperature at different strain levels shows three stage behaviour as depicted in figure 4.39b. However, it may be noted from this figure that at intermediate strains the first stage is not prominent. In the first stage (temperature range from room temperature to 200°C), $K(\epsilon)$ decreases with increasing temperature. $K(\epsilon)$ remains more or less unchanged or gradually decreases with increasing temperature in stage 2 (from 200°C to 600°C). Stage 3 proceeds with the rapid drop in $K(\epsilon)$ at approximately at 600°C . Armstrong [59] demonstrated that the parameter $\sigma_0(\epsilon)$ reflects the deformation processes in the grain interior while the parameter $K(\epsilon)$ reflects processes occurring in the grain boundary region. Thus the general tendency for $K(\epsilon)$ to decrease with temperature is interpreted as a weakening of the locking effects at grain boundaries. At lower strains (0.2 %) the initial decrease in $K(\epsilon)$ with temperature is due to the decrease in the short range stress field. Dynamic strain aging initiated at the end of this stage (at temperature above 200°C) leads to an additional locking at the grain boundaries. Thus the rate of accumulation of dislocations in the grain boundary region becomes higher in the DSA temperature range. This leads to very small differences in the values of $K(\epsilon)$ in the intermediate strain levels. However at higher strains cross-slip of dislocations becomes more favourable at 200°C than at room temperature (figure 4.37b) and hence there is an initial decrease in $K(\epsilon)$ with increasing temperature as illustrated in figure 4.39b.

After normalising $K(\epsilon)$ with respect to elastic modulus a small or no variation in $K(\epsilon)$ with temperature is observed in the temperature range of 200°C to 600°C as shown in figure 5.17b. This may be attributed to the combined but opposite effects of dynamic strain aging and relaxation of stress field of EGBDs. The dynamic strain aging results to increase in $K(\epsilon)$ value with increasing temperature. On the other hand, the relaxation of stress field of EGBDs in this temperature range takes place by the process of core

widening or dissociation into dislocations with small burger vectors. The reduction in the stress field of EGBDs at the grain boundaries directly leads to a decrease in the value of $K(\epsilon)$ (see section 5.3 for detail). The variation of average microhardness with temperature as depicted in figure 4.5-4b also reveals the increase in hardness in the intermediate temperature region. This type of variation in $K(\epsilon)$ with temperature is also observed by Kutumba Rao *et al.* [88], Mannan *et al.* [52] and Armstrong [59].

The rapid drop in $K(\epsilon)$ above 600°C may be ascribed to the recovery processes at and in the vicinity of the grain boundaries. The process of annihilation of EGBDs at the grain boundaries (to be discussed detail in section 5.3) and the occurrence of faster cross-slip of dislocations above 600°C (discussed in section 5.2.2) lead to a rapid drop in $K(\epsilon)$. The variation of average microhardness with temperature also reveals the rapid drop in hardness at higher temperature range as shown in figure 4.5-4b.

5.2.3.2 Fine grain regime

As discussed in section 5.2.2, the Hall-Petch model breaks down in the fine grain regime ($< 6\mu\text{m}$) over the temperature range of room temperature to 600°C . However Kocks composite model describes the flow stress dependence on the grain size adequately in this regime of grain size in above temperature range (from room temperature to 600°C). The variation of the parameters of Kocks composite model, $\sigma_0(\epsilon)$ and $K(\epsilon)$ (parameters of composite model) with temperature at different strains are shown in figures 4.40a and b respectively. The decrease in $\sigma_0(\epsilon)$ with temperature at 0.2% strain is in agreement with Seeger's theory as discussed in the previous section. However, at higher strains $\sigma_0(\epsilon)$ decreases below 200°C followed by a hump in the intermediate temperature (400°C). Since $\sigma_0(\epsilon)$ represents the resistance to dislocation motion in the grain interior, the increase in $\sigma_0(\epsilon)$ in the intermediate temperature range reveals the occurrence of dynamic strain aging (DSA) by which the additional locking in dislocation movement takes place. This effect can be more clearly seen in the variation of $\sigma_0(\epsilon)/E$ with temperature in figure

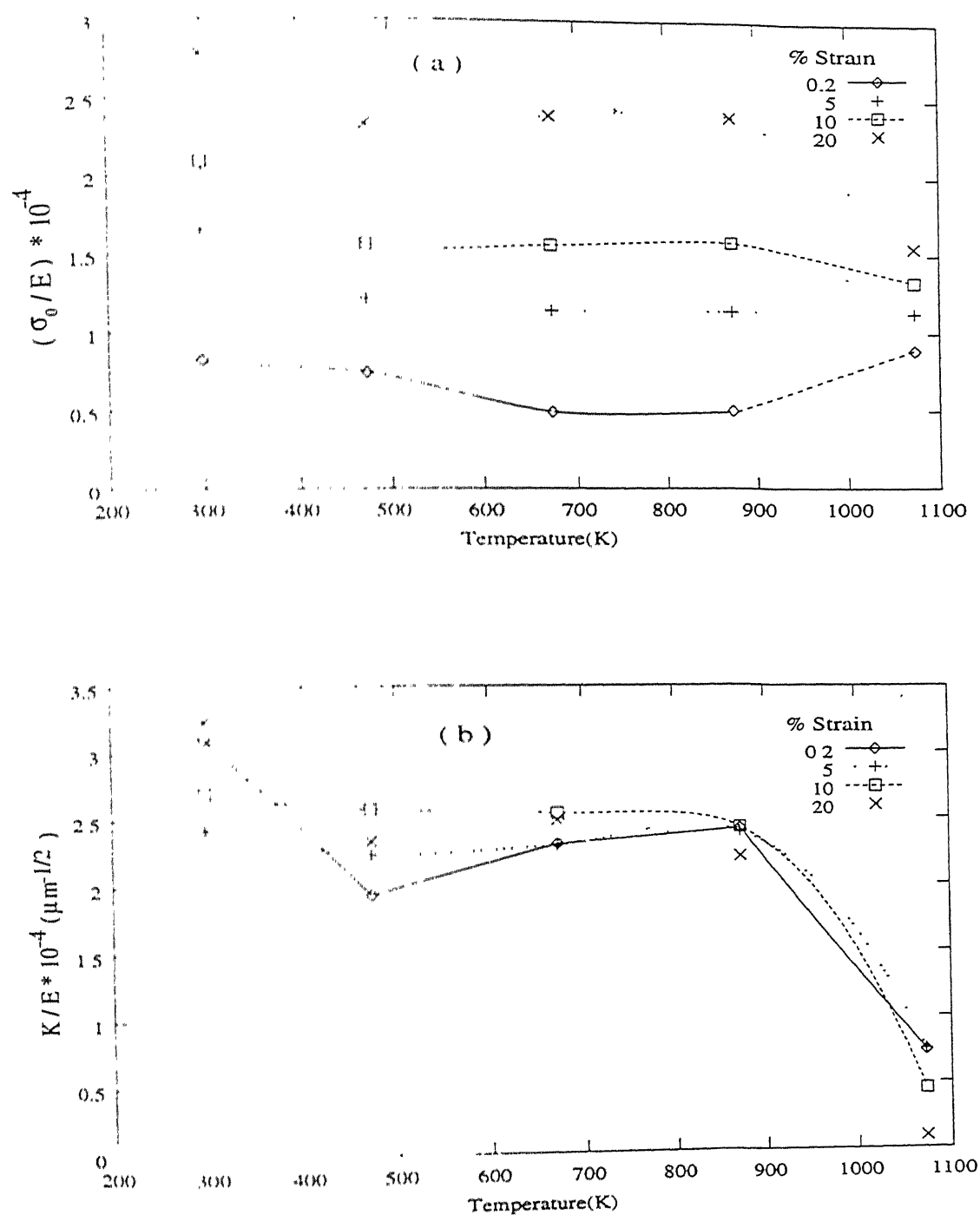


Figure 5.17: Variation of normalised Hall-Petch parameters: (a) σ_0/E (b) K/E with temperature in the coarse grain regime of batch 1.

5.18a. Further, slow decrease in $\sigma_0(\epsilon)$ above 400°C occurs due to the temperature assisted cross-slip of dislocations.

In the temperature range of room temperature to 200°C , $K(\epsilon)$ generally shows slow decrease with increasing temperature as illustrated in figure 4.40b. In this region the thermal activation aids the overcoming of short range stress field and it results in the decrease of $K(\epsilon)$ with temperature. Above 200°C , the combined effect of a work hardened mantle zone in the vicinity of the grain boundary and temperature leads to dynamic recovery via easy cross slip and cell formation. In addition to this, the relaxation of stress field of EGBDs above 200°C as discussed above leads to rapid decrease in $K(\epsilon)$. This decrease can also be seen in the variation of $K(\epsilon)/E$ with temperature (figure 5.18b). It is clear from figure 4.40b that the rate of drop in $K(\epsilon)$ increases with increasing strain. This is primarily due to the faster dynamic recovery with increasing strain. The initial slow decrease in $K(\epsilon)$ observed in figure 4.40b is due to the effect of temperature on elastic modulus. This is clearly evident in the normalised plots of $K(\epsilon)/E$ versus temperature in figure 5.18b.

5.3 Effect of temperature on flow stress

There are two contributions to the flow stress of polycrystals: (i) contribution from the grain interior and (ii) contribution from the grain boundary and its vicinity. The first term, in both the Hall-Petch model (equation 2.18) and the composite model (equation 2.34), represents the grain interior component of flow stress, while the second term in the two models represents the contribution from the grain boundaries and their vicinity. In order to analyse the variation of the relative importance of these two components as a function of strain, grain size and temperature, the fractional contributions of the grain interior (C_i) and the grain boundary regime (C_b) are calculated. The fractional

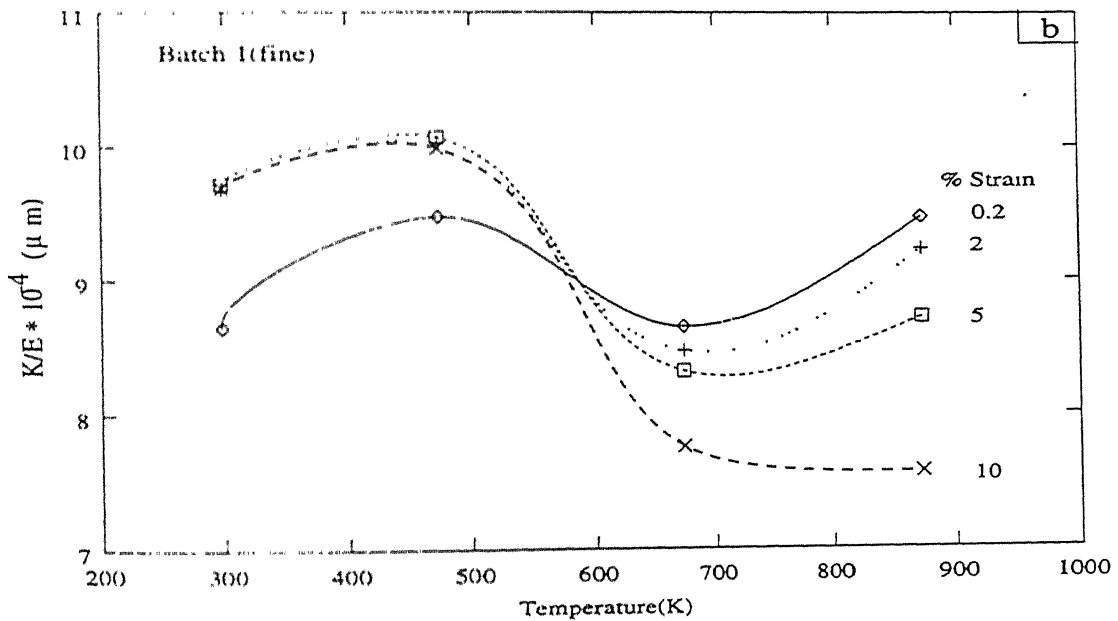
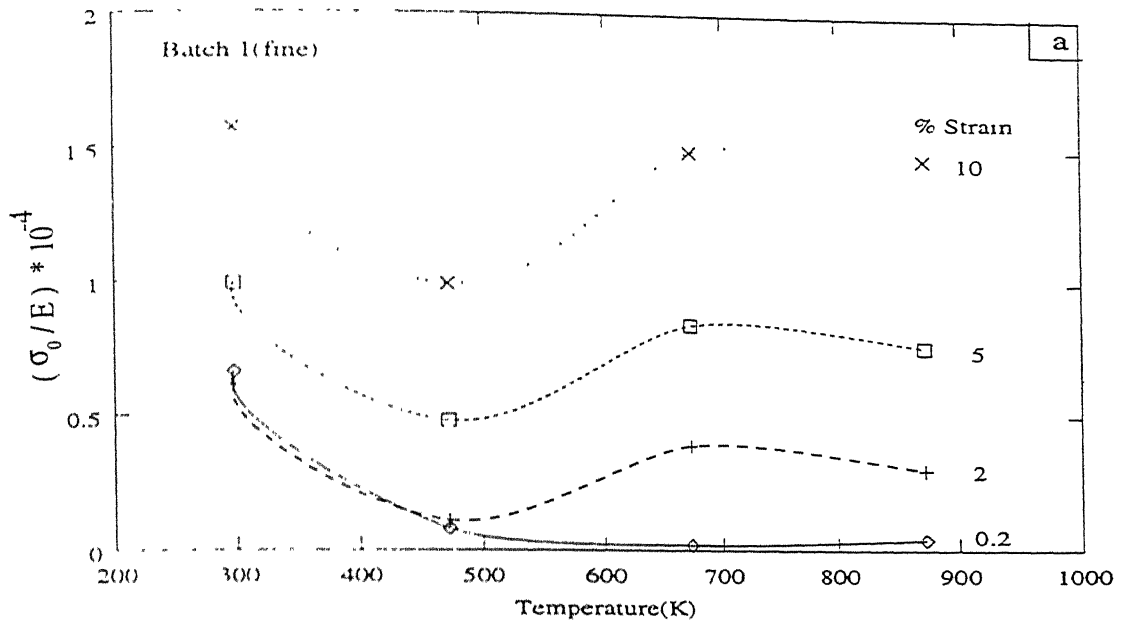


Figure 5.18: Variation of normalised Hall-Petch parameters: (a) σ_0/E (b) K/E with temperature in the fine grain regime of batch 1.

contribution from the grain interior (C_i) is defined as:

$$C_i = \frac{\sigma_0(\epsilon)}{\sigma(\epsilon)} \quad (5.4)$$

where, $\sigma_0(\epsilon)$ is the parameter in equation 2.18 (Hall-Petch model) or in equation 2.34 (composite model). Similarly the fractional contribution from the grain boundary regime (C_b) is defined as:

$$C_b = \frac{K(\epsilon)d^{-1/2}}{\sigma(\epsilon)} \quad (5.5)$$

also,

$$C_b = \frac{K(\epsilon)d^{-1}}{\sigma(\epsilon)} \quad (5.6)$$

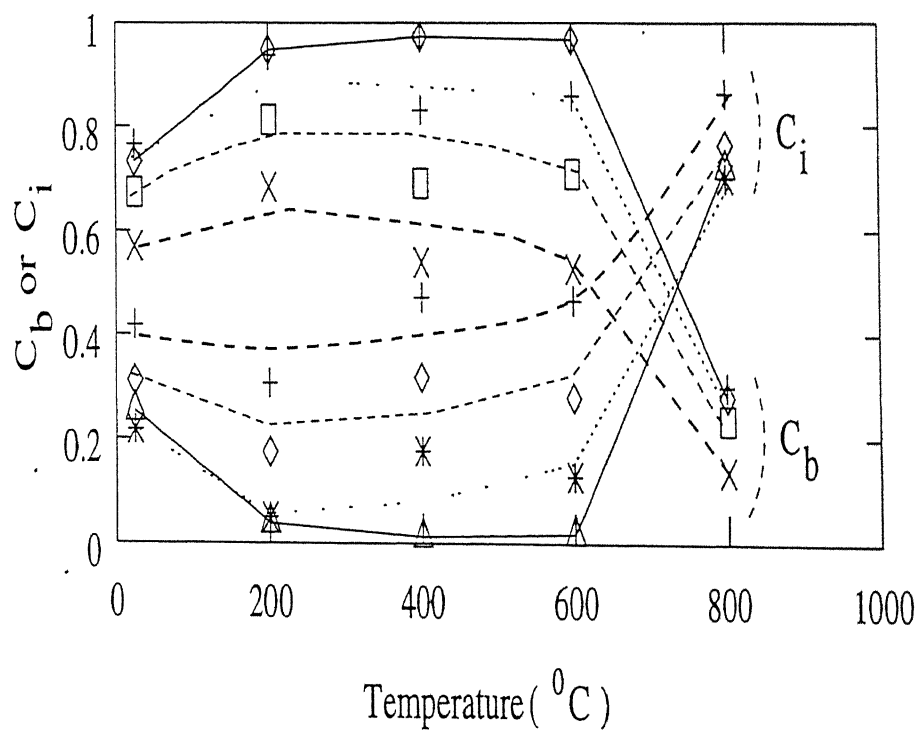
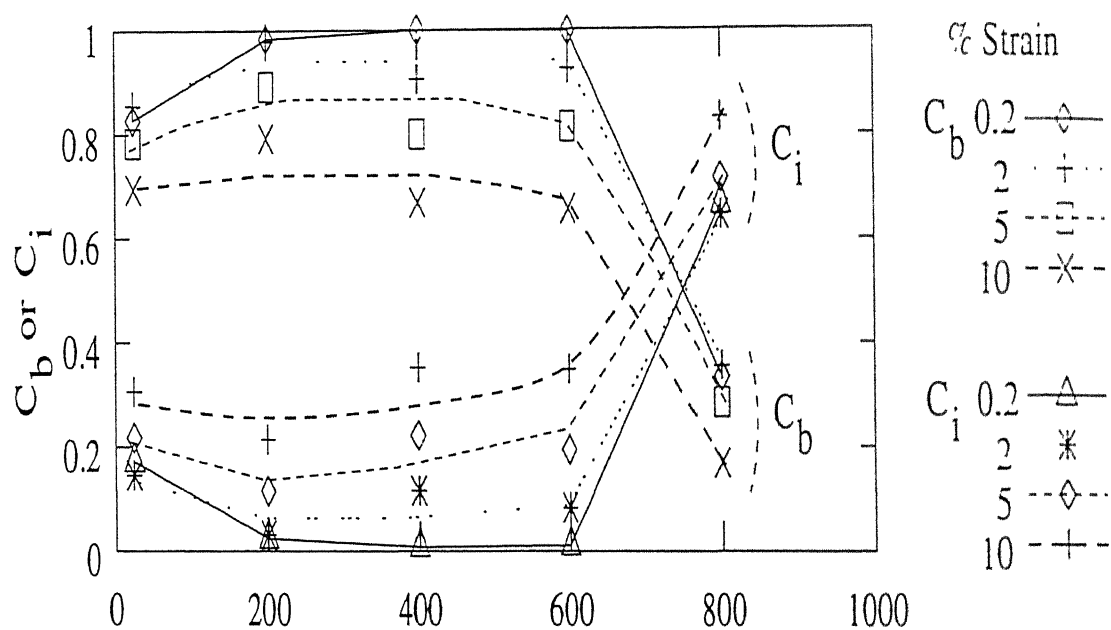
where, $K(\epsilon)$ in equation 5.5 corresponds to the parameter in equation 2.18 (Hall-Petch model), and $K(\epsilon)$ in equation 5.6 corresponds to the parameter in equation 2.34 (composite model). $\sigma(\epsilon)$ is the overall flow stress of the polycrystal. It is clear from above that the values of C_i and C_b will vary between 0 to 1, and the sum $C_i + C_b$ will always be unity.

The variation of C_i and C_b with temperature at different strains in samples of various grain size are shown in figure 5.19. In the fine grain regime ($< 6\mu m$) at low strains (below 2 %), C_i is negligible as compared to C_b in the temperature range of room temperature to $600^\circ C$ (figures 5.19a-b). At strains beyond 2% in the above temperature range, C_b remains higher than C_i . However, above $600^\circ C$, C_b rapidly decreases and consequently C_i increases with temperature at all strains. It can also be observed from figures 5.19a-b that at a given temperature, C_b decreases while C_i increases with increasing strain. In the coarse grain regime ($> 6\mu m$), C_i is comparatively higher than C_b at a given strain in the entire range of temperature from room temperature to $800^\circ C$ (figures 5.19c-d). Thus it can be concluded that the contribution to flow stress shifts from the grain boundary dominance to the grain interior dominance with increasing grain size and strain. Also the rapid drop in flow stress with temperature at approximately $600^\circ C$ (see figures 4.32a-d) in the fine grain regime can be mainly attributed to the rapid drop in the contribution of the grain boundaries to flow stress. While in the coarse grain regime, at strains above

2%, both the contributions from the grain interior and the grain boundary region are responsible for rapid drop in the flow stress at temperatures above 600°C .

As discussed in section 5.1.1 that prior to deformation, the substructure of fine grained specimens consists of hard mantle zone in the grain boundary region, while in the case of coarse grained specimens, there is no hard mantle zone. At temperatures of 600°C and above, the rapid drop in C_b in the fine grained samples occurs via high temperature recovery processes, such as annihilation of EGBDs, as discussed in section 5.2. This leads to the experimentally observed rapid drop in yield and flow stress. In the coarse grained samples, the occurrence of dynamic strain aging and intragranular dislocation slip even at 800°C for lower strains (as concluded in section 5.2) does not lead to significant change in the grain interior contribution over the entire temperature range (from room temperature to 800°C). The small decrease in the grain boundary contribution above 600°C is compensated by an increase in the grain interior contribution and no significant change in yield stress occurs with temperature in the coarse grain regime. However, at higher strains the combined effect of high temperature recovery processes in the grain interior and the grain boundary region leads to experimentally observed pronounced drop in flow stress above 600°C (see figures 4.32c-d). Thus it can be concluded that the rapid drop in flow stress in the fine grain regime is mainly due to the significant drop in the grain boundary contribution to flow stress. The occurrence of high temperature recovery processes both in the grain interior and in the grain boundary region is responsible for significant drop in flow stress at higher strains in the coarse grain regime.

Since the flow stress of the fine grained samples is mainly controlled by the grain boundary region, the variation of flow stress with temperature at different strain levels for samples of the fine grain sizes can be understood from the knowledge of dislocation processes in the grain boundary region. In the following section a model based on dislocation dynamics at and in the vicinity of the grain boundaries has been proposed to explain the variation of flow stress with temperature.



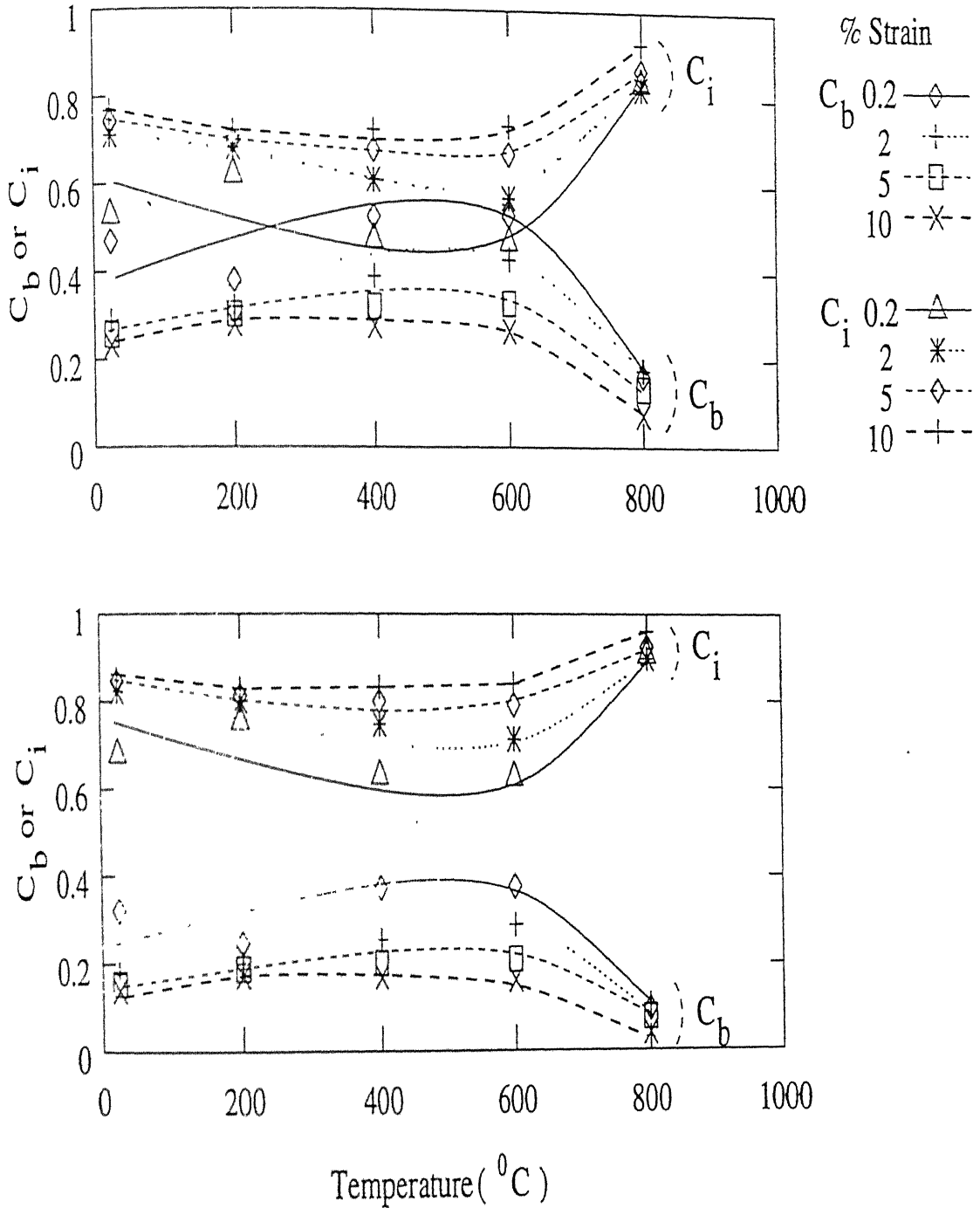


Figure 5.19: Variation of relative contribution of grain boundary regime (C_b) and grain interior regime (C_i) with temperature at different strain levels in the sample with grain sizes: (a) $2.7\mu\text{m}$, (b) $4.5\mu\text{m}$, (c) $18.3\mu\text{m}$ and (d) $64.0\mu\text{m}$.

5.3.1 A model based on dislocation dynamics to estimate the dislocation density at and in the vicinity of the grain boundaries

During plastic deformation, the mobile dislocations interact with the grain boundaries [123, 129, 130] resulting in the creation of extrinsic grain boundary dislocations (EGBDs), as shown in figure 2.8a. EGBDs are also created when migrating grain boundaries sweep up lattice dislocations during recrystallisation and grain growth, as already discussed in chapter 2 (section 2.4). At relatively low annealing temperatures and times (used in the production of fine grain size samples), the process of sweeping up of dislocations by grain boundaries and subsequent annihilation of EGBDs may remain incomplete. The microstructures of the fine grain size samples would contain non-equilibrium grain boundaries and adjacent region of high dislocation density (which has been termed as the mantle zone). The stress field of EGBDs can be partially relaxed by the process (discussed in chapter 2, section 2.4) of spreading of the EGBDs core [4] or by dissociation of EGBDs [131] into a number of dislocations with small burgers vectors. However, as discussed in section 5.2.3, such a process can only explain the disappearance of the EGBDs contrast in the TEM image but is unable to explain the complete annihilation of EGBDs which would require the value of the total burgers vector to go to zero.

The complete annihilation of EGBDs is believed to occur by the process of climb, under the influence of their interacting stress fields, towards the triple points [13, 89] as discussed in detail in chapter 2 (section 2.4). There are three processes occurring during deformation: (i) the mobile lattice dislocations entering in the vicinity of grain boundaries; (ii) the interaction of mobile dislocations with the grain boundaries leading to creation of EGBDs; and (iii) the annihilation of EGBDs by the process of climb at the grain boundaries. Thus the net density of dislocations in the grain boundary region can be estimated by the addition of the relative contribution of these processes. In order to estimate the net density of dislocations in the grain boundary region, the rate of

accumulation of dislocations in the grain boundary region and the rate of annihilation of EGBDs is estimated. These two rates of accumulation and annihilation is added to obtain the net density of dislocations in the grain boundary region.

5.3.1.1 Rate of accumulation of dislocations at and in the vicinity of the grain boundaries

Ashby's dislocation model [61] separates the grain interior and the grain boundary region with different densities of dislocations. This occurs because of the difference in dislocation behaviour in these two regions [35, 132, 133]. Ashby denoted the dislocation population well away from the boundary as ρ^s (statistically stored dislocations) and that in the vicinity of the grain boundaries by ρ^g (geometrically necessary dislocations). ρ^g depends on strain (ϵ) and grain size (d) as follows [61]:

$$\rho^g = \frac{\epsilon}{4 b d} \quad (5.7)$$

where, b is the burger vector. Further, Thompson *et al.* [57] suggested that ρ^g becomes independent of strain at higher strains. Bergstrom [134] in his formulation of dislocation model assumed that the rate of generation of dislocations with respect to strain is directly proportional to the instantaneous dislocation density. And at a constant strain the dislocation density is found to be inversely proportional to the grain size [135–138]. It is proposed by Varin *et al.* [11] that the rate of formation of EGBDs is constant for a constant strain rate. However, they assumed that the total length of mobile dislocations is shared by the grain boundaries only. This is not a reasonable assumption because a large density of mobile dislocations may remain in the grain interior.

Thus from above arguments, it is reasonable to assume that the rate of accumulation of dislocations entering in the grain boundary regime and the subsequent formation of EGBDs is inversely proportional to the grain size as follows:

$$\left. \frac{d\rho}{d\epsilon} \right|_{\text{accumulation}} = \frac{K_1}{d} \quad (5.8)$$

where, K_1 is a proportionality constant. The value of K_1 can be determined from the experimentally measured dislocation density. For a constant strain rate ($\dot{\epsilon}$), $\frac{d\rho}{dt}$ may be considered as a rate function.

5.3.1.2 Rate of annihilation of EGBDs

The schematic arrangement of EGBDs at the grain boundaries (during deformation) is shown in figure 5.20a. Figure 5.20b shows a magnified arrangement of EGBDs at a particular boundary and pile-up of dislocations. In this figure, S is the source of dislocation generation in the grain interior. At sufficiently high temperatures the EGBDs can be annihilated by the process of climb, under the influence of their interacting stress fields, towards the triple points [13]. However this climb process results in the displacement of adjacent grains which must be accommodated at triple points without destroying the integrity of the material. Such a process must result in the migration of the grain boundaries over small distances [9]. This is confirmed by the wavy nature of the grain boundaries observed in samples deformed at 800°C (see figures 4.42a-c). Thus for climb of EGBDs the required flow of vacancies to the end of extra half planes involves diffusion through the lattice as well as the grain boundary. Since diffusion through the lattice is the slower process, it would be the rate controlling step.

Figure 5.20b shows a schematic of EGBDs at a grain boundary at a given strain and temperature. From this figure it can be seen that an outward flow of vacancies from triple point B , will result in the climb of lead dislocation toward the triple point, while the reverse is true for triple point A . According to Grabski *et al.* [116] and Varin *et al.* [91], the annihilation occurs by the reaction with other EGBDs climbing to the triple point on adjacent grain boundaries. Applying the above hypothesis, Sangal *et al.* [13] obtained the rate of annihilation of EGBDs from the consideration of vacancy flow by the assistance of stress field of EGBDs as follows:

$$\left. \frac{d\rho}{dt} \right|_{\text{annihilation}} = - \frac{GVD_0 \exp(-Q/RT)[1 - 2\ln(r_0)/L]\rho^2}{L(1 - \nu)kT \ln(R_0/r_0)} \quad (5.9)$$

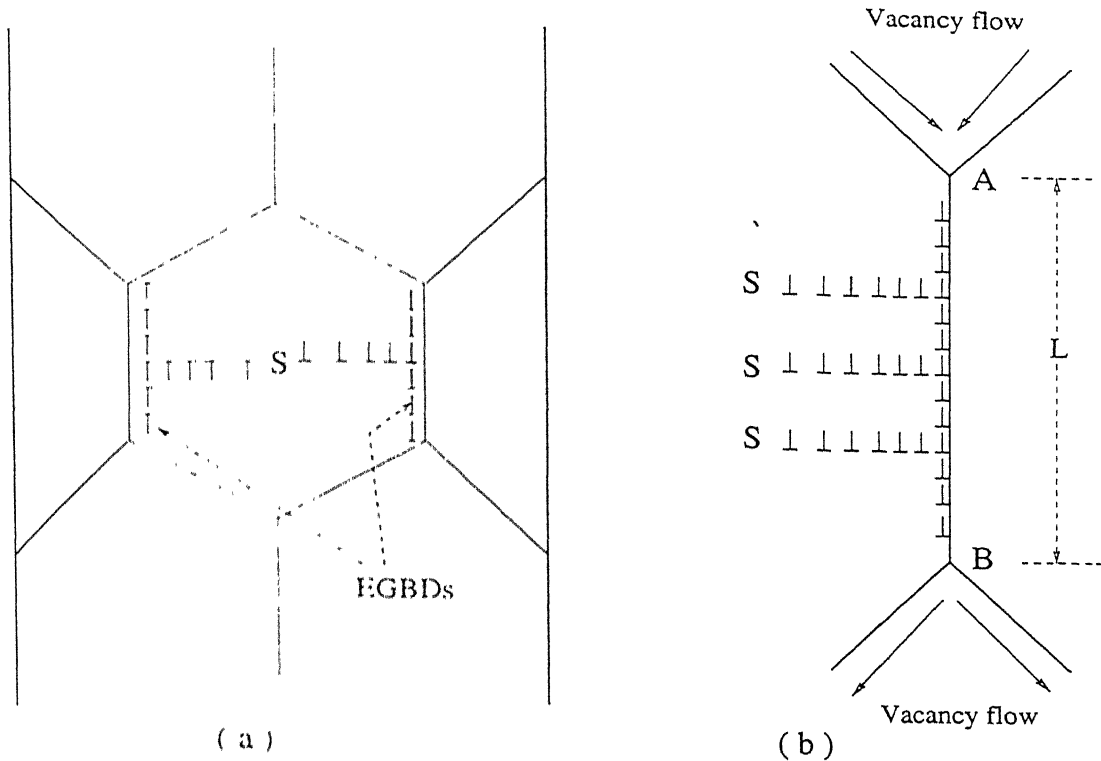


Figure 5.20: A schematic of (a) pile-up of dislocations and accumulated EGBDs at grain boundaries, and (b) Pile-ups and process of annihilation of EGBDs through vacancy flow at a grain boundary segment.

where, G = shear modulus, V = atomic volume, D_0 = lattice diffusion coefficient at absolute temperature, r_0 is taken to be equal to the magnitude of the burgers vector, b , R_0 is taken to be half the length (L) of the grain boundary segment², i.e., $L/2$, Q = activation energy for lattice diffusion, ρ = density of EGBDs, ν = Poisson's ratio and k = Boltzaman's constant.

In order to study the effect of test temperature in the present work, it is assumed that equation 5.9, which has been derived for the static case, is also applicable dynamically during deformation. Thus, from equation 5.9, the dynamic annihilation rate of EGBDs

²For the ideal six sided grains in two dimensional microstructure, $L = l/2$, where l is the mean intercept length and the grain size d has been defined as, $d = 1.74l$ (see section 3.3.2.1)

can be expressed as (L in equation 5.9 has been substituted by $d/3.28$):

$$\frac{d\rho}{d\epsilon}|_{\text{annihilation}} = \frac{d\rho}{dt} \frac{dt}{d\epsilon} = \frac{1}{\dot{\epsilon}} \frac{d\rho}{dt} = -\frac{3.28GV D_0 \exp(-Q/RT)[1 - 2\ln(3.28b/d)]\rho^2}{\dot{\epsilon}d(1-\nu)kT\ln(d/6.56b)} \quad (5.10)$$

5.3.1.3 Net density of dislocations at and in the vicinity of grain boundaries

The net rate of accumulation of dislocations in the grain boundary region is the sum of both the rates of accumulation and annihilation of dislocations at the grain boundaries. Thus from equations 5.8 and 5.10, the net rate of accumulation of dislocations in the grain boundary region can be expressed as follows:

$$\frac{d\rho}{d\epsilon}|_{\text{net}} = \frac{d\rho}{d\epsilon}|_{\text{accumulation}} + \frac{d\rho}{d\epsilon}|_{\text{annihilation}} \quad (5.11)$$

or,

$$\frac{d\rho}{d\epsilon}|_{\text{net}} = C_1 - C_2\rho^2 \quad (5.12)$$

where,

$$C_1 = \frac{K_1}{d} \text{ and, } C_2 = \frac{3.28GV D_0 \exp(-Q/RT)[1 - 2\ln(3.28b/d)]}{\dot{\epsilon}d(1-\nu)kT\ln(d/6.56b)} \quad (5.13)$$

Integrating equation 5.12 with the initial conditions: at $\epsilon = 0$, $\rho = \rho_0$ (initial dislocation density).

$$\int_{\rho_0}^{\rho} \frac{d\rho}{C_1 - C_2\rho^2} = \int_0^{\epsilon} d\epsilon \quad (5.14)$$

By taking partial fractions:

$$\frac{1}{2\sqrt{C_1}} \left[\int_{\rho_0}^{\rho} \frac{d\rho}{\sqrt{C_1} + \sqrt{C_2}\rho} + \int_{\rho_0}^{\rho} \frac{d\rho}{\sqrt{C_1} - \sqrt{C_2}\rho} \right] = \epsilon \quad (5.15)$$

or,

$$\ln \frac{\sqrt{C_1} + \sqrt{C_2}\rho}{\sqrt{C_1} - \sqrt{C_2}\rho} - \ln \frac{\sqrt{C_1} + \sqrt{C_2}\rho_0}{\sqrt{C_1} - \sqrt{C_2}\rho_0} = 2\sqrt{C_1 C_2} \epsilon \quad (5.16)$$

Let,

$$\frac{\sqrt{C_1} - \sqrt{C_2}\rho_0}{\sqrt{C_1} + \sqrt{C_2}\rho_0} = P \quad (5.17)$$

then, equation 5.16 can be written as follows:

$$\rho = \sqrt{\frac{C_1}{C_2}} \left[\frac{\exp(2\sqrt{\frac{C_1}{C_2}}\epsilon) - P}{\exp(2\sqrt{\frac{C_1}{C_2}}\epsilon) - P} \right] \quad (5.18)$$

Equation 5.18 along with equations 5.13 and 5.17 gives the variation of the net dislocation density in the grain boundary region with strain, temperature and grain size.

5.3.1.4 Computation of the net density of dislocations at and in the vicinity of grain boundaries

In the present case, the samples of batch 1 which had been annealed at higher temperatures to obtain the coarse grain size ($> 6\mu m$), are free from hard mantle zone (discussed in section 5.1.1). Thus it is reasonable to assume that the starting dislocation density is negligible in the samples of the coarse grain sizes. While the samples with the fine grain sizes are annealed at comparatively lower temperatures and times and thus possess hard mantle zone in the grain boundary region (see section 5.1.1). Hence, in these samples ρ_0 cannot be neglected. After giving 2 % strain in fully annealed samples of 316 L austenitic stainless steel, Sangal *et al.* [13] measured the dislocation density per unit length at the grain boundaries to be of the order of $10^8/m$. Thus a reasonable values of ρ_0 in the samples of the fine grain sizes can be taken to be 10^9 per unit length.

From equation 5.18, it can be noted that the net density of dislocations in the region of the grain boundaries is a complex function of grain size, strain, strain rate, temperature and initial density of dislocations. The values of the various parameters taken for the calculation of net dislocation density are listed in table 5.1.

At low temperatures, the rate of annihilation of EGBDs can be considered negligible in comparison to the rate of accumulation. Thus equation 5.11 can be written as follows

$$\frac{d\rho}{d\epsilon}|_{net} = \frac{d\rho}{d\epsilon}|_{accumulation} = \frac{K_1}{d} \quad (5.19)$$

Table 5.1: Values of the parameters of equation 5.18 for 316L austenitic stainless steel

Parameter	Value	Reference
k	1.18×10^{-23}	[139]
G	$8.43 \times 10^{10} N/m^2$	[139]
V	$8.38 \times 10^{-30} m^3$	[13]
D_0	$1.74 \times 10^{-4} m^2/s$	[140]
Q	$68 kcal/mol$	[140]
b	$2.52 \times 10^{-10} m$	
ρ_0	$10^9/m$ (in fine grains) 0 (in coarse grains)	

After integration equation 5.19 becomes

$$\rho - \rho_0 = \frac{K_1}{d} \epsilon \quad (5.20)$$

In coarse grained 316L austenitic stainless steel samples ($d = 18.0 \mu m$), ρ at 2 % strain is $10^8 /m$ (experimentally measured by Sangal *et al.* [13]). Substituting the values in the equation 5.20, we obtain $K_1 = 9 \times 10^4$. This value of K_1 is used for the calculation of ρ_{net} at different temperatures, strain and for grain sizes in equation 5.18.

5.3.2 Comparison of the calculated variation of dislocation density with the observed variation in the flow stress

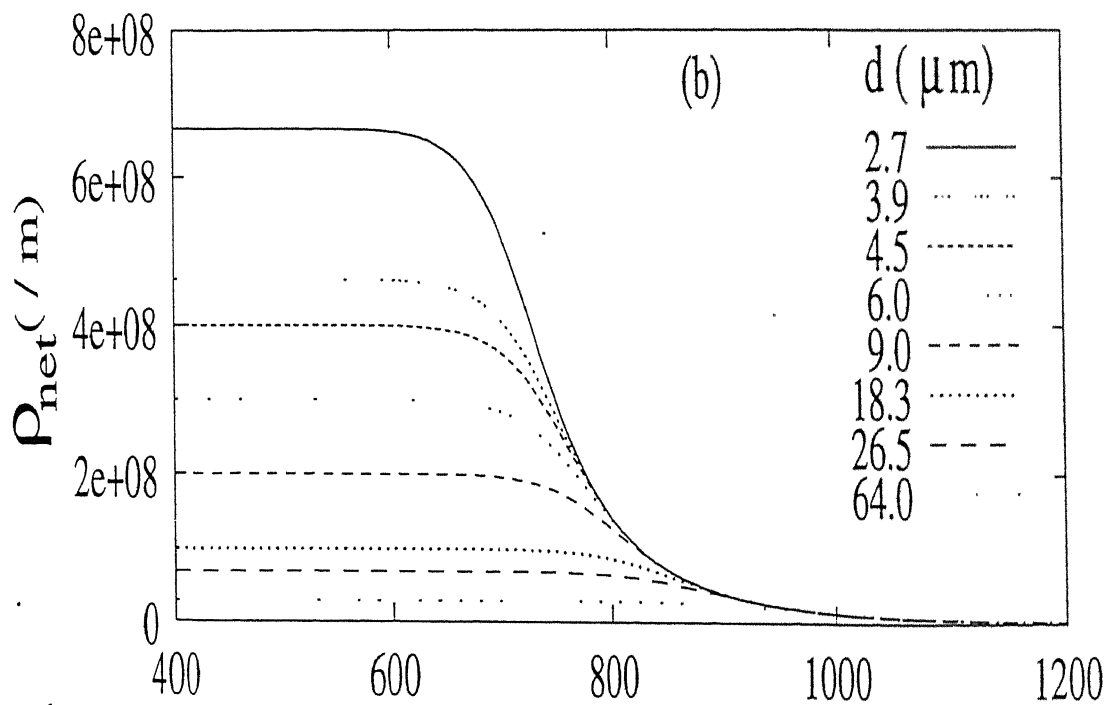
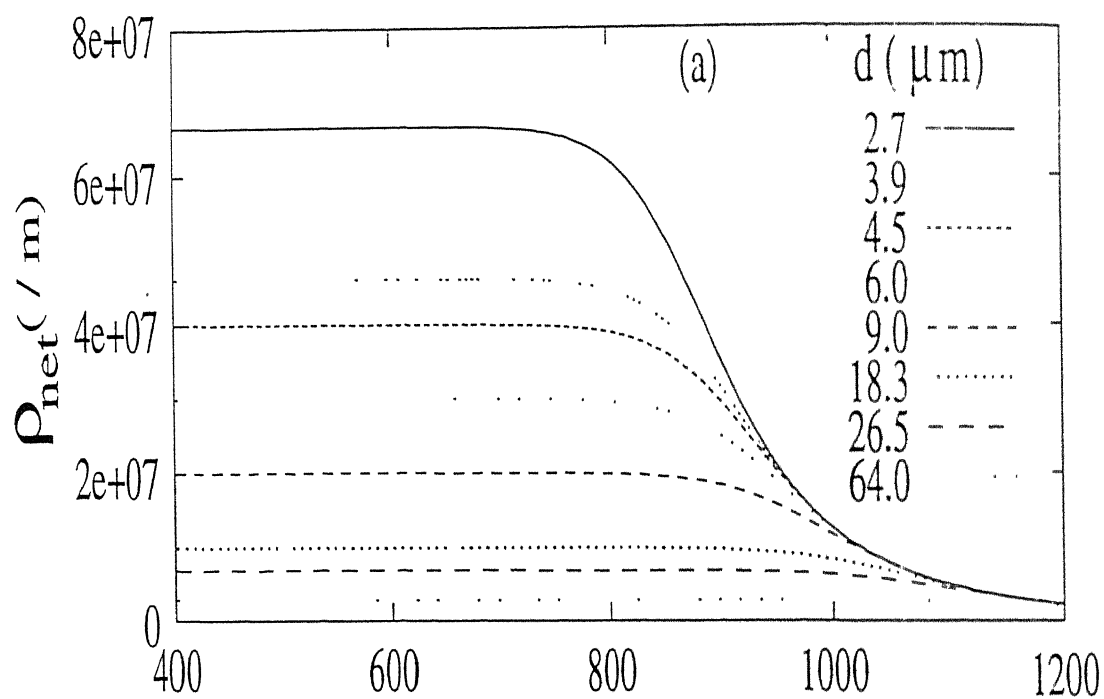
Figures 5.21a-d show the dependence of calculated net dislocation density in the grain boundary region with temperature for different grain sizes at 0.2 %, 2 %, 10 % and 20 % strain levels respectively for $\rho_0 = 0$. ρ_{net} remains more or less unchanged below a certain temperature and subsequently drops rapidly with increasing temperature. The effect of

initial dislocation density on variation of ρ_{net} in the fine and in the coarse grain regimes are shown in figures 5.22 and 5.23 respectively. It is clear from these figures that the sharp transition temperature³ is a function of grain size, strain and initial dislocation density. The variations of net dislocation density in the grain boundary region with temperature for fine ($d = 2.7\mu m$) and coarse ($d = 64.0\mu m$) grain size are shown in figures 5.24 and 5.25 respectively. The difference in ρ_{net} between two grain sizes increases with increasing strain. Figures 5.26a-b show the variation of ρ_{net} with strain at different temperatures for the fine and the coarse grain sizes. ρ_{net} increases linearly with strain below $500^\circ C$ and above $500^\circ C$ the rate gradually decreases with strain and temperature in the fine grain size. While in the coarse grain size the rate started to decrease above $600^\circ C$ with strain and temperature as shown in figure 5.26b. At a given strain, with increasing grain size the transition temperature increases (figures 5.27a-b). It can be noted from figures 5.27a-b that the transition temperature for a given ρ_0 , significantly decreases in the fine grain regime with decrease in grain size. It also decreases with increasing ρ_0 for a given grain size. Figures 5.28a-b show decrease in transition temperature with increase in strain for a given grain size and ρ_0 .

From a comparison of the computed results of dislocation density (figures 5.21-5.28) and the variations of experimental flow stress and Hall-Petch parameter $K(\epsilon)$ with temperature (figures 4.32a-d, 4.39b and 4.40b), the following important conclusions can be drawn.

1. The general trend of variation of ρ_{net} with temperature for different grain sizes at various strains and initial dislocation density, is similar to the experimental variation of yield or flow stress with temperature (figures 4.32a-d).
2. For low initial dislocation density ($< 10^6/m$), the transition temperature at 0.2 % strain is higher than $800^\circ C$, even in the fine grain size of $d = 2.7\mu m$ (figures 5.22a-b). However, for higher initial dislocation density ($10^9/m$), the transition temperature a

³The temperature at which the ρ_{net} drops by 10% from its stable value



Temperature ($^{\circ}\text{C}$)

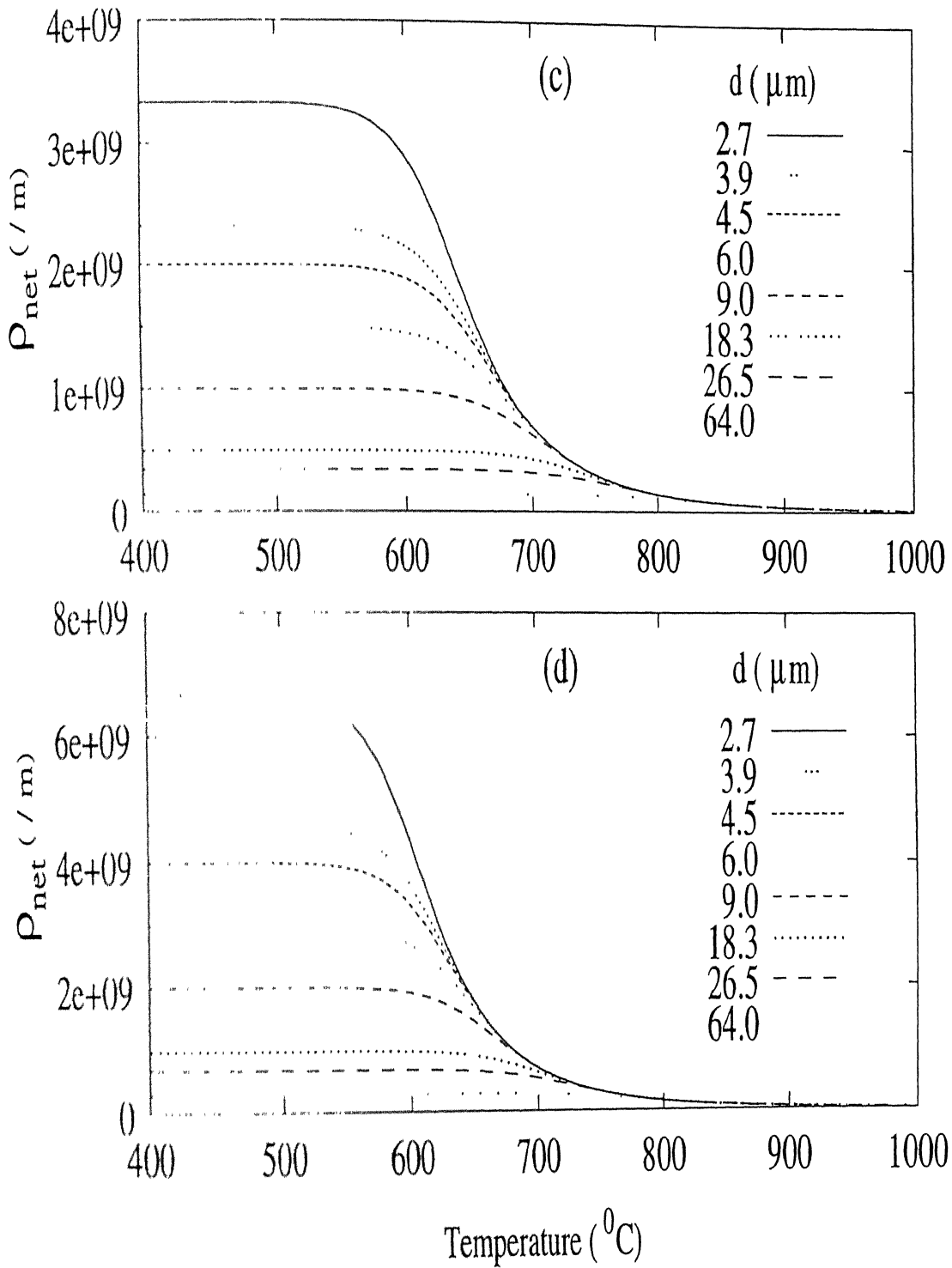


Figure 5.21: Variation of net dislocation density with temperature at % strains: (a) 0.2, (b) 2, (c) 10 and (d) 20.

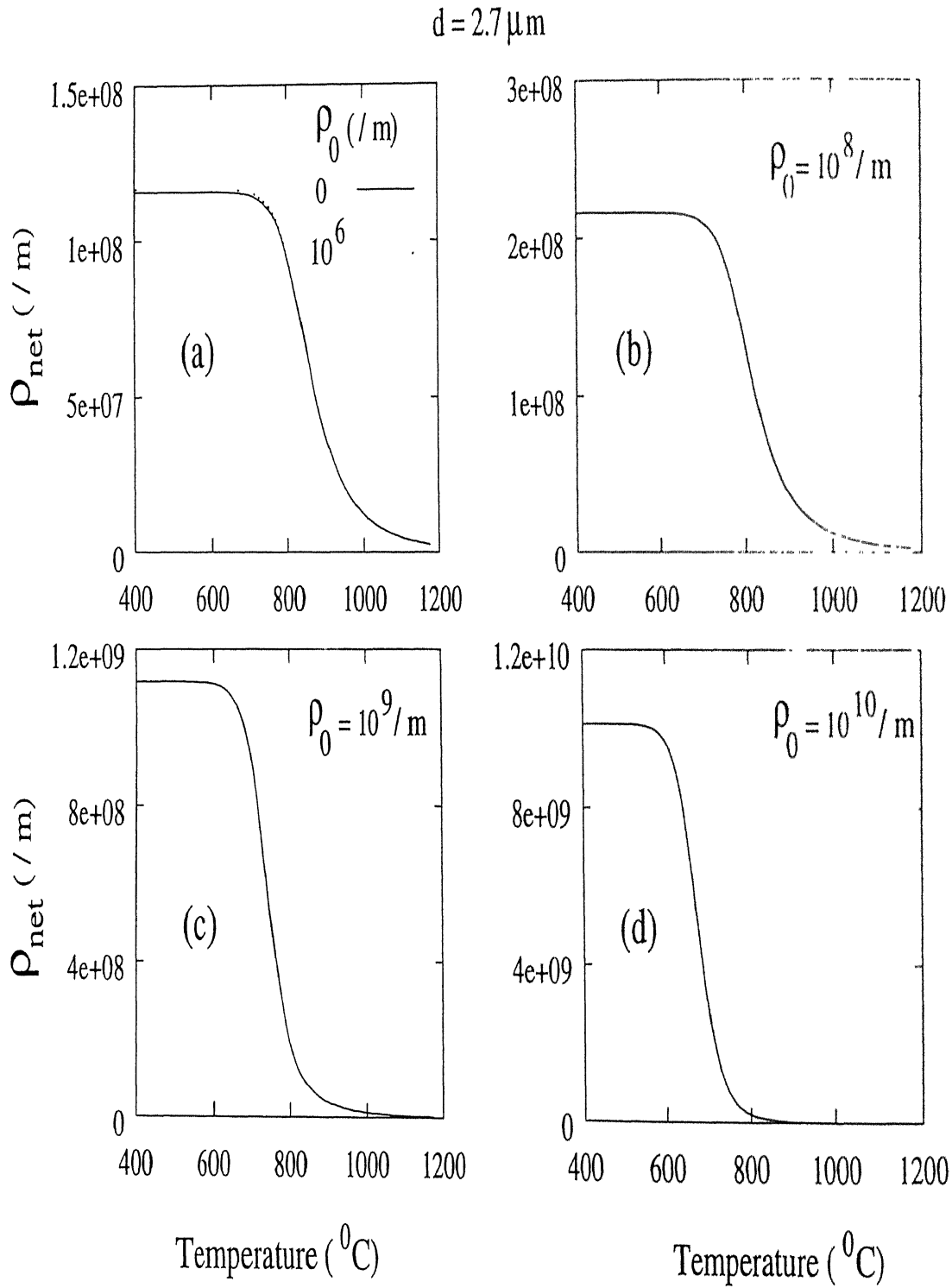


Figure 5.22: Variation of net dislocation density with temperature in the sample of $2.7 \mu\text{m}$ grain size at 0.2% strain for ρ_0 values of (a) 0 and 10^6 , (b) 10^8 , (c) 10^9 and (d) 10^{10} .

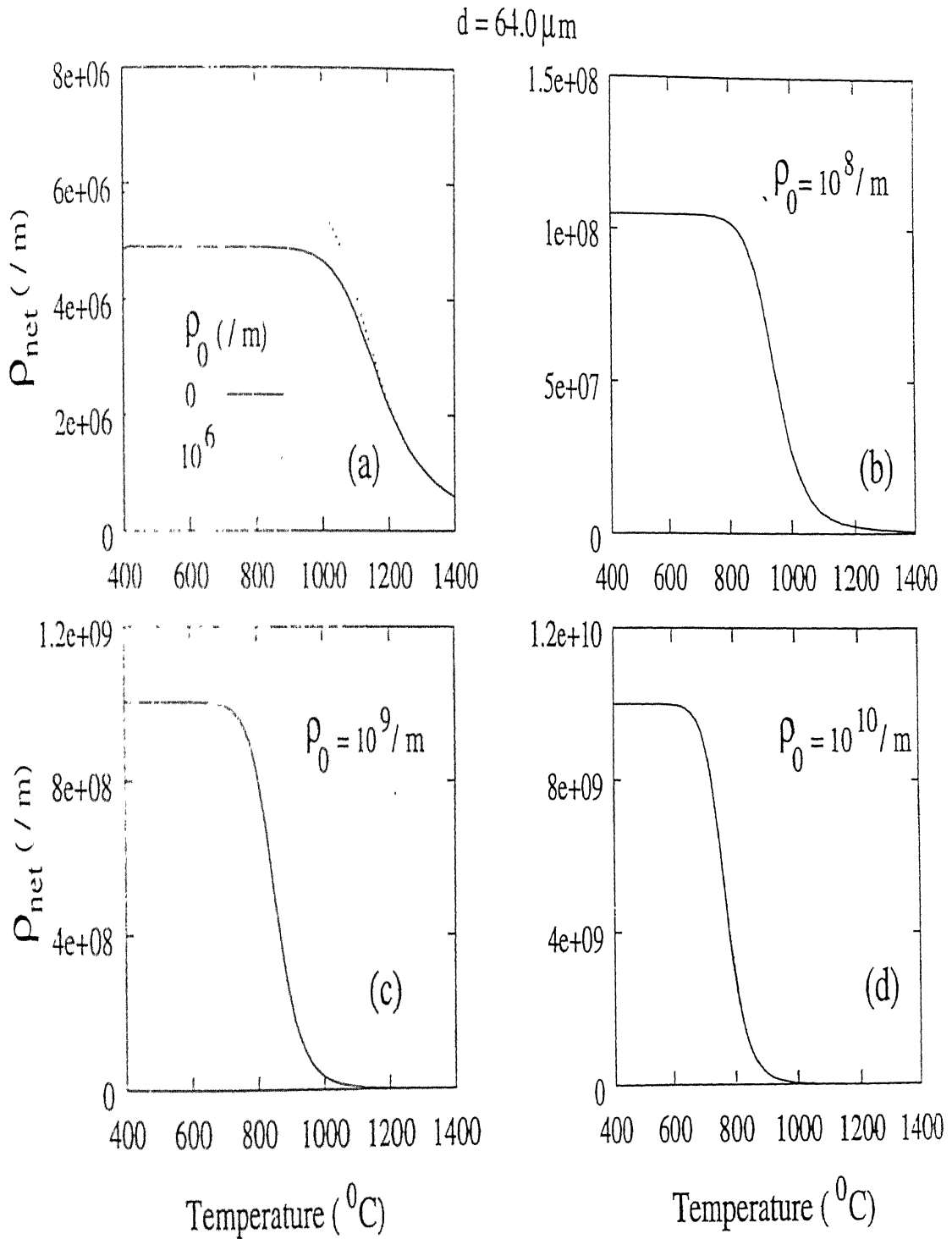


Figure 5.23: Variation of net dislocation density with temperature in the sample of $64 \mu\text{m}$ grain size at 0.2% strain for ρ_0 values of (a) 0 and 10^6 , (b) 10^8 , (c) 10^9 and (d) 10^{10} .

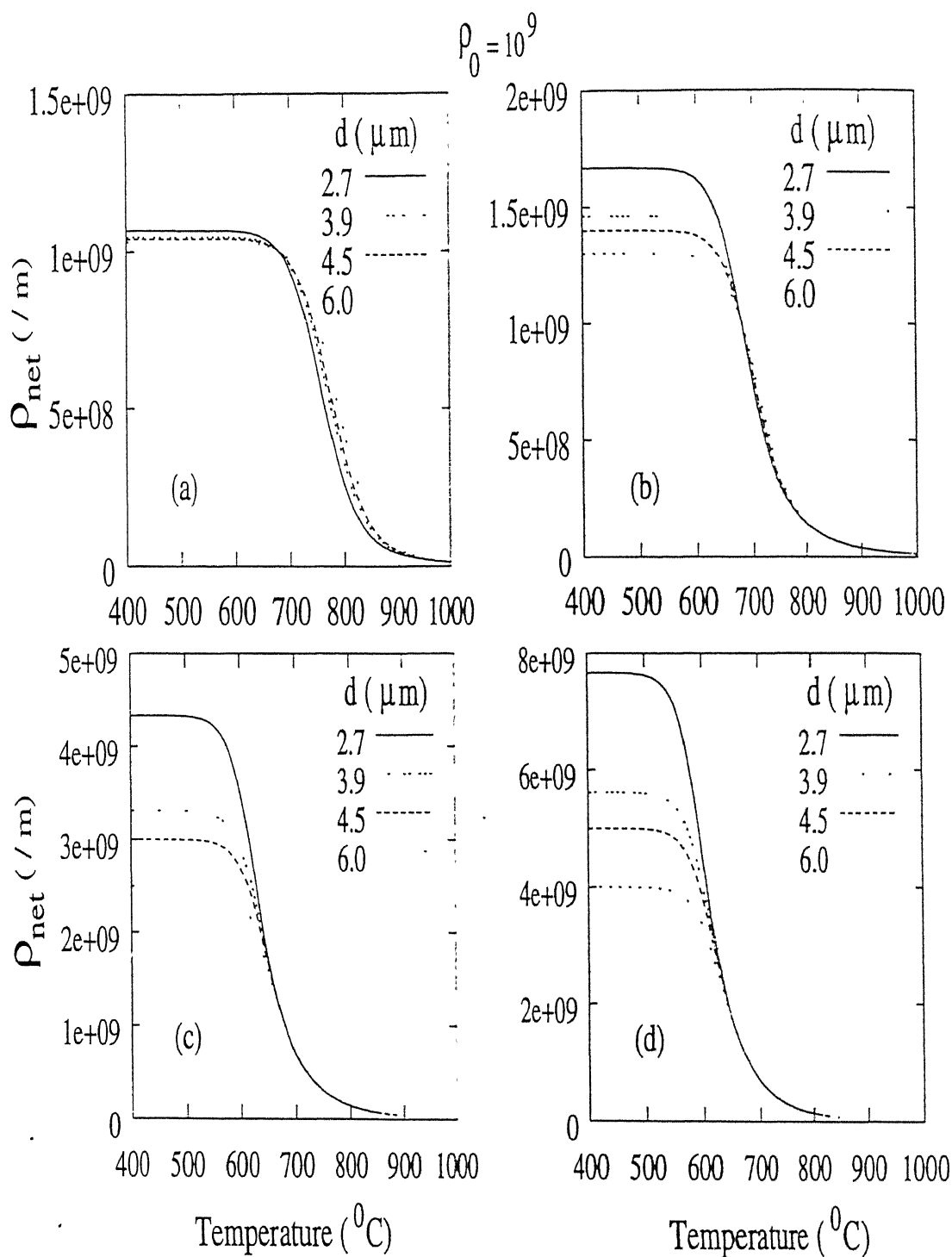


Figure 5.24: Variation of net dislocation density with temperature in the sample of 2.7 μm grain size at % strains: (a) 0.2, (b) 2, (c) 10 and (d) 20.

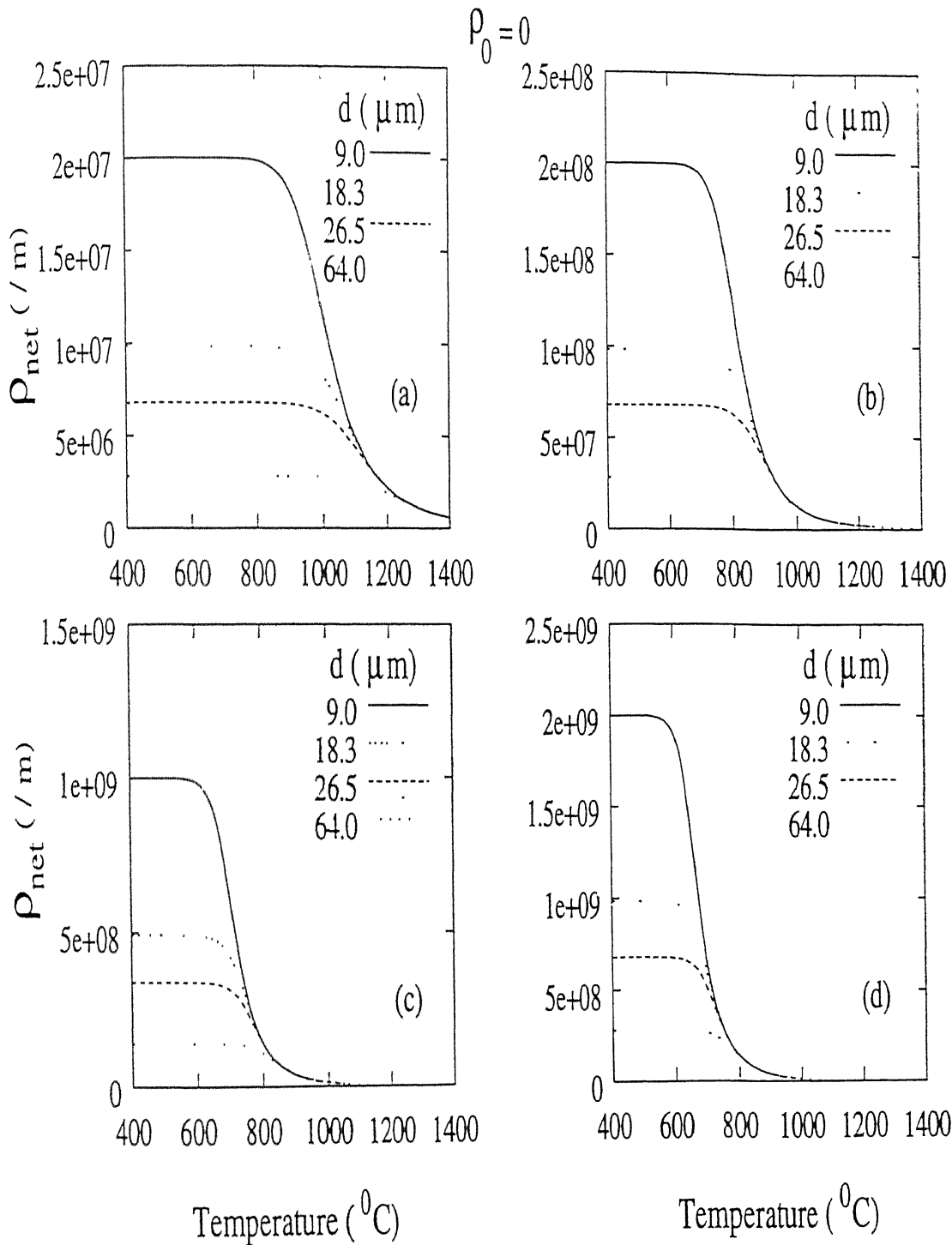


Figure 5.25: Variation of net dislocation density with temperature in the sample of 64. μm grain size at % strains: (a) 0.2, (b) 2, (c) 10 and (d) 20.

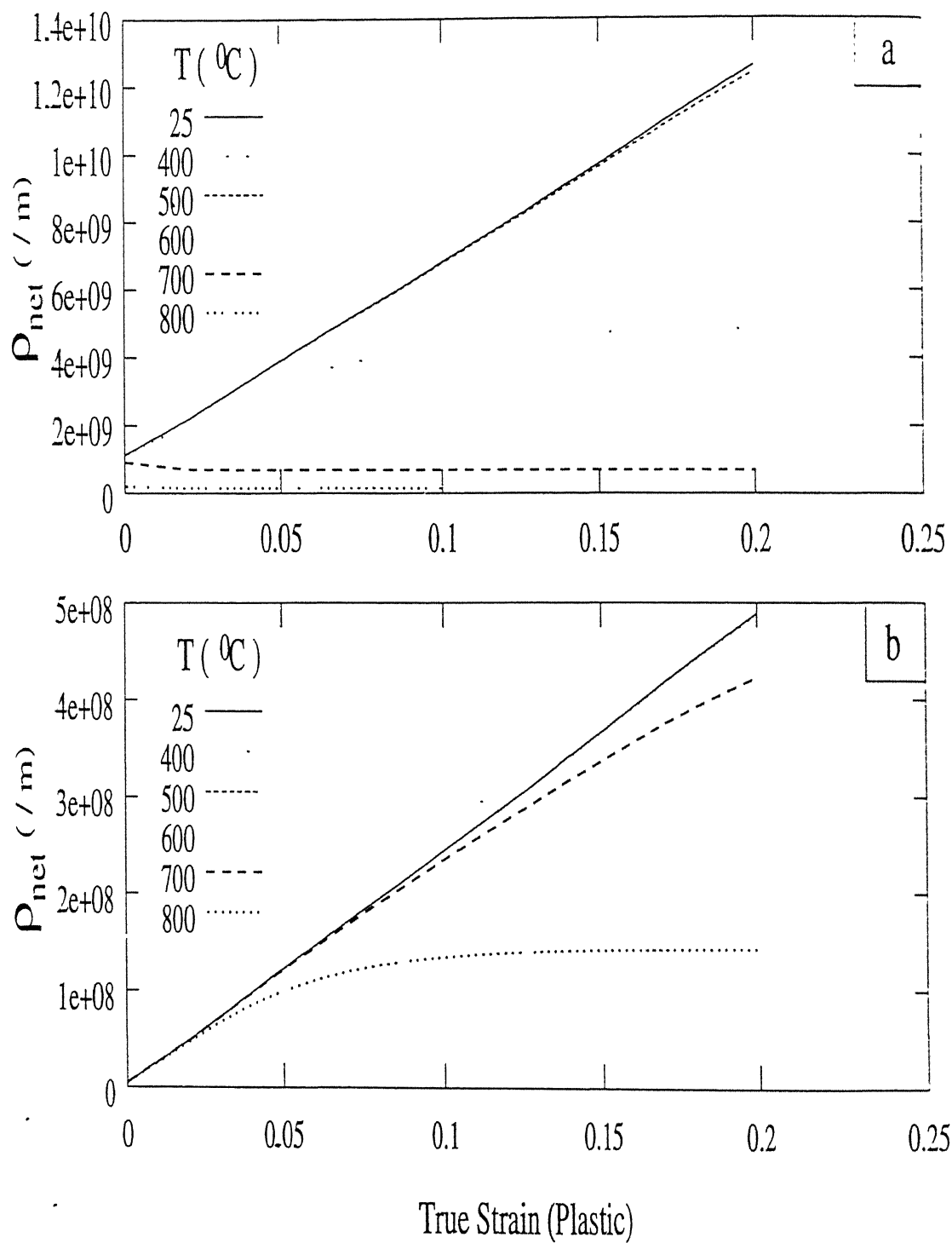


Figure 5.26: Variation of net dislocation density with strain at different temperatures in the sample with grain sizes of (a) $2.7 \mu\text{m}$ and (b) $64.0 \mu\text{m}$.

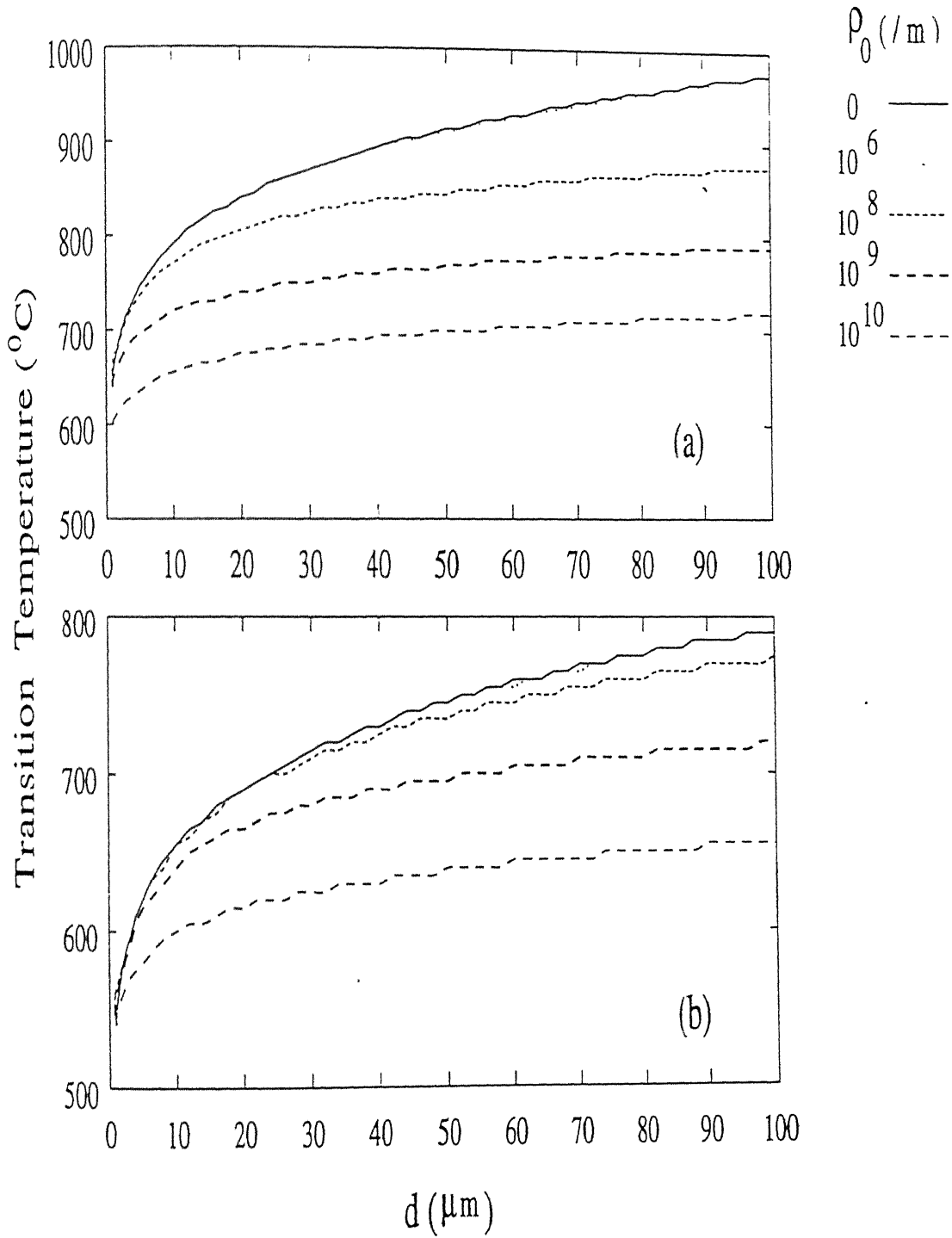


Figure 5.27: Variation of the transition temperature with grain size for different values ρ_0 at % strains: (a) 0.2 and (b) 2.

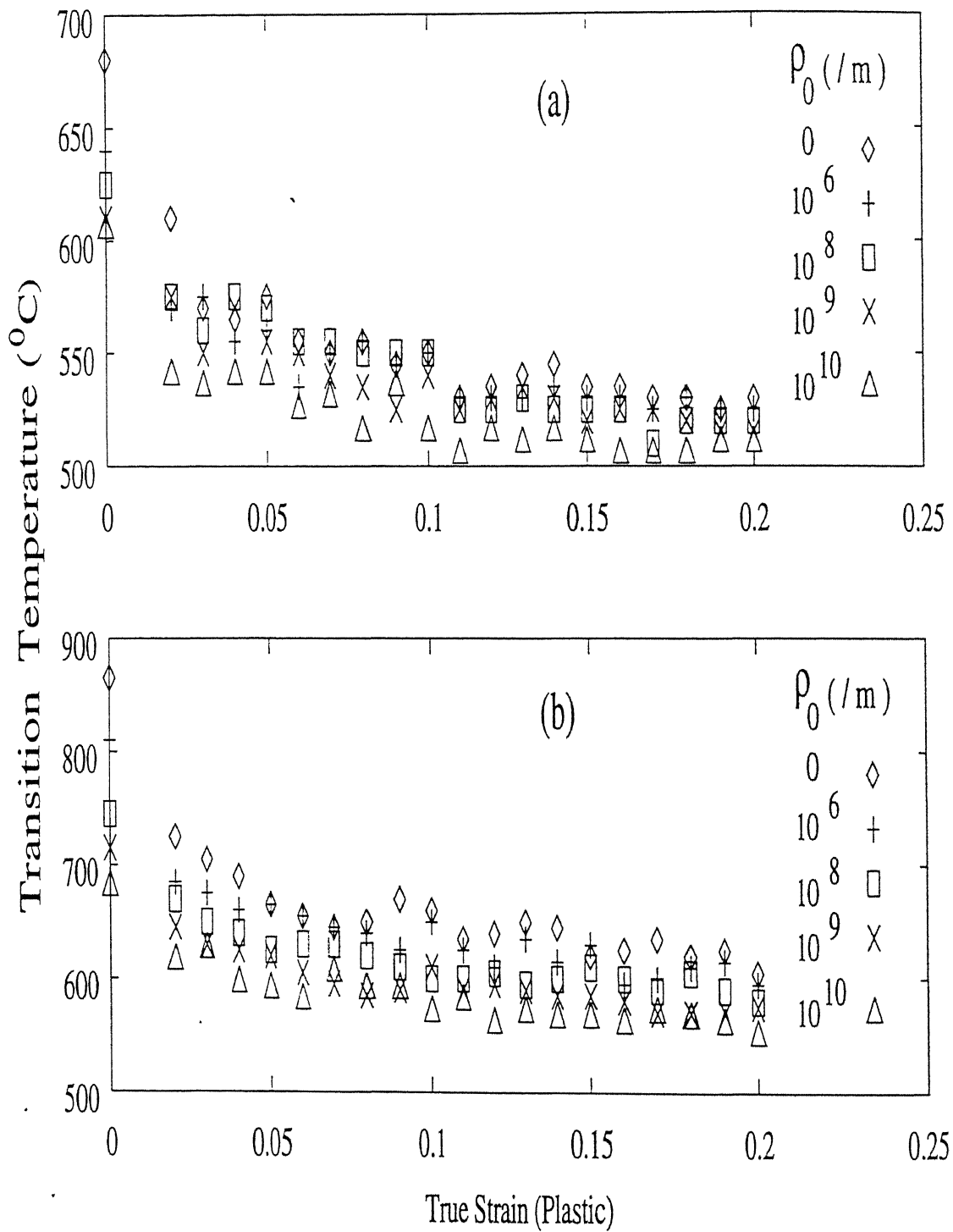


Figure 5.28: Variation of the transition temperature with strain for different values of ρ_0 in the sample of grain sizes of (a) $2.7 \mu\text{m}$ and (b) $64.0 \mu\text{m}$.

- 0.2 % strain is close to 600°C in the fine grain regime. This transition temperature is close to the temperature at which experimental yield stress drops rapidly in the fine grain samples. The measured value of $K(\epsilon)$ also significantly drops in the fine grain regime at approximately 600°C at 0.2 % strain. This is attributed to the presence of hard mantle zone in the fine grain regime which results in faster recovery by the annihilation of ECGBDs even at 0.2 % strain.
3. For the coarse grain size at $\rho_0 < 10^6 / \text{m}$, the transition temperature is very high. For example, for $d = 64.0 \mu\text{m}$, the transition temperature is greater than 1000°C at 0.2 % strain. Therefore, the presence of very low or almost zero initial dislocation density in the grain boundary region in the coarse grain regime (as discussed in section 5.1.1, equilibrated grain boundaries are present prior to deformation) leads to a high value of transition temperature. Consequently there is no significant drop in the yield stress in the samples of coarse grain size up to 800°C (figure 4.32a).
 4. The transition temperature decreases with increasing strain for a given ρ_0 and grain size (figures 5.28a-b). Since in the present investigation, the testing in tension has been done at 200°C intervals, the flow stress and Hall-Petch parameter $K(\epsilon)$ seem to drop at 600°C at all strains in figures 4.32a-c and 4.39b . However, it may be noted that the difference in the value of flow stress and $K(\epsilon)$ at 600°C and 800°C increases with increasing strain. Thus it can be stated that the the variation of transition temperature with strain is in the agreement with the experimentally observed variation of flow stress and $K(\epsilon)$.
 5. There is no significant difference in the net dislocation density with the grain size below the transition temperature at 0.2 % strain and $\rho_0 = 10^9 / \text{m}$ (figure 5.24a). However with further straining, ρ_{net} increases with decrease in the grain size below the transition temperature (figure 5.24b-d). Thus the variation of dislocation density in the grain boundary region in the samples of different grain sizes with strain suggest that the Hall-Petch parameter $K(\epsilon)$ will not be the same for the entire range of grain sizes (both in coarse and fine regimes). This would result in scatter of data in the

Hall-Petch or in composite plots with increasing strain. Further, the variation of dislocation density in the grain boundary region is more significant in the fine grain regime at higher strain (figure 5.24b-d), which suggests more scatter in Hall-Petch and composite plots with increase in strain. The above conclusions are in agreement with the experimental results (figures 4.33a-d and 4.35a-c).

6. At transition temperatures or above, ρ_{net} is significantly different for different grain sizes even at a low strain (0.2 %), as shown in figure 5.21a. Thus near or above the transition temperature, the the Hall-Petch data would show wide scatter even at lower strains. The experimental results shown in figures 4.33a-d and 4.35a-c confirm this conclusion.
7. The rapid drop in ρ_{net} above the transition temperature suggests that the recovery rate is very fast due to the annihilation of EGBDs. Under these conditions, the grain boundaries would not act as a barrier to dislocations movement. In fact the grain boundaries would act as sinks for dislocations. Also, the hard mantle zone will not remain in the grain boundaries region due to the fast recovery. Therefore the composite as well as the Hall-Petch relation cannot be used as grain size strengthening models above the transition temperatures. This is also in agreement with the Hall-Petch plots at 800°C (figure 4.33d) which show wide scatter in data.

The above conclusions suggest that the developed model is able to semi-qualitatively describe the variation of flow stress and Hall-Petch parameter $K(\epsilon)$ with temperature.

5.4 Strain hardening behaviour

The strain hardening behaviour of 316L austenitic stainless steel over wide range of temperature and grain size is discussed below.

5.4.1 Stress-Strain relation

There are several empirical relations (equations 2.13 to 2.17), which are commonly used to represent the true stress-true strain curves in the plastic region of polycrystalline metals. The above empirical equations are reproduced below.

$$\sigma = K_H \epsilon^{n_H} \quad (\text{Hollomon})$$

$$\sigma = \sigma_0 + K_L \epsilon^{n_L} \quad (\text{Ludwik})$$

$$\sigma = \sigma_s + (\sigma_s - \sigma_1) \exp(-n_v \epsilon) \quad (\text{Voce})$$

$$\sigma = K_S (\epsilon_1 + \epsilon)^{n_S} \quad (\text{Krupskowski/Swift})$$

$$\sigma = K_1 \epsilon^{n_1} + \exp(K_2 + n_2 \epsilon) \quad (\text{Ludwigson})$$

One of the most commonly used relation to model the stress-strain curves is the Hollomon relation (equation 2.13). The Hollomon parameters n_H and K_H are determined from the slope and intercept of $\log \sigma$ versus $\log \epsilon$ plots. Figures 5.29a-c show these plots in the fine and the coarse grain regimes and temperatures of room temperature, 400 °C and 800 °C. It can be seen that at low (room temperature) and intermediate (400 °C) temperatures, each curve can be delineated into three different regions I, II and III correspondings to lower, intermediate and higher strain regimes respectively. The values of Hollomon parameters in regions I and III are given in table E1 of appendix E. Region II is a transition regime between I and III. The transition strain between regions I and II (ϵ_{12}) and between regions II and III (ϵ_{23}) are also included in table E1 (appendix E). At high temperature (800 °C), only a single set of parameters n_H and K_H can describe the stress-strain curves over the entire strain range.

Ludwigson relation (equation 2.17), which is a modified Hollomon relation, is also commonly used to characterise the stress-strain curves of low SFE materials, such as

austenitic stainless steel (discussed in chapter 2, section 2.5). The first term in this relation is the Hollomon relation in region III (at high strain range). The second term at a given strain is the difference, Δ (illustrated in figure 5.29a), between the observed true stress and the stress calculated by the Hollomon equation (fitted in region III) extended to lower strains. The values of n_2 and K_2 were evaluated from the slope and intercept of the regression line of $\ln \Delta$ versus $\ln \epsilon$ plot. These values for different temperatures and grain sizes are included in table E1 of appendix E.

The minimum strain, ϵ_L , above which the Hollomon equation (2.13) fits the data, has been evaluated by setting the ratio of Δ to $K_1 \epsilon^{n_1}$, equal to some arbitrary small value, r , as:

$$\frac{\exp(K_2 + n_2 \epsilon)}{K_1 \epsilon^{n_1}} = r \quad (5.21)$$

In this equation 5.21, the commonly used value of $r = 0.005$, is used to evaluate ϵ_L .

Ludwik relation (equation 2.14) is also frequently used to represent the stress-strain curves of low SFE materials. Plots of $\log \frac{d\sigma}{d\epsilon}$ versus $\log \epsilon$ are obtained for different temperatures and grain sizes as shown in figures 5.30a-c. Each curve in these figures can be delineated into more than one linear region. The slope of each linear region gives the value of $n_L - 1$ and the intercept gives the product $n_L K_L$. Using the slope and intercept values, Ludwik parameter σ_0 can be easily calculated for different regions from equation 2.14. For the sake of completeness, the values of the Hollomon and Ludwik parameters for different strain regimes are given in tables E1 and E2 respectively of appendix E. An optimum set of parameters of Ludwik equation were derived for the entire range of stress-strain data using an optimization method (see appendix C), and listed in table E3 of appendix E. Swift relation (equation 2.16) did not produce a good fit to the experimental stress-strain curves and therefore it will not be analysed any further.

The Voce relation (equation 2.15), which is not much discussed in the literature is also analysed. The optimum values of Voce parameters σ_s , σ_1 and n_V , are estimated for a given stress-strain data by using an optimization method (see appendix C) and listed in

table E4 of appendix E. In order to compare the applicability of above relations over the entire strain range, the statistical error (SE) was estimated as follows:

$$SE = \left\{ \frac{\sum_{i=1}^N (\sigma_{i,cal} - \sigma_{i,exp})}{N(N-1)} \right\}^{1/2} \quad (5.22)$$

where, N is the number of data points, $\sigma_{i,cal}$ and $\sigma_{i,exp}$ are the calculated and experimental stress value at i^{th} strain (ϵ_i).

The comparison between statistical error (SE) is made by determining a single set of parameters for different relations over the entire strain range and presented in table 5.2. It can be seen from table 5.2 that the estimated error is generally less in the case of using Voce relation as compared to other relations at different temperatures and for grain sizes. Comparison between the calculated stress values obtained from different relations with experimental stress over the entire strain range at different temperatures and for different grain sizes are shown in figures 5.31a-c. At low (room temperature) and intermediate (400°C) temperatures, the Ludwigson and Ludwik equations fit the data more closely at lower strains ($< 5\%$) in different grain sizes. However, at higher strains, the Voce relation follows the experimental data more closely than other relations. At high temperature (800°C) the Voce equation produces a good fit to the experimental stress-strain data over the entire range of strain as compared to the Hollomon and Ludwik equations.

5.4.2 Dependence of strain hardening rate on flow stress

With the increasing test temperature and strain, there is a competition between the strain hardening and the dynamic recovery processes, owing to the generation, rearrangement and annihilation of dislocations. To understand the relative dominance of these processes at different temperatures and strains, the plots of $\sigma d\sigma/d\epsilon$ as a function of σ have been widely used to interpret the tensile work hardening behaviour (discussed in chapter section 2.4). Data of strain hardening rate for all the different temperatures and grain si

Table 5.2: Estimated statistical error (SE) in using different empirical equations at different temperatures and grain sizes

d (μm)	T ($^{\circ}C$)	SE in using Eq. of			T ($^{\circ}C$)	SE in using Eq. of		
		Ludwik	Ludwigson	Voce		Ludwik	Ludwigson	Voce
2.7	25	3.71	12.55	5.02	200	4.38	15.62	5.42
3.9		2.08	6.48	1.88		1.80	6.96	1.34
4.5		1.82	3.69	1.52		3.10	6.16	1.40
6.0		1.59	2.24	1.66		1.96	5.55	.23
9.0		1.25	3.04	.57		.92	2.85	.61
18.3		1.11	2.35	.88		.65	1.93	.95
26.5		1.31	2.10	.67		.61	1.31	.88
64.0		1.52	.94	3.02		.62	1.38	.89
2.7	400	1.49	19.06	.86	600	4.76	21.53	6.37
3.9		2.62	8.18	.81		3.24	6.32	3.38
4.5		1.48	3.05	1.28		1.53	6.01	.73
6.0		.73	2.47	1.07		.83	1.58	1.07
9.0		1.74	2.59	.77		.79	1.01	1.77
18.3		.84	1.16	1.48		.76	.81	1.00
26.5		.52	1.08	1.20		.57	1.87	.87
64.0		.45	.54	.73		.78	.97	.89
2.7	800	.58	3.08	.51				
3.9		.80	3.16	.29				
4.5		.21	4.98	.39				
9.0		.43	7.07	.59				
18.3		.51	5.65	.41				
26.5		.71	3.88	.58				
64.0		.94	4.79	.33				

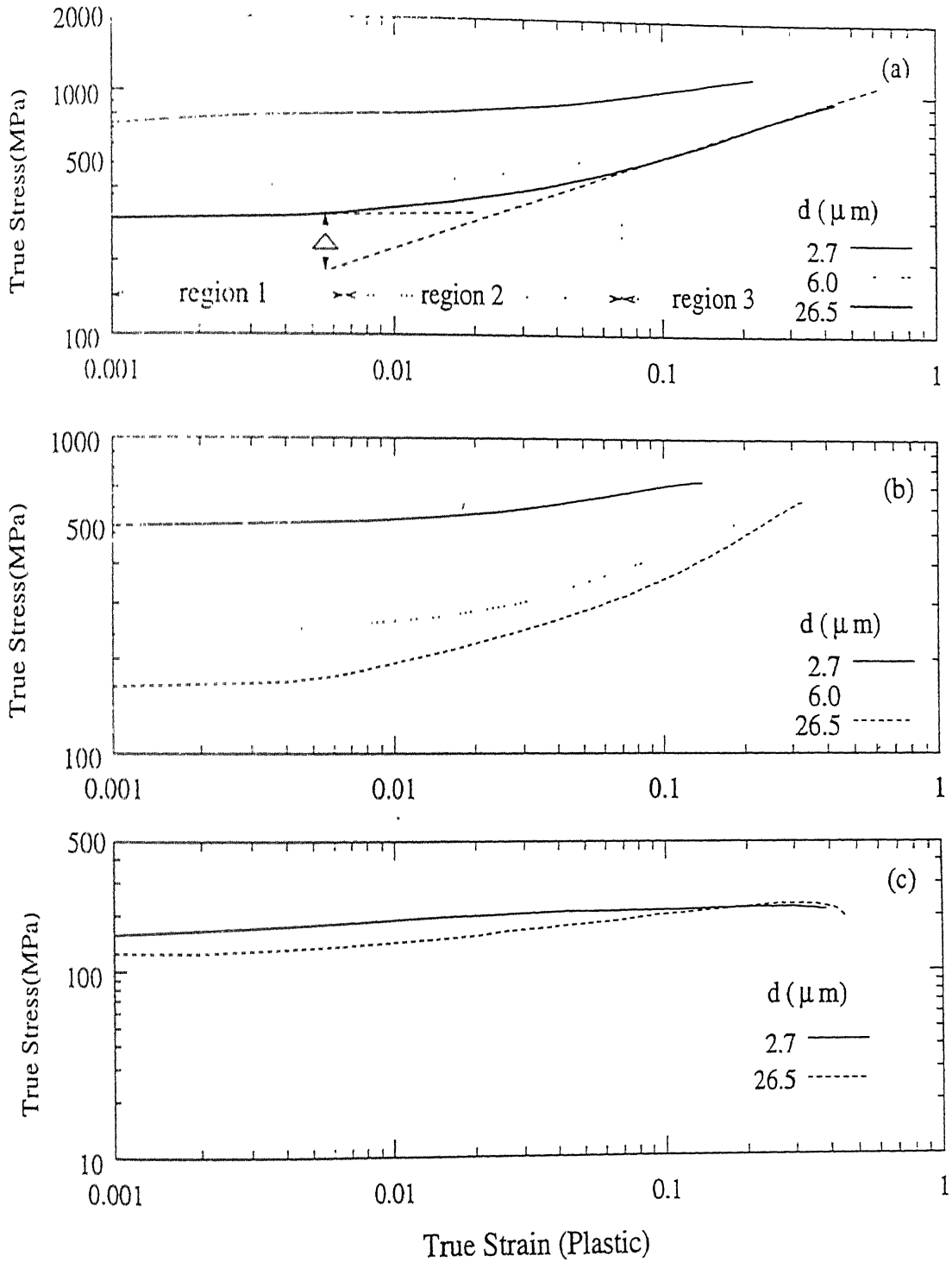


Figure 5.29: Plots of stress vs strain for different grain sizes at temperatures: (a) room temperature, (b) 400 °C and (c) 800 °C.

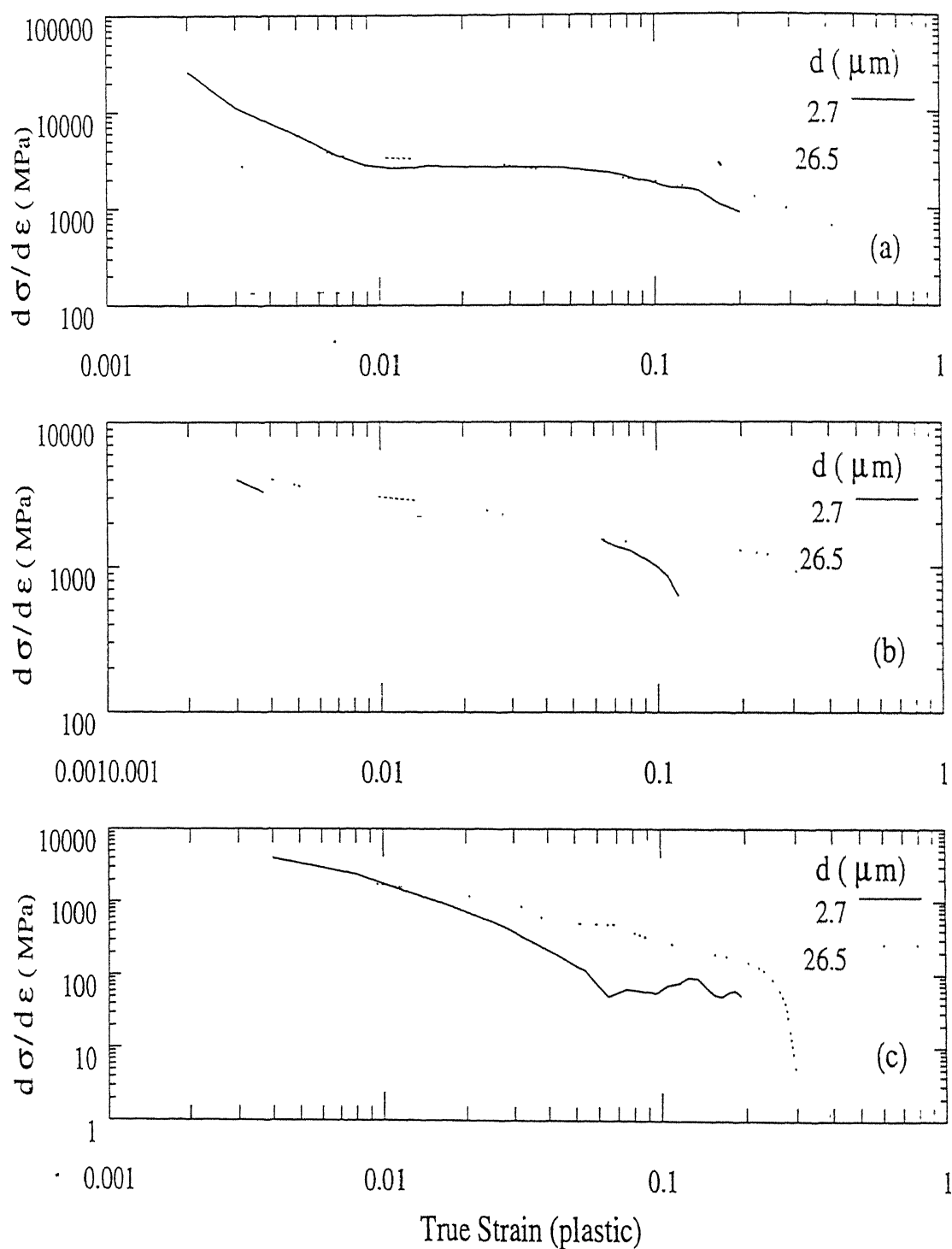
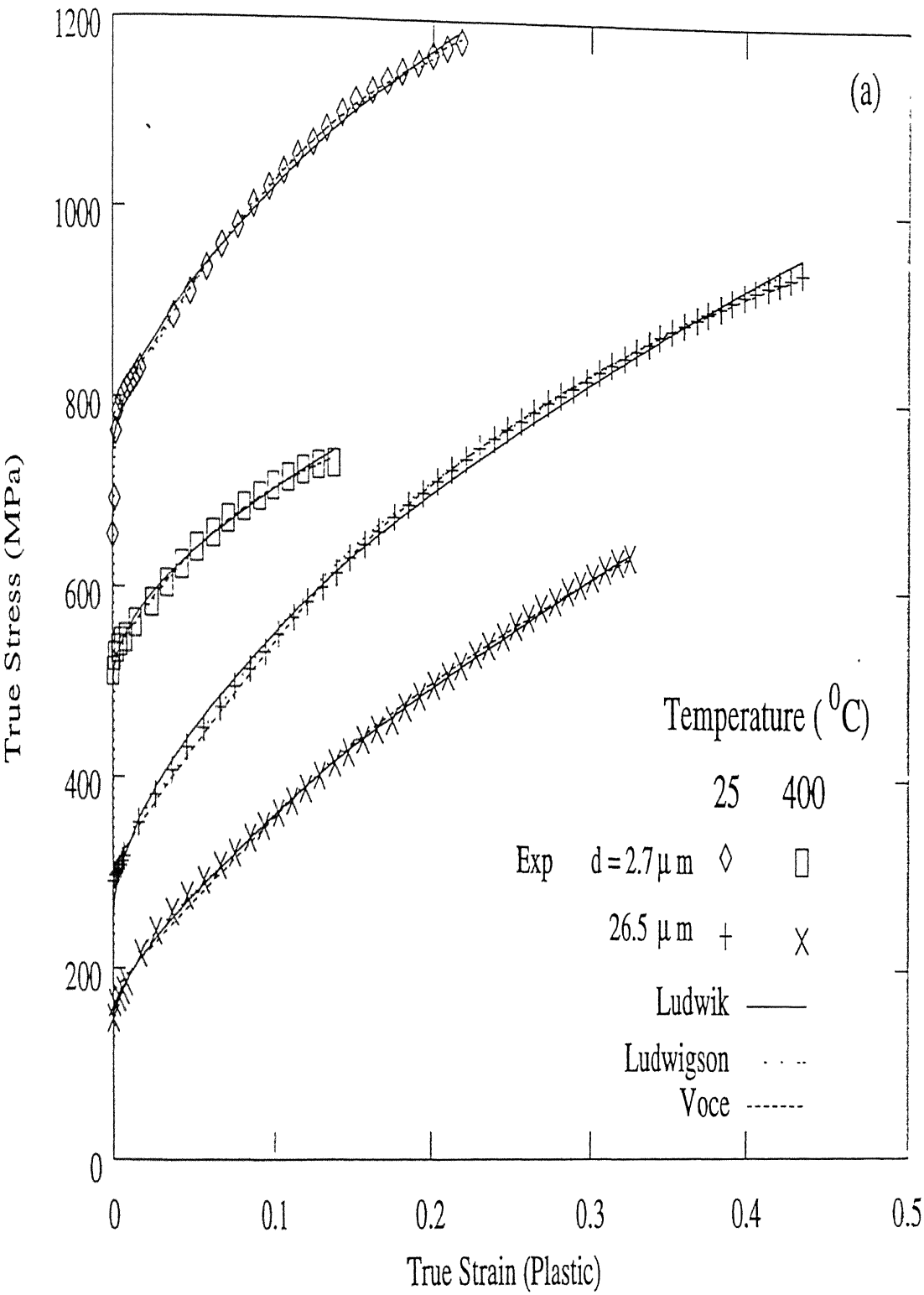


Figure 5.30: Plots of $d\sigma/d\epsilon$ vs strain for different grain sizes at temperatures: (a) room temperature, (b) 400°C and (c) 800°C.



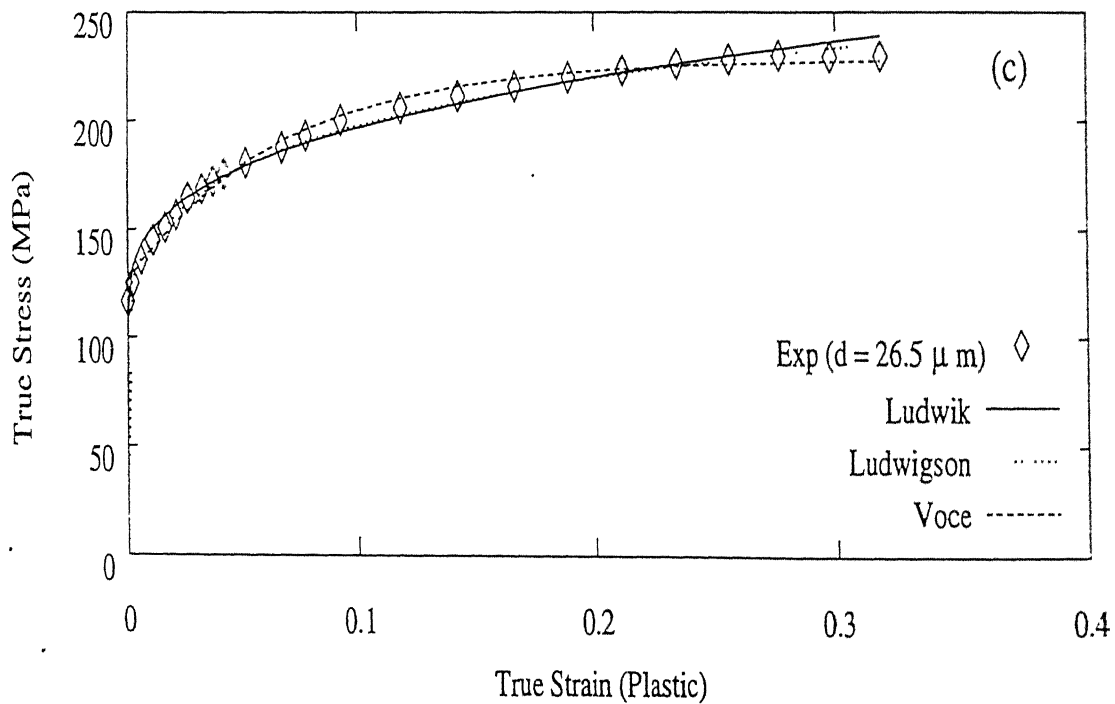
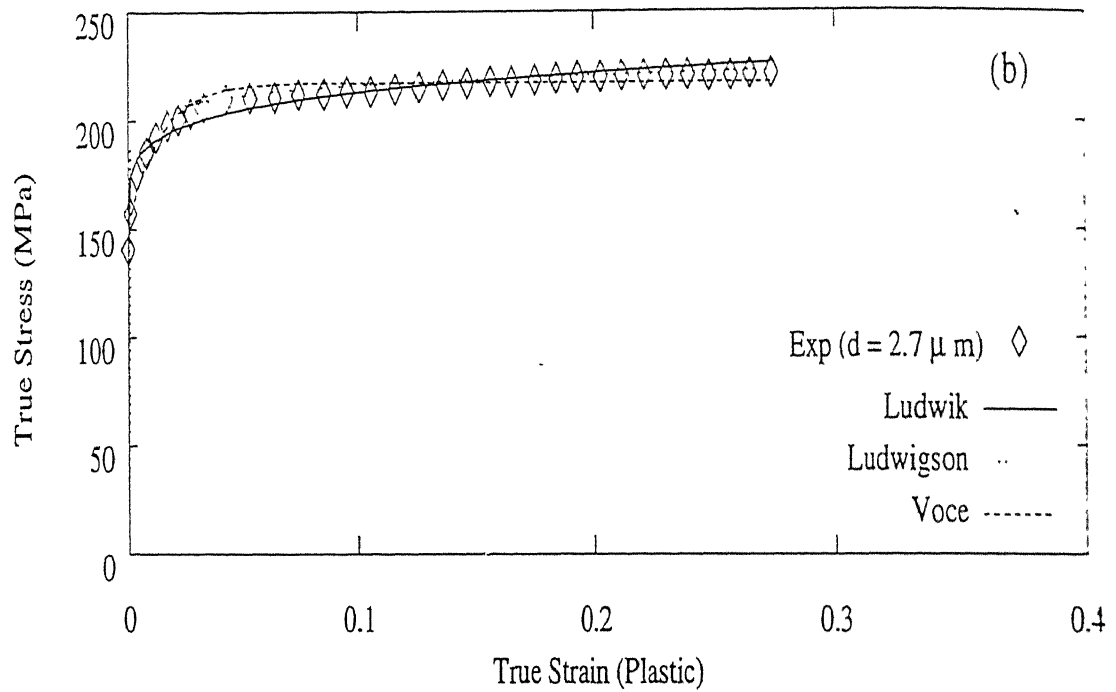


Figure 5.31: Comparison of stress vs strain curves calculated by using different strain hardening equations: (a) at room temperature and 400°C , (b) at 800°C for $2.7 \mu\text{m}$ grain size and (c) at 800°C for $26.5 \mu\text{m}$ grain size.

are analysed. However, only a few representative plots for the fine and the coarse grain sizes at low (room temperature), intermediate (400 °C) and high temperature (800 °C) are shown in figures 5.32 to 5.34. All the plots of $\sigma\theta$ versus σ in general show three stage behaviour: (1) initial transient stage, where $\sigma\theta$ decreases rapidly, (2) a plateau or hump region, defined usually as stage II, and (3) stage III where $\sigma\theta$ again decreases due to onset of recovery. The initial region of rapid decrease in $\sigma\theta$ with σ in austenitic stainless steel can be attributed to the stabilisation of the plastic strain rate associated with the dislocation density [141]. It can be noted that the derivative of Ludwik and Ludwigson equations follow the experimental $\sigma\theta$ more closely at lower stresses and Voce equation predicts $\sigma\theta$ more accurately at higher stresses.

Figures 5.35a-b show the variation of experimental $\sigma\theta$ with σ for the fine and the coarse grain sizes at different temperatures. The $\sigma\theta$ values in figures 5.35a-b fall in a narrow range in the temperature range of 200 °C to 600 °C. This suggests the dominance of DSA in the above temperature range of 200 °C to 600 °C. It can also be noted from above figures that with increasing temperature, due to process of dynamic recovery, the drop in $\sigma\theta$ starts at lower stress.

5.4.3 Effect of grain size and temperature on various parameters of empirical equations

Before coming to any conclusion about the fit of experimental stress-strain data with any empirical equation, it is desirable to study the physical significance of its parameters [44]. As discussed above, the Voce equation in general follows the experimental stress-strain data more closely than other relations. Therefore in this section the variation of parameters of Voce relation, with grain size and temperature is discussed. Figures 5.36 to 5.38 show the variation of Voce parameters with strain and temperature respectively. Both the saturation stress (σ_s) and n_V exhibit similar type of variation with grain size and temperature. These parameters decrease with an increase in the grain size at room temperature.

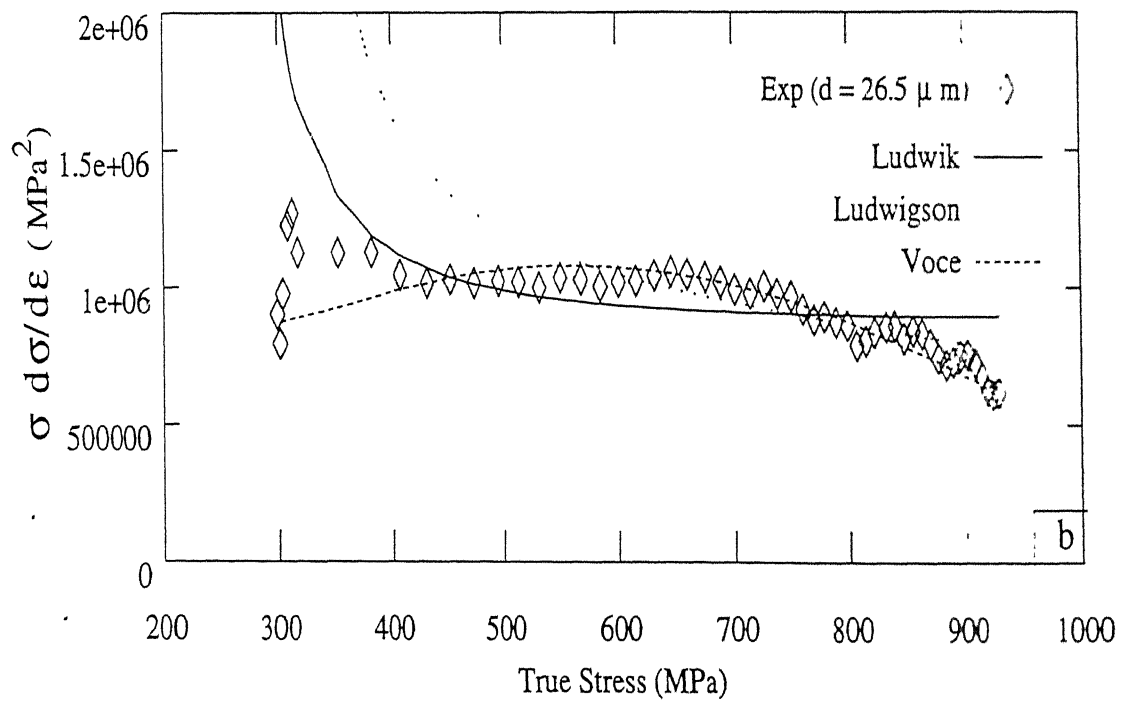
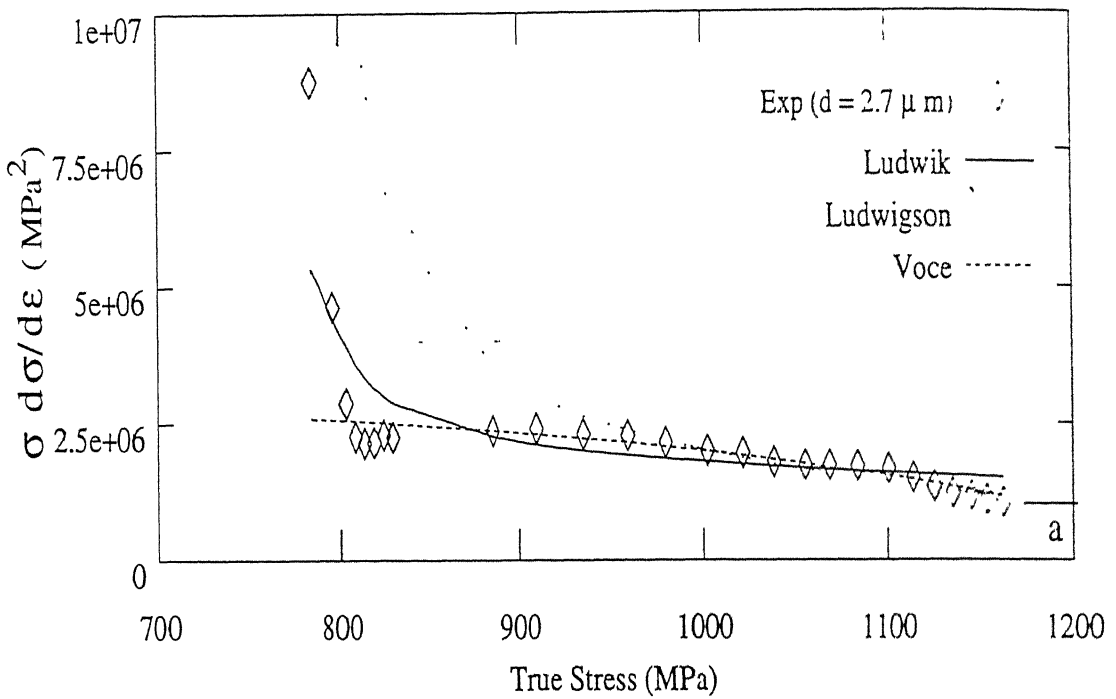


Figure 5.32: Variation of $\sigma\theta$ with stress at room temperature for grain sizes: (a) $2.7\mu\text{m}$ and (b) $26.5\mu\text{m}$.

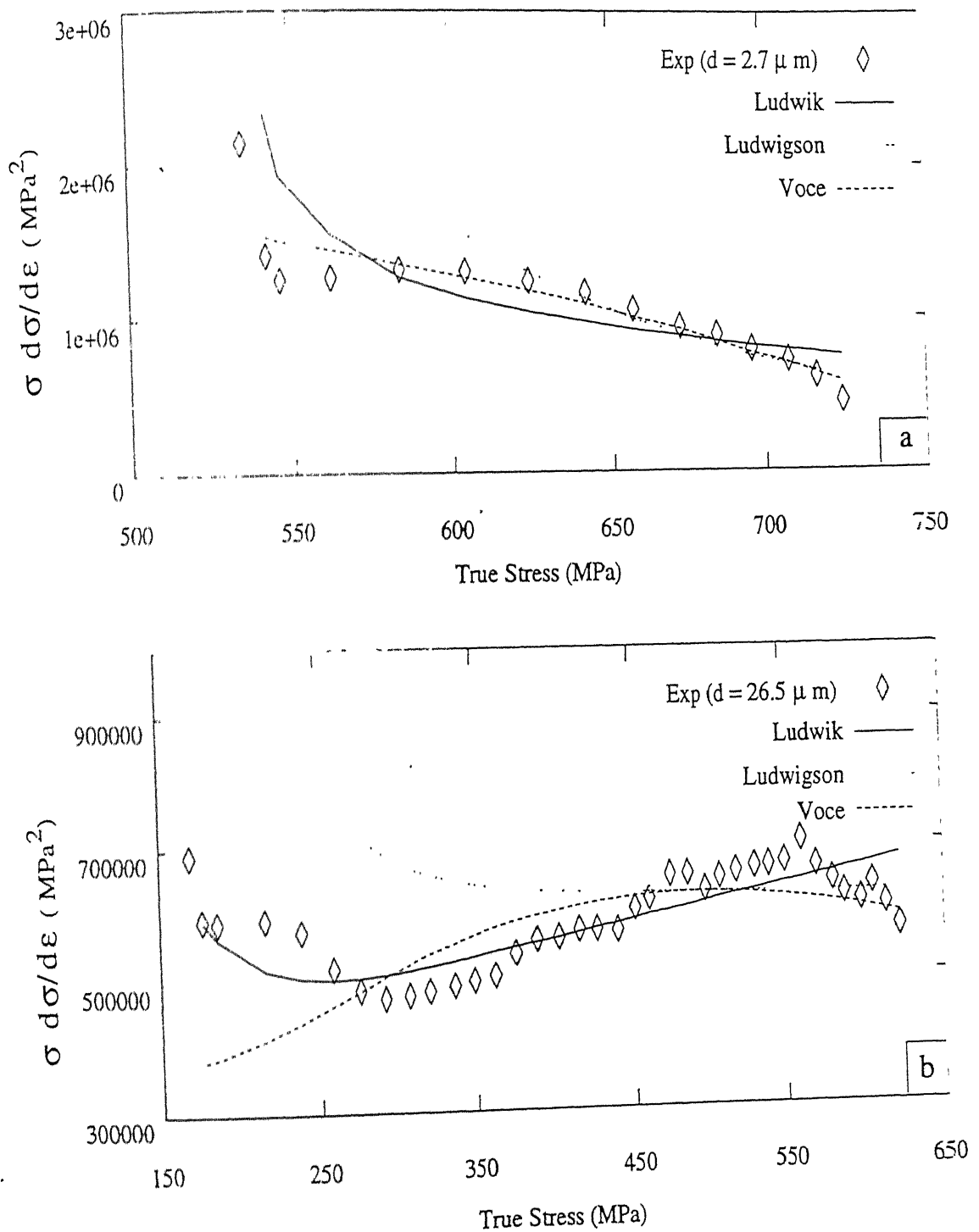


Figure 5.33: Variation of $\sigma\theta$ with stress at 400°C for grain sizes: (a) $2.7\mu\text{m}$ and $26.5\mu\text{m}$.

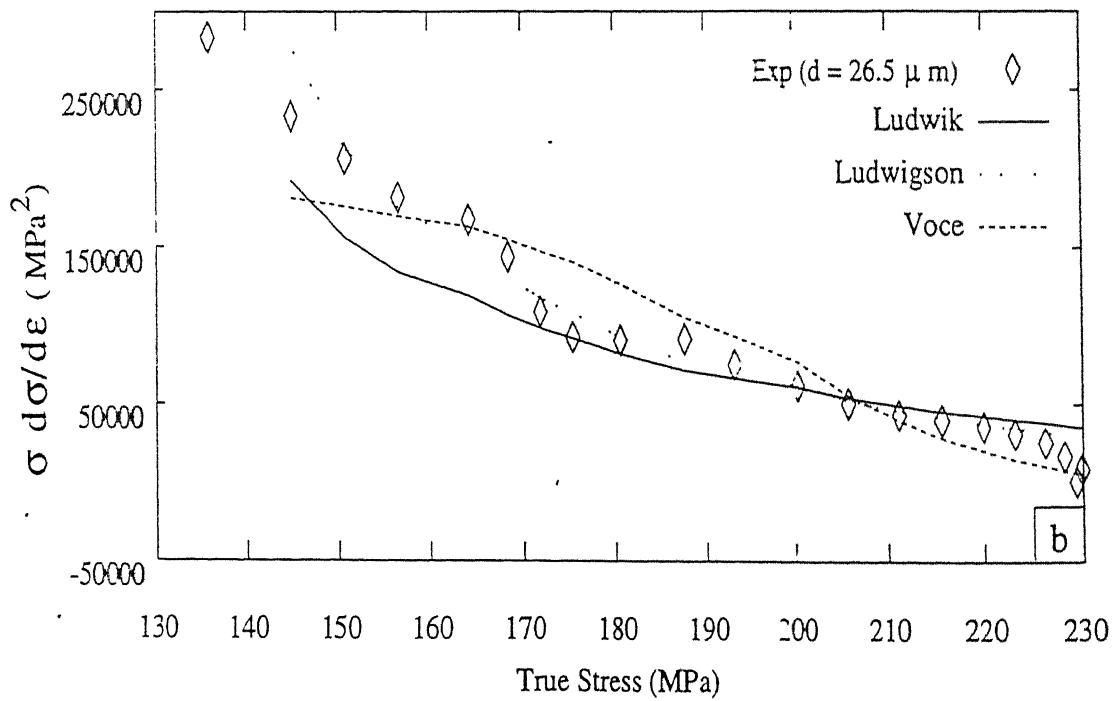
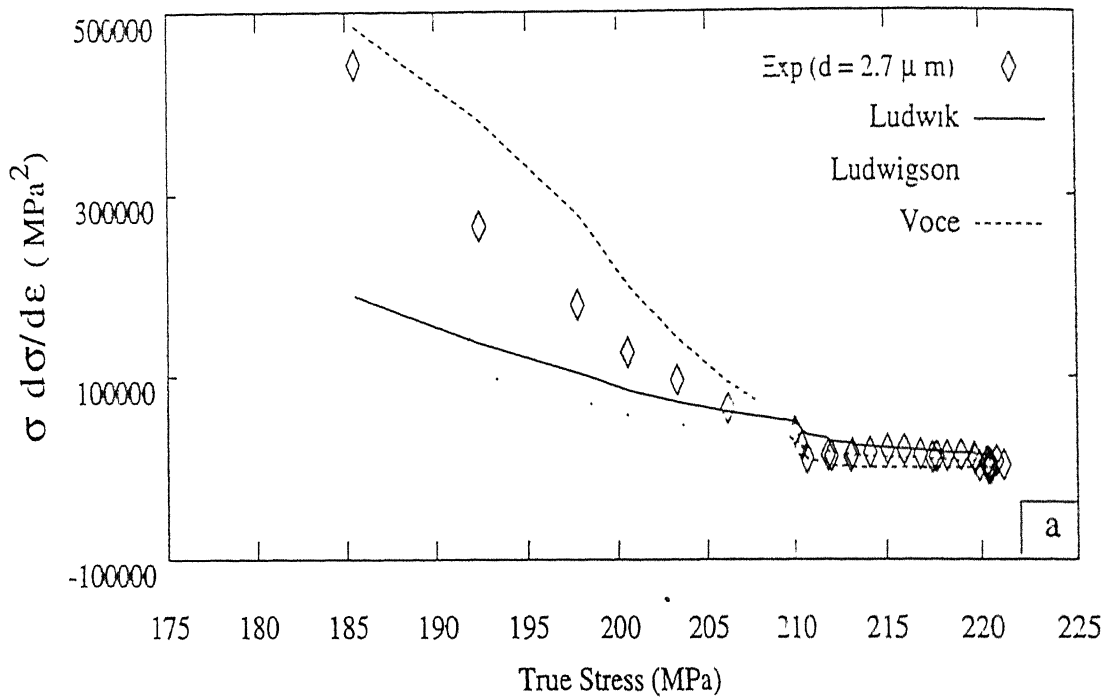


Figure 5.34: Variation of $\sigma\theta$ with stress at 800°C for grain sizes: (a) 2.7 μm and (b) 26.5 μm .

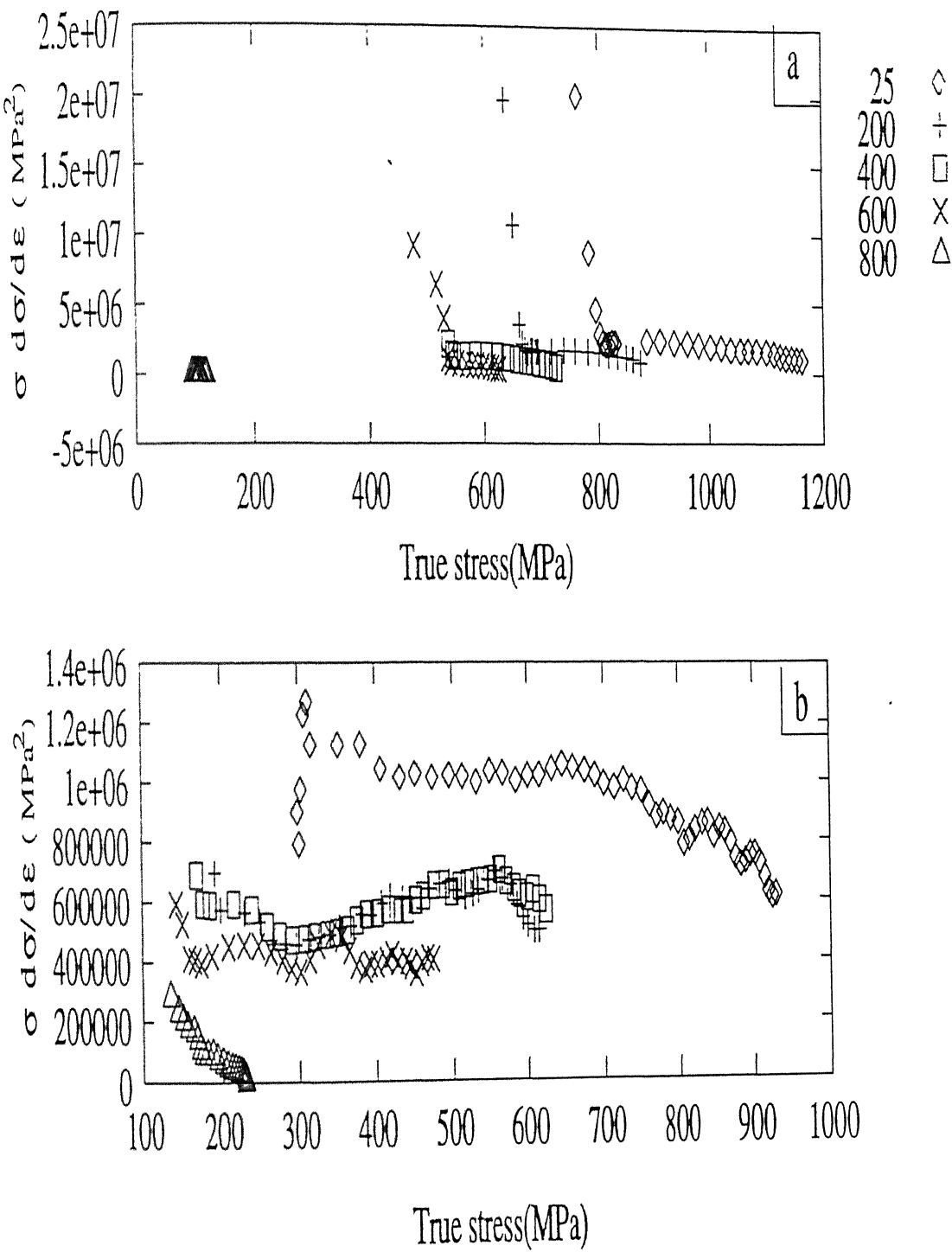


Figure 5.35: Variation of $\sigma\theta$ with stress at different temperatures for grain sizes: (a) $2.7\mu\text{m}$ and (b) $26.5\mu\text{m}$.

This is due to the presence of hard mantle zone in the fine grain regime (discussed in section 5.1.1). These parameters at elevated temperatures generally increase rapidly with the increasing grain size in the fine grain regime followed by a gradual increase in the coarse grain regime. This arises due to the increase in the rate of recovery processes with decrease in the grain size (see section 5.2). With increase in temperature these parameters reveal in general an initial decrease up to 200 °C followed by a plateau/hump in the temperature range of 200 °C to 600 °C (DSA range of temperature), and beyond approximately 600 °C, rapid drop takes place due to onset of recovery processes.

The variation of calculated yield stress (σ_1 from Voce equation) with grain size (figure 5.37a) demonstrates more or less similar type of behaviour as observed in the case of experimental Hall-Petch plots (figures 4.15, 4.33a-d). The calculated yield stress (σ_1) also reveals similar type of variation with temperature as observed in the case of experimental yield stress (see figures 5.37b and 4.32a).

The critical strain (ϵ_L) calculated using Ludwigson equation exhibits rapid increase in the fine grain regime followed by a gradual increase with the increasing grain size in the coarse grain regime (figure 5.39a). The rapid increase in ϵ_L with the grain size can be attributed to onset of recovery processes. At a given temperature the recovery starts at lower strain with decrease in the grain size due to the presence of high stress field near the grain boundaries (discussed in section 5.1.1). Therefore, in the Ludwigson equation, ϵ_L , is believed to be the transition strain between the planar glide mode of deformation to cross slip. ϵ_L remains more or less constant in the fine grain regime in the temperature range of room temperature to 600 °C and beyond 600 °C it rapidly drops with increasing temperature (figure 5.39b). In the coarse grains, ϵ_L increases in the temperature range of room temperature to 400 °C and thereafter it drops with increasing strain. In general, increasing temperature accelerates the recovery processes, however the occurrence of DSA in the intermediate temperature range delays the process of recovery. Therefore, the variation of ϵ_L at a given grain size exhibits either a constant or a small increase with increasing temperature (up to 600 °C).

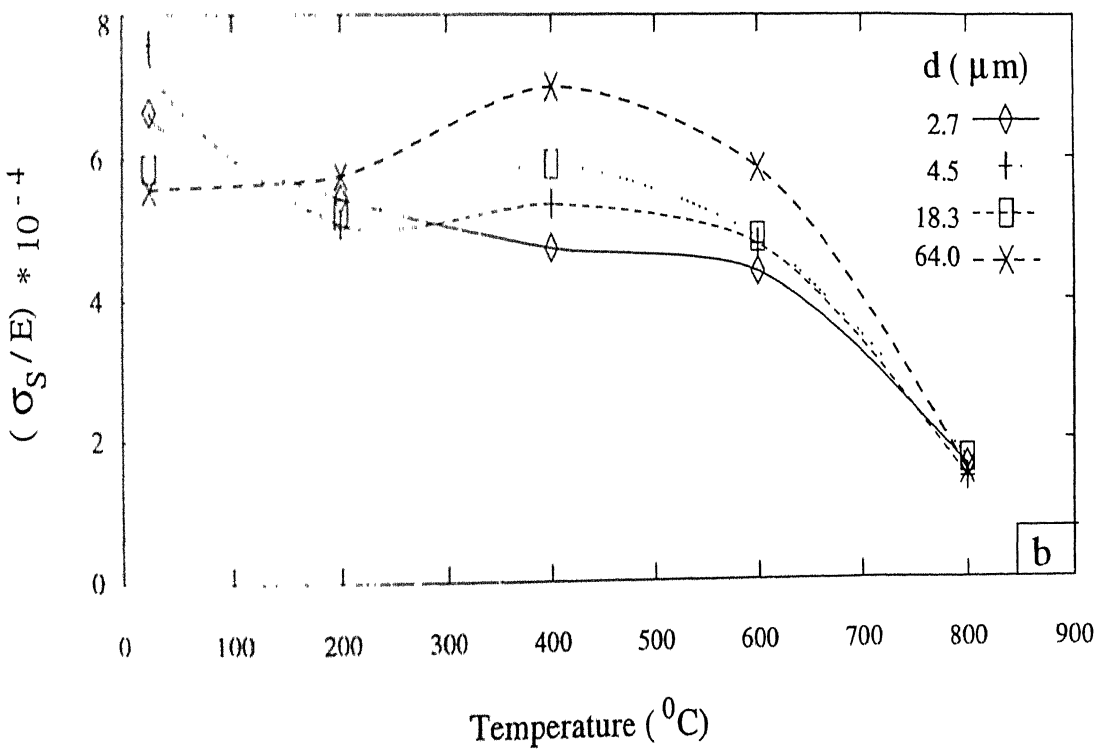
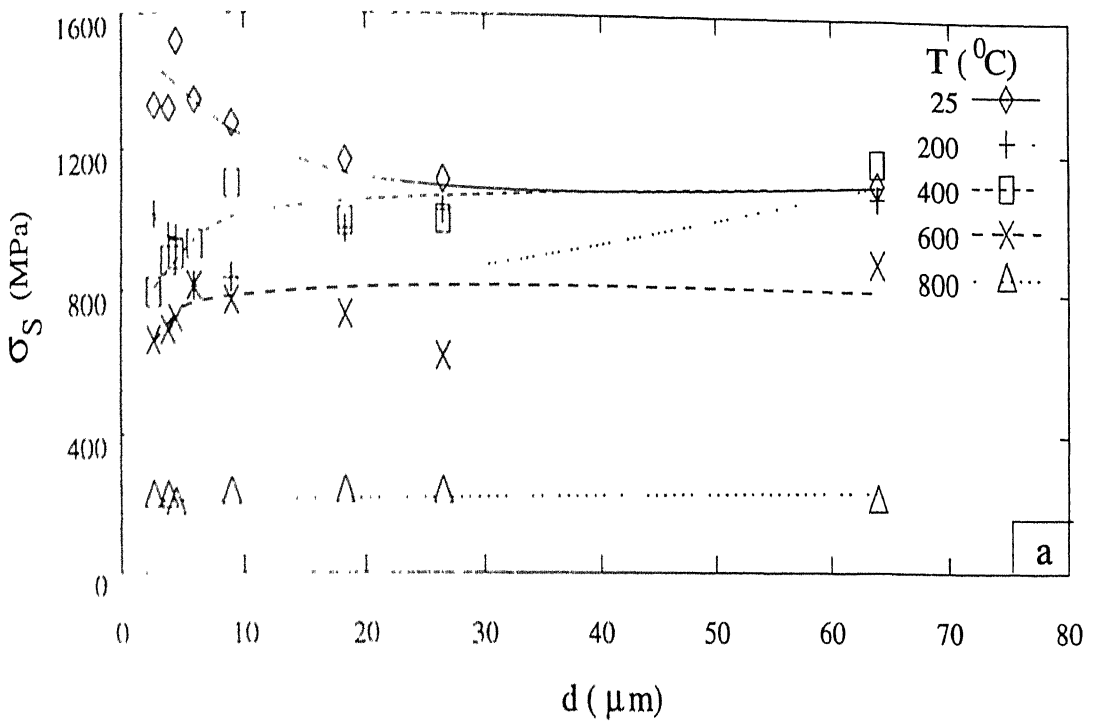


Figure 5.36: Variation of Voce parameter, σ_s , with (a) grain size and (b) temperature.

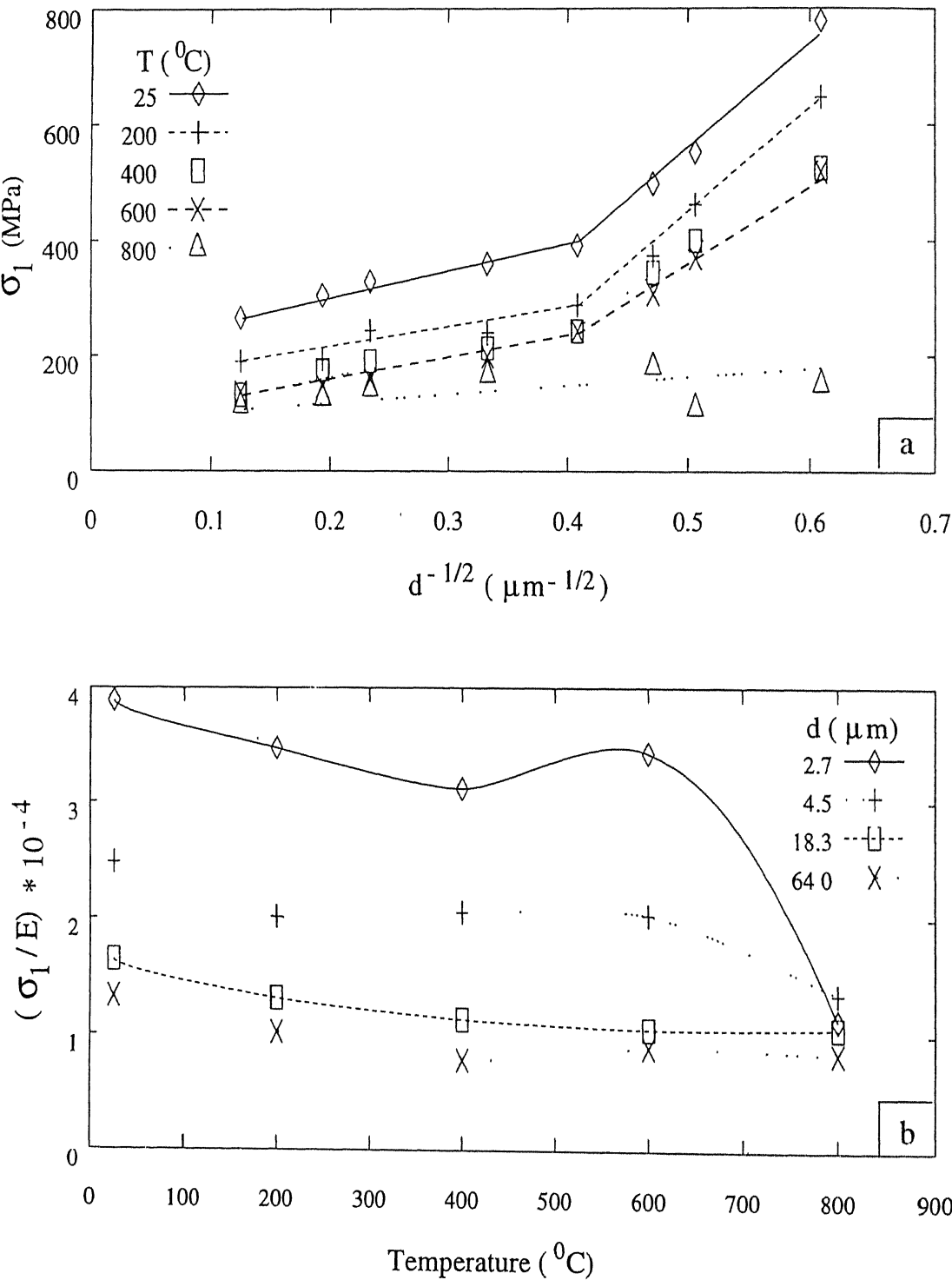


Figure 5.37: Variation of Voce parameter, σ_1 with (a) grain size and (b) temperature.

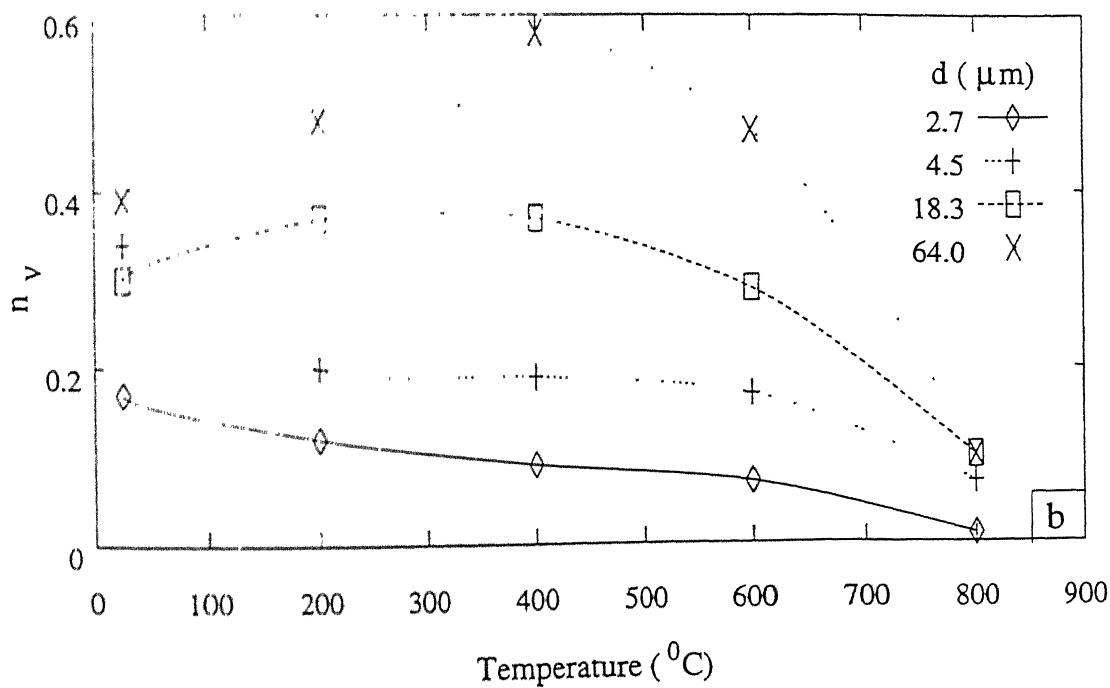
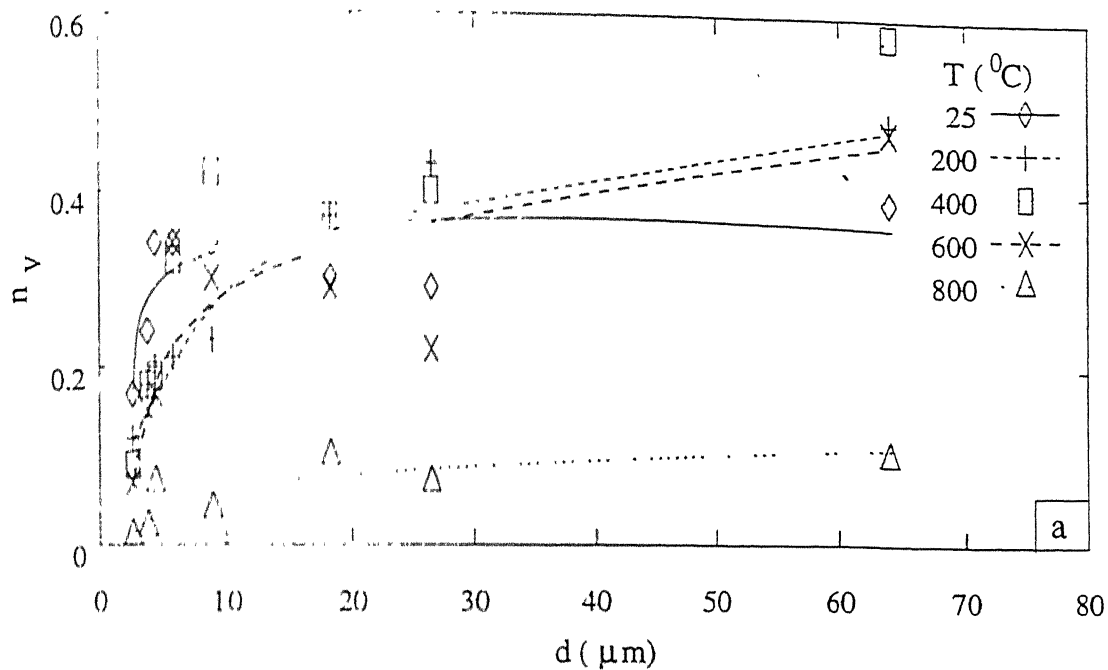


Figure 5.38: Variation of Voce parameter, n_V with (a) grain size and (b) temperature.

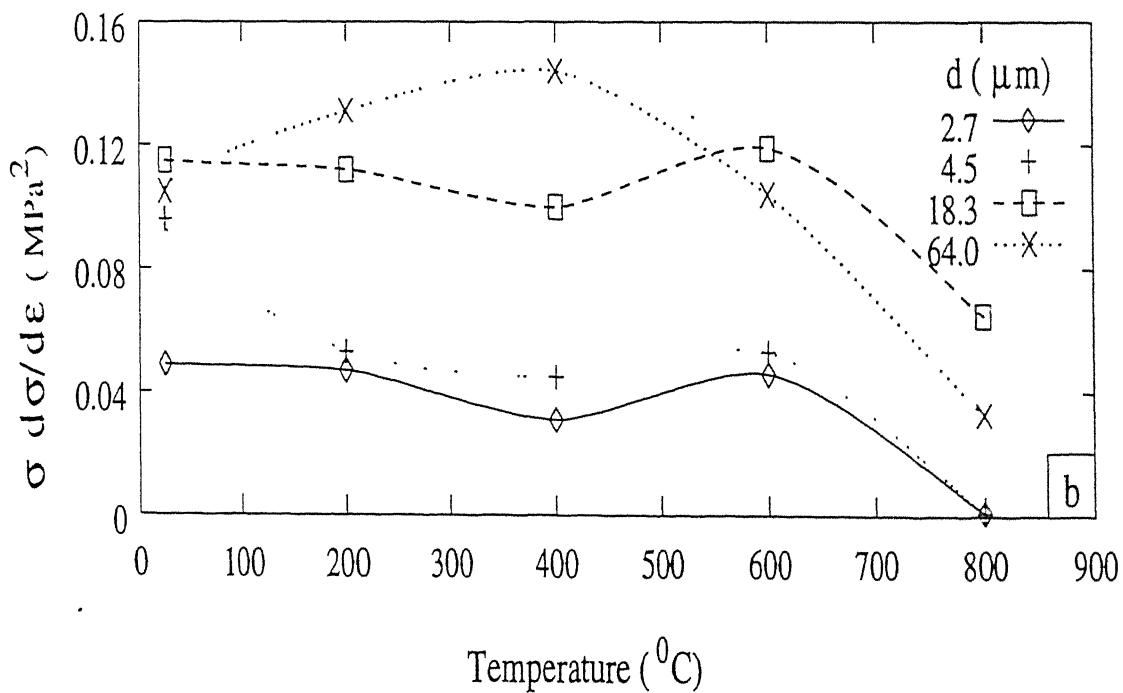
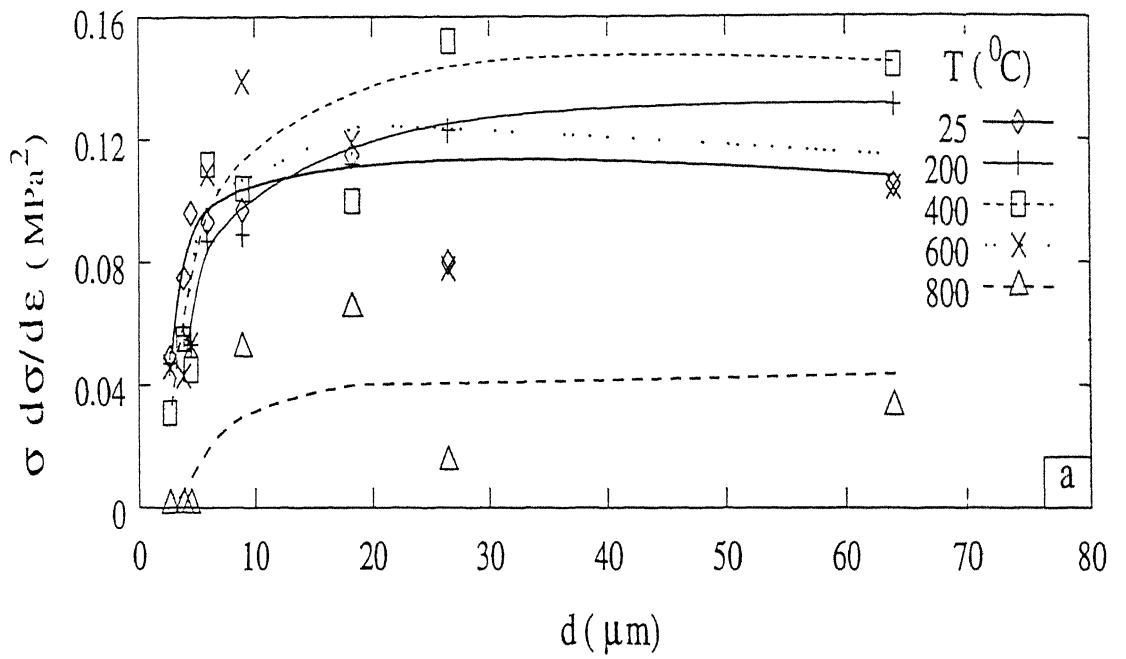


Figure 5.39: Variation of critical strain (ϵ_L) calculated using Ludwигson equation with (a) grain size and (b) temperature.

The above discussion can be summarised in the following points:

- 1 A single set of parameters of the Hollomon, Ludwik and Swift equations at temperature below 600°C cannot describe the stress-strain curves over the entire strain range.
- 2 At low (room temperature) and intermediate (400°C) temperature, the Ludwikson as well as Ludwik equations fit the stress-strain data more closely at lower strains ($< 5\%$) in different grain sizes. However, at higher strains, the Voce equation follows the experimental data more closely than other equations (figures 5.31a-c). At high temperature (800°C), the Voce equation fits the experimental stress-strain data in the entire range of strain as compared to the other empirical equations.
- 3 The $\sigma\theta$ variation obtained from Voce equation saturates at higher strain or stress. On the other hand, the $\sigma\theta$ monotonically increases with increasing stress for Ludwik and Ludwikson relations.
- 4 With increase in the grain size at room temperature, the Voce parameters (σ_s and n_V) decrease due to the decreasing effect of the grain boundary on strengthening. However, at elevated temperatures, these parameters show increase with increase in the grain size. This is due to the effect of increasing rate of recovery with decrease in the grain size (discussed in section 5.2).
- 5 Like the flow stress, σ_s and n_V also show three stage behaviour as a function of temperature. In the intermediate temperature range (from 200°C to 600°) these parameters reveal plateau or small increase due to the occurrence of DSA. Beyond 600°C , the predominance of recovery processes over the strain hardening results in the rapid drop of these parameters with increase in temperature.
- 6 The yield stress calculated from the Voce equation exhibits more or less similar type of variation as observed in the Hall-Petch plots at different temperatures. It also shows three stage behaviour with temperature just like the experimental variation of yield stress.

7 From the variation of ϵ_L with grain size and temperature, it may be noted that the change in mode of deformation from planar glide to cross-slip occurs at lower strains with decrease in the grain size and increase in temperature. The change in the deformation mode occurs due to the differences in the structure of the grain boundaries, as discussed in section 5.2.

The above observations suggest that the Voce equation in general gives better fit with the stress-strain curves. Also the variation of the parameters of this equation with grain size and temperature is in agreement with the conclusions derived in previous sections.

Chapter 6

Conclusions and suggestions

The major conclusions of this study can be summarised as follows:

1. In the temperature range of room temperature to 600°C , the Hall-Petch behaviour of 316L austenitic stainless steel (batch 1) shows two distinctly different linear regimes, one in the fine grain size range ($d \leq 6 \mu\text{m}$) and the other in the coarse grain size range ($d > 6 \mu\text{m}$). The Hall-Petch parameter $K(\epsilon)$ is significantly higher in the fine grain regime as compared to that of coarse grain regime at all strains. On the other hand, $\sigma_0(\epsilon)$ is negative in the fine grain regime. Since $\sigma_0(\epsilon)$ is interpreted as the friction stress, there is no physical significance of negative $\sigma_0(\epsilon)$. Therefore, it has been concluded that the Hall-Petch relation is not valid in the fine grain regime of batch 1.
2. The different thermo-mechanical treatments employed to obtain various grain sizes in batch 1 may lead to differences in the microstructural parameters. The distribution of grain size and grain shape of annealed samples of both the batches in the entire grain size range ($2.7\mu\text{m}$ to $64.0\mu\text{m}$) remains nearly same. However, the true dihedral angle (TDA) distribution obtained from the experimentally measured

distribution of PDA, by employing the mathematical transform developed in this work, reveals a significant difference in the fine and coarse grain regimes of batch 1. In the fine grain regime the standard deviation of TDA is higher and the relative frequency of 120° class of TDA is lower in comparison to the coarse grain regime. This suggests the presence of non-equilibrium state of grain boundaries in the fine grain regime of batch 1. The lower annealing temperatures employed to get the fine grain sizes, are unable to annihilate the EGBDs which are accumulated during the process of grain growth. On the other hand the higher annealing temperatures employed to produce coarse grain sizes lead to the annihilation of EGBDs and hence the grain boundaries are in equilibrium state. Thus the high density of EGBDs as well as the lattice dislocations in the vicinity of grain boundaries in the fine grain regime leads to the presence of a hard mantle zone. This has also been inferred from the results of hardness measurements.

3. Accordingly the fine grained microstructures may be considered as having two phases: a hard phase (mantle zone) in the vicinity of grain boundaries and a soft phase (grain interior). Kocks composite model is more appropriate for this type of structure rather than the Hall-Petch model. By applying this model in the fine grain regime of batch 1 in the temperature range of room temperature to 600°C , a positive value of $\sigma_0(\epsilon)$ at a given strain is obtained which is comparable in magnitude to $\sigma_0(\epsilon)$ obtained in the coarse grain regime (using the Hall-Petch relation).
4. In batch 2 of 316L austenitic stainless steel, a single Hall-Petch relation could describe the deformation behaviour over the entire range of grain size (from $2.9\mu\text{m}$ to $46.0\mu\text{m}$) in the temperature range of room temperature to 600°C . It has been shown that the faster equilibration kinetics of the samples of batch 2 as compared to batch 1 (due to compositional differences) leads to equilibrated grain boundaries in the entire range of grain size and hence there was no hard mantle zone after annealing even in the fine grain samples of batch 2.
5. At 800°C , the samples of batch 1 and batch 2 revealed a single linear Hall-Petch

behaviour in the entire range of grain size due to the fact that at this temperature, the non-equilibrium grain boundaries in the fine grain regime of batch 1 transform to equilibrium state by the annihilation of EGBDs. However, the Hall-Petch data are highly scattered in both the batches and the scatter increases with increasing strain.

6. The increase in grain aspect ratio and the decrease in grain shape factor at room temperature and 400°C reveal that the main deformation mode is intragranular dislocation slip. While no significant change in these parameters at 800°C , demonstrate that the grain boundary sliding and grain boundary migration are the important mode of deformation. Thus at 800°C the pile-up model of Hall-Petch cannot be applied as the grain size strengthening model. The small positive value of $K(\epsilon)$ in batch 1 and negative in batch 2 also strongly support the above conclusion.
7. The occurrence of dynamic strain aging in the temperature range of 200°C to 800°C in the lower strain range (below 5%) and from 200°C to 600°C in the entire range of strain results in jerky stress-strain curves. This is also reflected as plateau or hump between 200°C to 600°C in the variation of flow stress, Hall-Petch parameters and average microhardness with temperature.
8. The Hall-Petch parameter and the lock's parameter, $\sigma_0(\epsilon)$, in the coarse and fine grain regimes of batch 1, increase with increasing strain at room temperature due to the increasing effect of strain hardening in the grain interior. This conclusion is in agreement with the increase in grain aspect ratio, grain shape factor and grain interior microhardness. At higher temperatures, the rate of increase in $\sigma_0(\epsilon)$ with strain decreases due to the dominance of dynamic recovery processes over dynamic strain hardening. This effect is observed as almost no change in grain aspect ratio, grain shape factor and average microhardness with strain at higher temperatures (800°C).
9. At room temperature, $K(\epsilon)$ decreases with strain below 2 % followed by an increase

with increasing strain. The initial decrease in $K(\epsilon)$ with strain is due to the accumulation of extrinsic grain boundary dislocations (EGBDs) which act as a stress concentrators and lead to a significant decrease in the stress required to generate dislocations in the grain boundary region. The accumulation and interaction of EGBDs at grain boundaries transform the grain boundaries to a higher energy or non-equilibrium state. This may result in the formation of a mantle zone in the vicinity of grain boundaries. The increase in standard deviation of TDA and decrease in 120° class with increasing strain is in agreement with above conclusion. The increase in microhardness in the grain boundary region with strain also supports the above conclusion. However, the presence of hard mantle zone in the fine grained samples lead to the initial increase in the Kocks composite parameter, $K(\epsilon)$ with strain followed by a decrease with further straining. At higher temperature, both Hall-Petch parameter and Kocks parameter, $K(\epsilon)$, decrease with strain due to the dominance of grain boundary sliding and recovery process.

10. With increasing temperature, generally the Hall-Petch parameters show three stage behaviour as decrease in lower temperature followed by a plateau/hump in intermediate temperature range and thereafter rapid drop at higher temperatures. However, in the lower strain range, the rapid drop in $\sigma_0(\epsilon)$ is not observed due to the dominance of dynamic strain aging effect over recovery processes. The rapid drop in the Hall-Petch parameters at higher temperature is mainly due the process of annihilation of EGBDs at grain boundary.
11. In the fine grained samples of 316L austenitic stainless steel, the relative contribution of grain interior on flow stress is negligible in comparison to the grain boundary contribution in the temperature range of room temperature to 600°C and vice-versa above 600°C . With increase in grain size and strain the relative dominance of grain boundary on flow stress decreases and thus the grain interior dominance increases. Therefore, the rapid drop in the flow stress and the Hall-Petch parameters at lower strain can be described on the basis of dislocation processes in the grain

boundary region.

12. A model based on dislocation dynamics at and in the vicinity of grain boundaries is developed to explain the variation of flow stress with temperature. The rapid drop in the flow stress as well as the Hall-Petch parameter, $K(\epsilon)$ is observed to occur at the same temperature at which the net dislocation density in the grain boundary region drops rapidly.
13. The Ludwik and Ludwigson equations fit the experimental stress-strain data more closely at lower strains and Voce equation at higher strains at different temperatures and for various grain sizes. In the overall stress-strain curve, Voce equation gives better fit as compared to the other empirical stress-strain relations. With the increase in the temperature and the decrease in the grain size, the strain, above which the dynamic recovery dominates over strain hardening, decreases.
14. The technique developed in this work to estimate the distribution of true dihedral angles (TDA) from the experimentally measured distribution of plane dihedral angles (PDA) is not just limited to 316L austenitic stainless steel. This technique can also be employed in any polycrystalline materials.

The suggestions and the scope for future research are given below.

- The PDA to TDA transformation can be modified in order to consider all the angles at a triple point jointly. The modified method would then give a joint distribution of TDAs at triple edges. This will remove correlation effects (if any) between angles at triple edges.
- This technique could also be used to generate a distribution of relative grain boundary energies. Such a distribution could then be related to the mechanical properties of polycrystals.

- Better results from this technique can be achieved by accurate measurements of plane dihedral angles using automatic image analysis systems.
- To verify the hard mantle zone in the grain boundary region, the measurements of dislocation density both in the grain interior and grain boundary region of annealed samples through transmission electron microscopy can be done. Also the measurements of dislocation density both in the grain interior and grain boundary region can be used to correlate the microstructural changes at different strains and temperatures.
- Tensile testing of this material (316L austenitic stainless steel) over a wide range of grain size would be done in narrow intervals of temperature and correspondingly the microstructural measurements to detail study the deformation behaviour over a wide range of temperature and grain sizes.

Bibliography

- [1] N. A. Gjostein and F. N. Rhines. *Acta Metall.*, 7:319, 1959.
- [2] H. Udin, A. J. Shaler, and J. Wulff. *Trans. Met. Soc., AIME*, 185:186, 1949.
- [3] L. E. Murr, R. J. Horylev, and G. I. Wong. *Surf. Sci.*, 26:184, 1971.
- [4] P. H. Pumphery and H. Gleiter. *Phil. Mag. (a)*, 30:593, 1974.
- [5] P. H. Pumphery and H. Gleiter. *Phil. Mag. (a)*, 32:881, 1975.
- [6] L. E. Murr. *Jr. Appl. Phys.*, 39:5557, 1968.
- [7] L. E. Murr, P. J. Smith, and C. M. Glimore. *Phil. Mag. (a)*, 17:89, 1968.
- [8] L. E. Murr. *Phys. Stat. Sol.(a)*, 1:487, 1970.
- [9] C. S. Smith. *Trans. Metall. Soc., AIME*, 175:15, 1948.
- [10] H. Gleiter. *Z. Metallkunde*, 61:282, 1970.
- [11] R. A. Varin, K. J. Kurzydowski, and K. Tangri. *Mater. Sci. Engg.*, 80:L5, 1986.
- [12] R. A. Varin and K. Tangri. *Scripta Metall.*, 14:337, 1980.
- [13] S. Sangal and K. Tangri. *Metall. Trans.*, 20A:479, 1989.
- [14] K. J. Kurzydowski, S. Sangal, and K. Tangri. *Metall. Trans.*, 20A:471, 1989.

-
- 5] G. E. Dieter. *Mechanical Metallurgy, SI Metric Edition*. Mc Graw-Hill Book Company, 1988.
 - 6] P. Polukhin, S. Gorelik, and V. Vorontsov. *Physical Principles of Plastic Deformation*. Mir Publisher, Moscow, 1983.
 - 7] R. W. K. Honecombe. *The Plastic Deformation of Metals*. Buller and Tanner Ltd, London, 1984.
 - 8] G. I. Taylor. *Proc. Roy. Soc.*, A145:362, 1934.
 - 9] G. I. Taylor. *Proc. Roy. Soc.*, A145:388, 1934.
 - 10] N. F. Mott. *Phil. Mag. (a)*, 43:1151, 1952.
 - 11] A. Seeger, S. Mader, and H. Kronmuller. In G. Thomas and J. Washburn, editors, *Electron Microscopy and strength of crystals*. Int. Sci., Newyork and London, 1962.
 - 12] A. Seeger, J. Diehl, S. Mader, and K. Rebstock. *Phil. Mag. (a)*, 2:323, 1957.
 - 13] G. Sachs. *Z. Verein. Deut. Ing.*, 72:734, 1928.
 - 14] H. L. Cox and D. G. Sopwith. *Proc. Phys. Soc. London*, 49:134, 1937.
 - 15] A. Kochendorfer. *Plastische Eigenschaften von Kristallen and Metallischen Werkstoffen*, Springer Verlag, Berlin, page 203, 1941.
 - 16] A. Kochendorfer and M. Swonson. *Arch. Eisenhuttenuw*, 31:549, 1960.
 - 17] Ch. Schwink. *Phys. Stat. Sol. (a)*, 8:457, 1965.
 - 18] Ch. Schwink and W. Vorbrugg. *Z. Natureforsch*, 22A:626, 1967.
 - 19] G. I. Taylor. *Jr. Inst. Metals*, 62:307, 1938.
 - 20] J. F. W. Bishop and R. Hill. *Phil. Mag. (a)*, 42:414, 1951.
 - 21] J. F. W. Bishop and R. Hill. *Phil. Mag. (a)*, 42:1298, 1951.

- [32] B. Budianski and T. T. Wu. In *Fourth U. S. National Cong. of Appl. Mech.. ASME*. Newyork, NY, page 1175, 1962.
- [33] U. F. Kocks. *Acta Metall.*, 6:85, 1958.
- [34] U. F. Kocks. *Acta Metall.*, 8:345, 1960.
- [35] U. F. Kocks. *Metall. Trans.*, 1A:1121, 1970.
- [36] N. Hansen. *Metall. Trans.*, 16A:2167, 1985.
- [37] T. Leffers. In N. Hansen et al., editor, *Deformation of Polycrystals, Mechanism and Microstructures*, page 51, 1981.
- [38] L. Ratke and P. Ian Welch. *Z. Metallkunde*, 74:226, 1983.
- [39] J. R. Low and F. Garofalo. *Proc. Soc. Stress Anal.*, 4:16, 1947.
- [40] D. C. Ludwigson. *Metall. Trans.*, 2A:2825, 1971.
- [41] B. P. Kashyap and K. Tangri. *Acta Metall.*, 43:3971, 1995.
- [42] E. Ulvan and A. Koursaris. *Metall. Trans.*, 19A:2287, 1988.
- [43] K. G. Samuel, S. L. Mannan, and V. M. Radhakrishnan. *Int. J. Pres. Ves. and Piping*, 52:151, 1992.
- [44] P. V. Sivprasad, S. Venugopal, and S. Venkadesan. *Metall. Trans.*, 28A:171, 1997.
- [45] H. Mecking. In P. Hansen, V. Gerold, and G. Kostorz, editors, *Int. Conf. on Strength of metals and alloys (ICSMA5)*, volume 3, page 1573. Pergamon, Aachen, Germany, 1979.
- [46] H. Mecking. In A. W. Thompson, editor, *Work Hardening in Tension and Fatigue*. page 67, 1977.
- [47] H. Mecking and U. F. Kocks. *Acta Metall.*, 29:1865, 1981.

- [48] A. W. Thompson and M. J. Baskes. *Phil. Mag. (a)*, 28:301, 1973.
- [49] D. J. Lloyd. *Met. Sci.*, 14:193, 1980.
- [50] J. T. Barnby. *J. Iron Steel Inst.*, 203:392, 1965.
- [51] D. J. Michel, J. Moteff, and A. J. Lovell. *Acta Metall.*, 21:1269, 1973.
- [52] S. L. Mannan, K. G. Samuel, and P. Rodriguez. In R. C. Giffkin, editor, *Strength of Metals and Alloys*, volume 2, page 637. Pergmon Press, Oxford, 1982.
- [53] R. E. Reed-Hill. *Rev. High Temp. Mater.*, 2:214, 1974.
- [54] I. S. Kim and E. O. Hall. *Metals Forum*, 1:95, 1978.
- [55] E. O. Hall. *Proc. Phys. Soc. London*, 64B:747, 1951.
- [56] N. J. Petch. *J. Iron Steel Inst.*, 174:25, 1953.
- [57] A. W. Thompson, M. J. Baskes, and W. F. Flanagan. *Acta Metall.*, 21:1973, 1973.
- [58] A. H. Cottrell. *Trans. TMS-AIME*, 212:192, 1958.
- [59] R. W. Armstrong, I. Codd, R. M. Douthwaite, and N. J. Petch. *Phil. Mag. (a)*, 7:45, 1962.
- [60] R. W. Armstrong. *Adv. Mater. Res.*, 4:101, 1970.
- [61] M. F. Ashby. *Phil. Mag. (a)*, 21:399, 1970.
- [62] J. D. Meakin and N. J. Petch. *Phil. Mag. (a)*, 29:1149, 1974.
- [63] S. Sangal, K. J. Kurzydowski, and K. Tangri. *Acta Metall.*, 39:1281, 1991.
- [64] K. G. Samuel, S. L. Mannan, and P. Rodriguez. *Acta Metall.*, 36:2323, 1988.
- [65] J. D. Eshelby, F. C. Frank, and F. R. N. Nabarro. *Phil. Mag. (a)*, 42:351, 1951.
- [66] J. E. Baily and P. B. Hirsch. *Phil. Mag. (a)*, 5:485, 1960.

- [67] J. E. Baily. *Phil. Mag. (a)*, 8:223, 1963.
- [68] J. D. Meakin and N. J. Petch. In *Role of Substructure in Mechanical Behavior of Metals*, page 243, 1963.
- [69] J. C. M. Li. *Trans TMS-AIME*, 227:239, 1963.
- [70] M. F. Ashby. In A. Kelly and R. B. Nicholson, editors, *Strengthening methods in crystals*, page 137, New York, 1971. Wiley.
- [71] A. H. Cottrell. *The mechanical properties of matter*. Wiley, New York, NY, 1964.
- [72] J. D. Livingston and B. Chalmers. *Acta Metall.*, 5:322, 1957.
- [73] J. J. Hauser and B. Chalmers. *Acta Metall.*, 9:802, 1961.
- [74] A. W. Thompson, M. J. Baskes, and W. F. Flanagan. *Acta Metall.*, 21:1017, 1973.
- [75] A. W. Thompson. In A. W. Thompson, editor, *Work Hardening in Tension and Fatigue*, page 89, 1977.
- [76] N. Hansen and B. Ralph. *Acta Metall.*, 30:411, 1982.
- [77] R. W. Armstrong, Y. T. Chou, R. A. Fisher, and N. Louat. *Phil. Mag. (a)*, 14:943, 1966.
- [78] S. Sangal and K. Tangri. *Scripta Metall.*, 23:2079, 1989.
- [79] E. Macherauch. *Z. Metallkunde*, 59:669, 1968.
- [80] A. W. Thompson. *Acta Metall.*, 25:83, 1977.
- [81] A. W. Thompson and B. C. Wonsiewicz. *Metall. Trans.*, 12A:531, 1981.
- [82] S. Riegger, O. Vorhringer, and E. Macherauch. In *4th Int. Conf. Proc. on Strength of Metals and Alloys*, page 116, 1976.
- [83] N. Ono and S. Karishma. *Scripta Metall.*, 16:381, 1982.

-
- [84] R. A. Varin and K. Tangri. *Z. Metallkunde*, 73:144, 1982.
- [85] R. A. Varin and E. Romanowska-Haftek. *Metall. Trans.*, 17:1967, 1986.
- [86] M. W. Grabski and R. Korski. *Phil. Mag. (a)*, 22:707, 1970.
- [87] R. A. Varin. *Phys. Stat. Sol.(a)*, 52:347, 1979.
- [88] V. Kutumba Rao, D. M. R. Taplin, and P. Rama Rao. *Metall. Trans.*, 6A:77, 1975.
- [89] R. A. Varin. *Z. Metallkunde*, 73:654, 1982.
- [90] R. A. Varin and K. Tangri. *Metall. Trans.*, 12A:1859, 1981.
- [91] R. A. Varin and K. J. Kurzydowski. *Z. Metallkunde*, 74:177, 1983.
- [92] J. W. Cahn. *Journal of Phys.*, 43:66, 1982.
- [93] G. Goux. *Surface Science*, 31:496, 1972.
- [94] K. J. Kurzydowski and W. Przetakiewicz. *Scripta Metall.*, 22:249, 1988.
- [95] K. J. Kurzydowski. *Mat. Char.*, 26:57, 1990.
- [96] R. W. Armstrong. *Acta Metall.*, 16:347, 1968.
- [97] Y. Bergstron and H. Hallen. *Metal Science*, 17:341, 1983.
- [98] L. R. Morris, H. Song, and D. M. Moore. In *4th Int. Conf. Proc. on Strength of Metals and Alloys*, volume 1, page 131, 1976.
- [99] R. Z. Valiev and O. A. Kaibyshev. *Acta Metall.*, 31:2121, 1983.
- [100] P. B. Hirsch, A. Howie, R. B. Nicholson, D. W. Pashley, and M. J. Whelan. In E. Krieger Robert, editor, *Electron Microscopy of Thin Crystals*, page 485, Malabar, Florida, 1977. Pergmon Press, Oxford.
- [101] F. C. Bell and D. E. Sonon. *Metallography*, 9:91, 1976.

- [102] A. W. Thompson. *Metallography*, 5:366, 1972.
- [103] Ewald R. Weibel. *STEREOLOGICAL METHODS*, volume 2. Academic Press, 1980.
- [104] Robert T. Dehoff and Frederick N. Rhines. *Quantitative Microscopy*. Mc Graw-Hill Book Company, New York, 1968.
- [105] F. Garofalo. *Proc. ASTM*, 60:738, 1960.
- [106] D. Harker and E. R. Parker. *Trans. A. S. M.*, 34:156, 1945.
- [107] P. E. Gill and W. Murray. *Minimization subject to bounds on the variables*. National Physical Laboratory Report, 1976.
- [108] P. E. Gill and W. Murray. *SIAM Journal on Numerical Analysis*, 15:977, 1978.
- [109] N. Ohkubo, K. Miyakusu, Y. Uematsu, and H. Kimura. *ISIJ Int.*, 34:764, 1994.
- [110] R. E. Schramm and R. P. Reed. *Metall. Trans.*, 6A:1345, 1975.
- [111] D. Dulieu and J. Nutting. *J. Iron Steel Inst. Spec. Rep.*, 86:140, 1964.
- [112] J. F. Breedis. *Trans. AIME*, 230:1583, 1964.
- [113] B. P. Kashyap, K. Mc. Taggart, and K. Tangri. *Phil. Mag. (a)*, 57:97, 1988.
- [114] R. A. Jago and N. Hansen. *Acta Metall.*, 34:1711, 1986.
- [115] R. Z. Valiev, W. Yu. Gertsman, O. A. Kaibyshev, and Sh. Kh. Khannanov. *Phys. Stat. Sol. (a)*, 61:96, 1980.
- [116] M. W. Grabski, R. Z. Valiev, and W. Wyrzykowski. *Res. Mechanica Letter*, 1:489, 1981.
- [117] H. Gleiter. *Scripta Metall.*, 11:305, 1977.
- [118] H. Gleiter. *Phil. Mag. (a)*, 36:1109, 1977.

- [119] W. Lojkowski, H. O. K. Kirchner, and M. W. Grabski. *Scripta Metall.*, 11:1127, 1977.
- [120] R. Z. Valiev and O. A. Kaibyshev. *Phys. Stat. Sol.(a)*, 44:66, 1977.
- [121] T. P. Darby, R. Schindler, and R. W. Balluffi. *Phil. Mag. (a)*, 37A:245, 1978.
- [122] V. Vitek, A. P. Sutton, D. A. Smith, and R. C. Pond. *Phil. Mag. (a)*, 39A:213, 1979.
- [123] R. C. Pond and D. A. Smith. *Phil. Mag. (a)*, 36:353, 1977.
- [124] R. Z. Valiev, V. Yu. Gerchman, and O. A. Kaibyshev. *Phys. Stat. Sol.(a)*, 61:K95, 1980.
- [125] O. A. Kaibyshev and R. Z. Valiev. *JOURNAL DE PHYSIQUE*, 46:641, 1985.
- [126] D. Sil and S. K. Varma. *Metall. Trans.*, 24A:1153, 1993.
- [127] S. L. Mannan and P. Rodriguez. *Acta Metall.*, 23:221, 1975.
- [128] S. V. Ramani and P. Rodriguez. *Can. Met. Quart.*, 11:61, 1972.
- [129] R. W. Balluffi and T. Schober. *Scripta Metall.*, 6:697, 1972.
- [130] W. A. T. Clark and D. A. Smith. *Jr. Mat. Sci.*, 14:776, 1979.
- [131] T. Johannesson and A. Tholen. *Metal Sci.*, 6:189, 1972.
- [132] J. P. Hirth. *Metall. Trans.*, 3A:3047, 1972.
- [133] U. Essmann, M. Rapp, and M. Wilkins. *Acta Metall.*, 16:1275, 1968.
- [134] Y. Bergstrom. *Mater. Sci. Engg.*, 5:193, 1970.
- [135] H. Conrad, S. Feuerstein, and L. Rice. *Mater. Sci. Engg.*, 2:157, 1967.
- [136] D. J. Dingley and D. Mc Lean. *Acta Metall.*, 15:885, 1967.

-
- [137] J. P. Bailon, A. Loyer, and J. M. Dorlot. *Mater. Sci. Engg.*, 8:288, 1971.
- [138] A. S. Keh and S. Weissman. In G. Thomos and J. Washburn, editors. *Electron Microscopy and strength of crystals*, page 231. Interscience, New York, NY, 1963.
- [139] H. E. Boyer and T. L. Gall. *Metals Handbook*. Metals Park, Ohio, 1985.
- [140] A. F. Smith and G. B. Gibbs. *Metal Sci.*, 3:93, 1969.
- [141] S. Venkadesan, P. V. Sivprasad, S. Ray, and V. Seetharaman. *Z. Metallkunde*, 79:226, 1988.

Appendix A

Annealing data of 316L austenitic stainless steel

Table A.1: Grain size and hardness data for different annealing treatments.

Batch	Annealing		$d(\mu m)^*$	Hardness (VHN)
	Temperature($^{\circ}$ C)	Time(Min.)		
I	750	70	$2.7 \pm .06$	353
	800	25	$3.3 \pm .11$	294
	800	70	$3.7 \pm .11$	282
	800	90	$3.9 \pm .10$	279
	800	260	$4.3 \pm .08$	275
	850	25	$4.2 \pm .20$	253
	850	70	$4.3 \pm .20$	243
	850	260	$4.5 \pm .30$	237
	850	490	$5.1 \pm .28$	236

* by intercept method with 90% confidence limit

Table A1 (continued)

Batch	Annealing		$d(\mu\text{m})^*$	Hardness (VHN)
	Temperature($^{\circ}\text{C}$)	Time(Min.)		
1	900	70	$6.0 \pm .26$	205
	900	100	$8.5 \pm .29$	202
	900	120	$9.0 \pm .37$	202
	900	130	$12.1 \pm .69$	201
	900	230	$18.3 \pm .67$	201
	900	250	$20.8 \pm .68$	201
	900	1440	24.6 ± 1.07	201
	925	70	$13.4 \pm .73$	190
	925	90	$18.0 \pm .80$	187
	925	130	$23.6 \pm .94$	185
	925	205	$24.6 \pm .92$	182
	950	25	$15.9 \pm .48$	172
	950	35	$26.5 \pm .80$	169
	950	70	35.8 ± 1.14	165
	950	130	37.4 ± 1.12	159
	950	250	41.0 ± 1.49	159
	1000	25	44.8 ± 1.88	170
	1000	70	48.8 ± 2.08	161
	1000	250	62.0 ± 3.69	153
	1000	260	64.0 ± 2.09	152
	1050	25	48.0 ± 1.86	159
	1050	70	72.7 ± 3.94	155
	1050	250	82.2 ± 2.67	152
	1050	510	94.8 ± 3.76	151

* by intercept method with 90% confidence limit

Table A1 (continued)

Batch	Annealing		$d(\mu m)^*$	Hardness (VHN)
	Temperature($^{\circ}$ C)	Time(Min.)		
1	1100	25	63.9 ± 3.76	157
	1100	70	81.1 ± 3.62	151
	1100	250	109.0 ± 4.17	149
	1100	560	136.9 ± 6.27	148
	1150	25	94.9 ± 3.20	151
	1150	70	107.4 ± 2.94	151
	1150	130	116.0 ± 5.01	151
	1150	250	141.3 ± 6.35	150
2	800	30	3.9 ± 0.04	202
	800	60	4.0 ± 0.06	198
	800	125	4.3 ± 0.09	192
	850	60	5.3 ± 0.10	190
	850	165	5.8 ± 0.11	183
	850	180	5.9 ± 0.29	181
	875	60	9.0 ± 0.35	183
	900	20	15.0 ± 0.74	175
	900	60	29.0 ± 1.17	155
	900	120	33.5 ± 1.55	153
	950	60	45.9 ± 1.86	151

* by intercept method with 90% confidence limit

Appendix B

Probability of orientation in space

In real polycrystals the triple edges are randomly oriented. Therefore, it is necessary to average any property over the domain of all orientations to obtain total properties [103, 104]. Let the orientation of a triple edge be defined by angles θ and ϕ , as shown in figure B1. Consider some small range of orientations specified by θ and ϕ and varying by amounts $d\theta$ and $d\phi$ respectively. The spherical range of this orientation is shown in figure B1. If the test orientations are uniformly distributed over the sphere, the fraction which lies within the range θ to $\theta + d\theta$ and ϕ to $\phi + d\phi$ is equal to the fraction of sphere which is occupied by spherical image of the orientation range.

From figure B1, the enclosed area is $1(d\theta)(1)(\sin\theta \, d\phi)$, where 1 being the radius of the sphere. The spherical image of whole range of orientation is 4π . The ratios of these two quantities is equal to the probability that an orientation selected at random lies within the range $\theta + d\theta$ and ϕ to $\phi + d\phi$, the combined frequency function for θ and ϕ may be expressed as follows:

$$P(\theta, \phi) = \frac{\sin\theta \, d\phi \, d\theta}{4\pi} \quad (\text{B.1})$$

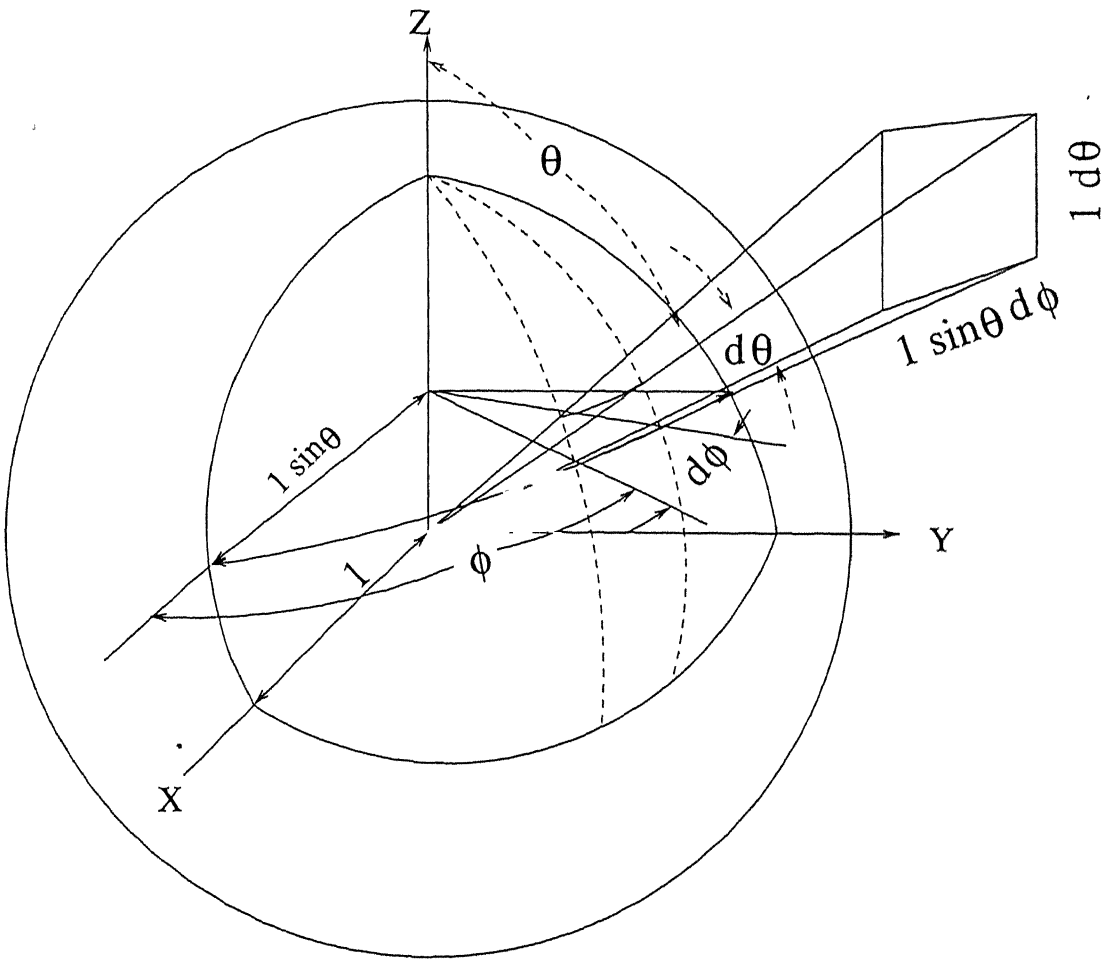


Figure B.1: The fraction of the surface area of the unit sphere occupied by the orientation range ϕ to $\phi + d\phi$, and θ to $\theta + d\theta$, is $1(d\theta)(1)(\sin\theta d\phi)$.

Appendix C

Optimization method to minimise a function

A optimum value of unknown x , can be obtained by applying this method at which function value is minimum. In this case it is assumed that the function has continuous second derivatives in the neighbourhood of the solution. This method [107,108] constructs a sequence $\{x^k\}$ satisfying:

$$x^{k+1} = x^k + \alpha^k p^k \quad (\text{C.1})$$

where α^k is the step length and the vector p^k is termed as the direction of search. The step length α^k is chosen so that $F(x^{k+1}) < F(x^k)$ and computed using Quasi-Newton method [107]. This method approximates the Hessian matrix $G(x)$, which is the second derivative of the function $F(x)$, by a matrix B^k . This matrix B^k is modified at each iteration to include information about the curvature of $F(x)$ along the current search direction p^k .

From the starting point supplied by the user, a sequence of feasible points generated which is intended to converge to a local minimum of the constrained function, on the basis of estimates of the gradient and the curvature of $F(x)$. An attempt is made in the

method to verify that the final point is a global minimum.

Appendix D

Optimization Programs

D.1 Program to generate the coefficients

c G05DAF Example Program Text

c Mark 14 Revised. NAG Copyright 1989.

integer l,la

parameter (l=M,la=l*1)

double precision z(la),y(l),r(l)

double precision x0,x1,x2,x3,x4,x5,x6,x7,x8,x9,x10,x11,x12,x13

double precision dd1,pd1,c1,c2,a,b,cm

c .. Local Scalars ..

INTEGER I

c .. External Functions ..

DOUBLE PRECISION G05DAF

```
EXTERNAL G05DAF
c .. External Subroutines ..
EXTERNAL G05CBF
open(unit=26,file='co-eff')
c .. Executable Statements ..
CALL G05CBF(0)
c GETTING PLANE DIHEDRAL ANGLE DISTRIBUTION FROM A
CLASS OF TRUE DIHEDRAL ANGLE
c *****
mn=0
width = 180.0/M
c1=0.0
c2= M
do 10 j=1,l
  ysum=0
  do i=1,l
    y(i)=0
  end do
  if(j eq. 1) c2=180.0
  nm=0
  do 70 i=1,10000
    aa = G05DAF(0.0D0,1.0D0)
    a=(acos(1.0-2*aa))*57.29578
    bb = G05DAF(0.0D0,1.0D0)
    b=bb*360.0
```

```

cm = G05DAF(c1,c2)
x0=cos(a*0.0174532)
e1 = G05DAF(0.0D0,1.0D0)
f=e1+0.5*x0
if(e1 .gt. 0.5 .and. f .gt. 0.5) go to 70
if(e1 .lt. 0.5 .and. f .lt. 0.5) go to 70
nm=nm+1
x1=x0**2
x2=cos(cm*0.0174532)
x3=1.0-x1
x4=cos(b*0.0174532)
x5=cos((b-cm)*0.0174532)
x6=1.0-x4**2
x7=1.0-x5**2
x8=x1*x2+x3*x4*x5
x9=1.0-x3*x6
x10=1.0-x3*x7
x11=x9*x10
x12=sqrt(x11)
x13=x8/x12
ddl=acos(x13)
pd1=57.29578*ddl
c  OBTAINING THE FREQUENCIES TABLE FROM THE pda DATA
c  *****
if(pd1.ge. 165 .and. pd1 .le. 180.0) y(l)=y(l)+1

```

```
      if(pd1.lt.15.0) y(1)=y(1)+1
      do 80 k=2,l-1
      n1=10*k-5
      n2=10*k+5
      if(pd1.ge.n1.and. pd1.lt. n2) y(k)=y(k)+1
80    continue
70    continue
      write(*,*) nm
      do lm=1,l
      ysum=ysum+y(lm)
      end do
      do k=1,l
      mn=mn+1
      z(mn)=y(k)/ysum
      end do
      c1=c2
      c2=c1+10.0
10    continue
      do n=1,l
      do ll=1,l
      m=l*(ll-1)+n
      r(ll)=z(m)
      end do
      Write(26,50) (r(ll),ll=1,l)
      end do
```

```
50  format(1x,17f4.2)
    STOP
    END
```

D.2 Optimization Program to calculate the unknown parameters of linear simultaneous equations by minimising the error

```
c  Mark 14 Revised. NAG Copyright 1989.
c  WRITE (NOUT,*) 'E04JAF Example Program Results'
c  .. Parameters ..
    INTEGER N, LIW, LW
    PARAMETER      (N=17,LIW=N+2,LW=N*(N-
    1)/2+12*N)
    INTEGER NOUT
    PARAMETER (NOUT=6)
c  .. Local Scalars ..
    DOUBLE PRECISION F
    INTEGER IBOUND, IFAIL, J
c  .. Local Arrays ..
    DOUBLE PRECISION BL(N), BU(N), W(LW), X(N)
    INTEGER IW(20)
c  .. External Subroutines ..
```

```
EXTERNAL E04JAF
open(unit=10,file='td26.5')
lp=10
X(1) = 0.0D0
X(2) = 0.0D0
X(3) = 0.0D0
X(4) = 0.0D0
X(5) = 0.0D0
X(6) = 0.0D0
X(7) = 0.0D0
X(8) = 0.05D0
X(9) = 0.02D0
X(10) = 0.05D0
X(11) = 0.08D0
X(12) = 0.3D0
X(13) = 0.25D0
X(14) = 0.18D0
X(15) = 0.03D0
X(16) = 0.01D0
X(17) = 0 0D0
IBOUND = 2
IFAIL = 1
CALL E04JAF(N,IBOUND,BL,BU,X,F,IW,LIW,W,LW,IFAIL)
IF (IFAIL.NE.0) THEN
WRITE (lp,99999) 'Error exit type', IFAIL,
```

```
+ ' - see routine document'
END IF
IF (IFAIL.NE.1) THEN
WRITE (lp,99998) 'Function value on exit is ', F
WRITE (lp,*) 'at the point'
do j=1,N
mm=10*j
WRITE (lp,99997) mm,X(j)
end do
end if
stop
99999 FORMAT (1X,A,I3,A)
99998 FORMAT (1X,A,F18.4)
99997 FORMAT (1X,i5,f5.3)
END
SUBROUTINE FUNCT1(N,XC,FC)
c Routine to evaluate objective function.
c This routine must be called FUNCT1.
c .. Scalar Arguments ..
DOUBLE PRECISION FC
INTEGER N
c .. Array Arguments ..
DOUBLE PRECISION XC(N),a(N,N),b(N),d(N)
DOUBLE PRECISION xy,xk,yy
open(unit=100,file='rfreq5')
```

```
open(unit=101,file='pd26.5')
lm=100
ln=101
c .. Executable Statements ..
do i=1,N
read(lm,*) (a(i,j),j=1,N)
read(ln,*) b(i),d(i)
end do
close(unit=lm)
close(unit=ln)
yy=0.0
xk=0.0
do i=1,N
xy=0.0
do j=1,N
xy=xy+a(i,j)*xc(j)
end do
xk=xk+xc(i)
yy=yy+(xy-d(i))**2
end do
xk=(xk-1.0)**2
fc=yy+xk
RETURN
END
```


Appendix E

Values of strain hardening parameters

Table E.1: Values of the parameters of Hollomon equation (2.13) and Ludwigson equation (2.17) in different regions of strains at various temperatures and for grain sizes.

T ($^{\circ}\text{C}$)	d (μm)	Hollomon parameters						Ludwigson parameters		
		Region 1			Region 3					
		K_1	n_1	ϵ_{12}	ϵ_{e23}	K_3	n_3	K_2	n_2	ϵ_L
25	2.7	985.8	0.04	0.015	0.04	1524.20	0.17	5.61	-84.84	.049
	3.9	630.9	0.02	0.02	0.06	1527.30	0.27	5.68	-58.64	.075
	4.5	550.3	0.01	0.013	0.06	1614.20	0.33	5.70	-45.98	.096
	6.0	535.9	0.05	0.005	0.09	1461.20	0.36	5.50	-47.43	.093
	9.0	393.1	0.01	0.01	0.07	1401.30	0.37	5.37	-44.42	.097
	18.3	383.3	0.03	0.007	0.08	1350.40	0.38	5.26	-36.29	.115
	26.5	365.1	0.03	0.007	0.07	1291.70	0.37	5.20	-53.96	.080
	64.0	557.5	0.15	0.03	0.06	1166.00	0.40	4.90	-38.72	.105
200	2.7	874.2	0.05	0.017	0.15	1197.90	0.15	5.20	-82.97	.047
	3.9	571.3	0.03	0.02	0.04	1135.90	0.23	5.40	-78.28	.056
	4.5	433.5	0.01	0.017	0.05	1148.80	0.28	5.40	-85.29	.053
	6.0	541.4	0.12	0.023	0.05	1003.60	0.32	4.75	-45.04	.087
	9.0	284.8	0.03	0.005	0.06	1054.10	0.37	4.80	-45.52	.089
	18.3	309.4	0.04	0.01	0.07	1042.40	0.40	5.03	-38.10	.112
	26.5	295.6	0.08	0.006	0.08	1083.90	0.47	4.89	-34.21	.123
	64.0	318.7	0.09	0.013	0.07	1040.40	0.47	4.85	-31.98	.131
400	2.7	595.4	0.02	0.008	0.03	972.00	0.14	5.07	-129.66	.031
	3.9	465.0	0.02	0.017	0.05	1082.80	0.25	5.29	-80.01	.055
	4.5	429.0	0.03	0.014	0.05	1134.00	0.29	5.33	-100.82	.045
	6.0	355.9	0.06	0.015	0.08	1054.90	0.39	4.80	-35.63	.112
	9.0	337.7	0.06	0.044	0.07	1152.20	0.46	5.07	-42.11	.104
	18.3	247.7	0.05	0.008	0.06	1082.80	0.45	4.78	-41.57	.100
	26.5	233.8	0.05	0.008	0.10	1117.30	0.50	4.75	-26.21	.152
	64.0	189.2	0.06	0.009	0.10	1106.10	0.58	4.61	-28.14	.144

Table E1 (continued)

T ($^{\circ}\text{C}$)	d (μm)	Hollomon parameters						Ludwigson parameters		
		Region 1			Region 3					
		K_1	n_1	ϵ_{12}	ϵ_{e23}	K_3	n_3	K_2	n_2	ϵ_L
600	2.7	715.7	0.06	0.03	0.04	768.00	0.09	4.09	-65.92	.046
	3.9	442.0	0.03	0.02	0.02	813.20	0.19	4.93	-96.89	.043
	4.5	362.6	0.02	0.013	0.04	903.20	0.26	4.95	-79.96	.053
	6.0	337.2	0.05	0.02	0.07	880.90	0.36	4.97	-39.51	.109
	9.0	410.8	0.14	0.02	0.09	911.10	0.41	4.62	-28.17	.139
	18.3	314.9	0.13	0.016	0.07	913.60	0.45	4.42	-32.53	.119
	26.5	255.1	0.09	0.015	0.05	829.50	0.41	4.26	-49.89	.078
	64.0	217.8	0.08	0.011	0.08	916.80	0.52	4.79	-42.93	.104
800	2.7					230.40	0.03			
	3.9					254.40	0.07			
	4.5					204.90	0.03			
	9.0					256.30	0.08			
	18.3					268.40	0.14			
	26.5					279.50	0.15			
	64.0					253.30	0.17			

Table E.2: Values of the parameters of Ludwik equation (2.14) in different regions of strains at various temperatures and for grain sizes.

T ($^{\circ}C$)	d (μm)	Region 1				Region 2				Region 3		
		σ_0	K_1	n_1	ϵ_{12}	σ_0	K_2	n_2	ϵ_{c23}	σ_0	K_3	n_3
25	2.7	865.9	-5.4	-.47	.010	782.4	2280.9	.95	.07	-750.1	2382.7	.10
	3.9	520.5	395.3	.34	.013	541.1	1819.9	.83	.04	75.9	1464.1	.30
	4.5	-	-	-	.013	509.3	2478.2	.97	.04	286.1	1427.5	.47
	6.0	124.3	404.9	.06	.010	378.8	1592.4	.80	.13	-1019.5	2426.9	.17
	9.0	365.3	2013.2	1.01	.013	337.7	1442.3	.76	.20	-4077.4	5514.6	.06
	18.3	193.3	221.5	.09	.005	312.6	1394.4	.74	.20	-9674.2	11007.7	.03
	26.5	293.0	11673.1	1.27	.007	274.0	1328.2	.69	.13	-771.5	1996.8	.18
	64.0	166.5	786.4	.44	.020	246.3	1221.2	.76	.20	-2289.8	3449.5	.10
200	2.7	695.6	-.2	-.92	.010	650.8	1922.1	.93	.06	2274.7	-877.6	-.11
	3.9	595.0	-50.7	-.14	.020	468.1	1899.3	.93	.08	3704.8	-2527.3	-.06
	4.5	-	-	-	.020	332.9	1174.2	.66	.11	-1588.6	2740.2	.09
	6.0	283.4	1666.9	.90	.060	176.9	935.5	.48	.20	1380.4	-122.7	-.62
	9.0	227.7	1445.3	.80	.080	133.2	1013.2	.49	.26	4100.7	-66.6	-.93
	18.3	200.1	222.1	.27	.005	236.1	1223.0	.83	.10	154.2	999.3	.57
	26.5	178.0	909.8	.69	.060	192.0	1176.8	.83	.23	3127.0	-72.4	-1.00
	64.0	170.7	852.8	.69	.060	186.9	1177.4	.85	.23	-	-	-
400	2.7	508.2	324.3	.43	.007	525.6	1427.6	.84	.04	1226.7	-188.7	-.27
	3.9	412.9	10658.0	1.49	.022	367.2	1284.3	.73	.08	-1077.4	2117.9	.09
	4.5	301.4	232.8	.25	.015	346.6	2114.6	.91	.05	31.3	1101.4	.30
	6.0	201.0	446.1	.42	.022	227.3	1334.8	.81	.18	168.6	959.6	.57
	9.0	221.4	1659.3	1.00	.040	161.9	1179.2	.70	.25	2347.5	-263.5	-.56
	18.3	157.7	641.1	.54	.005	163.0	1062.4	.69	.20	-1889.3	3088.5	.11
	26.5	143.5	831.7	.63	.008	152.2	1111.7	.73	.27	3504.2	-1361.2	-.17
	64.0	117.1	687.3	.67	.005	122.8	1188.4	.84	.20	-905.4	2108.1	.18

Table E.3: Values of the parameters of Ludwik equation (2.14) in different regions of strains at various temperatures and for grain sizes

T (°C)	d (μm)	Region 1				Region 2				Region 3		
		σ_0	K_1	n_1	ϵ_{12}	σ_0	K_2	n_2	ϵ_{e23}	σ_0	K_3	n_3
600	2.7	569.8	-1.3	-.64	.007	506.8	646.7	.75	.06	1234.5	-377.1	-.11
	3.9	286.9	246.5	.17	.030	307.1	763.1	.51	.10	11897.4	-1.4	-1.76
	4.5	310.4	2943.3	1.09	.030	179.2	779.7	.39	.13	334.5	1022.2	1.02
	6.0	149.9	274.1	.19	.015	231.4	887.3	.76	.20	1285.2	-81.8	-.80
	9.0	216.1	-1.7	-.54	.004	158.1	838.7	.63	.30	-	-	-
	18.3	104.1	328.2	.33	.015	138.6	966.1	.72	.20	-	-	-
	26.5	115.5	409.2	.46	.007	137.6	1401.3	.84	.15	91.7	818.1	.55
	64.0	117.6	639.4	.64	.060	120.6	997.4	.82	.26	-	-	-
800	2.7	232.5	-7.7	-.37	.060	204.0	62.1	.98	.20	-	-	-
	3.9	304.0	-49.1	-.23	.060	-	-	-	.15	-	-	-
	4.5	-	-	-	.015	187.1	90.7	1.24	.20	-	-	-
	9.0	86.4	175.1	.13	.020	171.7	128.8	.50	.12	-	-	-
	18.3	121.8	185.7	.40	.150	155.3	98.2	.62	.25	-	-	-
	26.5	111.2	347.7	.52	.006	-22.0	299.9	.13	.20	-	-	-
	64.0	108.4	242.0	.57	.120	448.7	-1.3	-1.49	.26	-	-	-

Table E.4: Values of the parameters of Ludwik equation (2.14) at various temperatures and for grain sizes in the entire range of strains.

d (μm)	T ($^{\circ}C$)	σ_0	K	n	T ($^{\circ}C$)	σ_0	K	n
2.7	25	739.3	1123.4	.60	200	624.2	989.4	.64
3.9		516.0	1300.8	.64		446.7	1058.2	.68
4.5		483.4	1531.8	.75		329.1	1042.0	.60
6.0		363.8	1340.4	.69		230.6	915.9	.56
9.0		335.3	1287.1	.69		213.2	1019.3	.63
18.3		285.4	1200.5	.62		224.7	1046.4	.73
26.5		252.1	1138.8	.58		175.2	1087.4	.75
64.0		208.5	1080.8	.63		177.6	1109.2	.79
2.7	400	499.4	727.0	.55	600	491.1	384.5	.45
3.9		357.7	972.9	.60		362.0	827.5	.72
4.5		306.0	1048.6	.60		277.7	843.3	.59
6.0		214.6	1010.3	.67		221.5	810.7	.69
9.0		206.1	1190.2	.79		158.3	830.5	.61
18.3		162.2	1094.6	.70		130.0	904.9	.66
26.5		152.6	1090.5	.72		121.9	855.8	.63
64.0		118.6	1156.2	.81		120.1	921.7	.76
2.7	800	137.6	108.9	.16				
3.9		99.7	244.4	.29				
4.5		170.8	27.8	.13				
9.0		155.9	112.8	.29				
18.3		133.5	160.9	.42				
26.5		109.4	191.3	.34				
64.0		103.7	169.3	.42				

Table E.5: Values of the parameters of Voce equation (2.15) at various temperatures and for grain sizes in the entire range of strains.

d (μm)	T ($^{\circ}C$)	σ_s	σ_1	n_v	T ($^{\circ}C$)	σ_s	σ_1	n_v
2.7	25	1328.2	777.3	6.06	200	1012.6	646.2	8.38
3.9		1318.4	551.5	4.17		947.7	461.8	5.65
4.5		1517.2	497.0	2.94		942.9	373.4	4.92
6.0		1344.8	391.3	2.90		811.5	287.7	4.66
9.0		1275.9	359.0	2.93		834.5	240.5	4.39
18.3		1171.0	328.5	3.32		971.2	243.6	2.71
26.5		1116.1	304.2	3.46		1025.8	192.6	2.35
64.0		1110.6	265.8	2.56		1070.4	189.6	2.09
2.7	400	795.3	524.0	11.08	600	663.2	517.5	14.01
3.9		880.6	399.4	5.64		692.8	369.3	6.57
4.5		899.3	344.1	5.34		721.6	307.1	6.06
6.0		926.7	243.3	3.11		812.0	243.2	2.91
9.0		1101.9	213.2	2.38		773.2	198.2	3.28
18.3		993.3	189.9	2.67		734.9	157.9	3.43
26.5		1000.2	175.2	2.50		622.2	146.2	4.64
64.0		1173.5	130.8	1.71		883.0	134.8	2.14
2.7	800	217.3	150.8	71.98				
3.9		214.5	109.4	62.91				
4.5		194.6	180.9	14.71				
9.0		223.9	166.4	24.61				
18.3		230.2	142.4	9.95				
26.5		228.2	126.2	14.79				
64.0		206.1	113.1	10.50				

128771

128771

date last stamped.